



INSTITUUT VOOR MARIEN EN ATMOSFERISCH ONDERZOEK UTRECHT


De functie en het gedrag van kortsluitgeulen in het westelijk
deel van de Westerschelde (eindrapport contract ZL-3612)

Deel 2: figuren, tabellen en bijlagen

drs M.C.J.L. Jeuken

R 98-06

DE FUNCTIE EN HET GEDRAG VAN KORTSLUITGEULEN IN HET
WESTELIJK DEEL VAN DE WESTERSCHELDE.

 Deel 2: figuren, tabellen en bijlagen.

Eindrapport voor het contract ZL-3612

Juli 1998

M.C.J.L. Jeuken

List of Figures

- 2.1 Schematic representation of a morphodynamic system
- 2.2 The funnel shaped geometry of the Schelde estuary and the four morphologically distinct zones:
 - a) tidal delta;
 - b) multiple tidal channel system in the Westerschelde;
 - c) single tidal channel system;
 - 4) tidal channel directly linked to the river channel.
- 2.3 The three recurring arrangements of ebb and flood channels according to van Veen (1950):
 - a) the forked tongue pattern
 - b) the flanking attack pattern
 - c) the wide estuary pattern
- 2.4 Tidal meanders.
 - a) the ideal channel pattern of Van Veen (1950), consisting of sine-shaped ebb channels and straight flood channels that start in each bend. The arrows show the expected circulation cells.
 - b) 'the estuarine meander' of Ahnert (1960).
 - c) the cusped 'estuarine meanders' of South Alligator River. The arrows show the course of the maximum flood velocity path and the large eddies around mid the channel flats (after Vertessy, 1990, in Carter and Woodroffe, 1994).
- 2.5 Bathymetric map of the Westerschelde in greyscale. Dark shades indicate deep areas, light shades are shallow areas. White spots indicate 'no data areas'.
- 2.6 Schematized geomorphology of the various ebb and flood channels within the Westerschelde. The bathymetric map of 1990 was used as a basis for schematizing. Three different types of tidal channels exist: main channels, secondary channels and connecting channels.
- 2.7 Subdivision into three different types of connecting channels based on the geographical location within the main channel system. a) bar channels, b) cross channels, c) margin channels.
- 2.8 The subdivision of the channel and flat system into six estuarine sections. Each estuarine section has a mutually evasive meandering ebb channel and a straight flood channel separated by tidal flats and connected by connecting channels. 1= Vlissingen section, 2= Terneuzen section, 3= Hansweert section, 4= Baalhoek section, 5= Bath section, 6= border section.
- 2.9 The meandering of the main ebb channels, and accompanied extension of the flood channels and flats between 1860 and 1994 (after Van den Berg. et.al., in prep.).
- 2.10 Time and space scales of the estuarine morphology
- 2.11 Time and space scales of the estuarine hydrodynamics.
- 2.12 Deformation of the tidal wave along the Schelde estuary.
 - a) vertical tide along the Schelde with the horizontal tide at Vlissinge.
 - b) tidal range.
 - c) mean high water and mean low water along the estuary.

- d) tidal basin storage and flood volume along the estuary.
- 2.13 The subdivision of the channels into channel sections according to the Duflow schematization. The heavy, interrupted lines indicate the channel axes. Two depth contours of the bathymetric map of 1982 are indicated: ---- = Mean Low Water Spring (NAP-2.5m), ——— = Mean Low Water Spring -8m (NAP-10.5m).
- 2.14 Along channel morphometry based on the Duflow schematization.
- a) the ebb channel;
 - b) the flood channel;
 - c) the channel sections and nodes according to Duflow;
- A dimensionless hydraulic radius (R/R_{mean}) shows the averaged depth along the channel. The cross-sectional area is divided by the averaged cross-sectional area of the entire ebb channel. The averaged cross-sectional area and hydraulic radius are weighted for the channel length as
- $$A_{\text{mean}} = \sum_{i=28}^{i=37} \left(\frac{L_{\text{section } i}}{L_{\text{channel}}} * A_{\text{section } i} \right)$$
- The dimensionless parameter $(1-(R/R_o))$ visualizes the channel bed ($R_o=30\text{m}$). The sections 45 and 52 are joined by considering the averaged depth and the sum of the cross-sectional areas. The values of the parameters are plotted in the middle of each channel section.
- 2.15 Water levels and current velocities in the main ebb and flood channel at maximum tidal flow.
- a) flow response in the ebb channel at maximum flood
 - b) flow response in the flood channel at maximum flood
 - c) flow response in the ebb channel during maximum ebb
 - d) flow response in the flood channel during maximum ebb.
- The waterlevel of section 45 is plotted. (R =hydraulic radius, $R_o=30\text{m}$). Note that the ebb values are negative and flood values positive.
- 2.16 Values of the variables in the simplified momentum equation at maximum flow ($\Delta h/\Delta L = Q^2/A^2 R^2 C^2$).
- a) Values of the various variables at maximum ebb flow
 - b) Values of the various variables at maximum flood flow.
- The variables discharge (Q), cross-sectional area (A), cross-sectional velocity (U), and hydraulic radius (R), are weighted for the length of the specific channel section, according to e.g. $A_{\text{mean}} = \sum_{i=28}^{i=37} \left(\frac{L_{\text{section } i}}{L_{\text{channel}}} * A_{\text{section } i} \right)$
- 2.17 The initial adaptations in flow pattern and water level pattern due to morphological changes. Each figure presents the following four situations: A) reference situation. B) the channel pattern without the large cross channel, C) the effect of a clockwise rotation of the cross channel of 30° . D) the effect of a deepening of the flood channel bar by 15 %. Solid heavy line = increase with respect to the reference situation, dotted line indicates a decrease.
- a) situation at maximum ebb;
 - b) situation at maximum flood;

- 2.18 Calculated sediment transport capacity (kg/s) according to Van Rijn (1990) at maximum flow, using the the flow response of DufLOW.
(R =hydraulic radius, R_o =30m).
a) flood transport capacity in the ebb channel
b) flood transport capacity in the flood channel
c) ebb transport capacity in the ebb channel
d) ebb transport capacity in the flood channel.
- 2.19 Calculated erosion and sedimentation pattern near the flood channel bar. Calculation of the sediment transport is based on a DufLOW simulation and the application of Van Rijn's (1990) formula for suspended and bed load transport.
a) bar morphology and the channel sections according to DufLOW
b) erosion and sedimentation at maximum flood and ebb
- 2.20 Expected patterns of primary flow and erosion and sedimentation related to the morphology of bar channels
a) channel morphology of the bar channels at flood channel bar in 1982 and 1992.
b) flow pattern at ebb and flood across the bar channel morphology in 1992.
c) expected patterns of erosion and sedimentation at ebb and flood.
- 2.21 Expected patterns of flow and erosion and sedimentation in the ebb-dominated bar channel.
a) Channel morphology of 1992
b) expected secondary flow phenomena and the course of the primary flow at ebb and flood.
c) expected locations of erosion and sedimentation at ebb and flood
- 2.22 Expected patterns of flow and erosion and sedimentation in the ebb-dominated cross channel.
a) Channel morphology of 1992
b) expected secondary flow phenomena and the course of the primary flow at ebb and flood.
c) expected locations of erosion and sedimentation at ebb and flood
- 3.1 Bathymetric maps of the Westerschelde in 1994 (a), the Terneuzen and Hansweert section in 1994 (b) and the bar channels in 1974 (c) and 1994 (d).
FC#= main flood channel (and number)
EC=main ebb channel
BC & CC = connecting channels: CC = cross channel BC= bar channel (+number)
B#= bar in main channel.
NAP= Dutch Ordnance level.
These abbreviations of the channel types are used throughout the chapter.
- 3.2 The schematisation of the main channels into channel sections, to compute the changes in the sediment budgets and the average cross-sectional channel geometry.
- 3.3 Definition sketch of the computation of the channel migration.

- 3.4 The total sediment reworking at the bar B1 in the main flood channel FC1(section 4, Fig. 3.2) versus time interval.
- 3.5 Erosion-sedimentation patterns over the period 1955-1996.
- 3.6 Large-scale changes in the sediment budget (in Mm^3) in the Terneuzen and Hansweert section between 1955 and 1996. The changes refer to the water volume below NAP+2.5m
- 3.7 Small-scale changes in the sediment budget (in Mm^3) in the Terneuzen and Hansweert section between 1955 and 1996. The changes refer to the water volume below NAP+2.5m
- 3.8 Small-scale evolution of the sediment budgets (in Mm^3) in the main flood channel FC1 in the Terneuzen section between 1955 and 1996. FC1 is the entire main flood channel (= sum of changes in sections 1,2,3 and 4).
 - a) changes in the channel volume (water volume below NAP-2m)
 - b) changes in the intertidal shoal volume (sand volume above NAP-2m)
 - c) cumulative net magnitude of dredging and dumping. Positive values mean a net dredging, whereas negative values indicate a net dumping.
- 3.9 Small-scale evolution of the sediment budgets (in Mm^3) in the main ebb channel EC1 in the Terneuzen section between 1955 and 1996. EC1 is the entire main ebb channel (= sum of changes in sections 5,6,7,8 and 9).
 - a) changes in the channel volume (water volume below NAP-2m)
 - b) changes in the intertidal shoal volume (sand volume above NAP-2m)
 - c) cumulative net magnitude of dredging and dumping. Positive values mean a net dredging, whereas negative values indicate a net dumping.
- 3.10 Small-scale evolution of the sediment budgets (in Mm^3) in the main flood channel FC2 in the Hansweert section between 1955 and 1996. FC2 is the entire main flood channel (= sum of changes in sections 15, 16 and 17).
 - a) changes in the channel volume (water volume below NAP-2m)
 - b) changes in the intertidal shoal volume (sand volume above NAP-2m)
 - c) cumulative net magnitude of dredging and dumping. Positive values mean a net dredging, whereas negative values indicate a net dumping.
- 3.11 Small-scale evolution of the sediment budgets (in Mm^3) in the main ebb channel EC2 in the Hansweert section between 1955 and 1996. EC2 is the entire main ebb channel (= sum of changes in sections 11, 12, 13 and 14).
 - a) changes in the channel volume (water volume below NAP-2m)
 - b) changes in the intertidal shoal volume (sand volume above NAP-2m)
 - c) cumulative net magnitude of dredging and dumping. Positive values mean a net dredging, whereas negative values indicate a net dumping.
- 3.12 Evolution of the cross-sectional channel geometry of the main channels FC1 and EC1 in the Terneuzen section between 1955 and 1996. FC1 = entire main flood channel, EC1=entire main ebb channel
 - a) average cross sectional area of the main flood channel
 - b) average hydraulic radius of the main flood channel
 - c) average cross sectional area of the main ebb channel
 - d) average hydraulic radius of the main ebb channel
- 3.13 Evolution of the cross-sectional channel geometry of the main channels FC2 and EC2 in the Hansweert section between 1955 and 1996. FC2 = entire main flood channel, EC2=entire main ebb channel

- a) average cross sectional area of the main flood channel
 - b) average hydraulic radius of the main flood channel
 - c) average cross sectional area of the main ebb channel
 - d) average hydraulic radius of the main ebb channel
- 3.14 Changes in the distribution of the tidal volumes (in Mm^3) between the main ebb and flood channel in the Terneuzen and Hansweert section since 1932, based on discharge measurements.
- a) ebb volumes in the main channels of the Terneuzen section
 - b) flood volumes in the main channels of the Terneuzen section
 - c) ebb volumes in the main channels of the Hansweert section
 - d) flood volumes in the main channels of the Hansweert section
- 3.15 The three patterns of bar channels between 1955 and 1996.
- 3.16 The morphological evolution of channel pattern 1 in the Terneuzen section.
- a) changes in the average cross-sectional area of the channels.
 - b) changes in the average hydraulic radius of the channels.
 - c) average migration rates and cumulative channel displacement
 - d) changes in the location of the channel axis.
- 3.17 The observed changes in the cross sectional area of channel pattern 1 (in %) and the potential changes in the channel cross section as result of dredging and dumping. Positive values indicate an increase of the channel cross section. Negative values indicate a decrease of the channel cross section.
- a) the flood bar channel BC1
 - b) the ebb bar channel BC2
- 3.18 The morphological evolution of channel pattern 2 in the Terneuzen section.
- a) changes in the average cross-sectional area of the channels.
 - b) changes in the average hydraulic radius of the channels.
 - c) average migration rates and cumulative channel displacement
 - d) changes in the location of the channel axis.
- 3.19 The observed changes in the cross sectional area of the bar channels of pattern 1 (in %) and the potential changes in the channel cross section as result of dredging and dumping. Positive values indicate an increase of the channel cross section. Negative values indicate a decrease of the channel cross section.
- a) the ebb bar channel BC3
 - b) the flood bar channel BC4
 - c) the flood bar channel BC5
- 3.20 The total sediment reworking at the bar B1 together with the reworking induced by the migration of the bar channels BC1, BC2, BC12, BC3, BC4.
- a) sediment reworking during pattern 1 (based on the 'standard echosoundings').
 - b) sediment reworking during pattern 2 (based on the 'specific echosoundings').
- 3.21 The morphological evolution of the cross channel (cc in Fig. 3.1) in the Terneuzen section
- a) changes in the location of the channel axis.
 - b) average migration rates and cumulative channel displacement
 - c) changes in the average cross-sectional area and hydraulic radius of the channel.

d) net changes in cross-sectional area and the potential changes of dredging.

- 4.1 The location and morphology of the three different types of connecting channels in 1994/1995
- 4.2 The general hydrodynamics in the study area: overview of the measurements.
- 4.3 Overview of the measurements in the connecting channels in 1994
- 4.4 Overview of the measurements in the connecting channels in 1995
- 4.5 Overview of the measurements in the connecting channels in 1996
- 4.6 Definition sketch of the coordinate systems used in the analysis of discharge measurements and ADCP observations of the vertical current structure.
- 4.7 Relationships between channel geometry and tidal flow parameters for the Westerschelde and measurement values obtained in the present study (for location of transects see Figure 4.2).
 - a) ebb volume versus cross-sectional area, b) flood volume versus cross-sectional area, c) dominant volume versus cross-sectional area, d) dominant volume versus streampower.
- 4.8 Tidal wave propagation along the estuary during neap, mean and spring tide. a) tidal range, b) delay of high water with respect to Vlissingen (hours), c) delay of low water with respect to Vlissingen d) difference in delay between low water and high water (hours), e) duration of tidal rise, f) duration of tidal fall, g) duration difference between fall and rise, h) tidal period, i) discharge and water level at the landward boundary, j) discharge and water level at the seaward boundary.
- 4.9 Water levels at the seaward and landward boundary of the study area and the water level difference (water level station 1 and 2, for locations see Fig. 4.2).
 - a) spring tide, b) mean tide, c) neap tide.
- 4.10 Duration of tidal fall and tidal rise versus tidal range at Terneuzen, as occurred during the water level measurements.
- 4.11 Temporal variation in falls along the five channel sections in the study area. During spring tide (a & b), during mean tide (c & d) and during neap tide (e & f).
- 4.12 Temporal variation in discharge and cross-sectional velocities as occurred during the measurements (for locations see Fig. 4.2).
 - a) discharges in transect 1, b) velocities in transect 1
 - c) discharges in transect 2, d) velocities in transect 2
 - e) discharges in transect 4, f) velocities in transect 4
 - g) discharges in transect 3, h) velocities in transect 3
 - i) discharges in transect 5, j) velocities in transect 5
 - j) discharges in transect 6, k) velocities in transect 6
- 4.13 Overview of the time of maximum flood and maximum ebb flow in the study area.
- 4.14 Temporal variation in depth-averaged current velocities and falls in the cross channel (for locations see Fig. 4.3 and 4.4).a) current velocities at location 5 and 6, b) current velocities at location 13 and falls along the channel.
- 4.15 Variation in mean and maximum falls and surface slopes along the five channel sections during ebb. Maximum refers to the condition of maximum

currents (= 4 hours after high water). Mean refers to the average values over the ebb period.

- 4.16 Spatial patterns of ebb volumes for neap, mean and spring tide together with the water budgets for mean tide.
- 4.17 Spatial patterns of maximum ebb discharges during mean, neap and spring tide.
- 4.18 Variation in mean and maximum falls and surface slopes along the five channel sections during flood. Maximum refers to the condition of maximum flood currents (= 11.6 hours after high water). Mean refers to the average values over the flood period.
- 4.19 Spatial patterns of flood volumes for neap, mean and spring tide together with the water budgets for mean tide.
- 4.20 Spatial patterns of maximum flood discharges during mean, neap and spring tide.
- 4.21 Spatial patterns of current asymmetry and the maximum values of tidal flow during ebb and flood for mean, neap and spring tide. a) tidal volumes, b) maximum discharges, c) cross-sectional velocities.
- 4.22 Residual cross-sectional velocities as occurred during the measurements.
- 4.23 Spatial pattern of residual water transports and transport velocities for mean, neap and spring tide.
- 4.24 Mean lagrangian current patterns in the cross channel during ebb.
- 4.25 Depth-averaged tidal current patterns in the cross channel during ebb and mean tidal conditions in April 1994 (locations 5 and 6) and November 1994 (11 to 13).
- 4.26 Differences in current direction between near-surface and near-bed significant current vectors versus near-bed current velocity and velocity difference in the cross channel during ebb (locations 11 and 13, Figure 4.3).
- 4.27 Mean lagrangian current patterns in the cross channel during flood and mean tidal conditions.
- 4.28 Depth-averaged tidal current patterns in the cross channel during flood and mean tidal conditions in April 1994 (locations 5 and 6) and November 1994 (11 to 13).
- 4.29 Current asymmetry in the cross channel. a) measurement locations, b) significant current vector and asymmetry ratio's during mean tide, c) asymmetry ratio's for neap and spring tide, d) significant velocity and asymmetry versus tidal range.
- 4.30 Long-term mean depth-averaged residual current vectors in the cross channel. a) measurement locations, b) residual currents.
- 4.31 Mean lagrangian current patterns in the ebb bar channel during accelerating ebb on 4 November 1994.
- 4.32 Mean lagrangian current patterns in the ebb bar channel during maximum and decelerating ebb on 8 November 1994
- 4.33 Depth-averaged current current patterns in the ebb bar channel during ebb and mean tidal conditions in November 1994
- 4.34 Depth-averaged current current patterns in the ebb bar channel during ebb and mean tidal conditions in June 1995.
- 4.35 Cross-sectionally averaged and depth-averaged currents in the ebb bar channel along transect 5_2 and 5_3 during ebb. a) locations and orientations of ADCP-

- transects, b) time-series of the cross-sectionally averaged currents, c) magnitude of depth-averaged current vectors along transect 5_2. d) direction of depth-averaged current vectors along transect 5_2. e) magnitude of depth-averaged current vectors along transect 5_3. f) direction of depth-averaged current vectors along transect 5_3.
- 4.36 Depth-averaged along-channel and cross-channel velocity patterns over the bar of the ebb bar channel during ebb (transect 5_1), ac= acceleration of the flow, dc=deceleration of the flow, dsb=downstream side of the bar, usb=ustream side of the bar. Negative along-channel component is ebb, positive component is flood.
- 4.37 Countour plots of the relative magnitude of the secondary flow (in % of the magnitude of the depth-averaged current velocity) and current veering with respect to the depth-averaged current direction in the central part of the ebb bar channel (transect 5_2, Fig. 5.4). a & b) accelerating ebb, c & d) maximum ebb, e & f) decelerating ebb.
- 4.38 Contourplots of the relative magnitude of secondary flow and current veering near the bar in the ebb bar channel durinf ebb (transect 5_3, for location see Fig. 4.5).
- 4.39 Mean lagrangian current patterns in the ebb bar channel during flood on 4 November 1994
- 4.40 Depth-averaged current current patterns in the ebb bar channel during flood and mean tidal conditions in November 1994
- 4.41 Depth-averaged current current patterns in the ebb bar channel during flood and mean tidal conditions in June 1995.
- 4.42 Cross-sectionally averaged and depth-averaged currents in the ebb bar channel along transect 5_2 and 5_3 during flood. a) locations and orientations of ADCP-transects, b) time-series of the cross-sectionally averaged currents, c) magintude of depth-averaged current vectors along transect 5_2. d) direction of depth-averaged current vectors along transect 5_2. e) magintude of depth-averaged current vectors along transect 5_3. f) direction of depth-averaged current vectors along transect 5_3.
- 4.43 Depth-averaged along-channel and cross-channel velocity patterns over the bar of the ebb bar channel during flood (transect 5_1), ac= acceleration of the flow, dc=deceleration of the flow, dsb=downstream side of the bar, usb=ustream side of the bar. Negative along-channel component is ebb, positive component is flood.
- 4.44 Countour plots of the relative magnitude of the secondary flow (in % of the magnitude of the depth-averaged current velocity) and current veering with respect to the depth-averaged current direction in the central part of the ebb bar channel during flood (transect 5_2, Fig. 5.4). a & b) accelerating flood, c & d) maximum flood, e & f) decelerating flood.
- 4.45 Contourplots of the relative magnitude of secondary flow and current veering near the bar in the ebb bar channel during flood (transect 5_3, for location see Fig. 4.5).
- 4.46 Current asymmetry in the ebb bar channel channel in November 1994 and June 1995. a & b) measurement locations, c & d) significant current vector and

asymmetry ratio's during mean tide, e & f) asymmetry ratio's for neap and spring tide

- 4.47 Residual current vectors in the ebb bar channel in November 1994 and June 1995. a & b) measurement locations, c & d) long-term mean residual current vectors.
- 4.48 Depth-averaged current current patterns in the flood bar channel during ebb and mean tidal conditions in August 1995.
- 4.49 Depth-averaged current current patterns in the flood bar channel during ebb and mean tidal conditions in February 1996.
- 4.50 Cross-sectionally averaged and depth-averaged currents in the flood bar channel along transect 6_2 and 6_3 during ebb. a) locations and orientations of ADCP-transects, b) time-series of the cross-sectionally averaged currents, c) magintude of depth-averaged current vectors along transect 6_2. d) direction of depth-averaged current vectors along transect 6_2. e) magintude of depth-averaged current vectors along transect 6_3. f) direction of depth-averaged current vectors along transect 6_3.
- 4.51 Depth-averaged along-channel and cross-channel velocity patterns over the bar of the ebb bar channel during ebb (transect 6_1), ac= acceleration of the flow, dc=deceleration of the flow, dsb=downstream side of the bar, usb=ustream side of the bar. Negative along-channel component is ebb, positive component is flood.
- 4.52 Countour plots of the relative magnitude of the secondary flow (in %) and current veering in the central part of the flood bar channel (transect 6_2, Fig. 5.4) during maximum ebb flow. a & b) transect 6_2, c & d) transect 6_3.
- 4.53 Depth-averaged current current patterns in the flood bar channel during flood and mean tidal conditions in August 1995.
- 4.54 Depth-averaged current current patterns in the flood bar channel during flood and mean tidal conditions in February 1996.
- 4.55 Cross-sectionally averaged and depth-averaged currents in the flood bar channel along transect 6_2 and 6_3 during flood. a) locations and orientations of ADCP-transects, b) time-series of the cross-sectionally averaged currents, c) magintude of depth-averaged current vectors along transect 6_2. d) direction of depth-averaged current vectors along transect 6_2. e) magintude of depth-averaged current vectors along transect 6_3. f) direction of depth-averaged current vectors along transect 6_3.
- 4.56 Depth-averaged along-channel and cross-channel velocity patterns over the bar in the flood bar channel during flood (transect 6_1), ac= acceleration of the flow, dc=deceleration of the flow, dsb=downstream side of the bar, usb=ustream side of the bar. Negative along-channel component is ebb, positive component is flood.
- 4.57 Countour plots of the relative magnitude of the secondary flow (in %) and current veering in the central part of the flood bar channel (transect 6_2, Fig. 5.4) near maximum flood flow. a & b) transect 6_2, c & d) transect 6_3.
- 4.58 Current asymmetry in the flood bar channel channel in August 1995 and February 1996. a & b) measurement locations, c & d) significant current vector and asymmetry ratio's during mean tide, e & f) asymmetry ratio's for neap and spring tide

- 4.59 Residual current vectors in the flood bar channel in August 1995 and February 1996. a & b) measurement locations, c & d) long-term mean residual current vectors.
- 4.60 Large and small-scale circulations of flow in the study area.

List of Tables

- 3.1 Budget changes (in Mm^3) in the Terneuzen and Hansweert section between 1955 and 1996
- 3.2 Budget changes (in Mm^3) in the Terneuzen section between 1955 and 1996
- 3.3 Budget changes (in Mm^3) in the Hansweert section between 1955 and 1996

- 4.1 Hydrodynamic and meteorological conditions during the discharge measurements
- 4.2 Accuracy of water level measurements
- 4.3 System configurations during the two ADCP surveys
- 4.4 Configuration and summary of the sampling procedures of the EMF-frame.
- 4.5 Current veering in the cross channel based on significant current vectors at 'Flachsee' locations 11 and 13 during ebb.
- 4.6 Overview of the conditions and observations during the near-bed current measurements in the channel bend of the cross channel.
- 4.7 Current veering in the cross channel based on significant current vectors at 'Flachsee' locations 11 and 13 during flood.
- 4.8 Comparison of measured and computed secondary flow in the central part of the ebb bar channel during ebb and flood.

List of Appendices

- 3.0 Computation of the average cross-sectional area and hydraulic radius.
- 3.1 Location and legend of Enclosures 2 and 3
- 3.2 Bathymetric maps of the Terneuzen and the Hansweert section in 1955, 1964, 1974, 1982, 1990, 1996.
- 3.3 Bathymetric maps of the bar area in the main flood channel in the Terneuzen section during the period 1955 up to 1996 (based on 'standard' echosoundings).
- 4.1 Overview of measurement locations and periods (ontbreekt)
- 4.2 Filtering of the ADCP-velocity profiles (ontbreekt)
- 4.3 Application of the shape-function approach to the filtered ADCP profiles (ontbreekt).
- A Congrespublicatie
- B Vrdere uitwerking van de verkennende modelsommen uit hoofdstuk 2.

List of Photos

- 4.1 Water level station 3 (ontbreekt)
- 4.2 EMF-frame (ontbreekt)

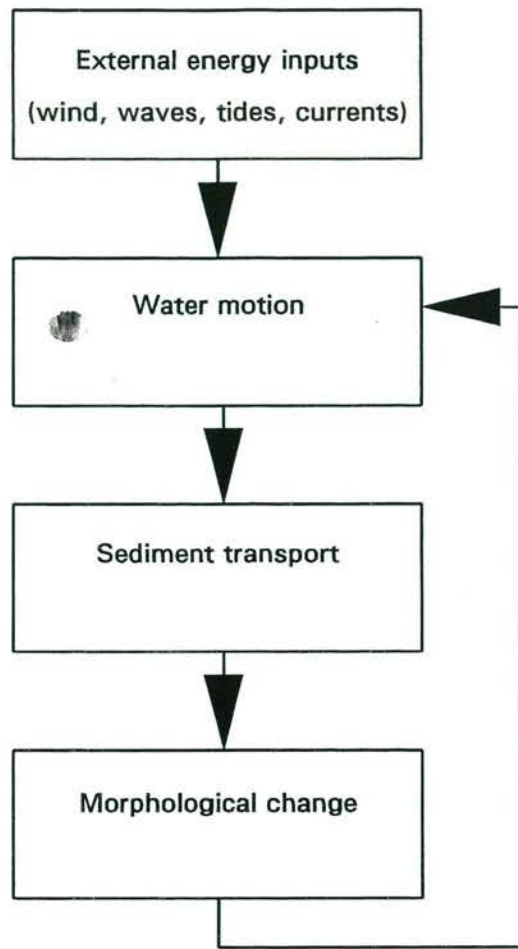


Figure 2.1 *Schematic representation of a morphodynamic system*

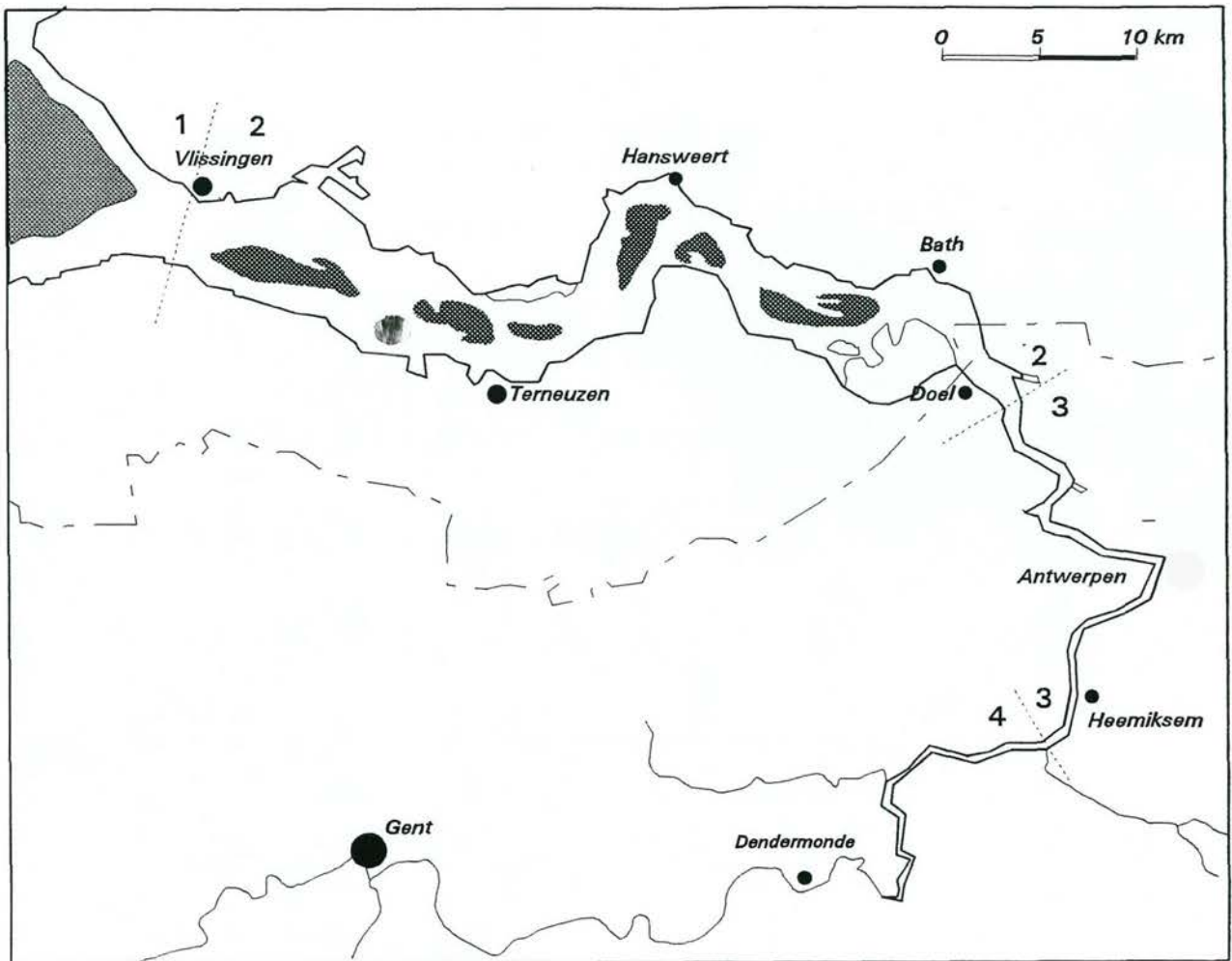


Figure 2.2 *The funnel shaped geometry of the Schelde estuary and the four morphologically distinct zones:*
a) tidal delta;
b) multiple tidal channel system in the Westerschelde;
c) single tidal channel system;
4) tidal channel directly linked to the river channel.

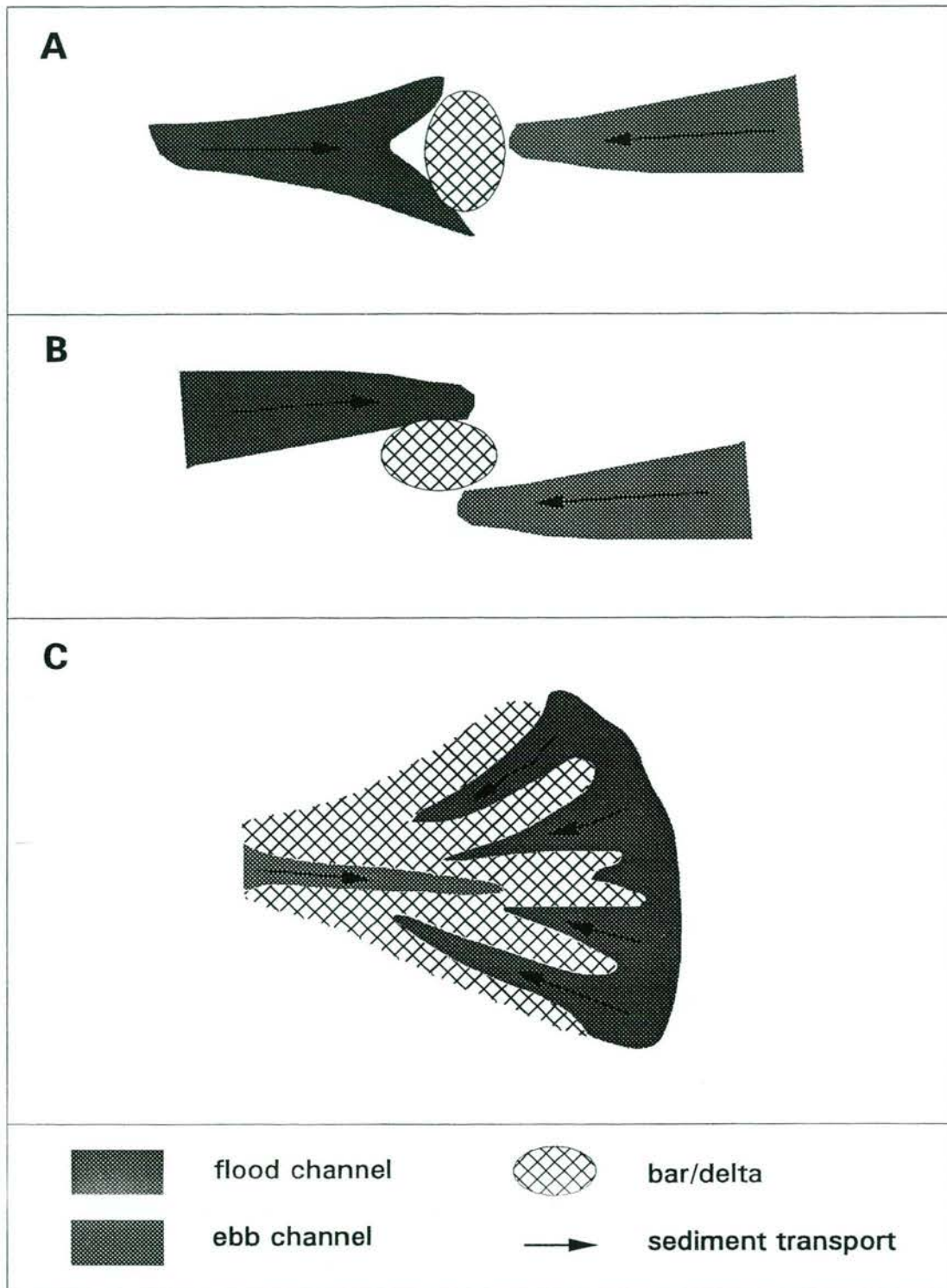


Figure 2.3 *The three recurring arrangements of ebb and flood channels according to van Veen (1950):*
a) the forked tongue pattern
b) the flanking attack pattern
c) the wide estuary pattern

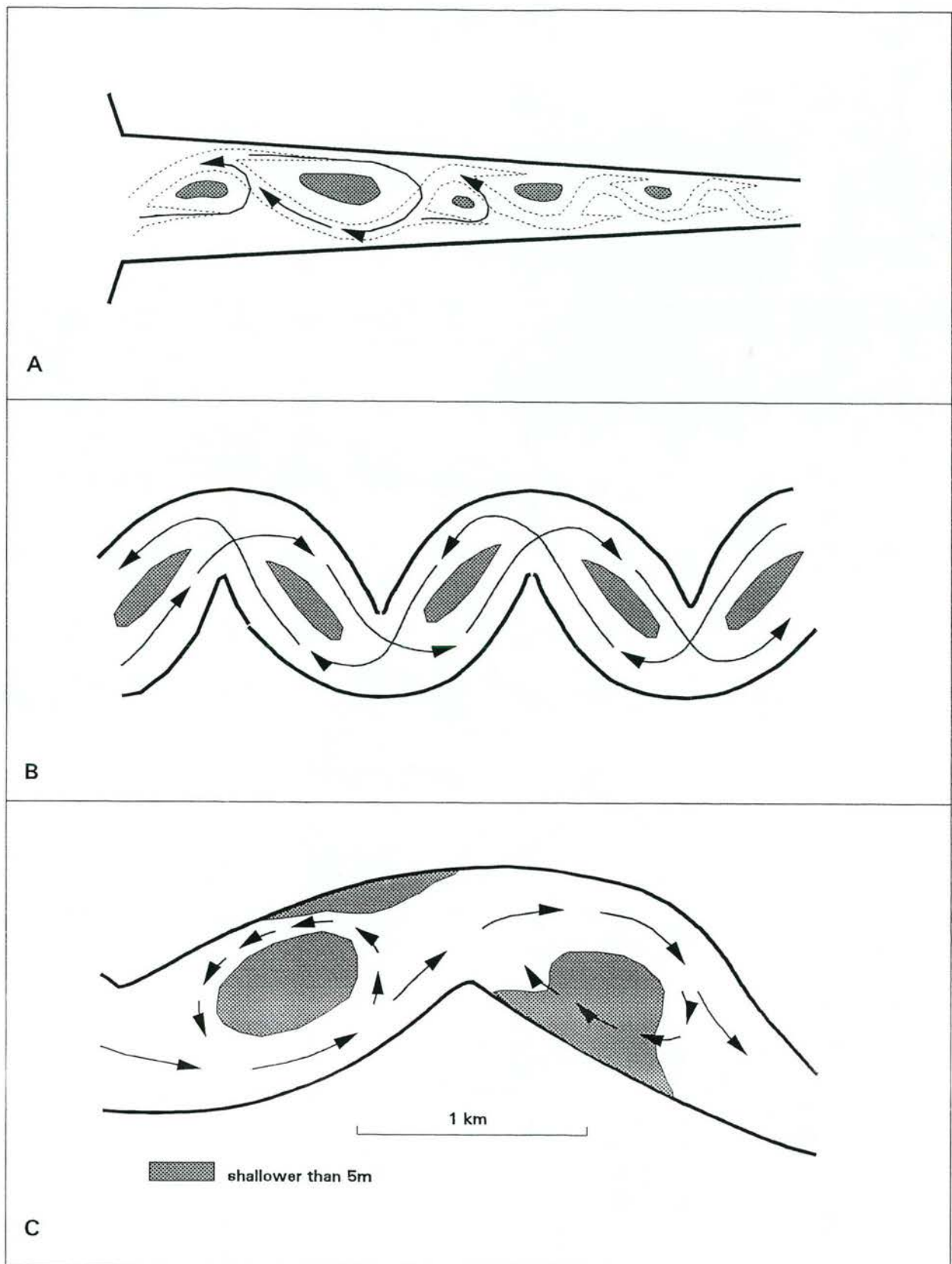


Figure 2.4

Tidal meanders.

a) the ideal channel pattern of Van Veen (1950), consisting of sine-shaped ebb channels and straight flood channels that start in each bend. The arrows show the expected circulation cells.

b) 'the estuarine meander' of Ahnert (1960).

c) the cusped 'estuarine meanders' of South Alligator River. The arrows show the course of the maximum flood velocity path and the large eddies around mid the channel flats (after Vertessy, 1990, in Carter and Woodroffe, 1994).

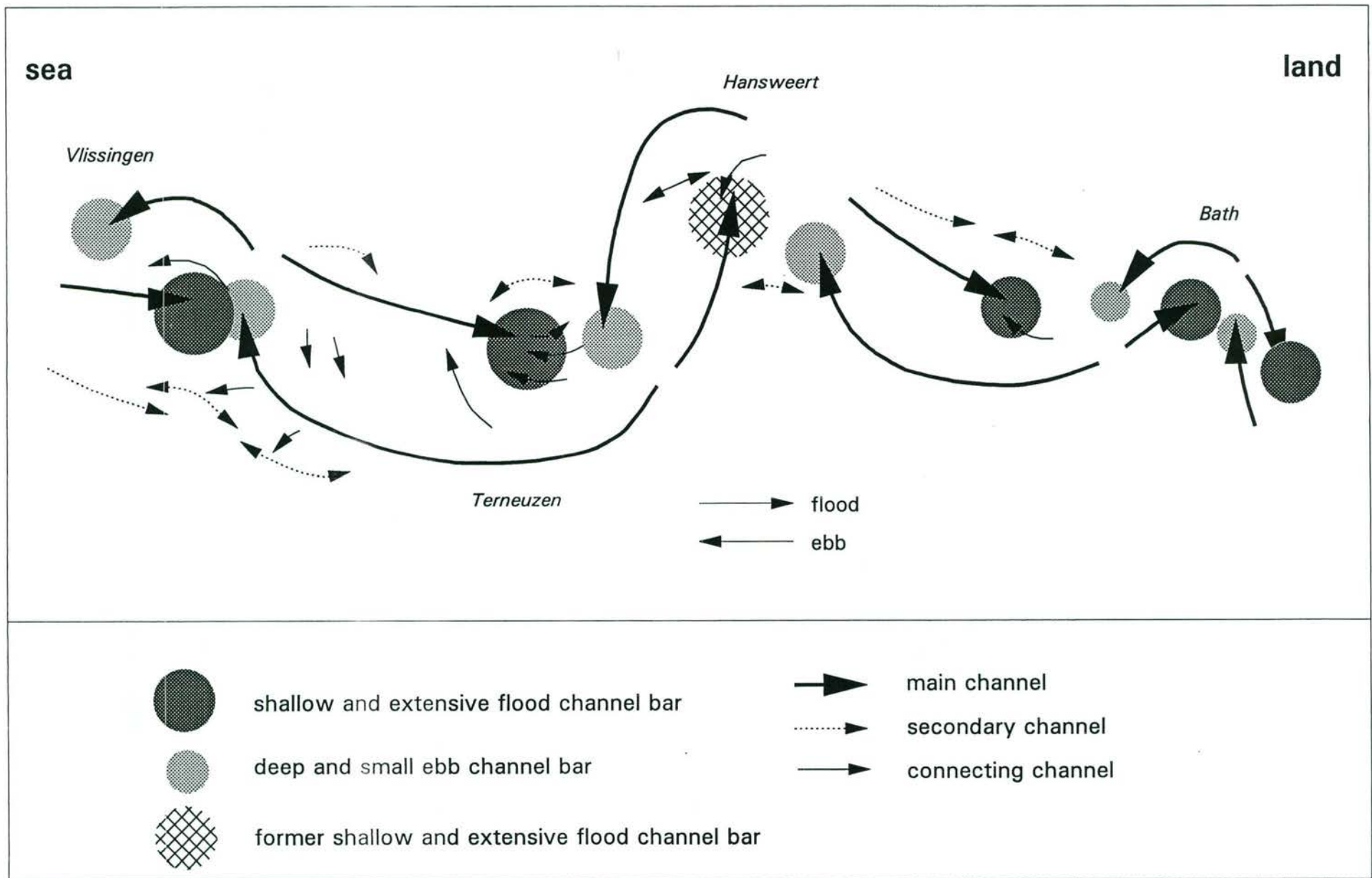


Figure 2.6

Schematized geomorphology of the various ebb and flood channels within the Westerschelde. The bathymetric map of 1990 was used as a basis for schematizing. Three different types of tidal channels exist: main channels, secondary channels and connecting channels.

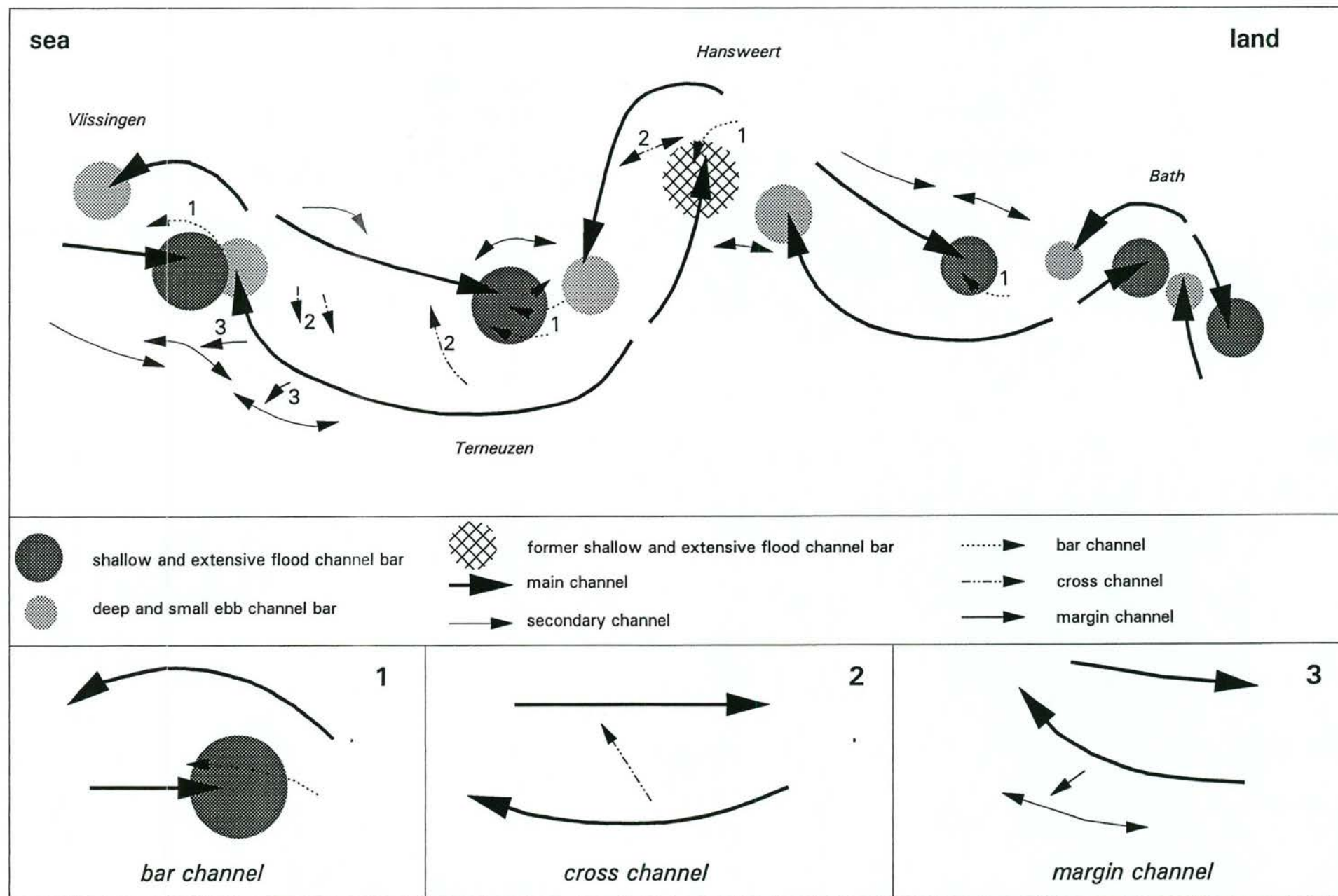


Figure 2.7 Subdivision into three different types of connecting channels based on the geographical location within the main channel system. a)

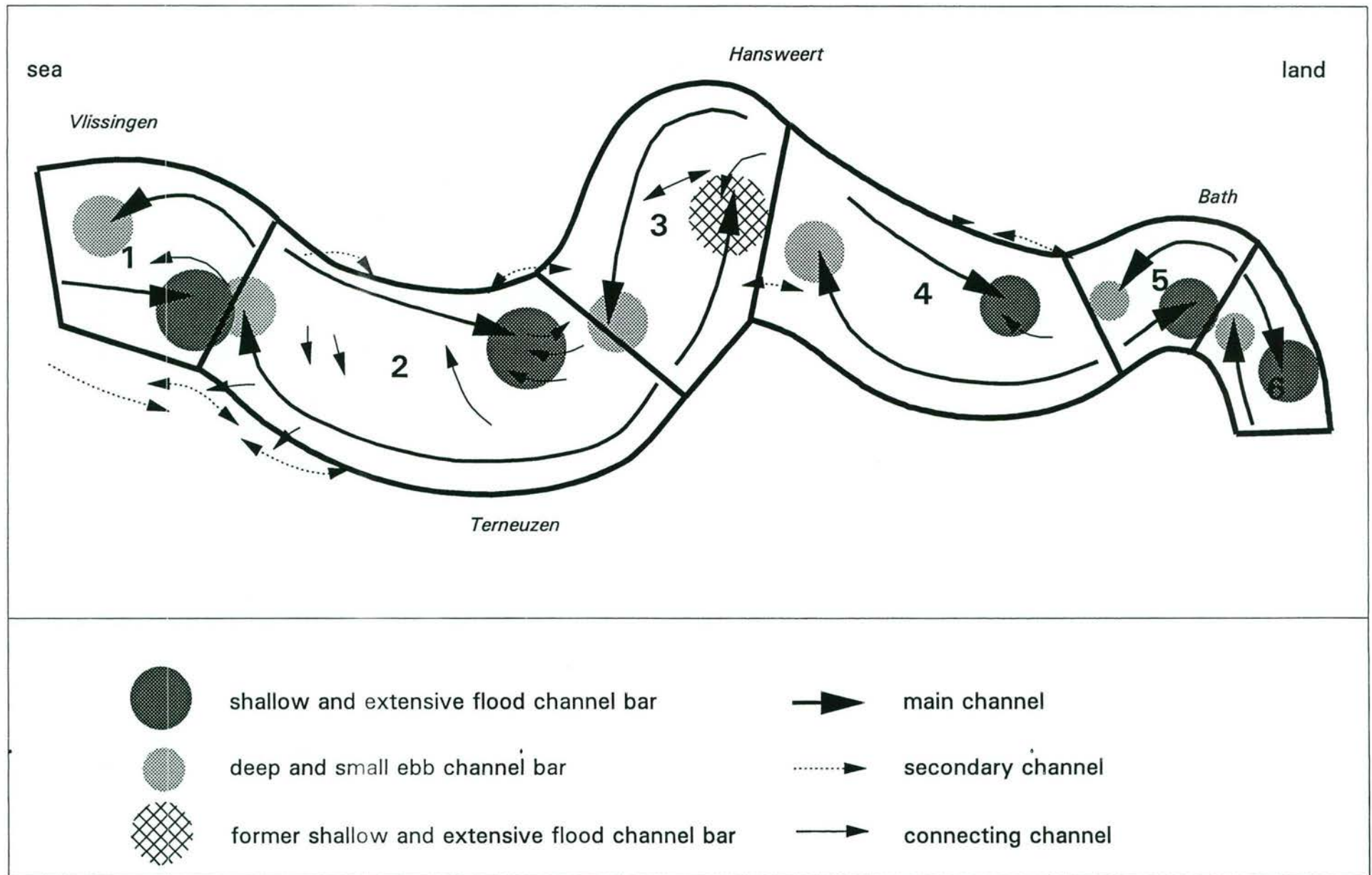


Figure 2.8

The subdivision of the channel and flat system into six estuarine sections. Each estuarine section has a mutually evasive meandering ebb channel and a straight flood channel separated by tidal flats and connected by connecting channels. 1= Vlissingen section, 2= Terneuzen section, 3= Hansweert section, 4= Baalhoek section, 5= Bath section, 6= border section.

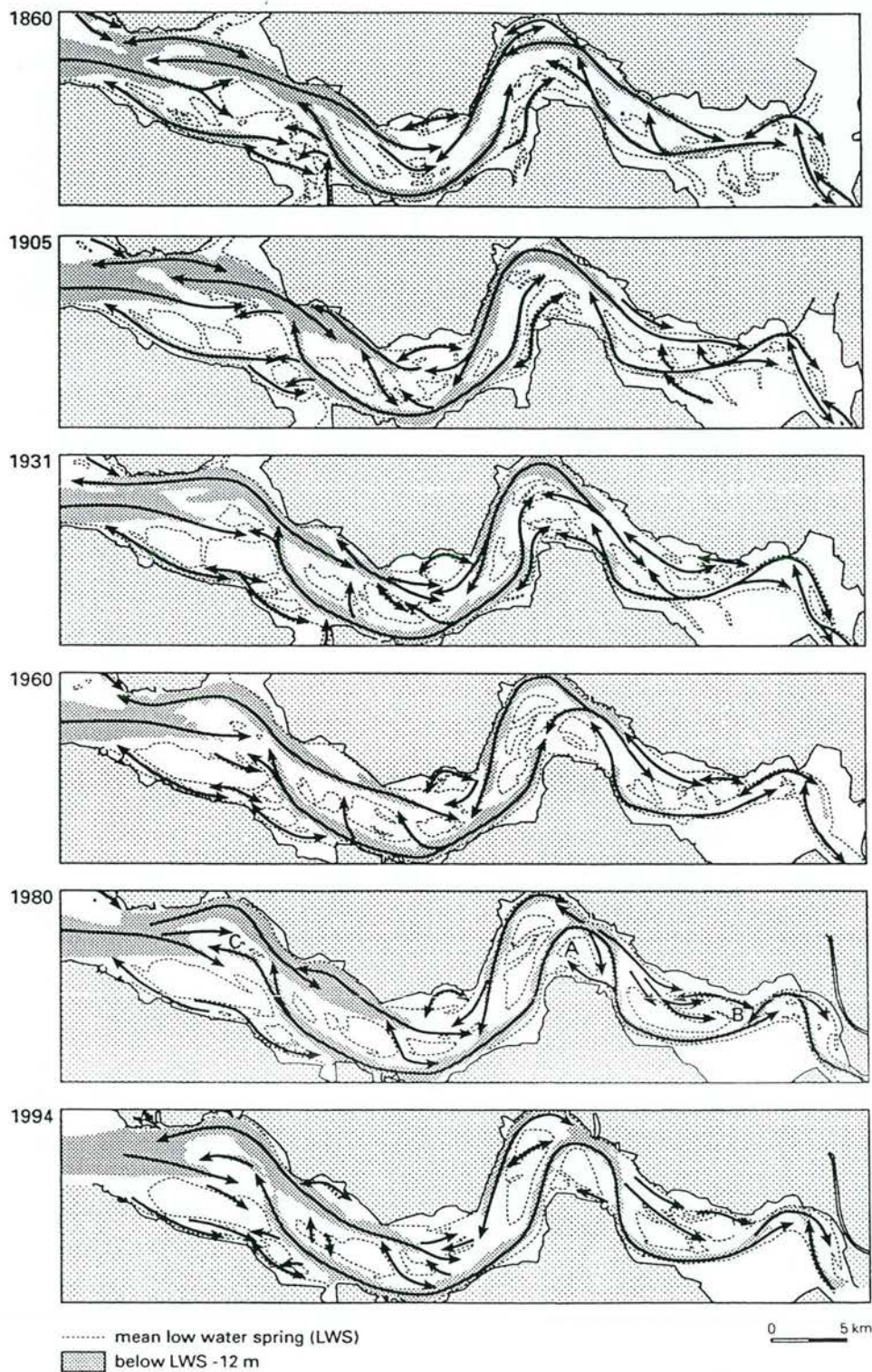


Figure 2.9 The meandering of the main ebb channels, and accompanied extension of the flood channels and flats between 1860 and 1994 (after Van den Berg. et.al., in prep.).

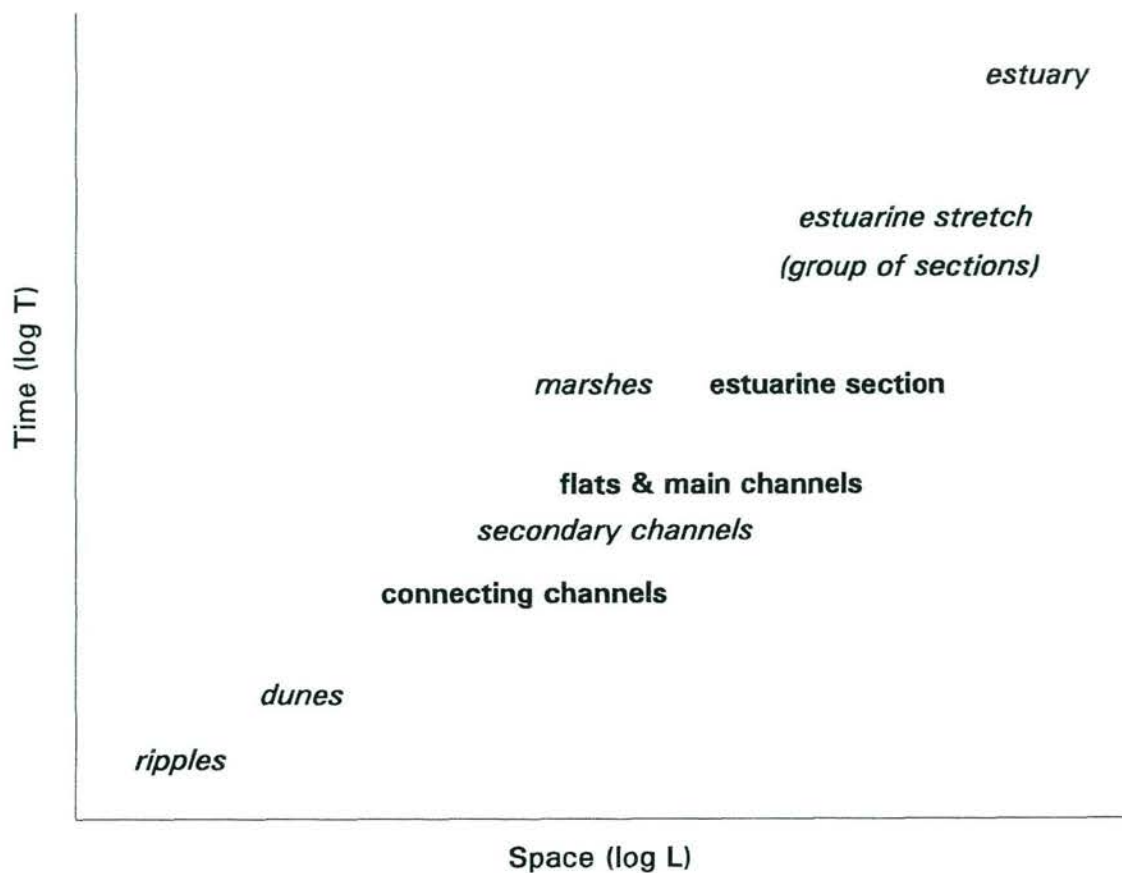


Figure 2.10 Time and space scales of the estuarine morphology

ENERGY INPUT	TIME SCALES	PROCESS/INTERNAL STEERING	SPATIAL SCALE
astronomical tide	18.6 yr nodal cycle equinoctical tides neap-spring cycle ↓ daily cycle	tidal wave deformation and asymmetry topographical eddies secondary circulations	↓ estuary estuarine section channel
wind	storms (seasonal)	set-up wind driven currents sea waves	↓ estuary - estuarine stretch estuary - estuarine stretch tidal flats
river	seasonal fluctuations	gravitational circulation	estuarine section - channel

Figure 2.11 Time and space scales of the estuarine hydrodynamics.

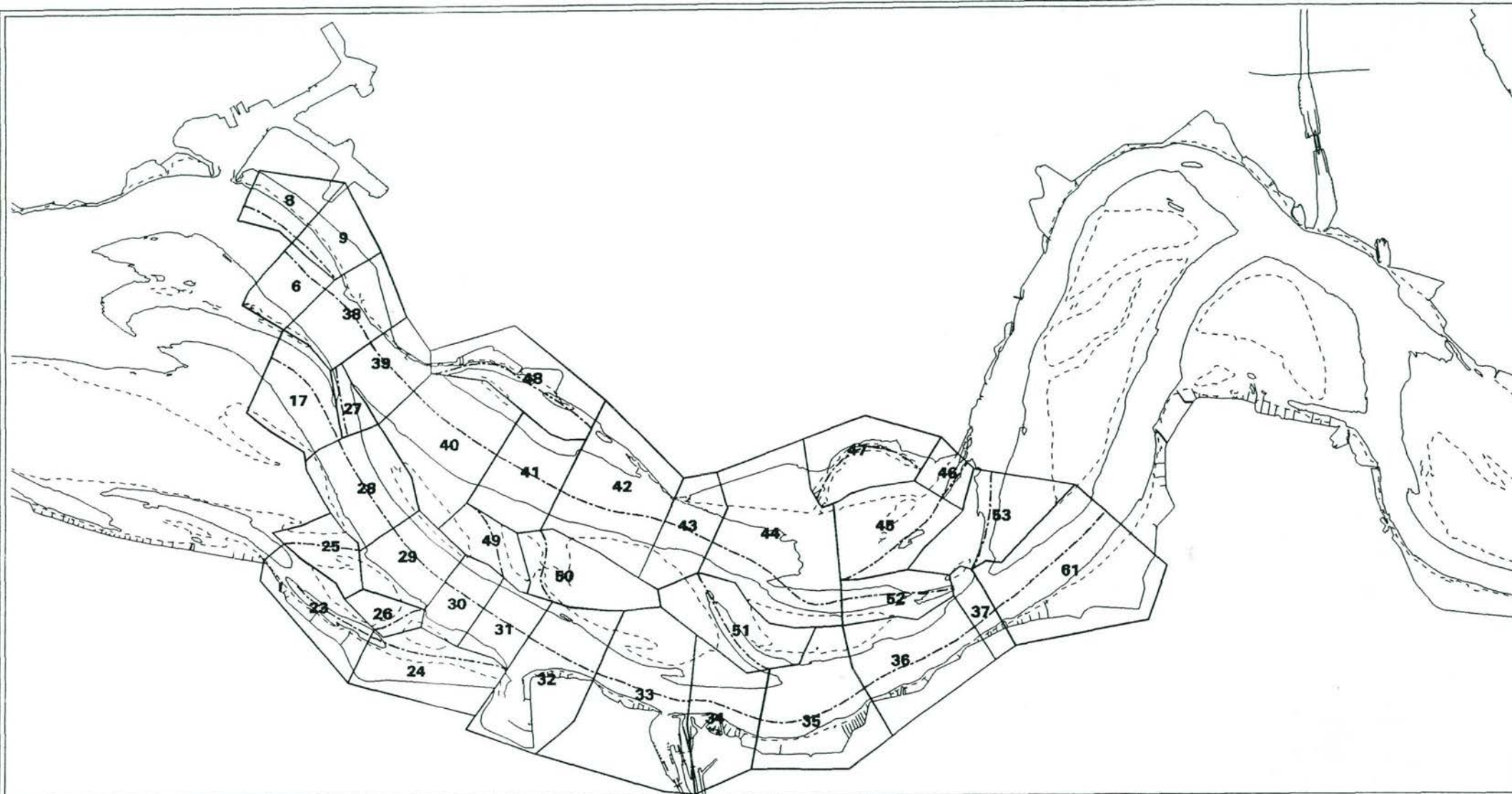


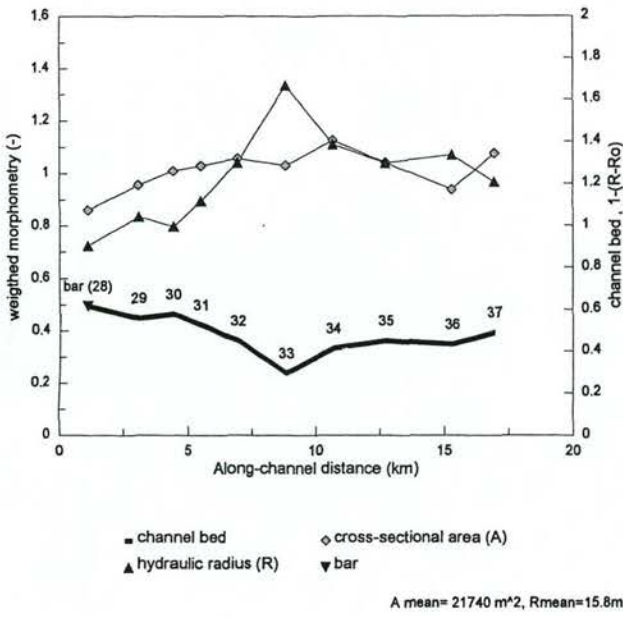
Figure 2.13

The subdivision of the channels into channel sections according to the Duflow schematization. The heavy, interrupted lines indicate the channel axes. Two depth contours of the bathymetric map of 1982 are indicated:

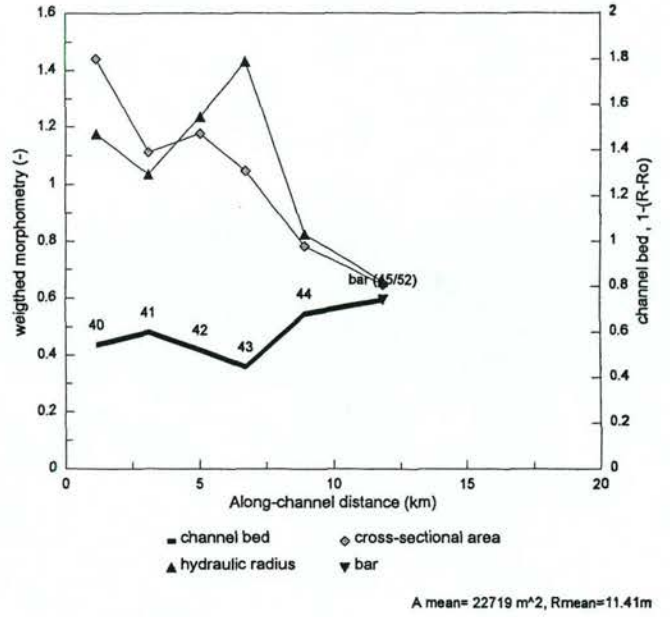
- = Mean Low Water Spring (NAP-2.5m)*
- = Mean Low Water Spring -8m (NAP-10.5m).*



a) Ebb channel



b) Flood channel



c) Channel sections and nodes in the Terneuzen section according to Dufrow

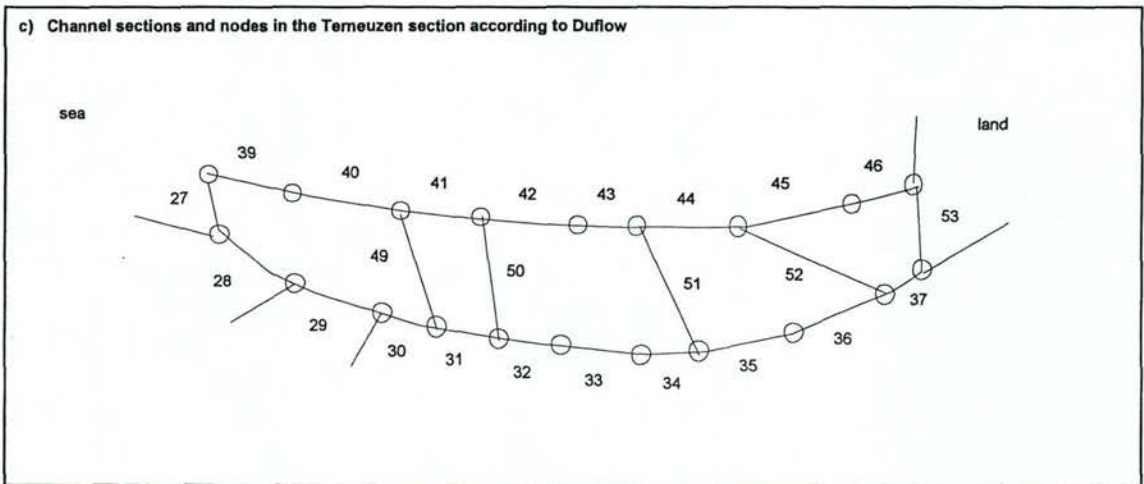


Figure 2.14

Along channel morphometry based on the Dufrow schematization.

a) the ebb channel;

b) the flood channel;

c) the channel sections and nodes according to Dufrow;

A dimensionless hydraulic radius (R/R_{mean}) shows the averaged depth along the channel. The cross-sectional area is divided by the averaged cross-sectional area of the entire ebb channel. The averaged cross-sectional area and hydraulic radius are weighted for the channel length as

$$A_{mean} = \sum_{i=28}^{i=37} \left(\frac{L_{section\ i}}{L_{channel}} * A_{section\ i} \right)$$

The dimensionless parameter $(1-(R/R_o))$ visualizes the channel bed ($R_o=30m$). The sections 45 and 52 are joined by considering the averaged depth and the sum of the cross-sectional areas. The values of the parameters are plotted in the middle of each channel section.

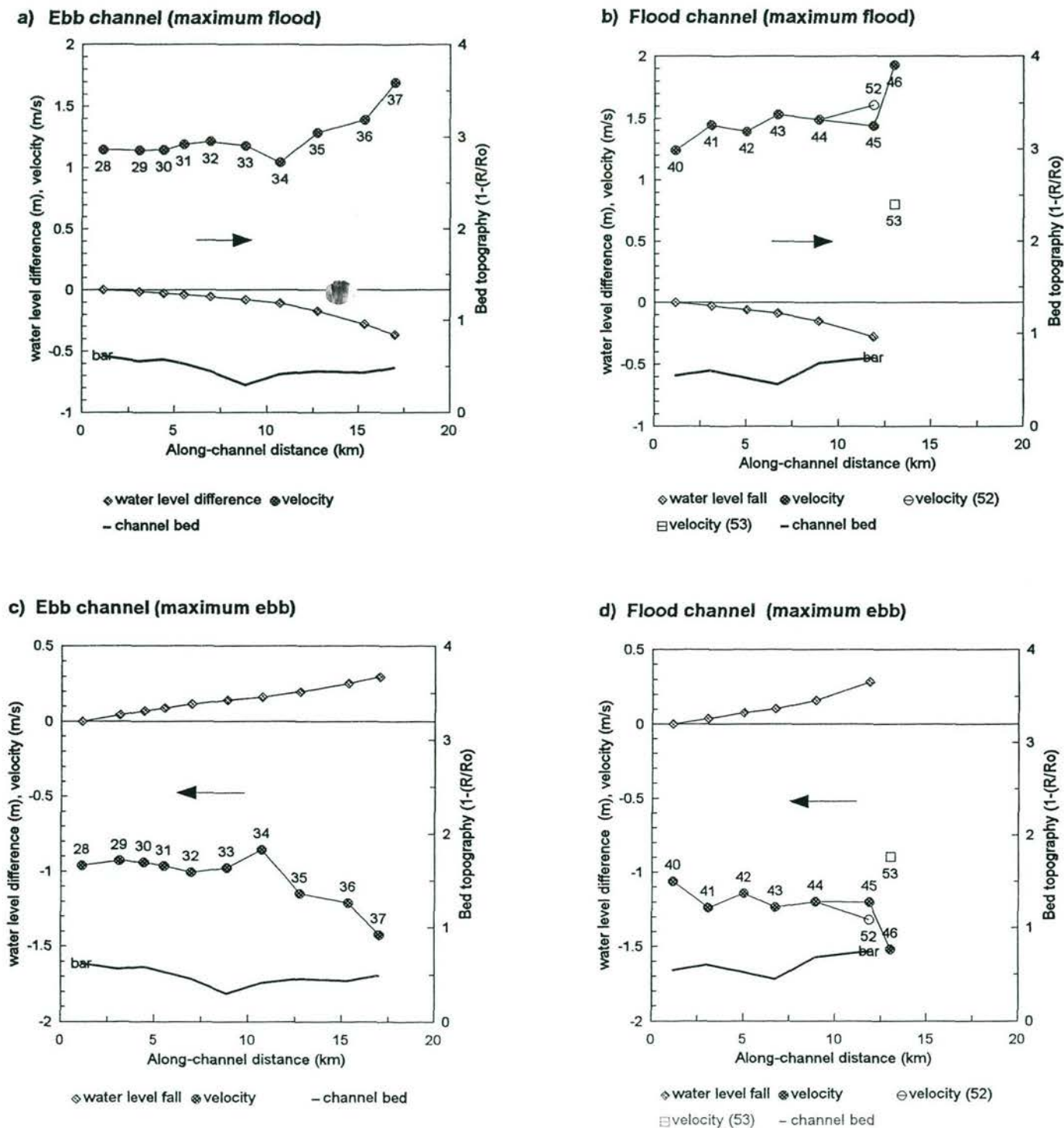


Figure 2.15

Water levels and current velocities in the main ebb and flood channel at maximum tidal flow.

a) flow response in the ebb channel at maximum flood

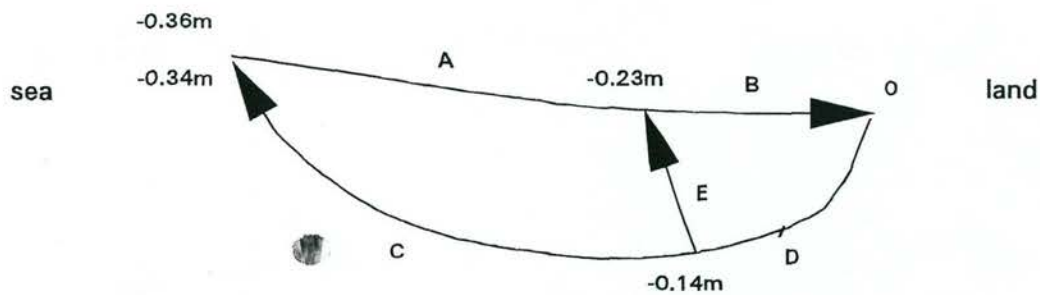
b) flow response in the flood channel at maximum flood

c) flow response in the ebb channel during maximum ebb

d) flow response in the flood channel during maximum ebb.

The waterlevel of section 45 is plotted. (R =hydraulic radius, $R_o=30m$).

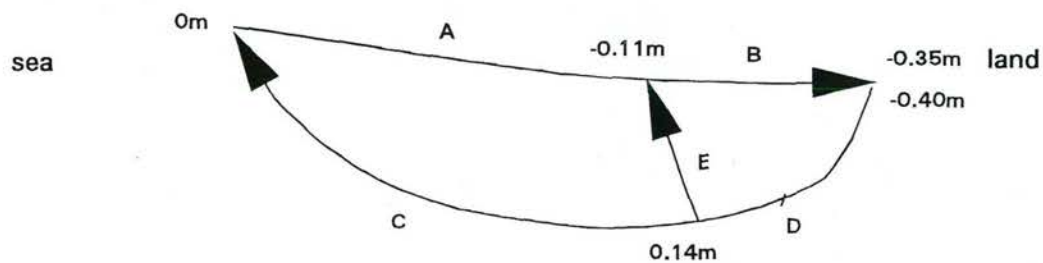
Note that the ebb values are negative and flood values positive.



MAXIMUM EBB FLOW

section	Q (m ³ /s)	A (m ²)	U (m/s)	R (m)	C (m ^{0.5} /s)	h1-h2 (m)	friction (m)	L (m)
A	-31416	27492	-1.15	13.6	85	-0.13	0.1	7290
B	-19842	16214	-1.23	8.6	77	-0.23	0.19	5900
C	-20167	21279	-0.95	15.2	69	-0.2	0.15	11510
D	-25819	21407	-1.21	16.4	70	-0.14	0.11	5780
E	-6885	6617	-1.04	8.4	70	-0.09	0.06	2680

h1 = seaward node, h2 = landward node



MAXIMUM FLOOD FLOW

section	Q (m ³ /s)	A (m ²)	U (m/s)	R (m)	C (m ^{0.5} /s)	h1-h2 (m)	friction (m)	L (m)
A	43772	32067	1.38	15.5	87	0.11	-0.12	7290
B	29762	19830	1.5	9.5	78	0.24	-0.24	5900
C	28274	24571	1.15	16.6	77	0.14	-0.17	11510
D	32992	23939	1.38	17.3	53	0.26	-0.23	5780
E	7707	8883	0.87	9.4	71	-0.03	-0.04	2680

h1 = seaward node, h2 = landward node

Figure 2.16 Values of the variables in the simplified momentum equation at maximum flow ($\Delta h / \Delta L = Q^2 / A^2 R^2 C^2$).

a) Values of the various variables at maximum ebb flow
b) Values of the various variables at maximum flood flow.

The variables discharge (Q), cross-sectional area (A), cross-sectional velocity (U), and hydraulic radius (R), are weighted for the length of the specific channel section, according to e.g. $A_{mean} = \sum_{i=28}^{i=37} \left(\frac{L_{section\ i}}{L_{channel}} * A_{section\ i} \right)$

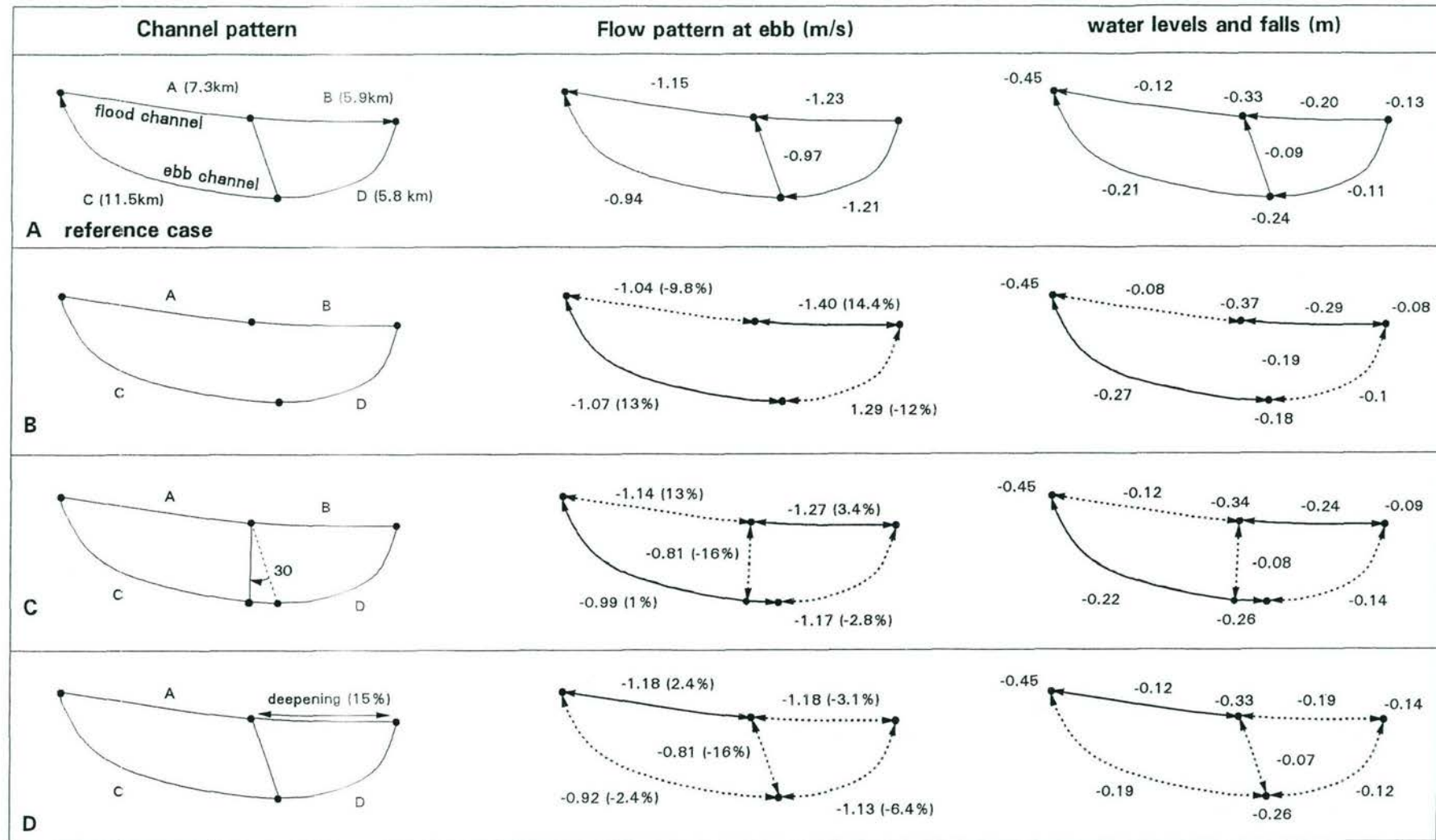


Figure 2.17a The initial adaptations in flow pattern and water level pattern due to morphological changes. Each figure presents the following four situations:

A) reference situation. B) the channel pattern without the large cross channel, C) the effect of a clockwise rotation of the cross channel of 30° . D) the effect of a deepening of the flood channel bar by 15%. Solid heavy line = increase with respect to the reference situation, dotted line indicates a decrease.

a) situation at maximum ebb;

b) situation at maximum flood;

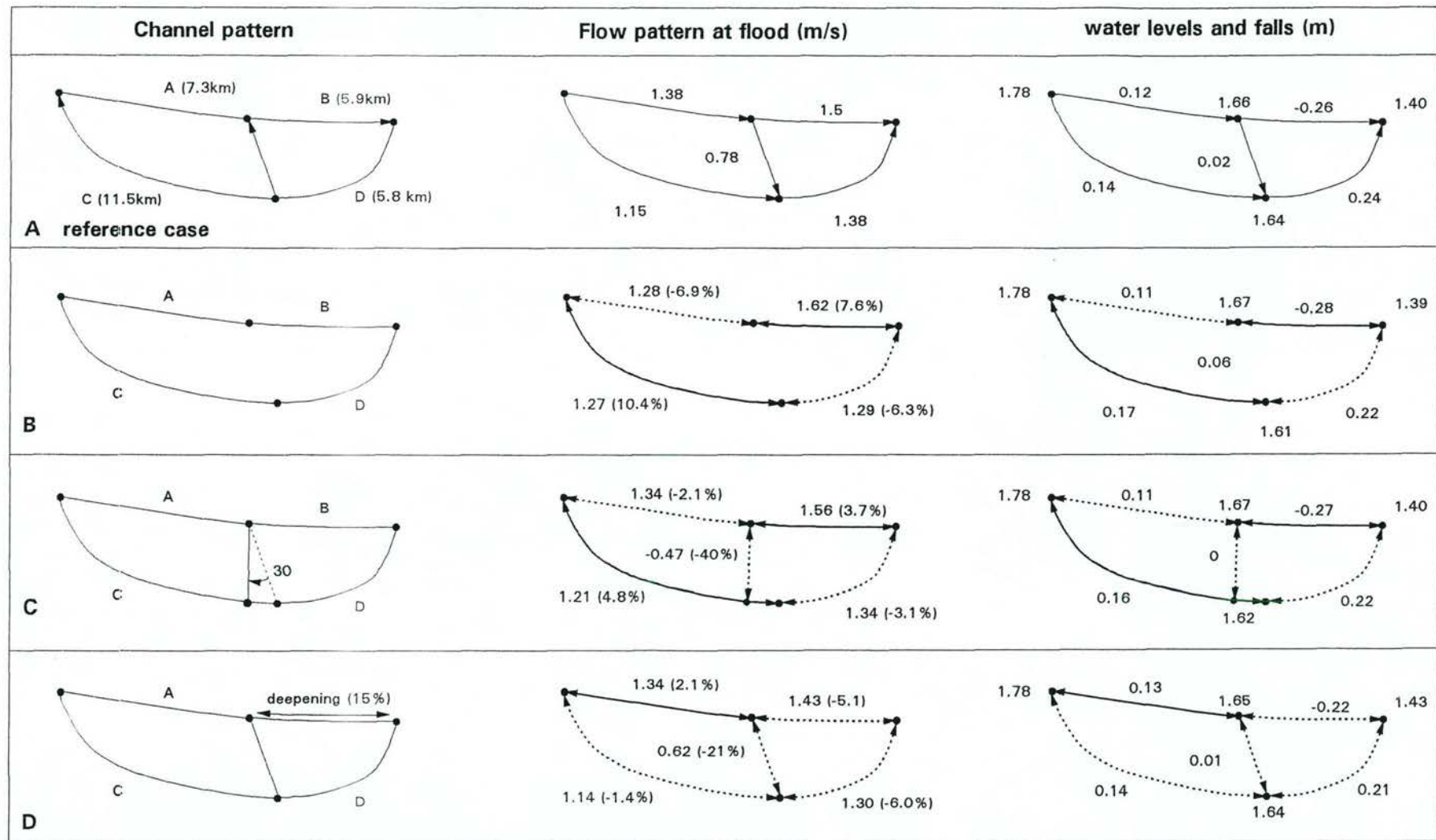


Figure 2.17b *The initial adaptations in flow pattern and water level pattern due to morphological changes. Each figure presents the following four situations:*

A) reference situation. B) the channel pattern without the large cross channel, C) the effect of a clockwise rotation of the cross channel of 30°. D) the effect of a deepening of the flood channel bar by 15 %.

Solid heavy line = increase with respect to the reference situation, dotted line indicates a decrease.

*a) situation at maximum ebb;
b) situation at maximum flood;*

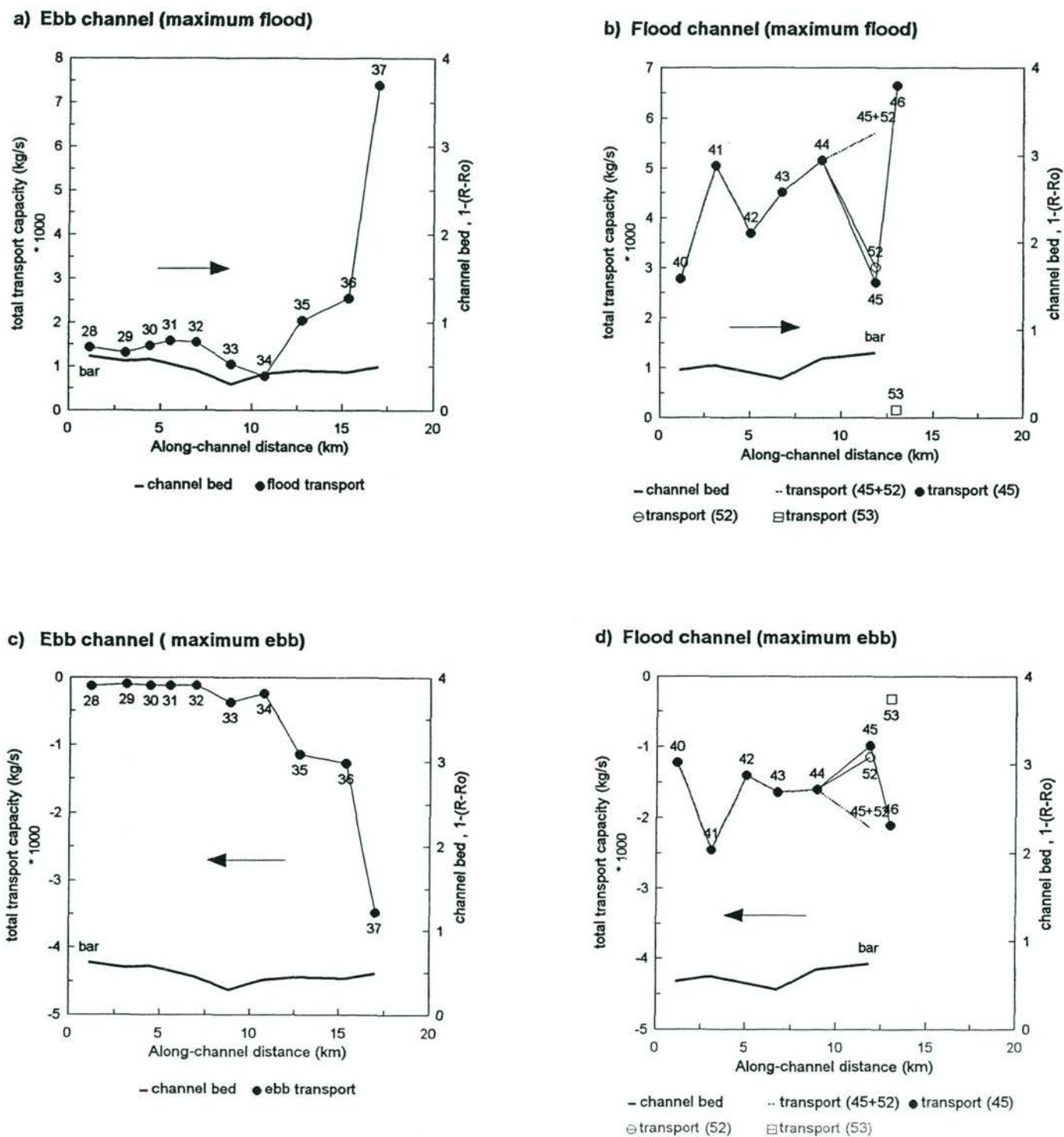


Figure 2.18 Calculated sediment transport capacity (kg/s) according to Van Rijn (1990) at maximum flow, using the the flow response of Dufrow. (R =hydraulic radius, $R_o=30m$).

a) flood transport capacity in the ebb channel
 b) flood transport capacity in the flood channel
 c) ebb transport capacity in the ebb channel
 d) ebb transport capacity in the flood channel.

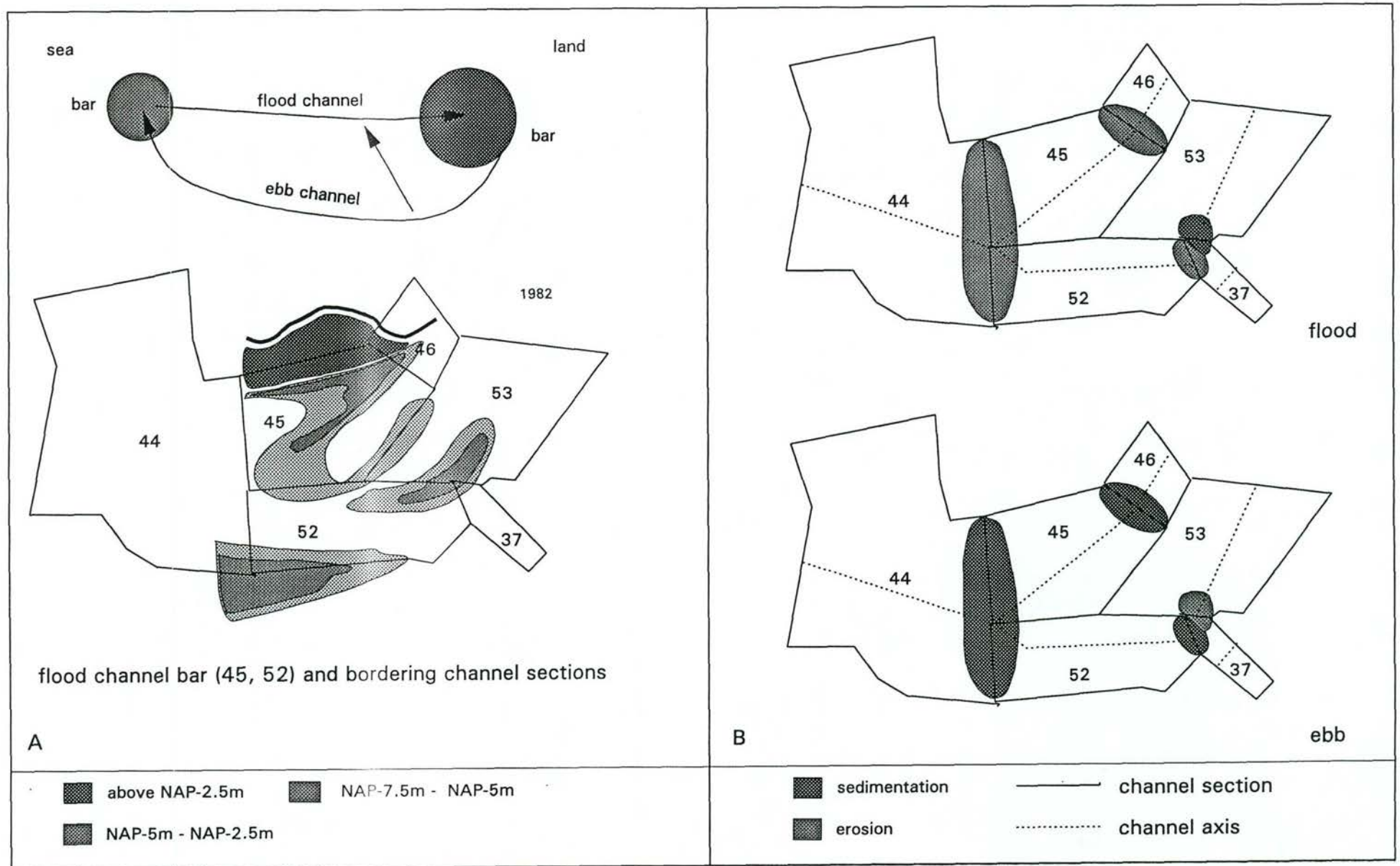


Figure 2.19 Calculated erosion and sedimentation pattern near the flood channel bar. Calculation of the sediment transport is based on a DufLOW simulation and the application of Van Rijn's (1990) formula for suspended and bed load transport.

a) bar morphology and the channel sections according to DufLOW

b) erosion and sedimentation at maximum flood and ebb

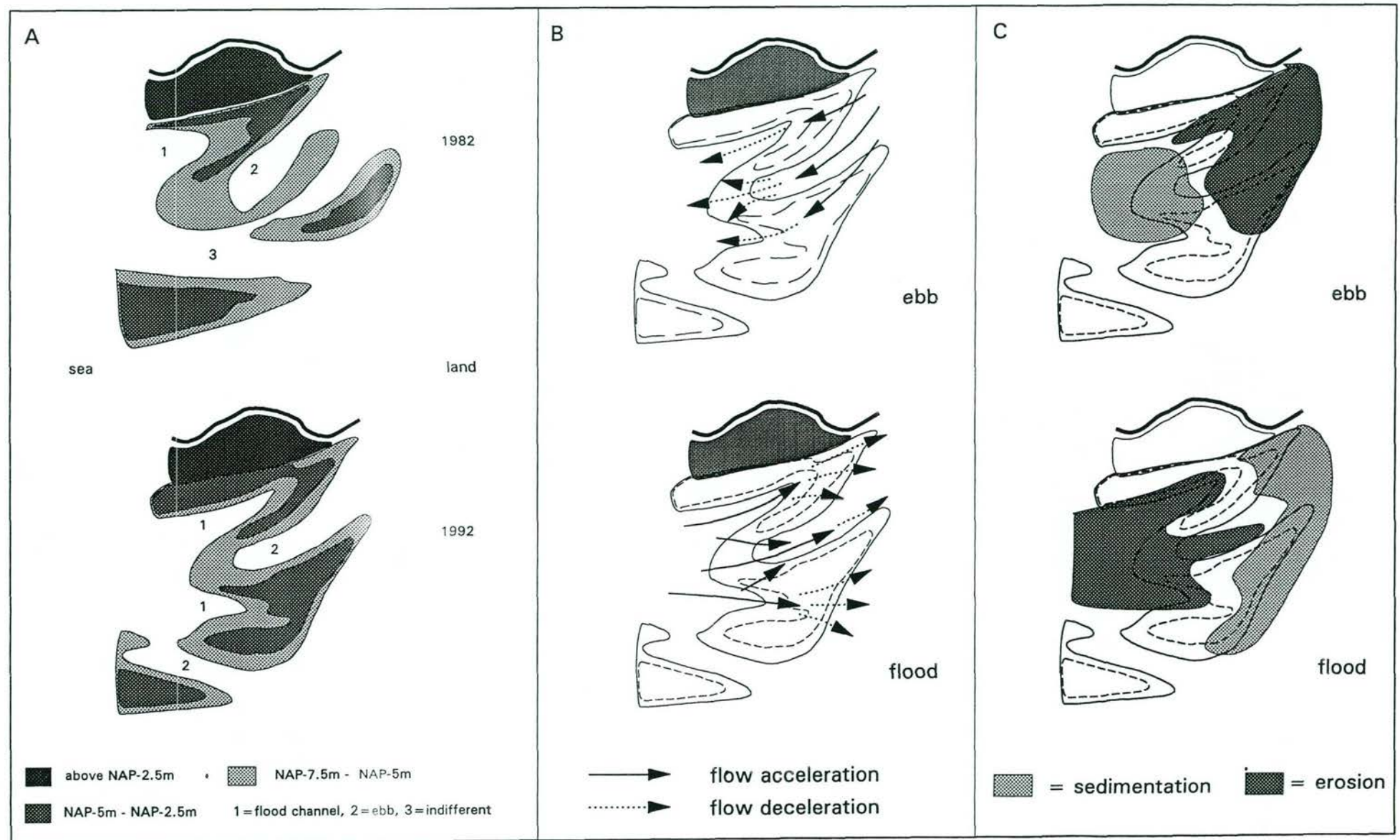


Figure 2.20 Expected patterns of primary flow and erosion and sedimentation related to the morphology of bar channels
 a) channel morphology of the bar channels at flood channel bar in 1982 and 1992.
 b) flow pattern at ebb and flood across the bar channel morphology in 1992.
 c) expected patterns of erosion and sedimentation at ebb and flood.

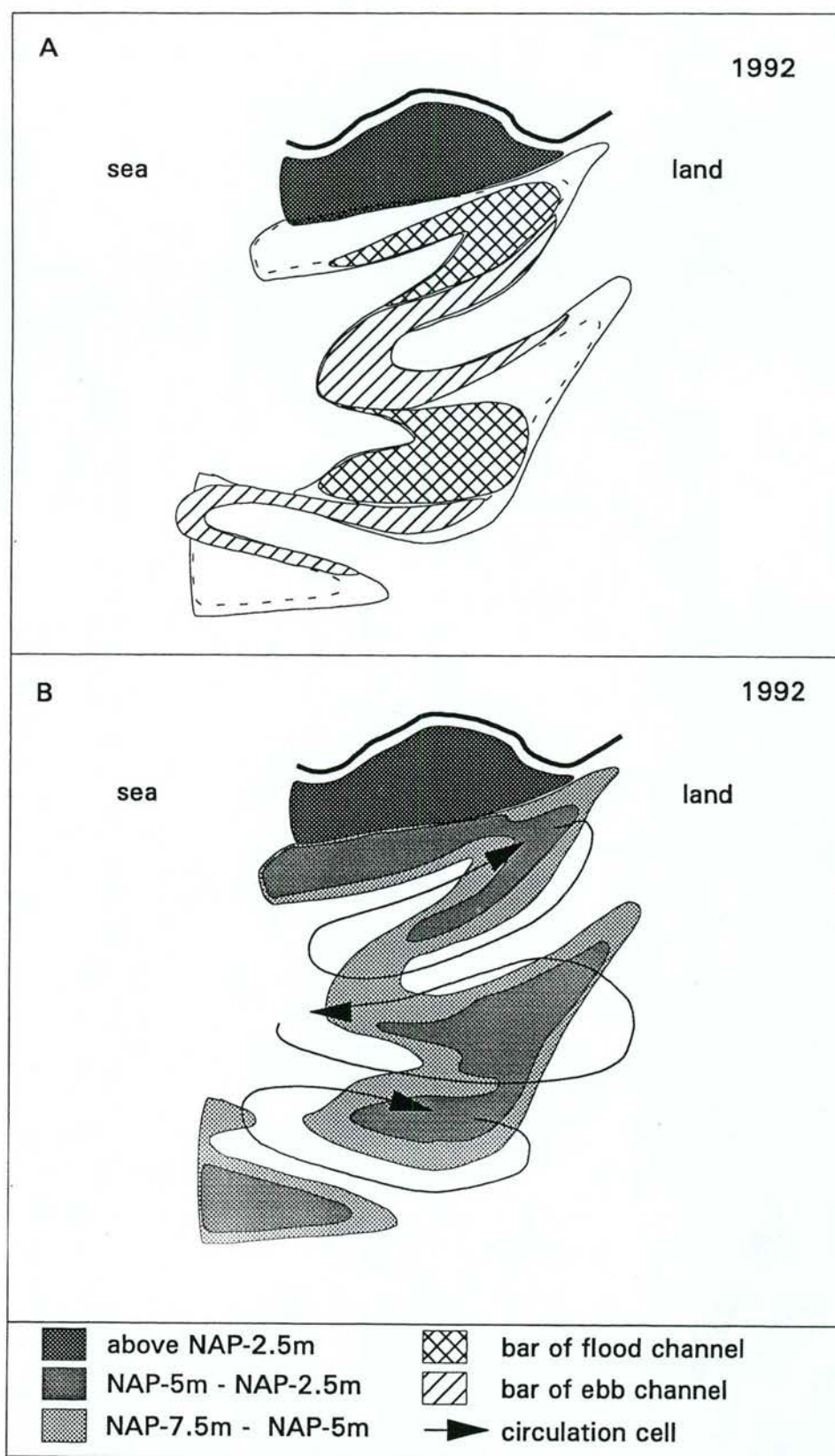


Figure 2.21

The combined effect of flood-dominated and ebb-dominated bar channels.
 a) the formation of a zig-shaped shoal consisting of the small bars of the individual bar channels.
 b) the presence of (eulerian) circulation cells of flow and sediment.

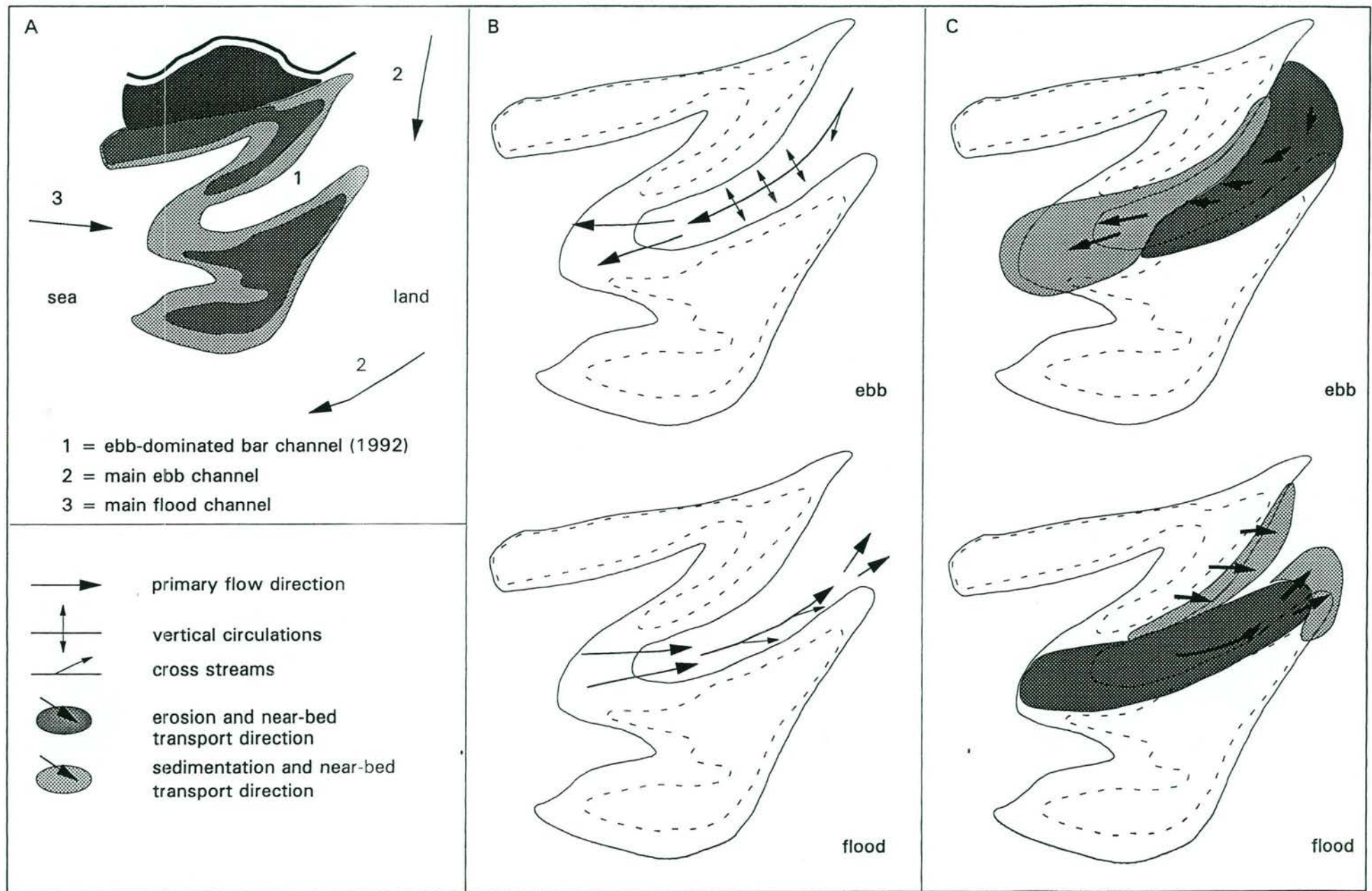


Figure 2.2/ Expected patterns of flow and erosion and sedimentation in the ebb-dominated bar channel.

a) Channel morphology of 1992

b) expected secondary flow phenomena and the course of the primary flow at ebb and flood.

c) expected locations of erosion and sedimentation at ebb and flood

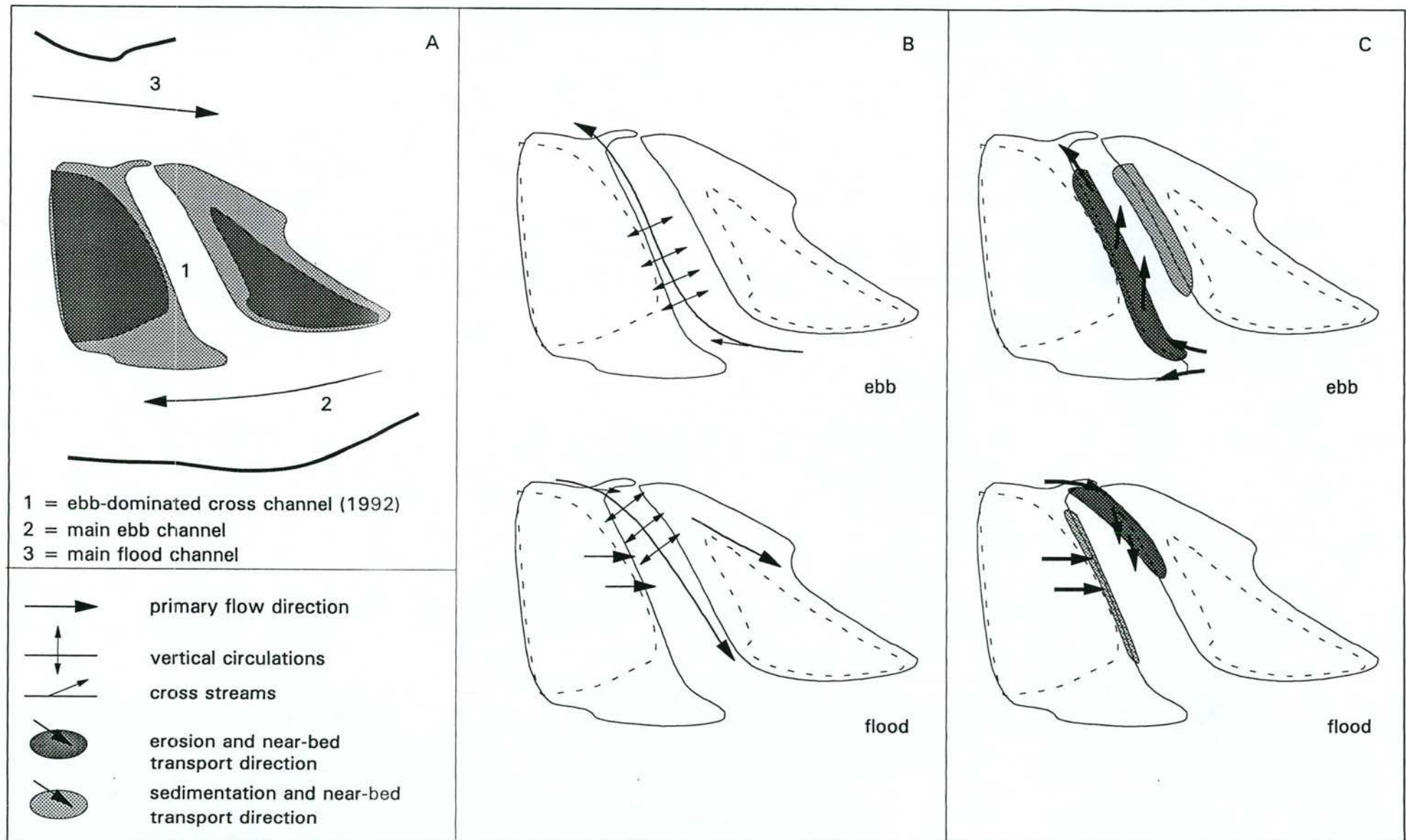


Figure 2.22 Expected patterns of flow and erosion and sedimentation in the ebb-dominated cross channel.
 a) Channel morphology of 1992
 b) expected secondary flow phenomena and the course of the primary flow at ebb and flood.
 c) expected locations of erosion and sedimentation at ebb and flood

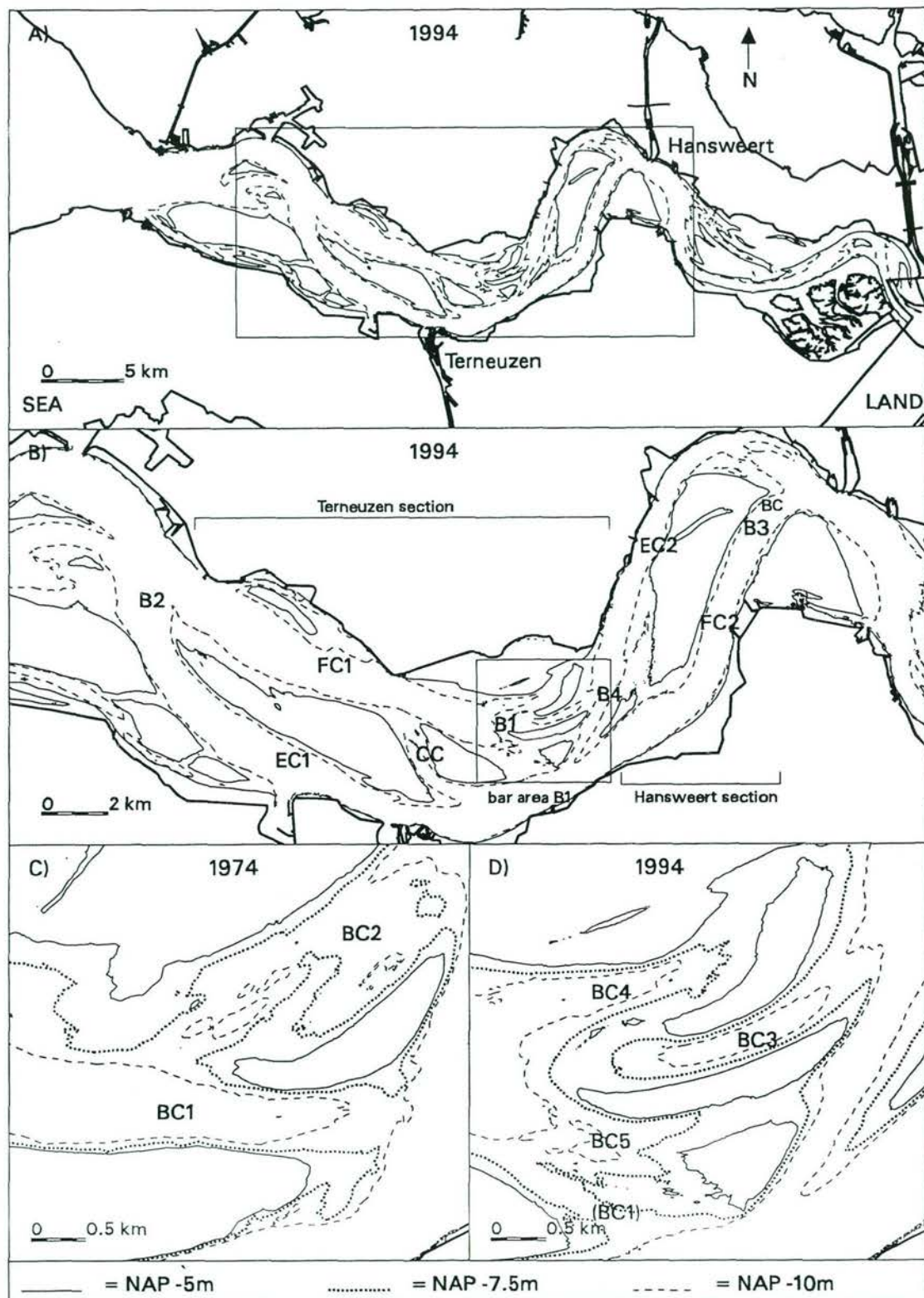


Fig. 3.1

Bathymetric maps of the Westerschelde in 1994 (a), the Terneuzen and Hansweert section in 1994 (b) and the bar channels in 1974 (c) and 1994 (d).

FC# = main flood channel (and number)

EC = main ebb channel

BC & CC = connecting channels: CC = cross channel BC = bar channel (+number)

B# = bar in main channel.

NAP = Dutch Ordnance level.

These abbreviations of the channel types are used throughout the chapter.

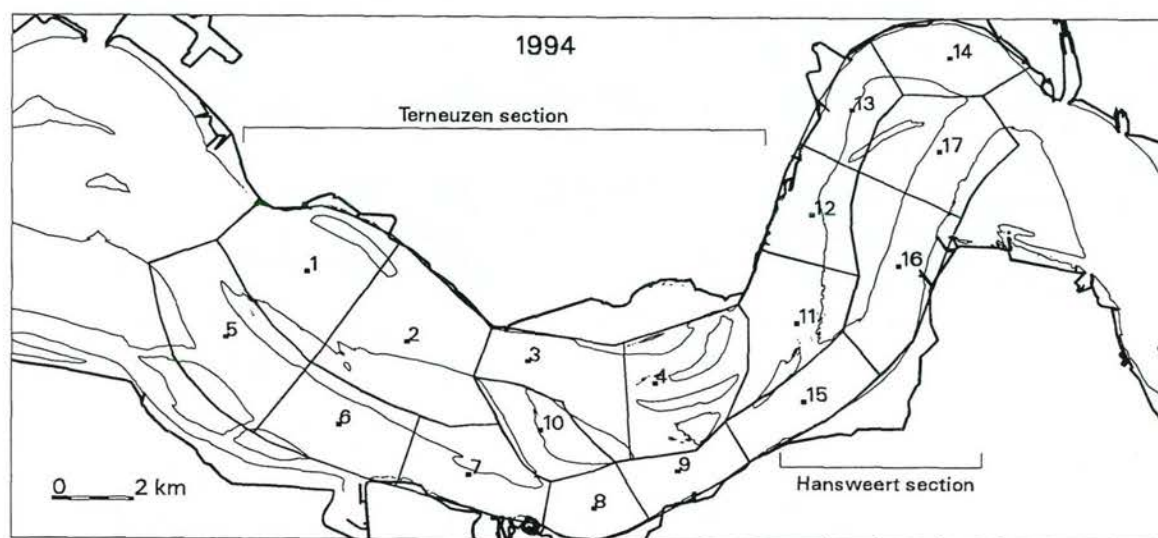


Fig. 3.2 The schematisation of the main channels into channel sections, to compute the changes in the sediment budgets and the average cross-sectional channel geometry.

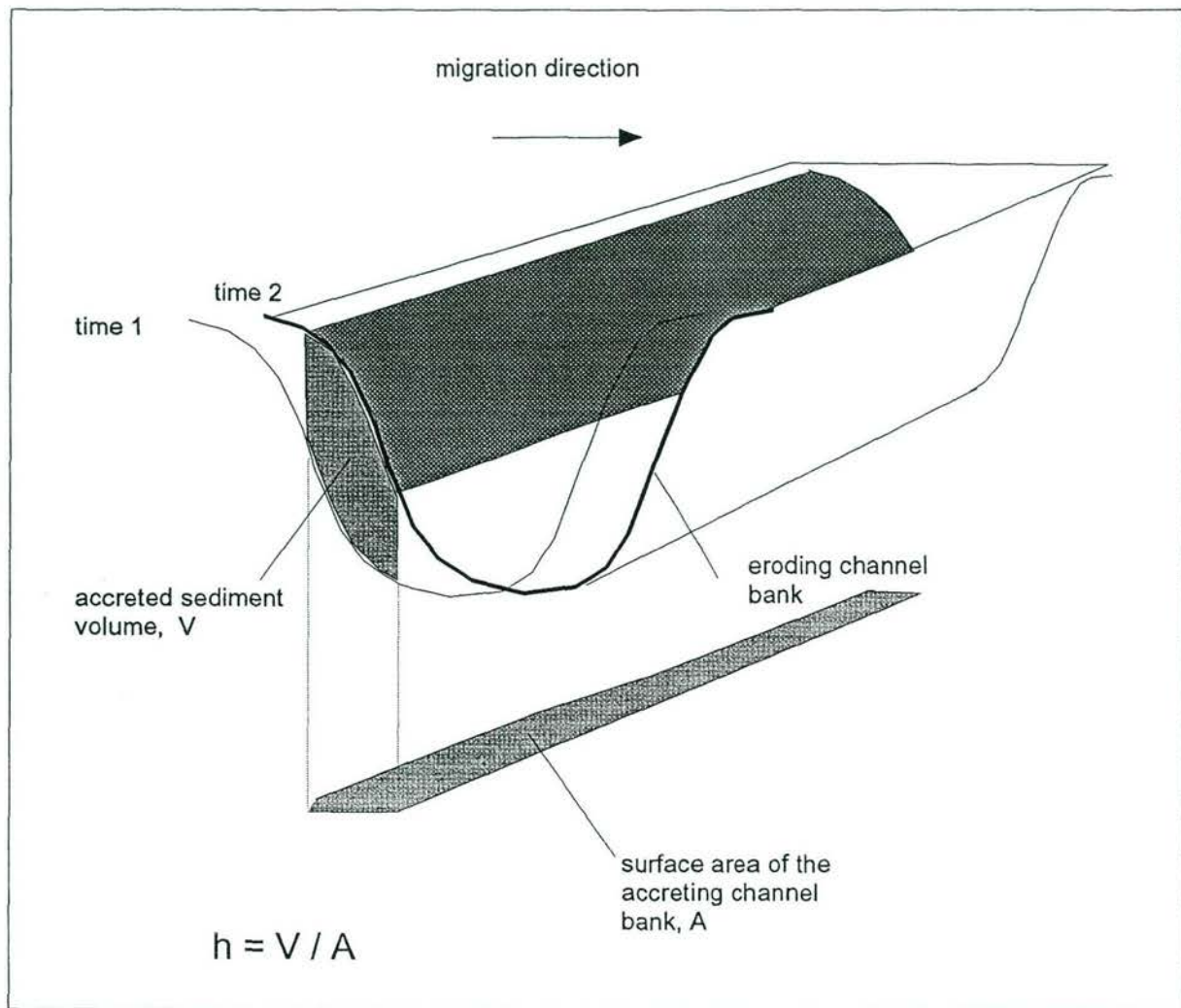


Fig. 3.3 Definition sketch of the computation of the channel migration.

sediment reworking (Mm³/2yrs)

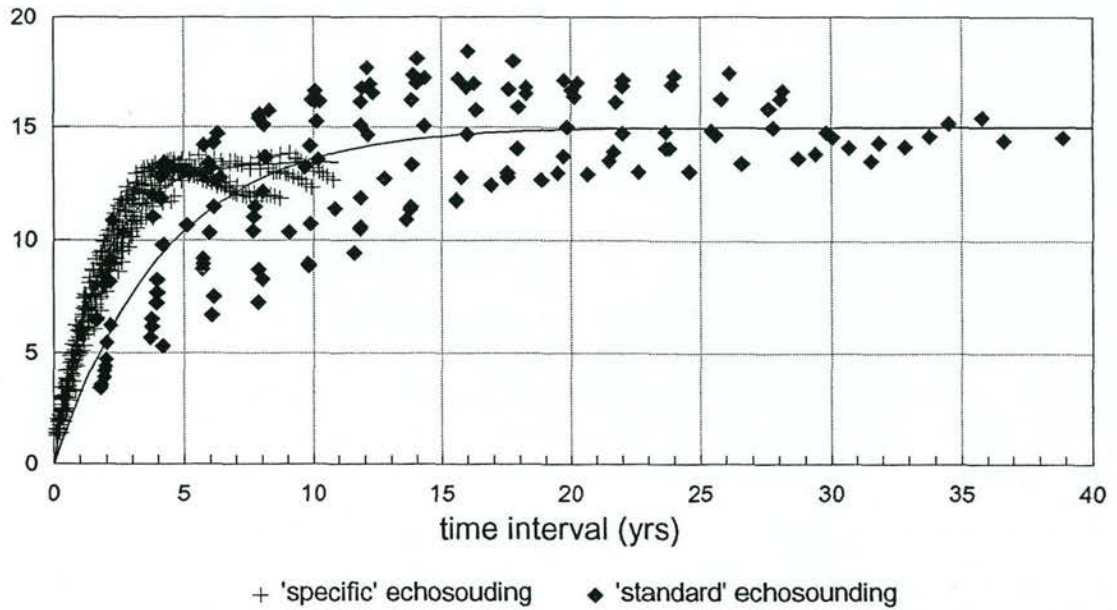


Fig. 3.4 The total sediment reworking at the bar B1 in the main flood channel FC1(section 4, Fig. 3.2) versus time interval.

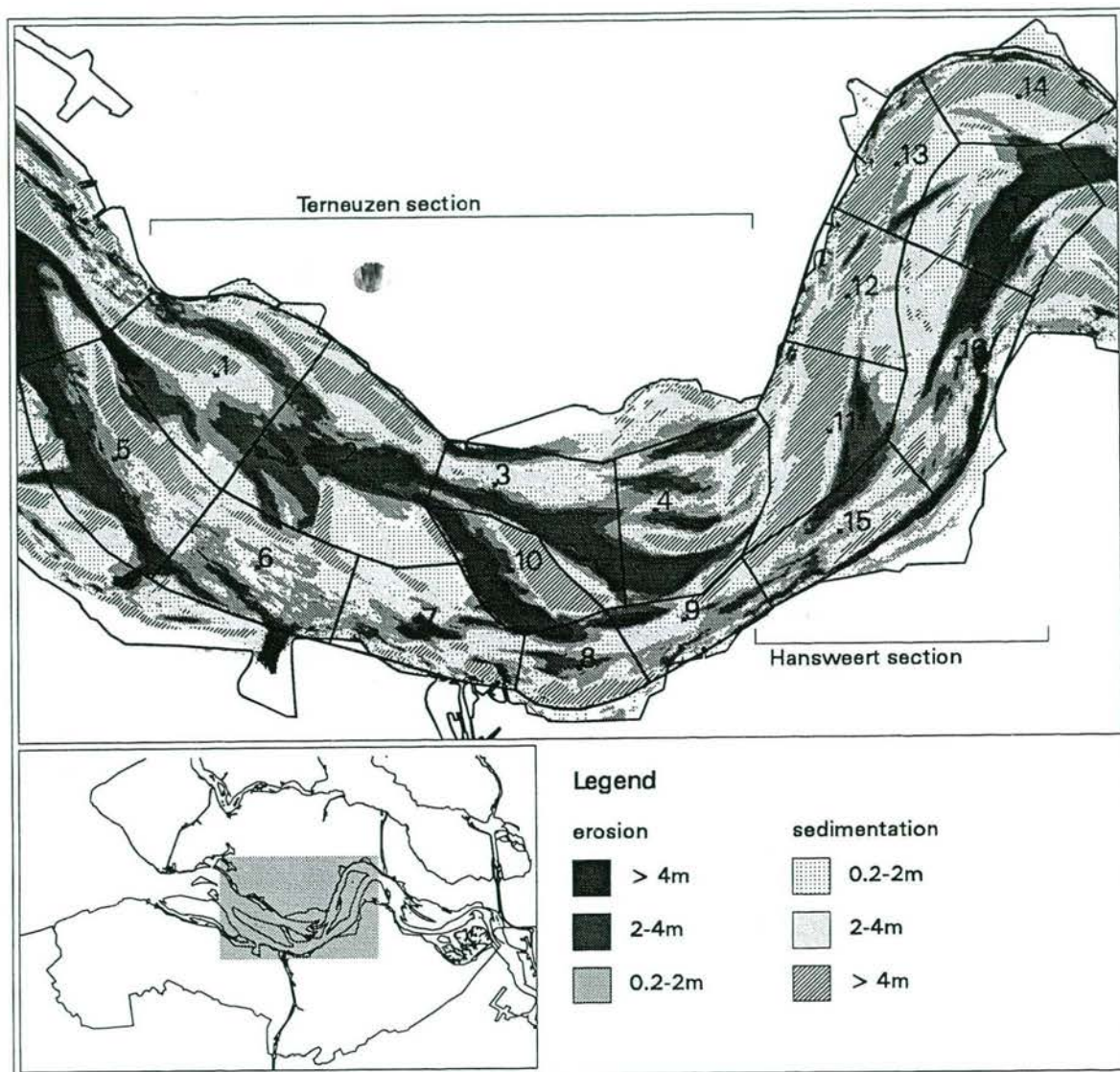


Fig. 3.5 Erosion-sedimentation patterns over the period 1955-1996.

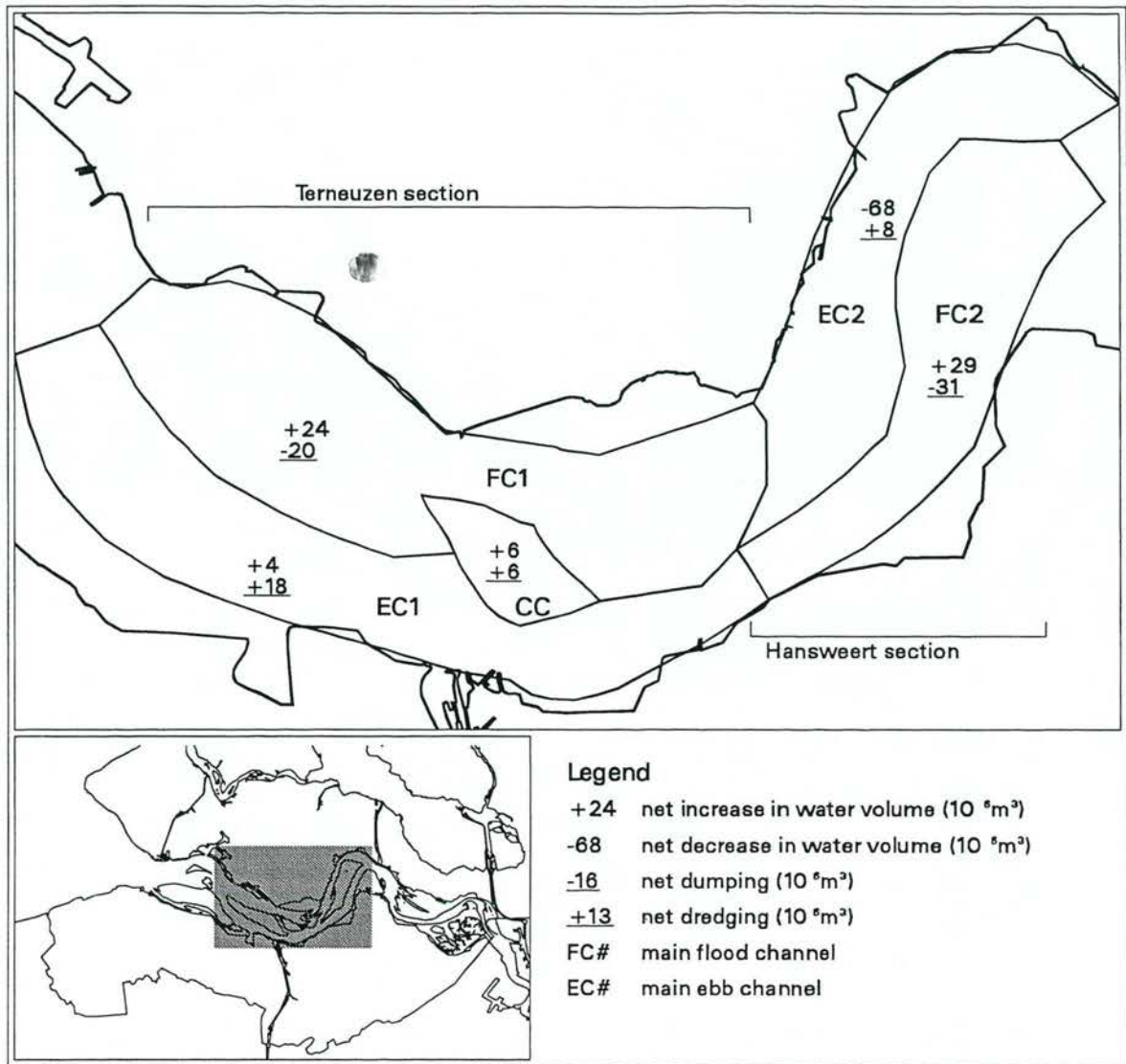


Fig. 3.6 Large-scale changes in the sediment budget (in Mm³) in the Terneuzen and Hansweert section between 1955 and 1996. The changes refer to the water volume below NAP+2.5m

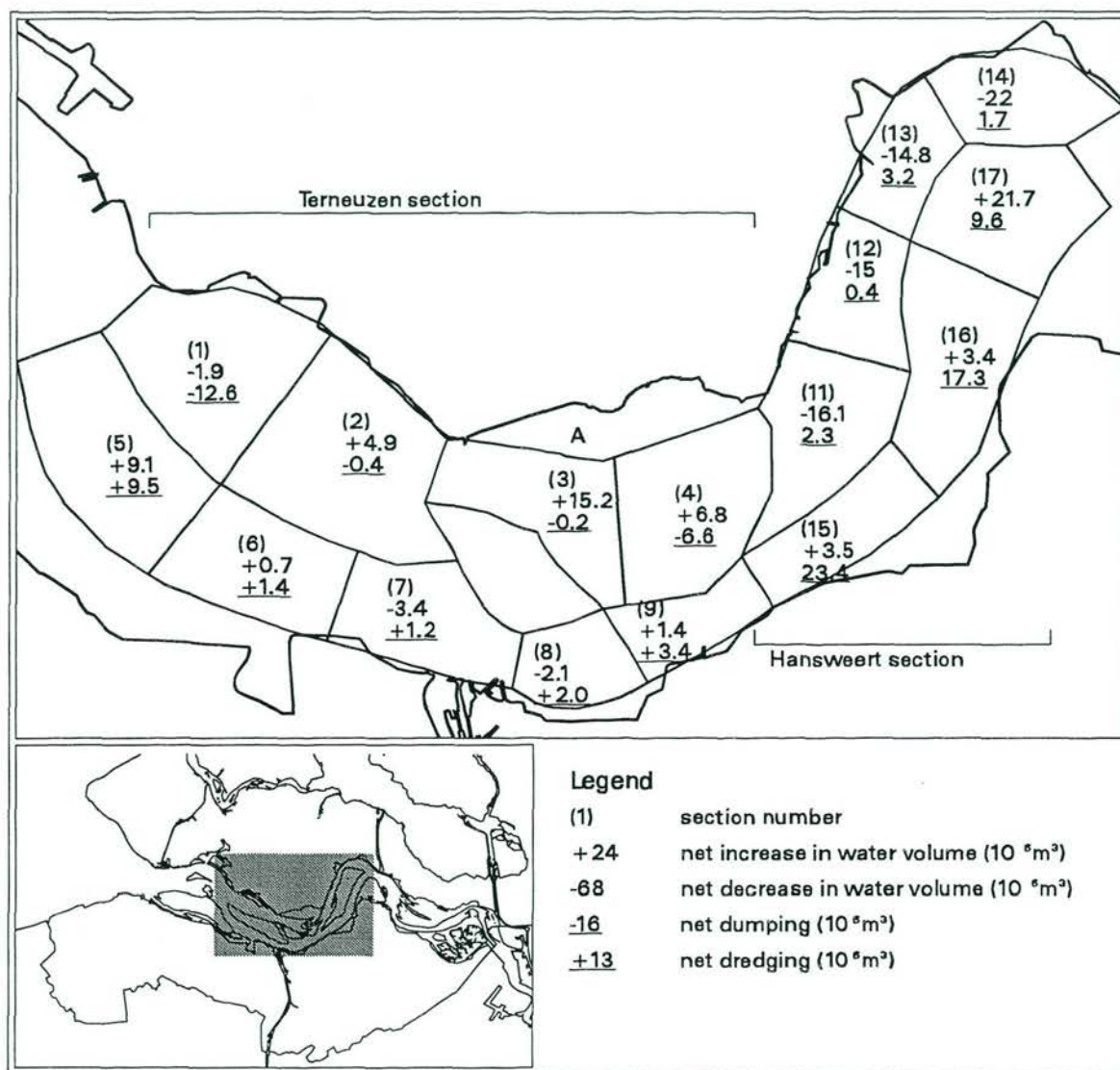


Fig. 3.7 Small-scale changes in the sediment budget (in Mm^3) in the Terneuzen and Hansweert section between 1955 and 1996. The changes refer to the water volume below NAP+2.5m

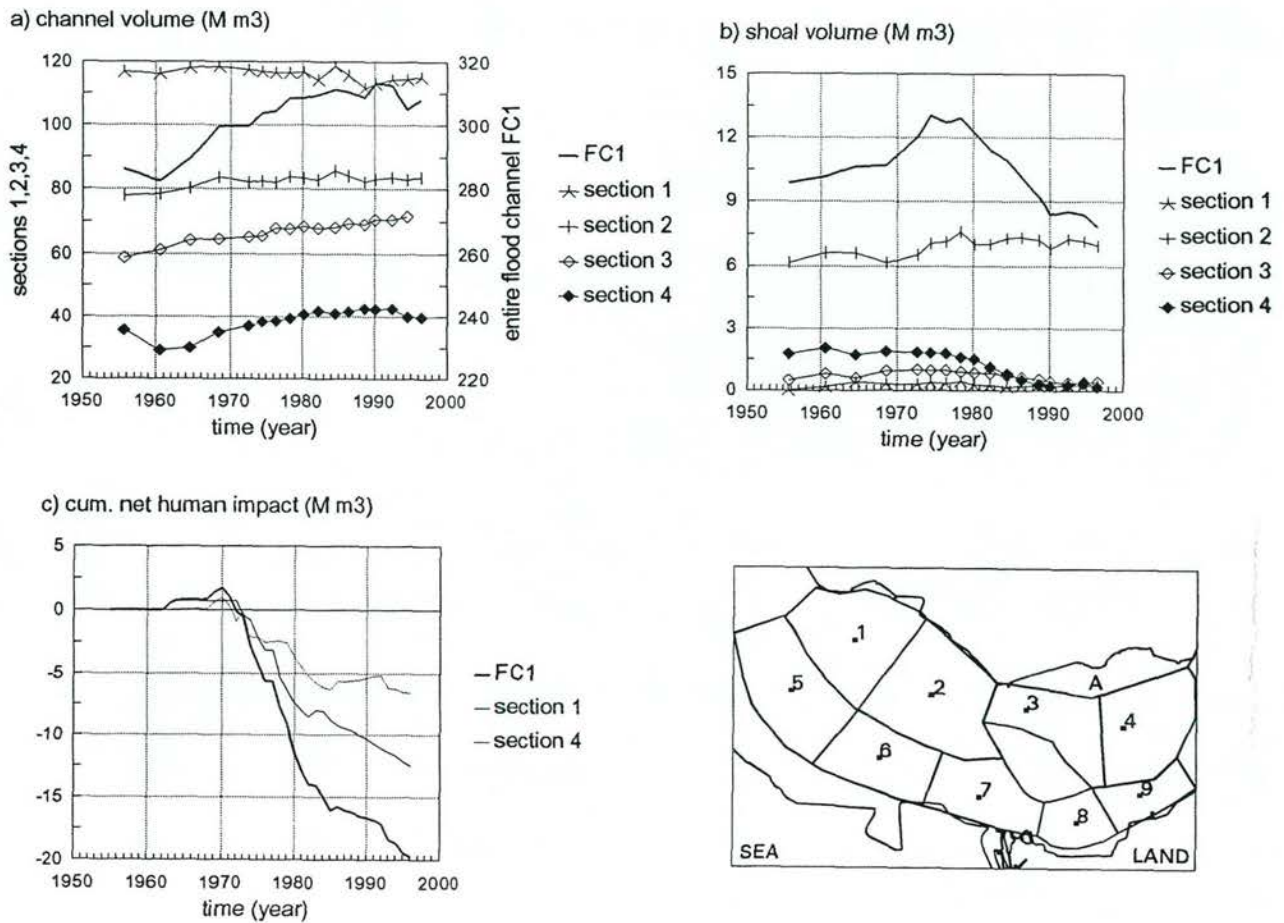


Fig. 3.8 Small-scale evolution of the sediment budgets (in Mm^3) in the main flood channel FC1 in the Terneuzen section between 1955 and 1996. FC1 is the entire main flood channel (= sum of changes in sections 1,2,3 and 4).

a) changes in the channel volume (water volume below NAP-2m)

b) changes in the intertidal shoal volume (sand volume above NAP-2m)

c) cumulative net magnitude of dredging and dumping. Positive values mean a net dredging, whereas negative values indicate a net dumping.

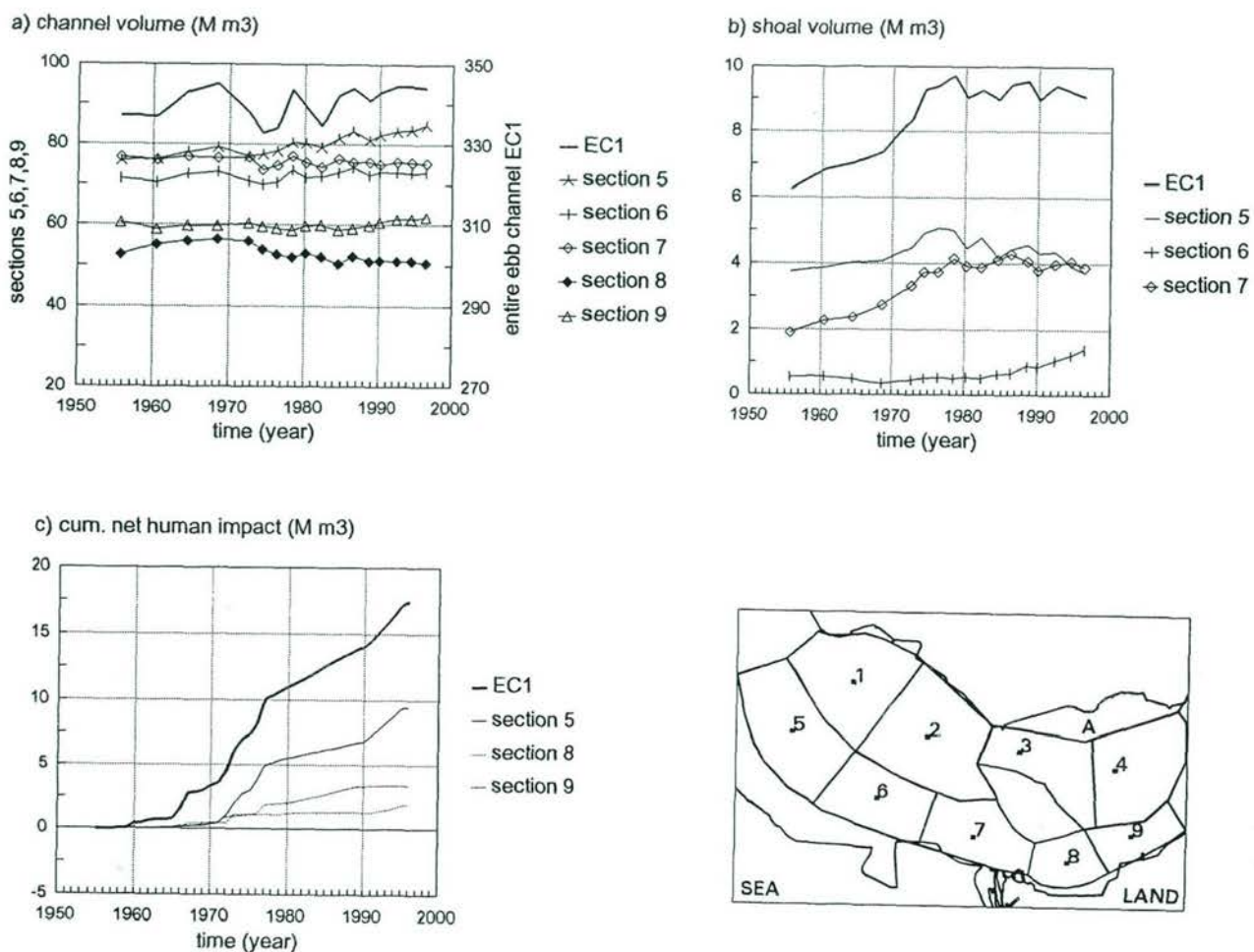


Fig. 3.9 Small-scale evolution of the sediment budgets (in Mm^3) in the main ebb channel EC1 in the Terneuzen section between 1955 and 1996. EC1 is the entire main ebb channel (= sum of changes in sections 5,6,7,8 and 9).

a) changes in the channel volume (water volume below NAP-2m)

b) changes in the intertidal shoal volume (sand volume above NAP-2m)

c) cumulative net magnitude of dredging and dumping. Positive values mean a net dredging, whereas negative values indicate a net dumping.

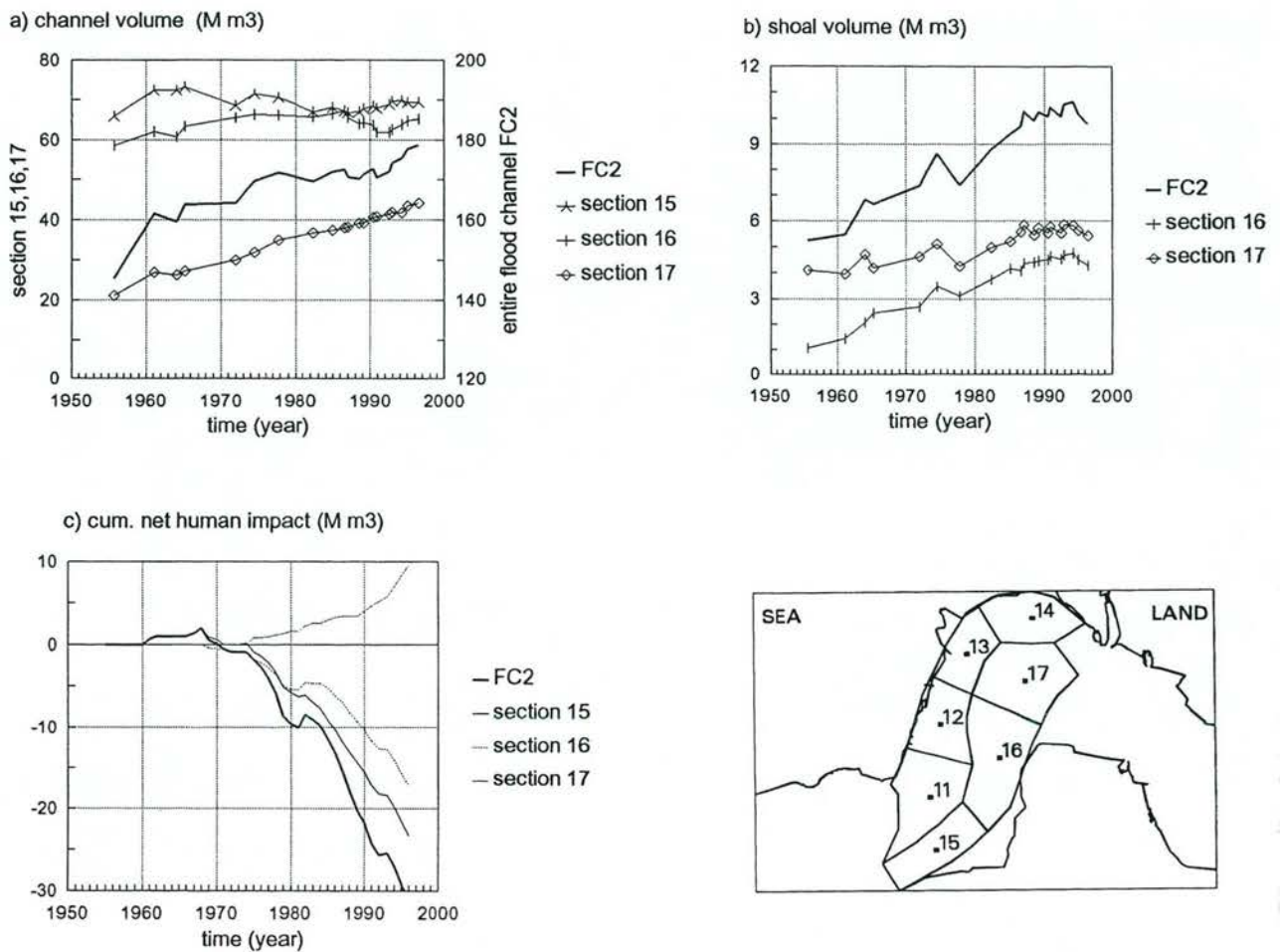


Fig. 3.10

Small-scale evolution of the sediment budgets (in Mm³) in the main flood channel FC2 in the Hansweert section between 1955 and 1996. FC2 is the entire main flood channel (= sum of changes in sections 15, 16 and 17).

- changes in the channel volume (water volume below NAP-2m)
- changes in the intertidal shoal volume (sand volume above NAP-2m)
- cumulative net magnitude of dredging and dumping. Positive values mean a net dredging, whereas negative values indicate a net dumping.

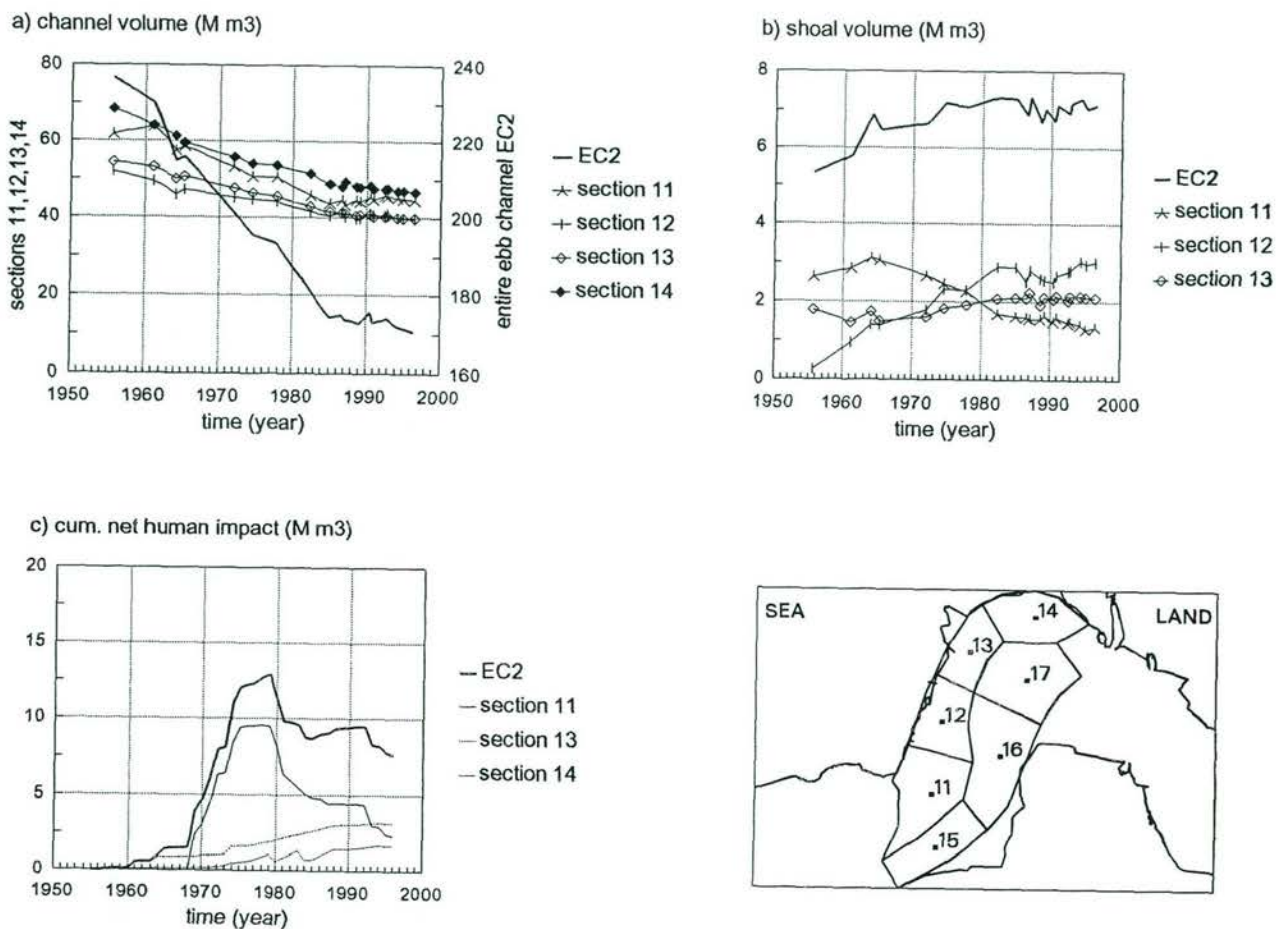


Fig. 3.11 Small-scale evolution of the sediment budgets (in Mm^3) in the main ebb channel EC2 in the Hansweert section between 1955 and 1996. EC2 is the entire main ebb channel (= sum of changes in sections 11, 12, 13 and 14).

a) changes in the channel volume (water volume below NAP-2m)

b) changes in the intertidal shoal volume (sand volume above NAP-2m)

c) cumulative net magnitude of dredging and dumping. Positive values mean a net dredging, whereas negative values indicate a net dumping.

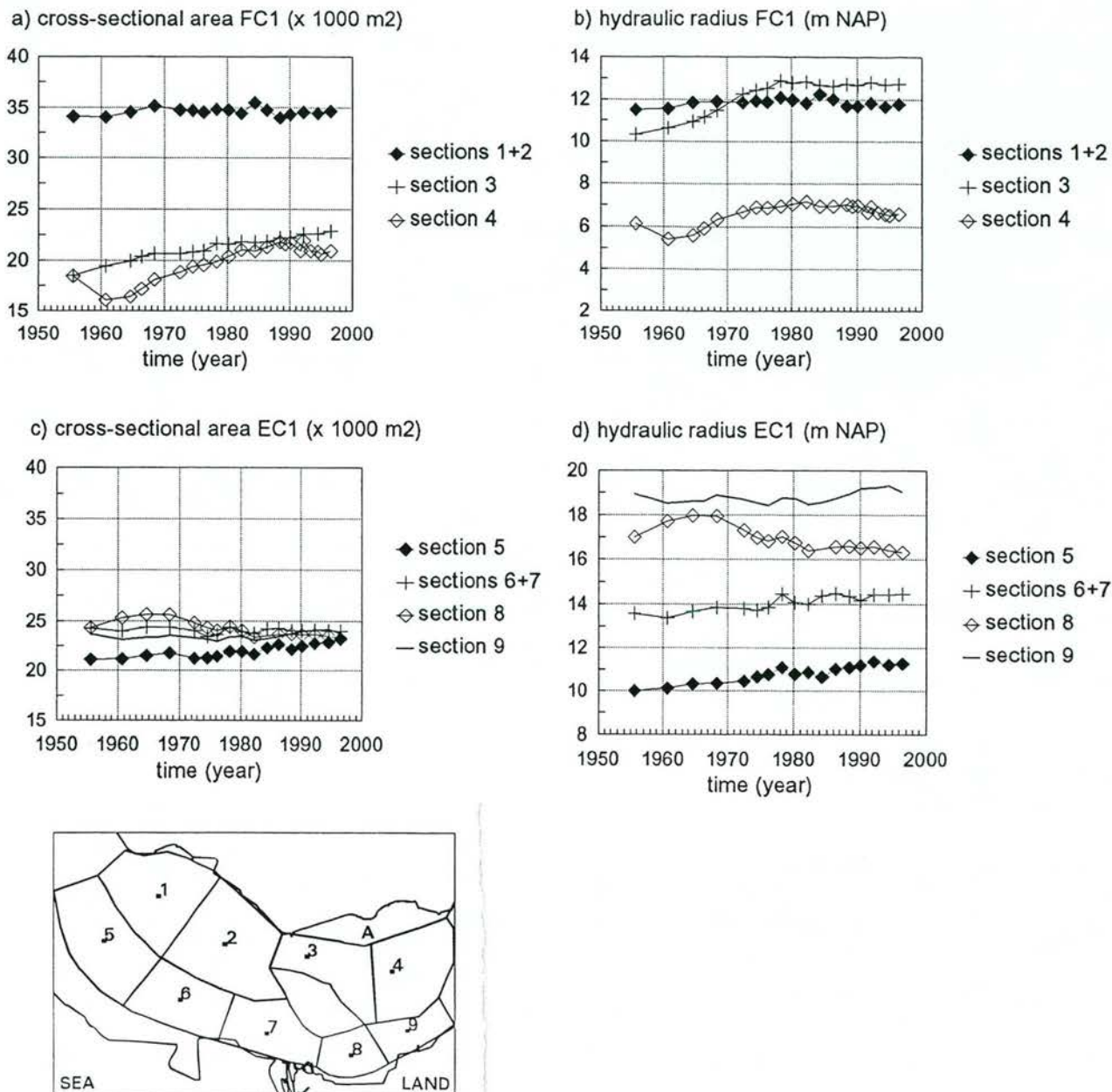


Fig. 3.12

Evolution of the cross-sectional channel geometry of the main channels FC1 and EC1 in the Terneuzen section between 1955 and 1996. FC1 = entire main flood channel, EC1=entire main ebb channel

- average cross section area of the main flood channel
- average hydraulic radius of the main flood channel
- average cross section area of the main ebb channel
- average hydraulic radius of the main ebb channel

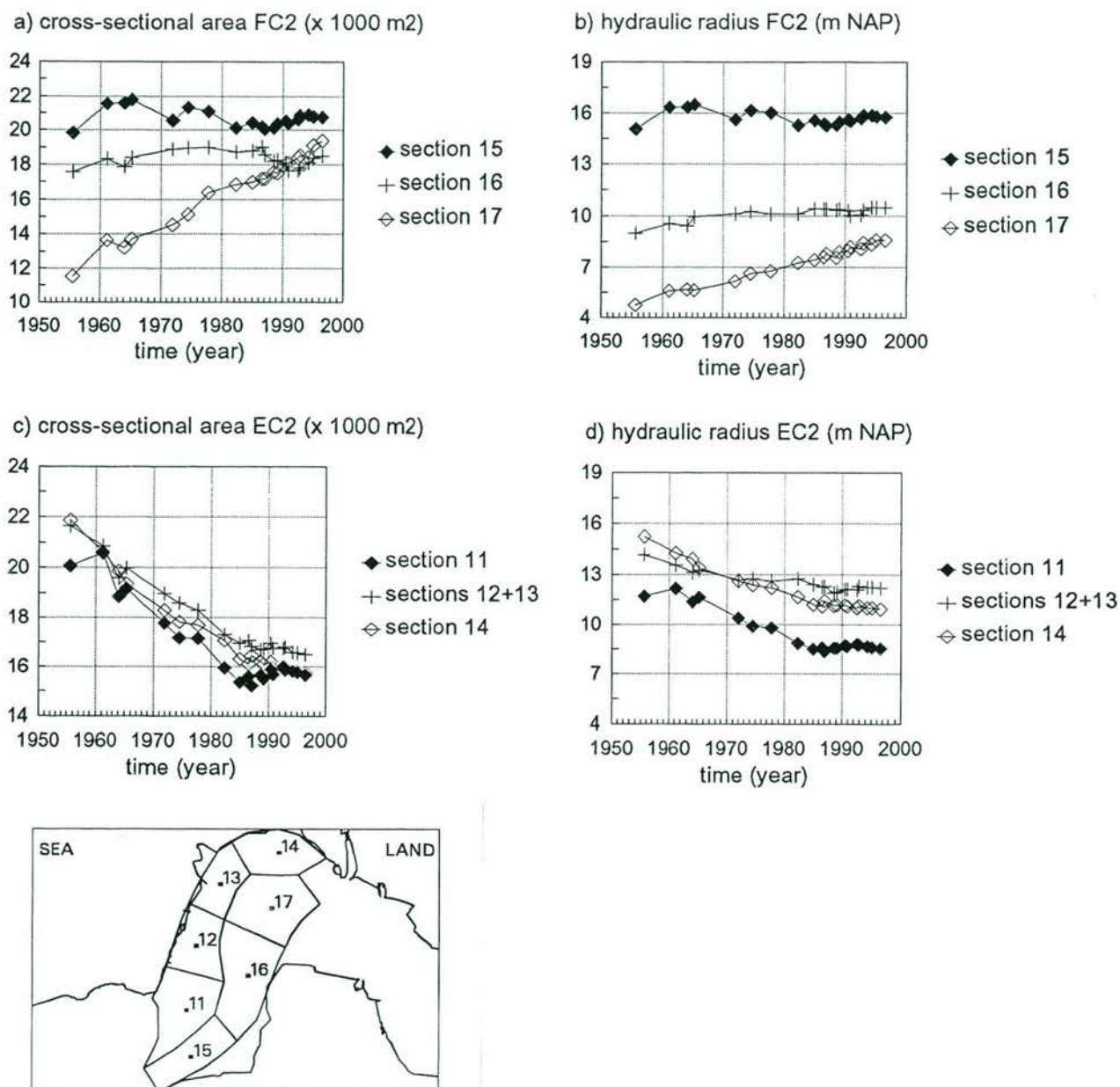
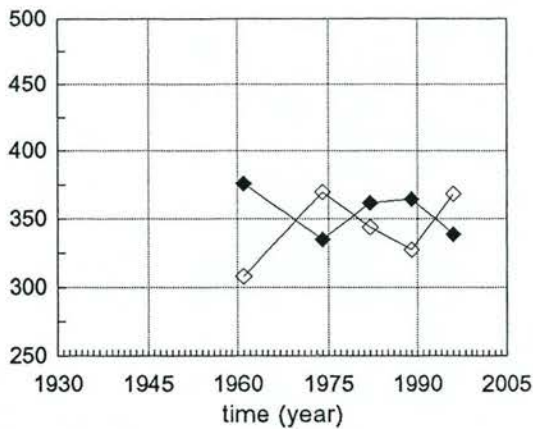


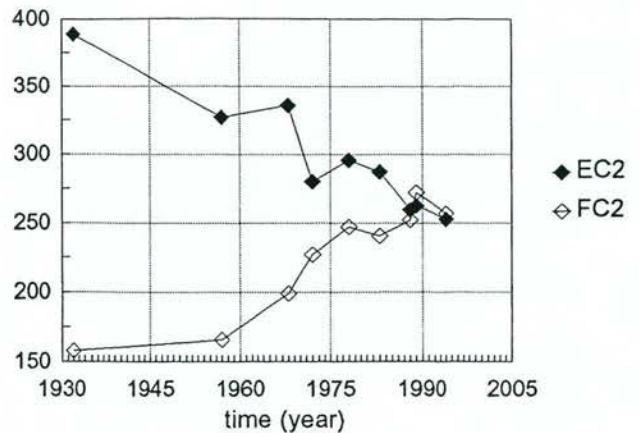
Fig. 3.13 Evolution of the cross-sectional channel geometry of the main channels FC2 and EC2 in the Hansweert section between 1955 and 1996. FC2 = entire main flood channel, EC2=entire main ebb channel

- average cross sectional area of the main flood channel
- average hydraulic radius of the main flood channel
- average cross sectional area of the main ebb channel
- average hydraulic radius of the main ebb channel

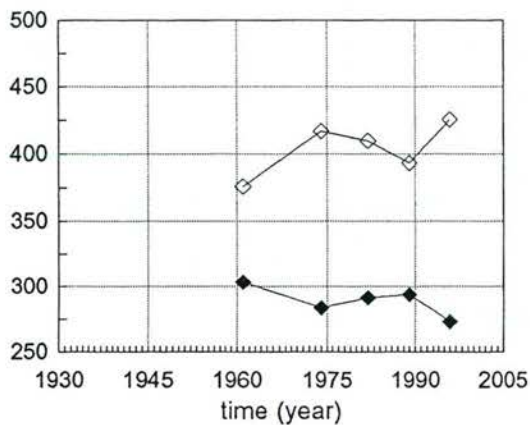
a) ebb volume (Mm³) Terneuzen section



c) ebb volume (Mm³) Hansweert section



b) flood volume (Mm³) Terneuzen section



d) flood volume (Mm³) Hansweert section

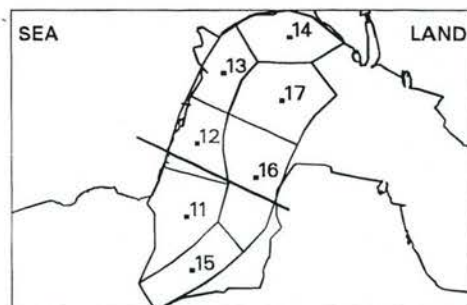
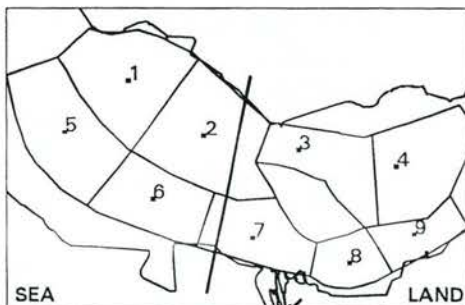
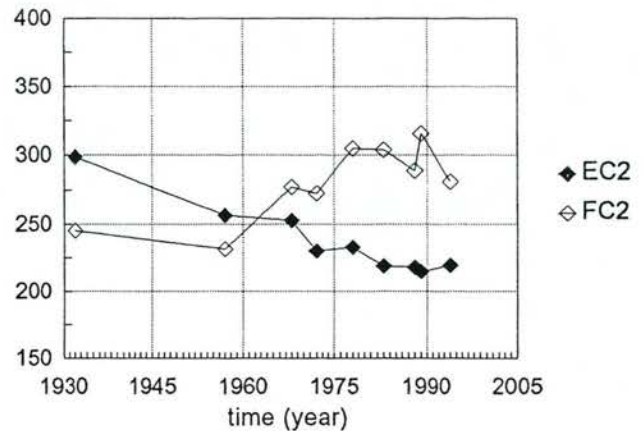


Fig. 3.14

Changes in the distribution of the tidal volumes (in Mm³) between the main ebb and flood channel in the Terneuzen and Hansweert section since 1932, based on discharge measurements.

- a) ebb volumes in the main channels of the Terneuzen section
- b) flood volumes in the main channels of the Terneuzen section
- c) ebb volumes in the main channels of the Hansweert section
- d) flood volumes in the main channels of the Hansweert section

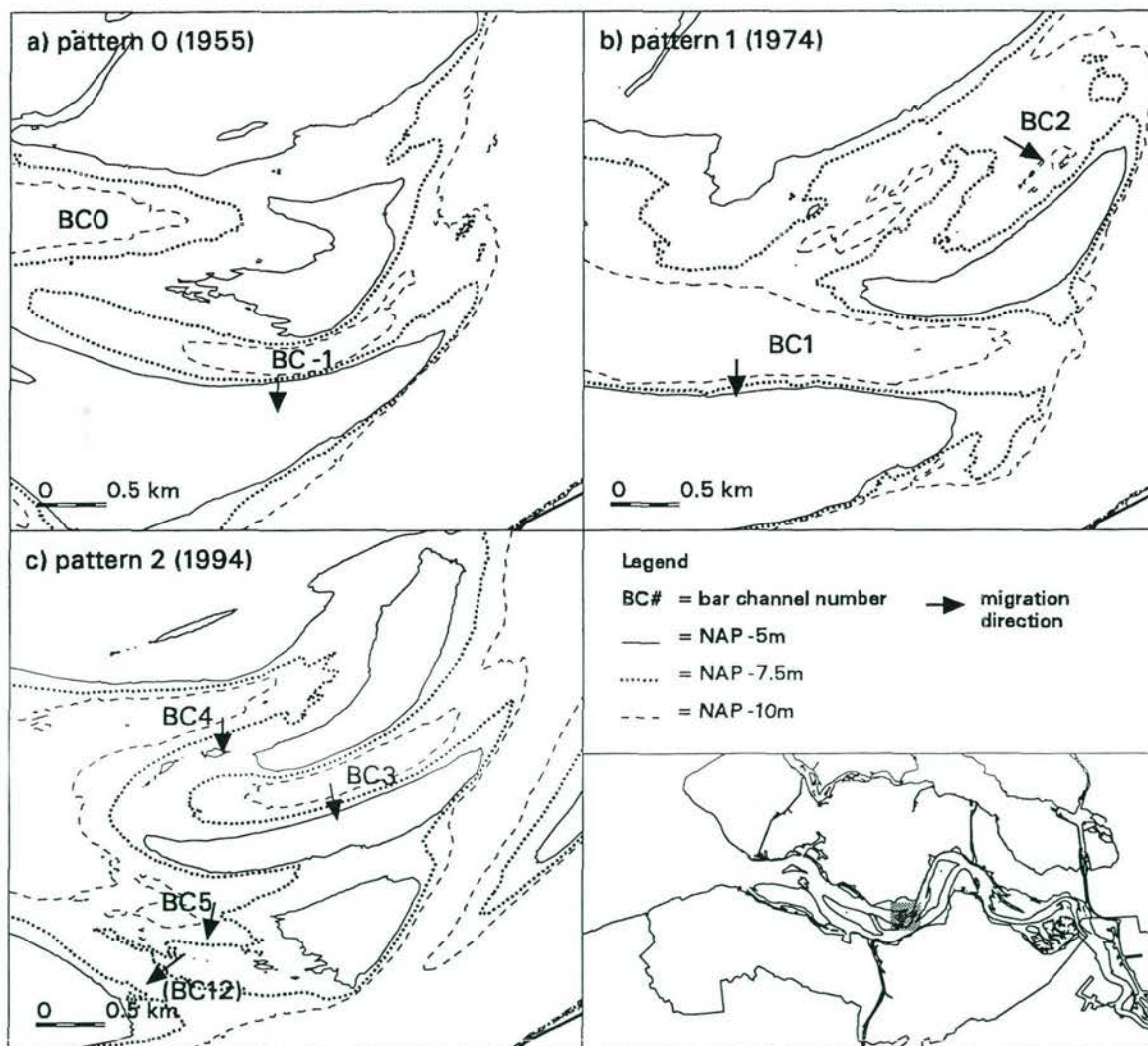


Fig. 3.15 The three patterns of bar channels between 1955 and 1996.

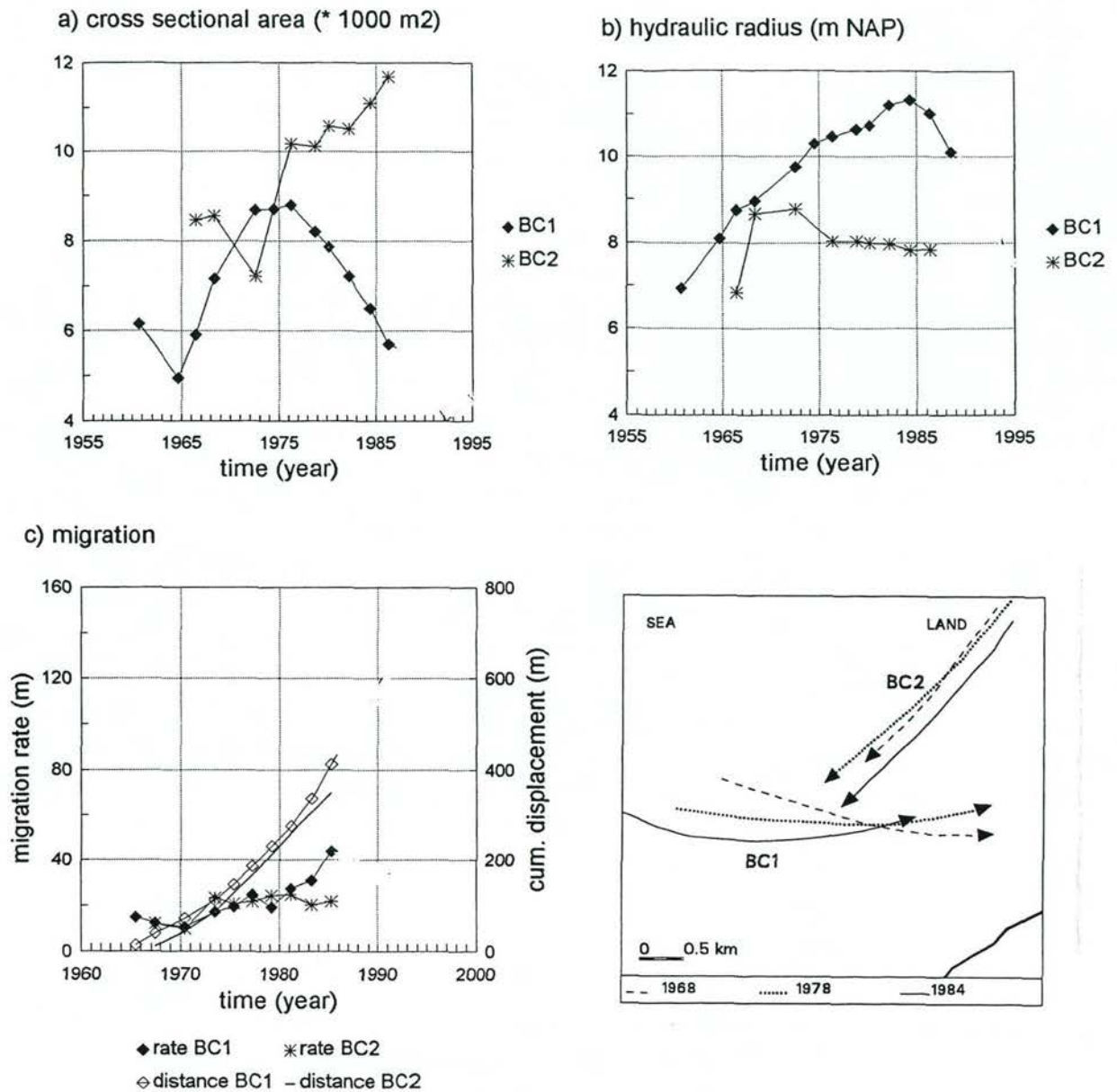
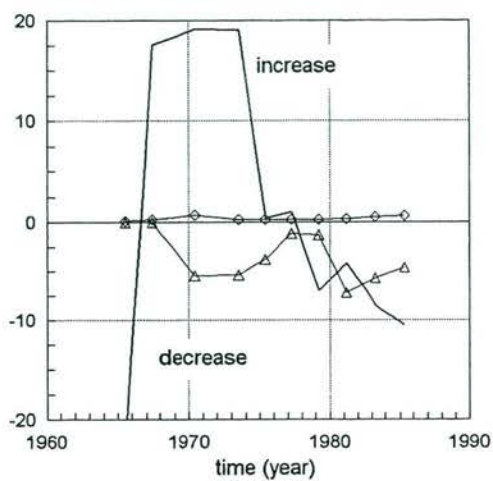


Fig. 3.16

The morphological evolution of channel pattern 1 in the Terneuzen section.

- changes in the average cross-sectional area of the channels.
- changes in the average hydraulic radius of the channels.
- average migration rates and cumulative channel displacement
- changes in the location of the channel axis.

a) change in cross section BC1 (%)



b) change in cross section BC2 (%)

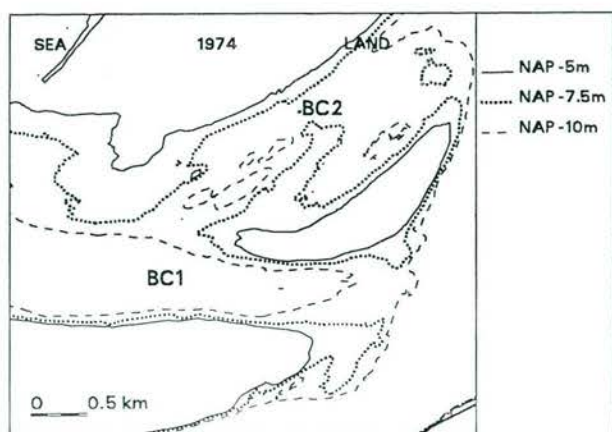
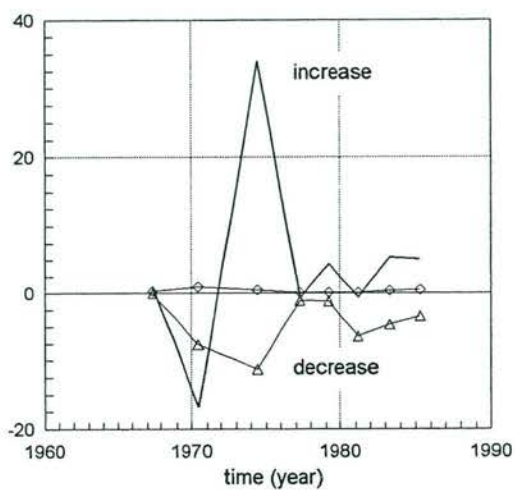


Fig. 3.17

The observed changes in the cross sectional area of channel pattern 1 (in %) and the potential changes in the channel cross section as result of dredging and dumping. Positive values indicate an increase of the channel cross section. Negative values indicate a decrease of the channel cross section.

- a) the flood bar channel BC1
- b) the ebb bar channel BC2

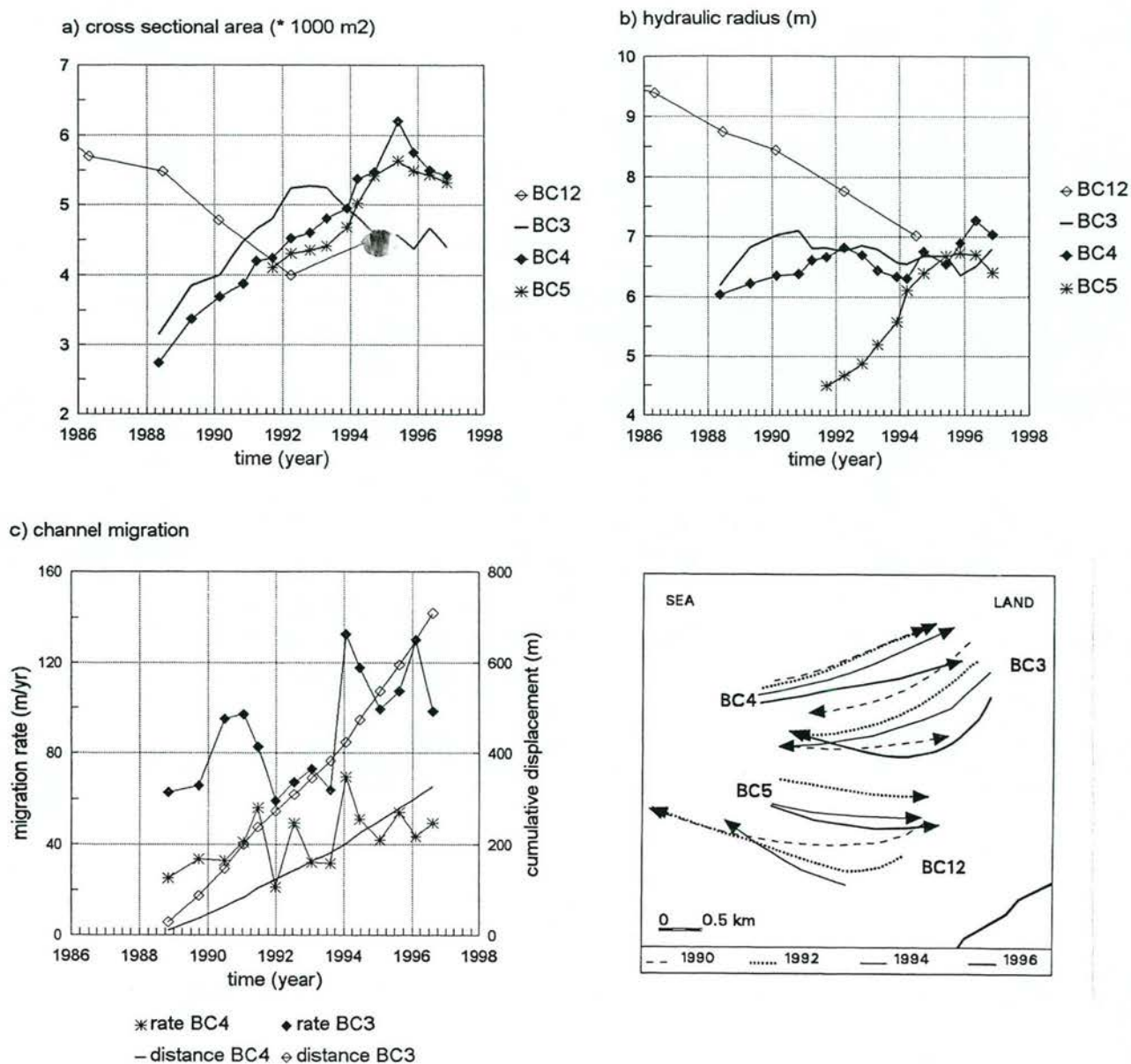
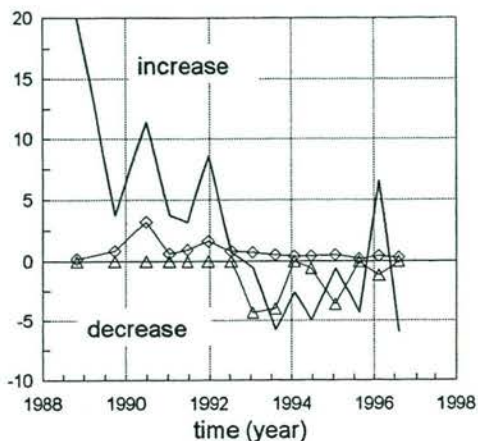


Fig. 3.18

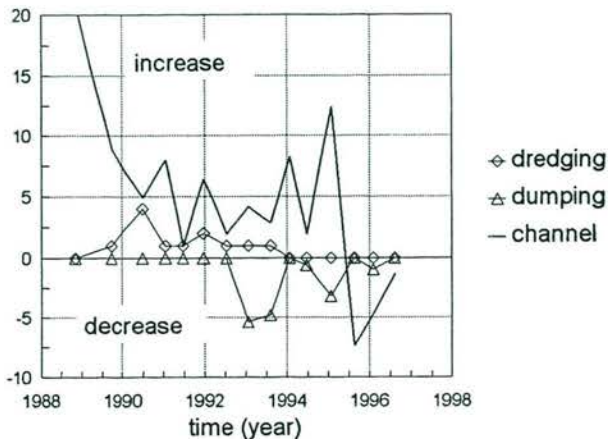
The morphological evolution of channel pattern 2 in the Terneuzen section.

- changes in the average cross-sectional area of the channels.
- changes in the average hydraulic radius of the channels.
- average migration rates and cumulative channel displacement
- changes in the location of the channel axis.

a) change in cross section, BC3 (%)



b) change in cross section, BC4 (%)



c) change in cross section BC5 (%)

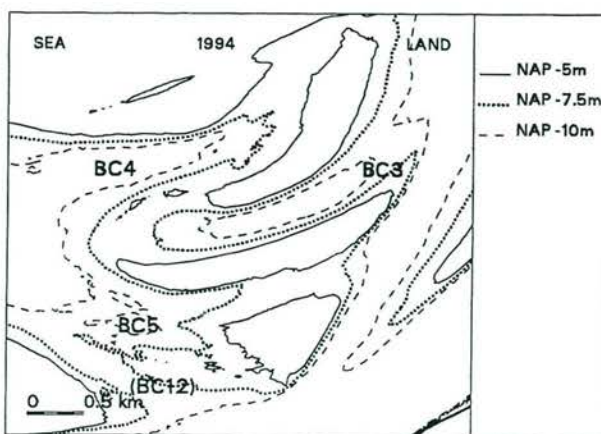
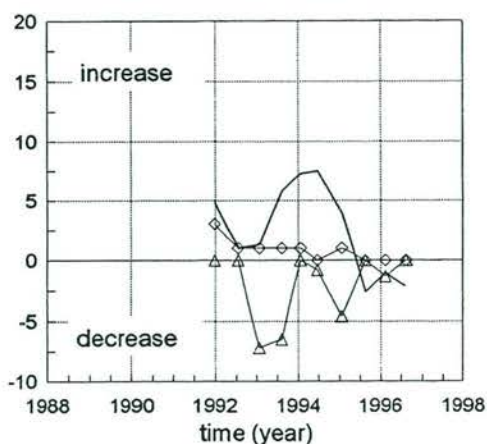
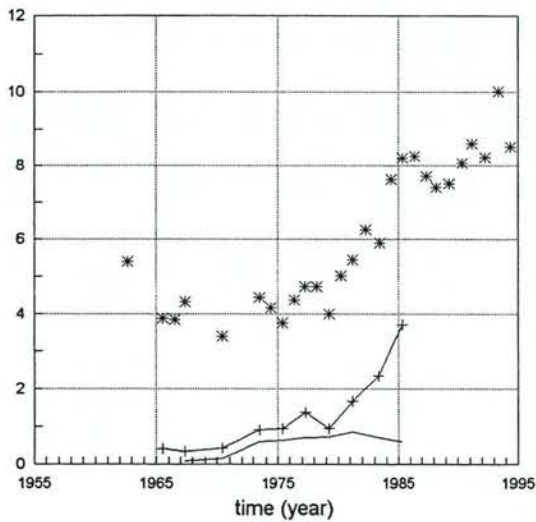


Fig. 3.19

The observed changes in the cross sectional area of the bar channels of pattern 1 (in %) and the potential changes in the channel cross section as result of dredging and dumping. Positive values indicate an increase of the channel cross section. Negative values indicate a decrease of the channel cross section.

- a) the ebb bar channel BC3
- b) the flood bar channel BC4
- c) the flood bar channel BC5

a) sediment reworking (Mm3/2yr), pattern 1



b) sediment reworking (Mm3/yr), pattern 2

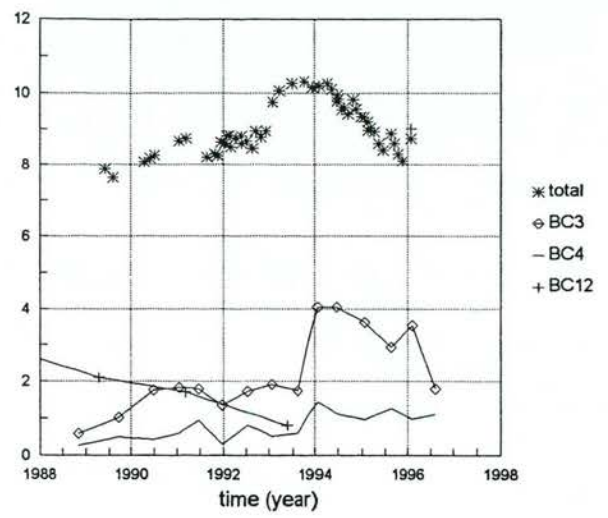


Fig. 3.20

The total sediment reworking at the bar B1 together with the reworking induced by the migration of the bar channels BC1, BC2, BC12, BC3, BC4.

- a) sediment reworking during pattern 1 (based on the 'standard echosoundings').
- b) sediment reworking during pattern 2 (based on the 'specific echosoundings').

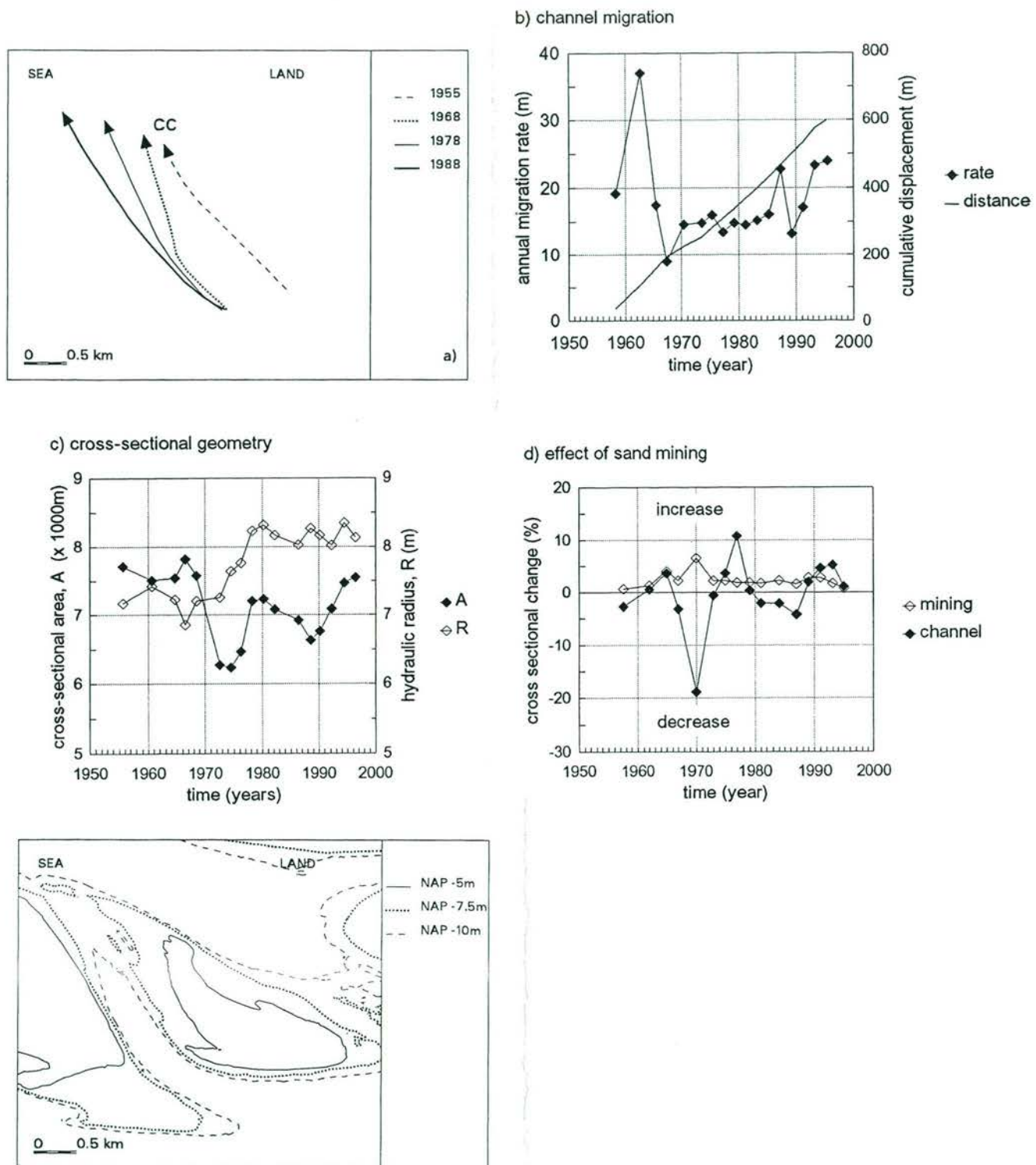


Fig. 3.21

The morphological evolution of the cross channel (cc in Fig. 3.1) in the Terneuzen section

- changes in the location of the channel axis.
- average migration rates and cumulative channel displacement
- changes in the average cross-sectional area and hydraulic radius of the channel.
- net changes in cross-sectional area and the potential changes of sand mining.

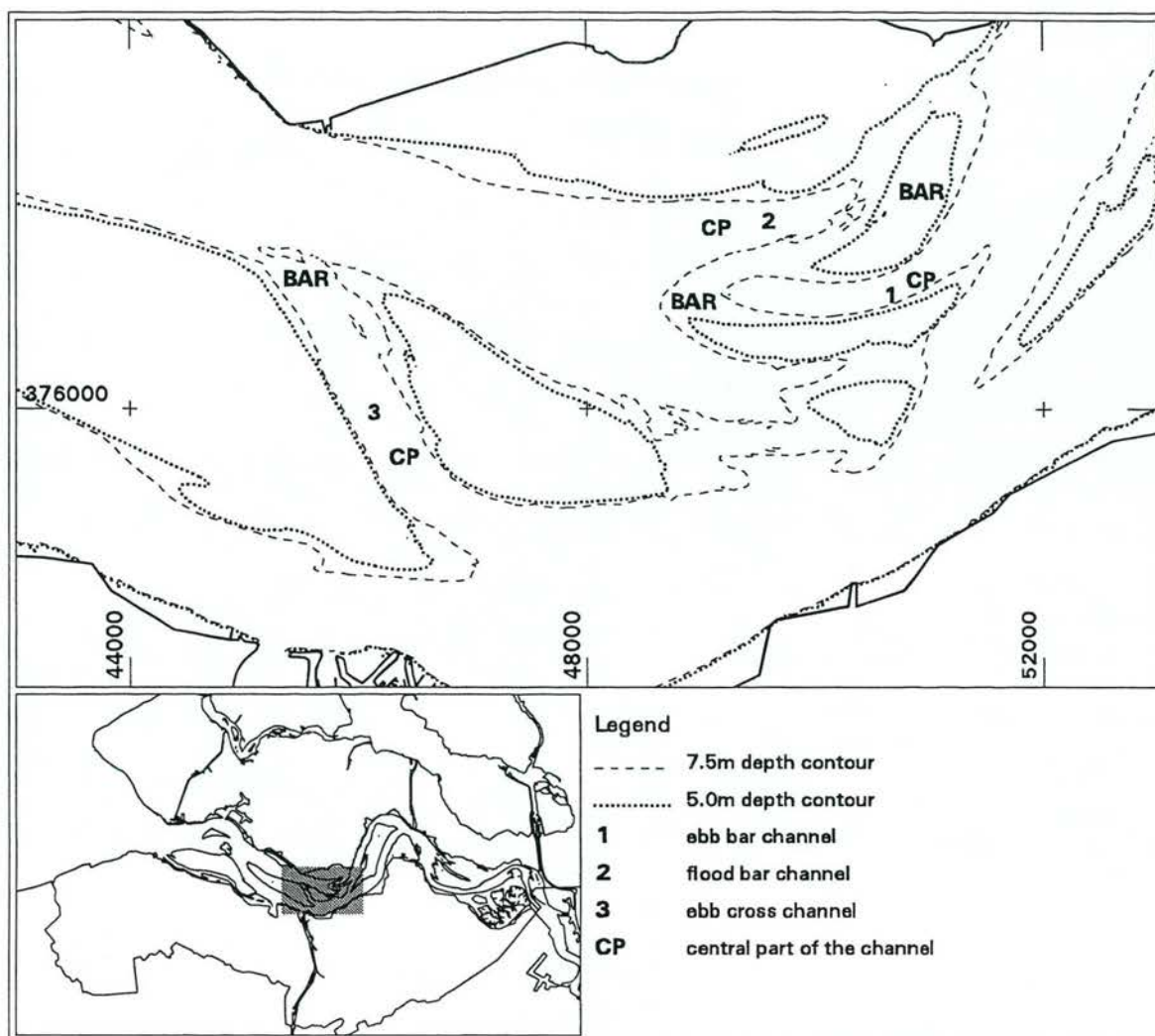


Fig. 4.1 The location and morphology of the three different types of connecting channels in 1994/1995

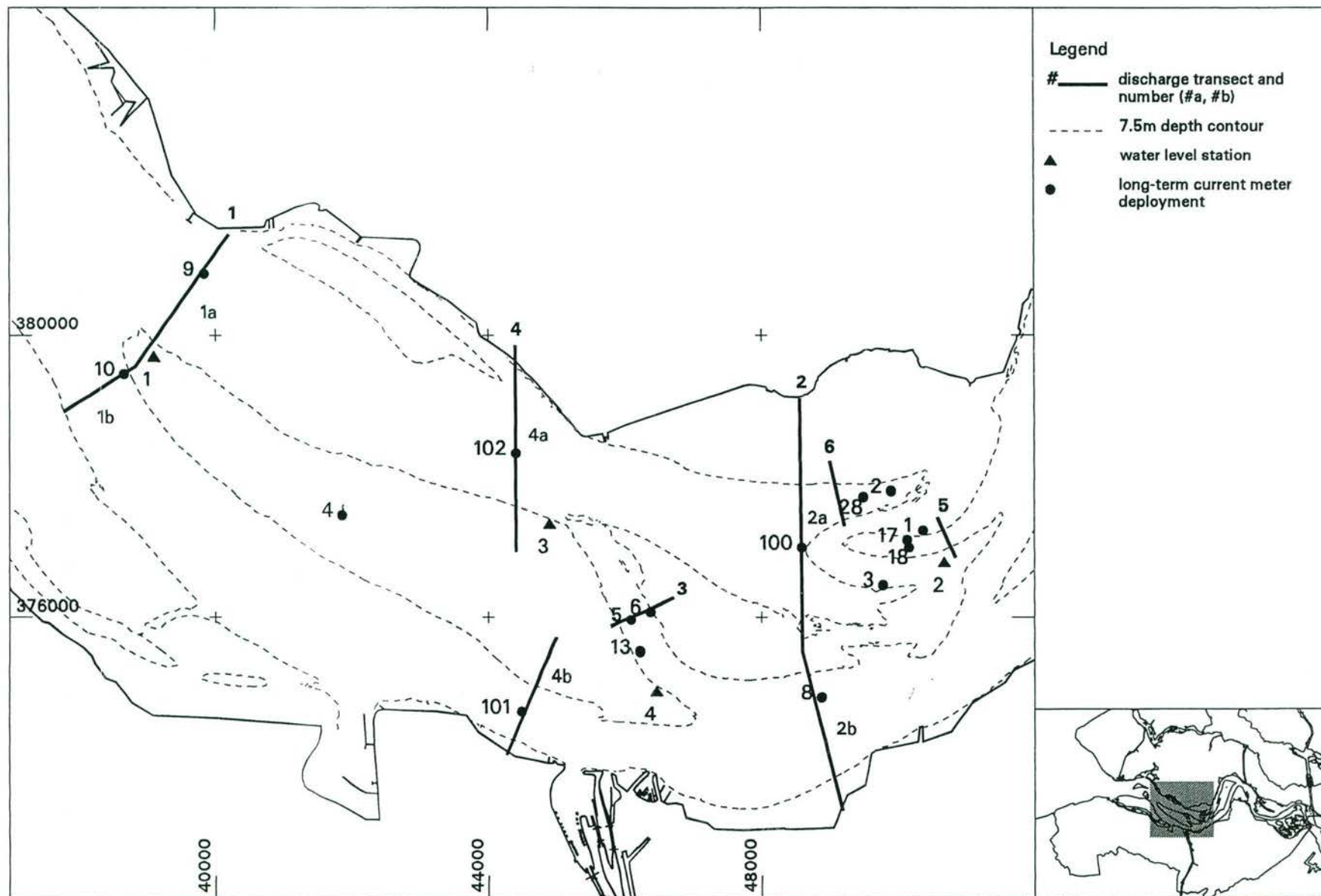


Fig. 4.2 The general hydrodynamics in the study area: overview of the measurements.

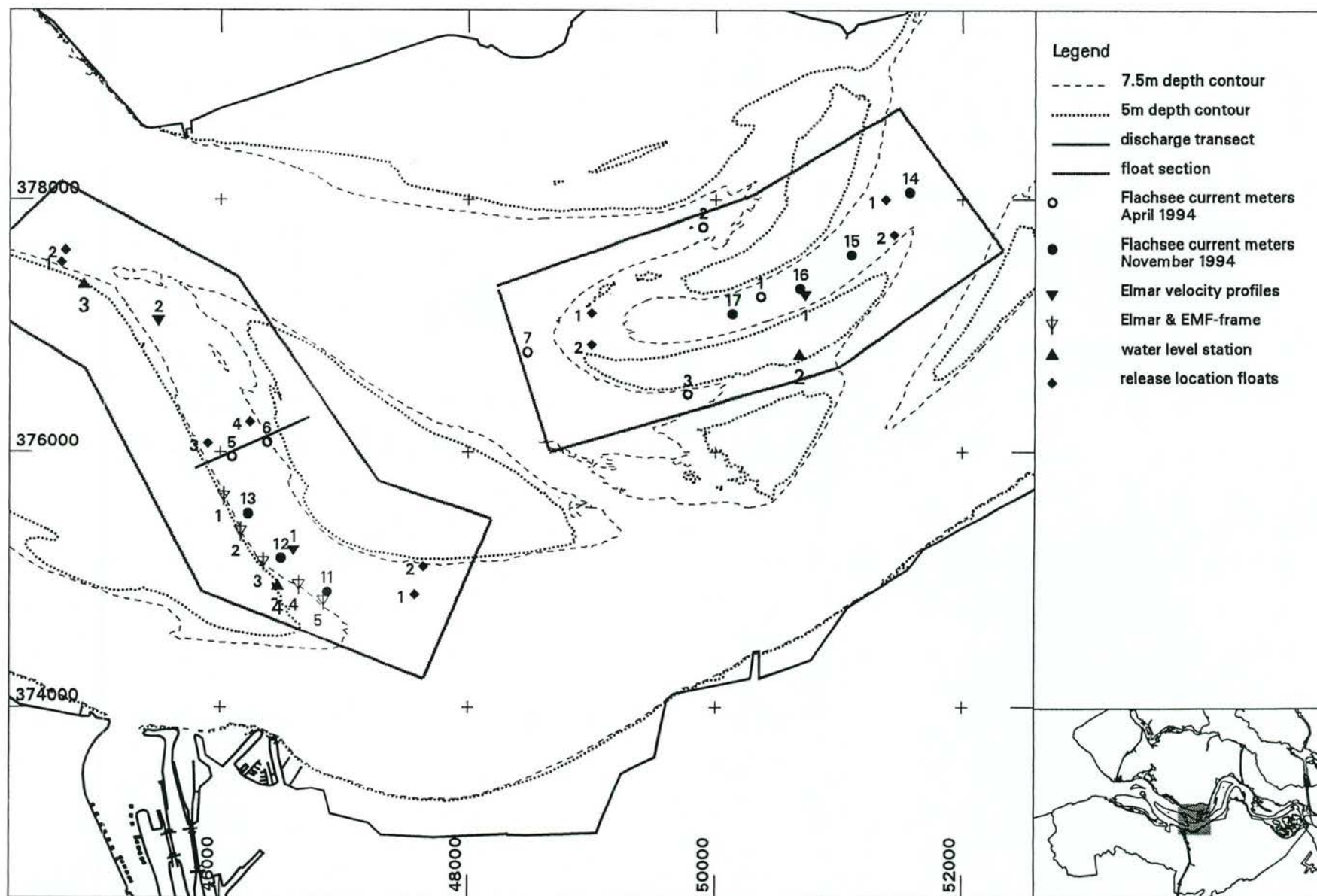


Fig. 4.3 Overview of the measurements in the connecting channels in 1994

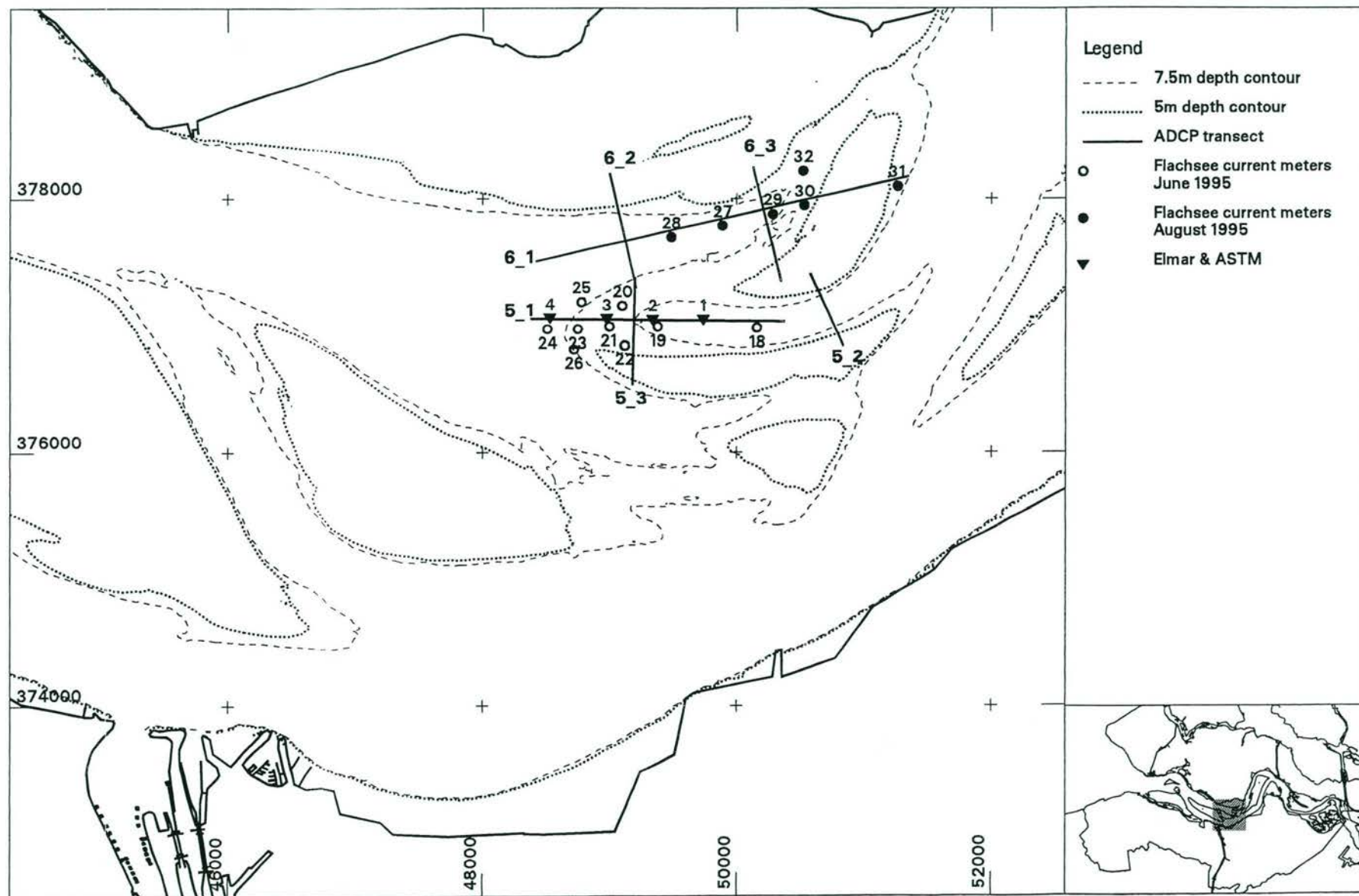


Fig. 4.4 Overview of the measurements in the connecting channels in 1995

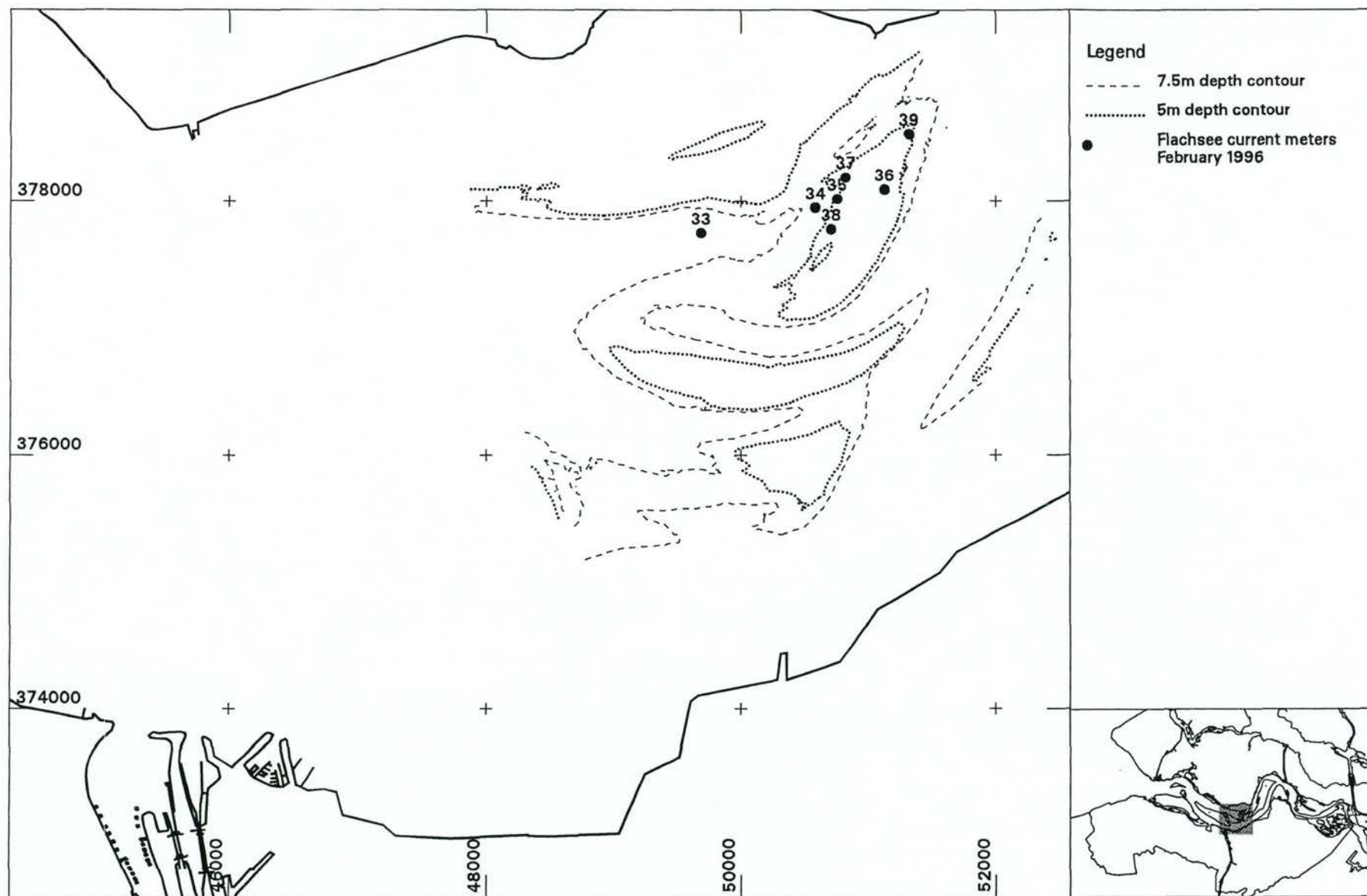
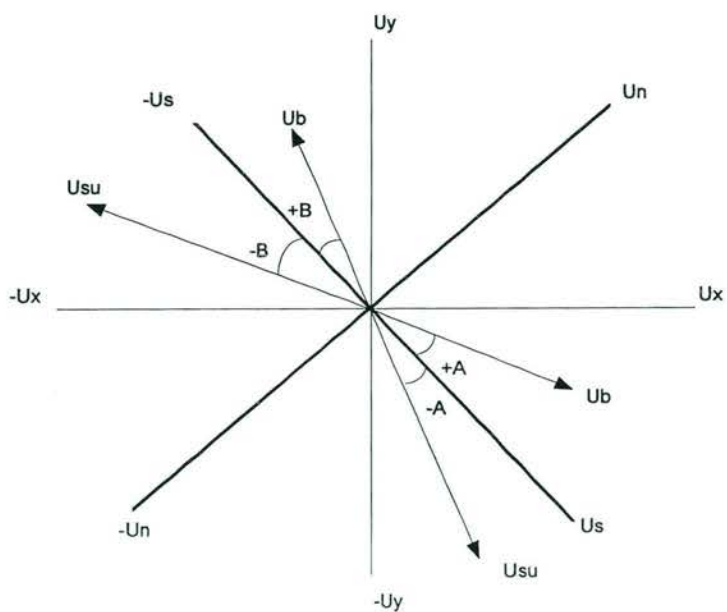
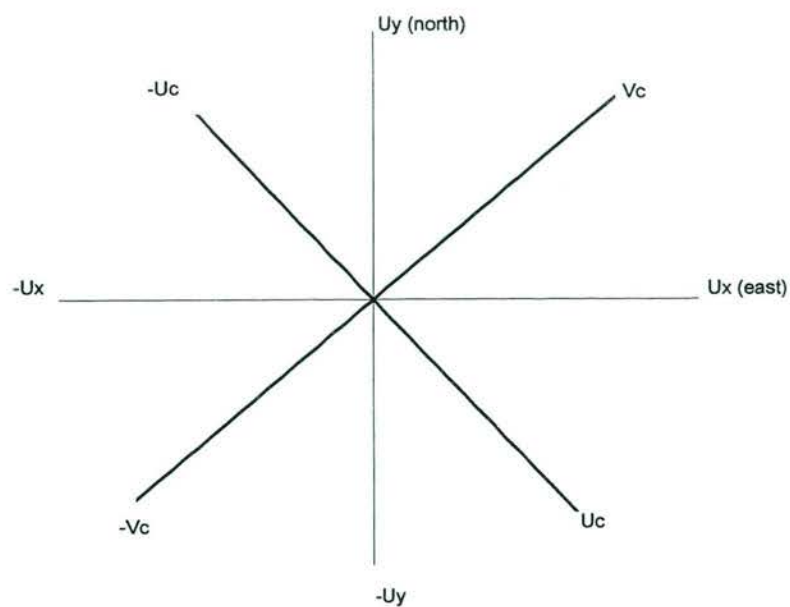


Fig. 4.5 Overview of the measurements in the connecting channels in 1996



Legend

U_x, U_y = north / south coordinate system

U_c, U_v = along-channel / cross-channel coordinate system

U_s, U_n = primary / secondary coordinate system

A, B = angle of current veering

U_{su} = near-surface current

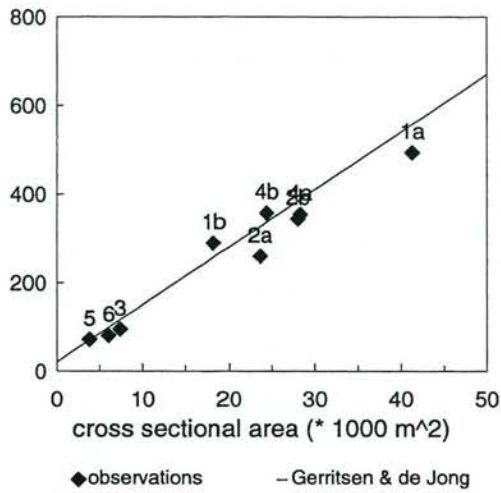
U_b = near-bed current

$-U_c, -U_s$ = ebb direction

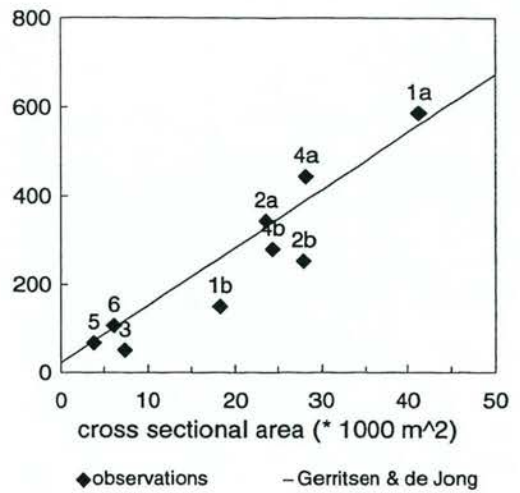
$+U_c, +U_s$ = flood direction

Fig. 4.6 Definition sketch of the coordinate systems used in the analysis of discharge measurements and ADCP observations

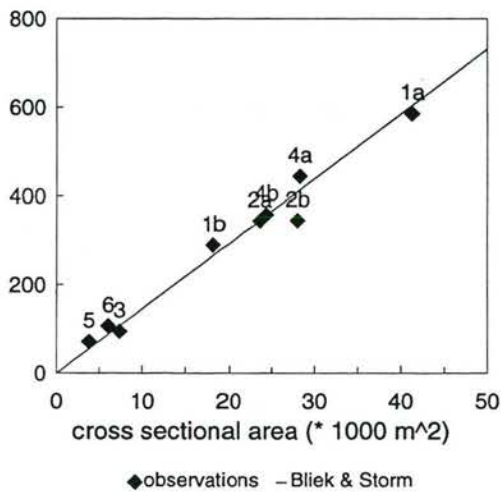
a) ebb volume (million m^3)



b) flood volume (million m^3)



c) dominant volume (million m^3)



d) dominant tidal volume (million m^3)

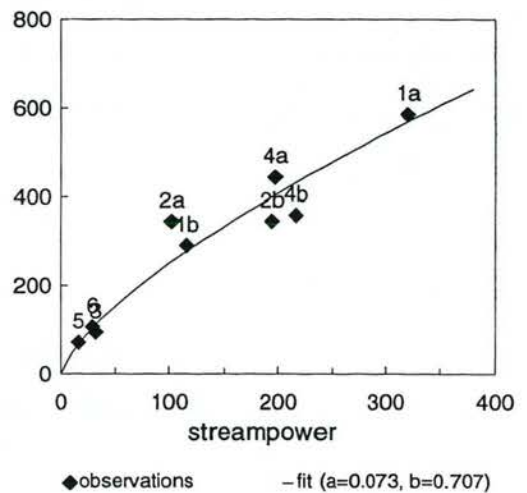


Fig. 4.7 Relationships between channel geometry and tidal flow parameters for the Westerschelde and measurement values obtained in the present study (for location of transects see Figure 4.2). a) ebb volume versus cross-sectional area, b) flood volume versus cross-sectional area, c) dominant volume versus cross-sectional area, d) dominant volume versus streampower.

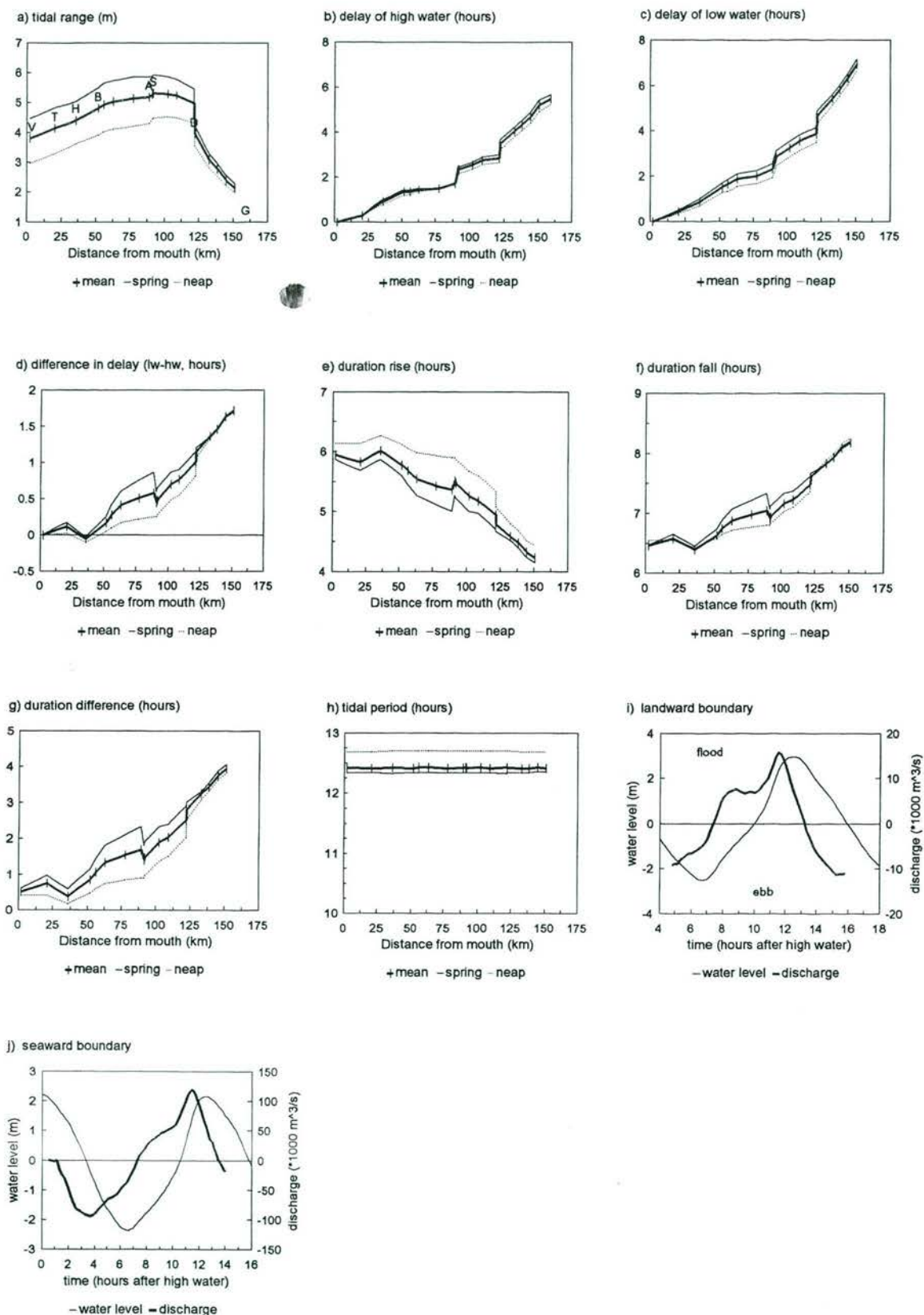
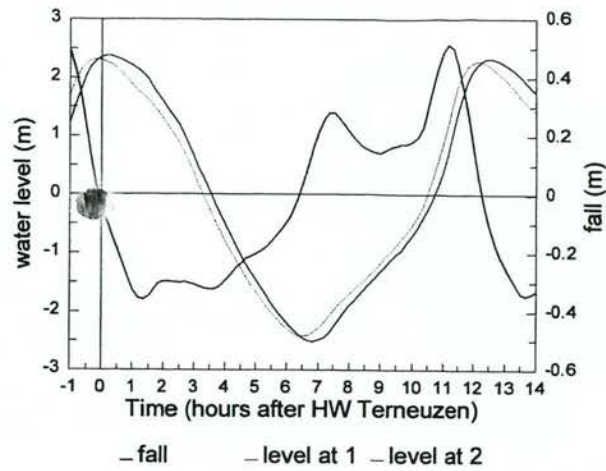
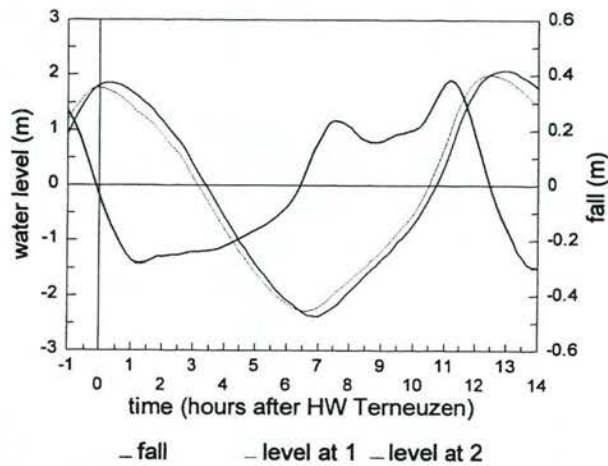


Fig. 4.8 Tidal wave propagation along the estuary during neap, mean and spring tide. a) tidal range, b) delay of high water with respect to Vlissingen (hours), c) delay of low water with respect to Vlissingen d) difference in delay between low water and high water (hours), e) duration of tidal rise, f) duration of tidal fall, g) duration difference between fall and rise, h) tidal period, i) discharge and water level at the landward boundary, j) discharge and water level at the seaward boundary.

a) water level & fall (m) at spring tide



b) water level & fall (m) at mean tide



c) water level & fall (m) at neap tide

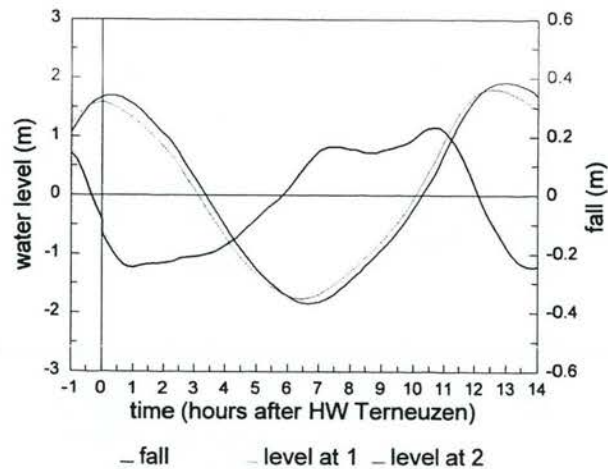


Fig. 4.9 Water levels at the seaward and landward boundary of the study area and the water level difference (water level station 1 and 2, for locations see Fig. 4.2). a) spring tide, b) mean tide, c) neap tide.

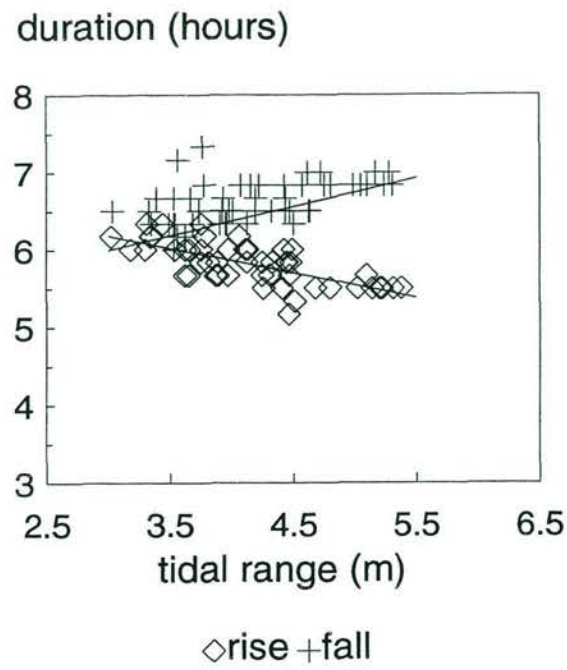


Fig. 4.10 Duration of tidal fall and tidal rise versus tidal range at Terneuzen, as occurred during the water level measurements.

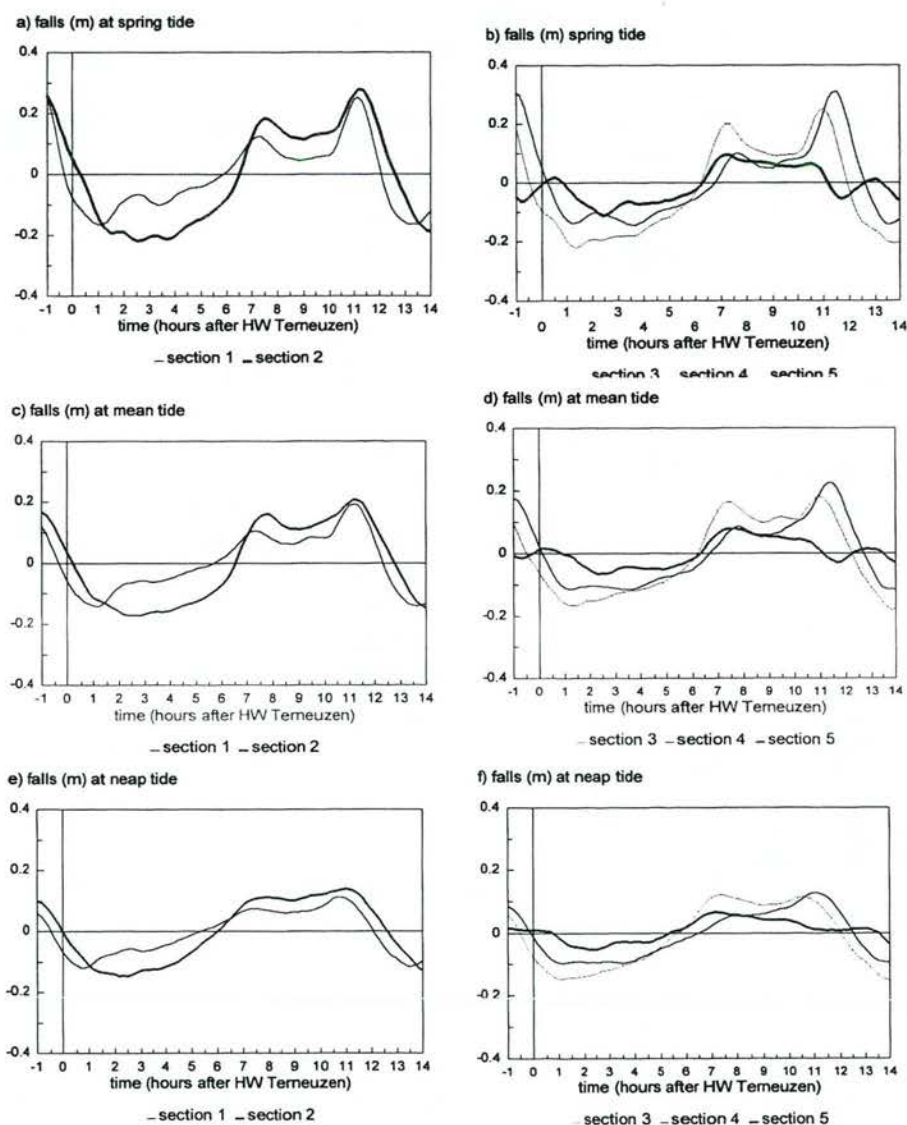
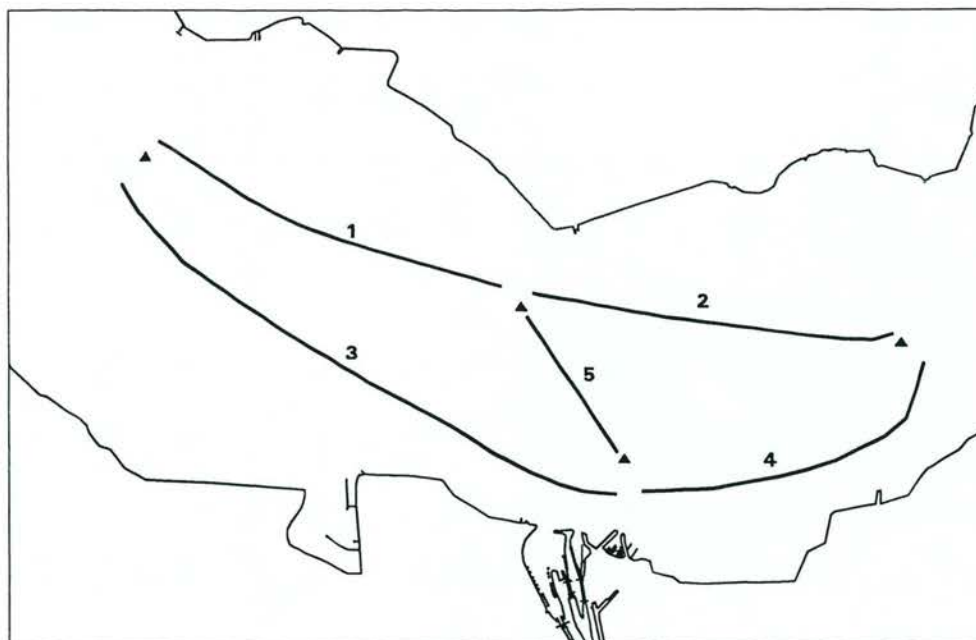


Fig. 4.11 Temporal variation in falls along the five channel sections in the study area. During spring tide (a & b), during mean tide (c & d) and during neap tide (e & f).

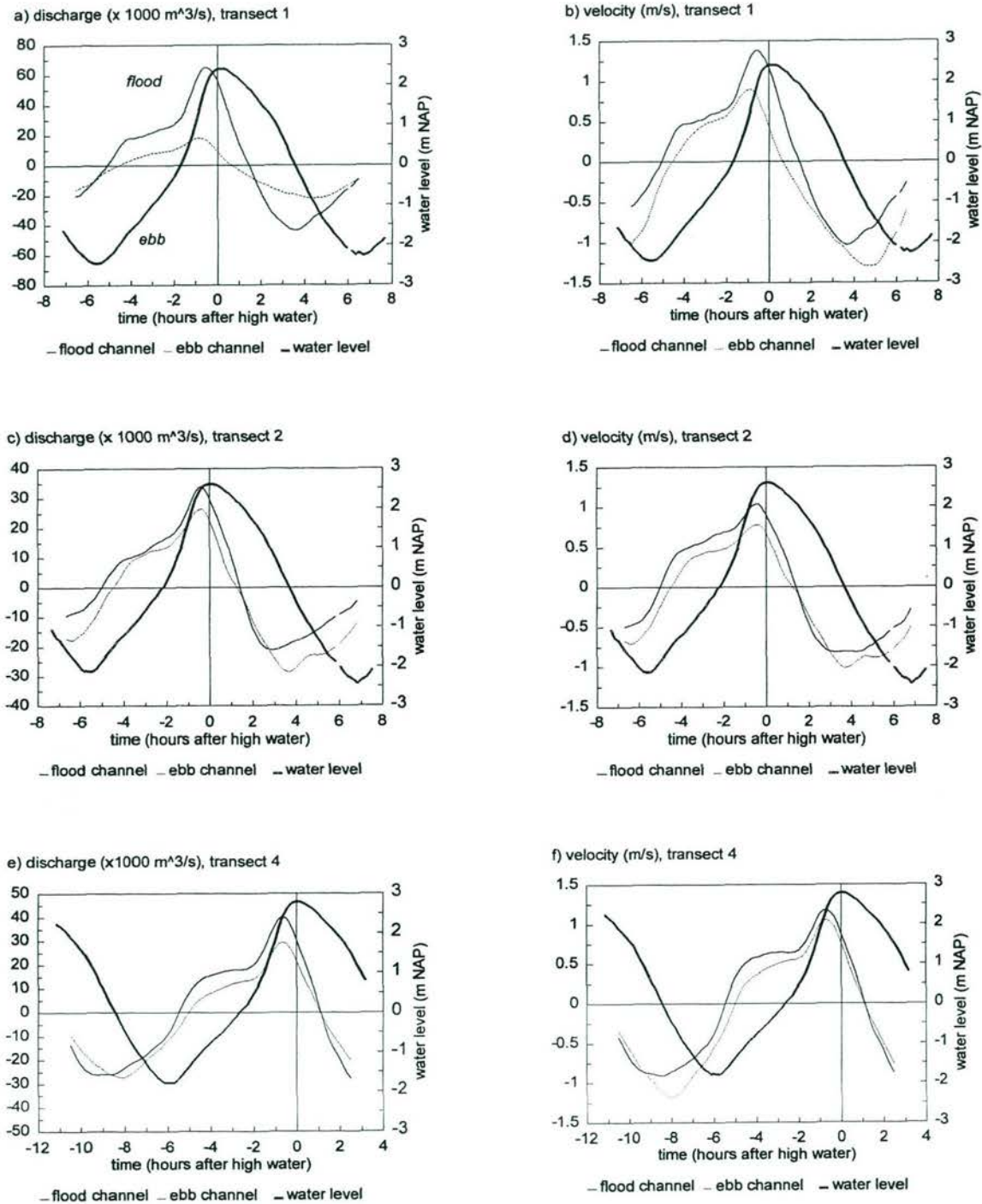
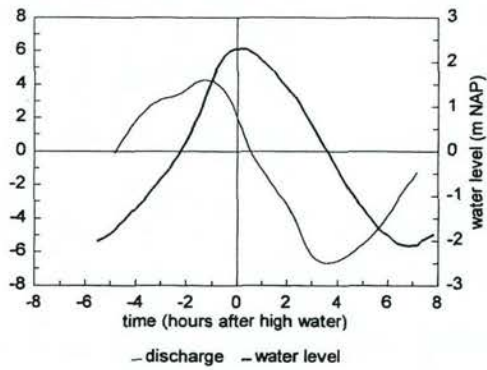


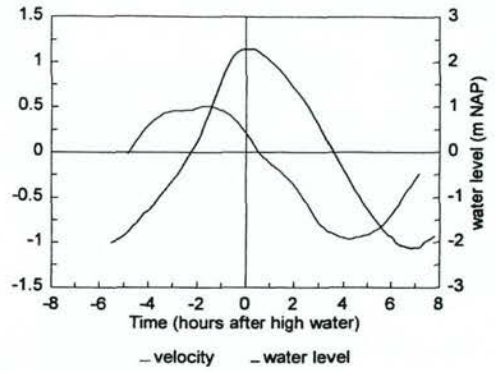
Fig. 4.12 Temporal variation in discharge and cross-sectional velocities as occurred during the measurements (for locations see Fig. 4.2).

- a) discharges in transect 1, b) velocities in transect 1
- c) discharges in transect 2, d) velocities in transect 2
- e) discharges in transect 4, f) velocities in transect 4
- g) discharges in transect 3, h) velocities in transect 3
- i) discharges in transect 5, j) velocities in transect 5
- k) discharges in transect 6, l) velocities in transect 6

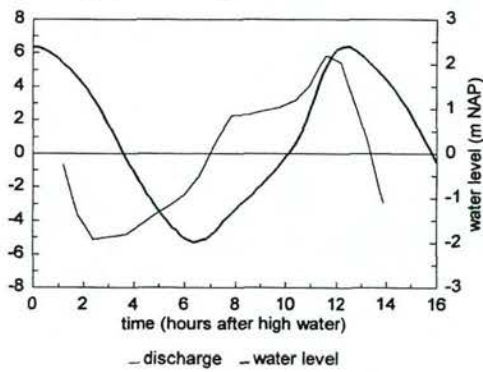
g) discharge ($\times 1000\text{m}^3/\text{s}$), transect 3



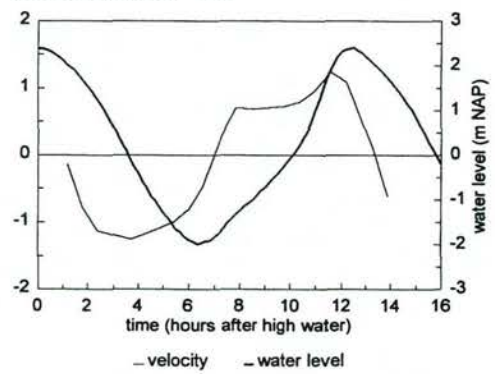
h) velocity (m/s), transect 3



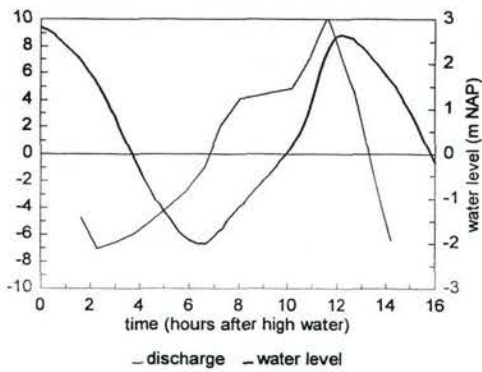
i) discharge ($\times 1000\text{m}^3/\text{s}$), transect 5



j) velocity (m/s), transect 5



k) discharge ($\times 1000\text{m}^3/\text{s}$), transect 6



l) velocity (m/s), transect 6

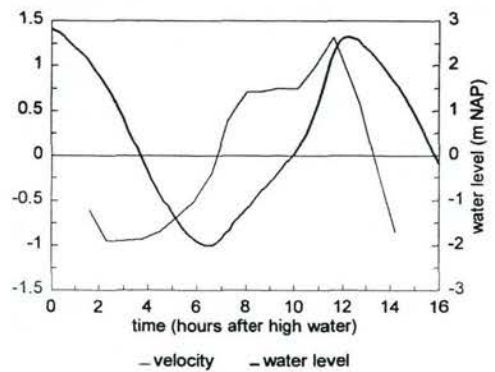


Fig. 4.12 Temporal variation in discharge and cross-sectional velocities as occurred during the measurements (for locations see Fig. 4.2).

- a) discharges in transect 1, b) velocities in transect 1
- b) discharges in transect 2, c) velocities in transect 2
- d) discharges in transect 4, e) velocities in transect 4
- f) discharges in transect 3, g) velocities in transect 3
- h) discharges in transect 5, i) velocities in transect 5
- j) discharges in transect 6, k) velocities in transect 6

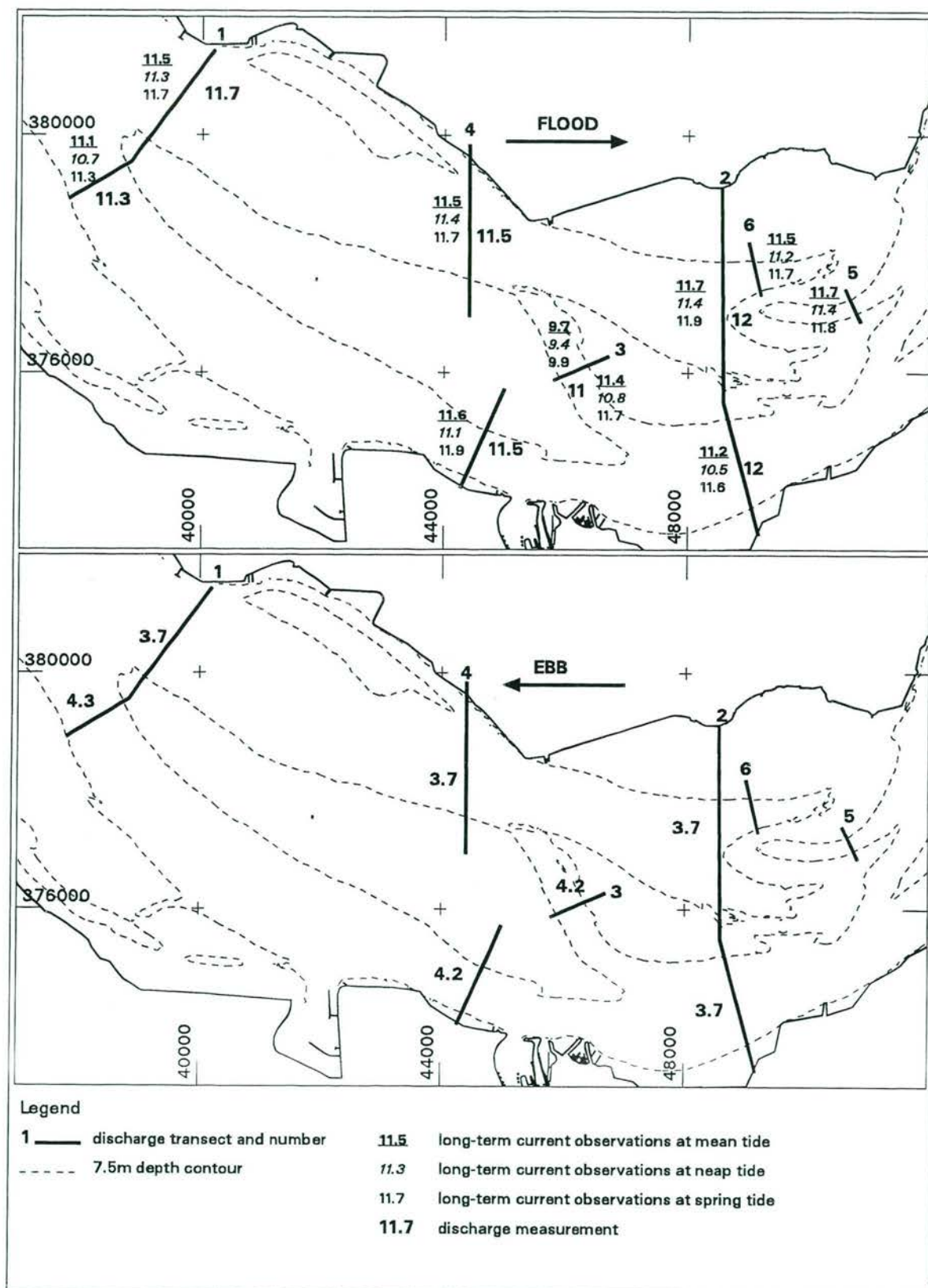
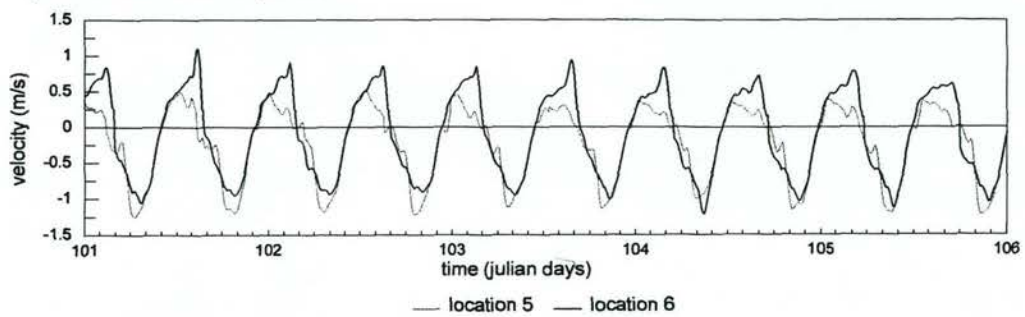


Fig. 4.13 Overview of the time of maximum flood and maximum ebb flow in the study area.

a) current observations in April 1994



b) current & fall observations in November 1994

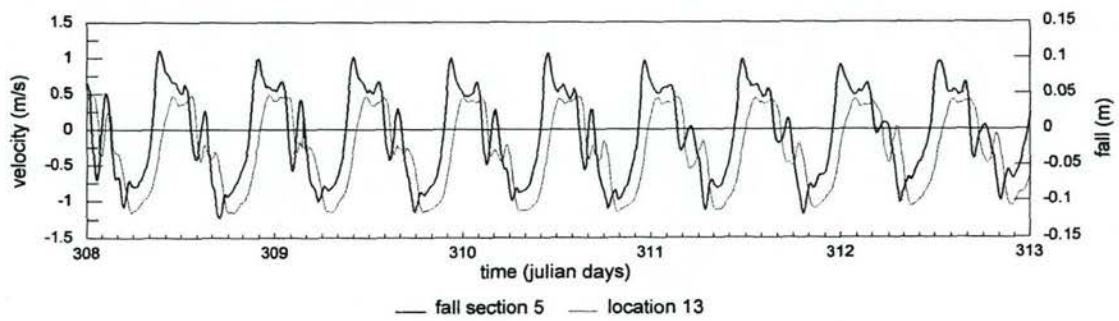


Fig. 4.14 Temporal variation in depth-averaged current velocities and falls in the cross channel (for locations see Fig. 4.3 and 4.4). a) current velocities at location 5 and 6, b) current velocities at location 13 and falls along the channel.

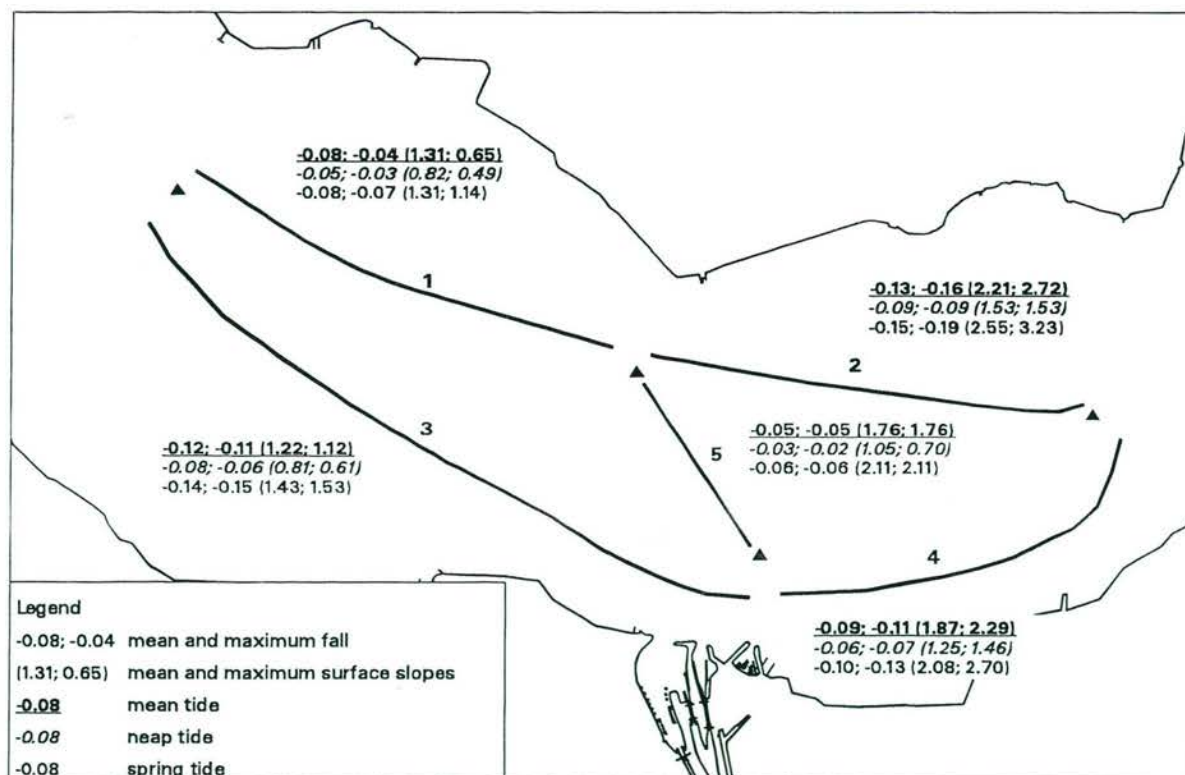
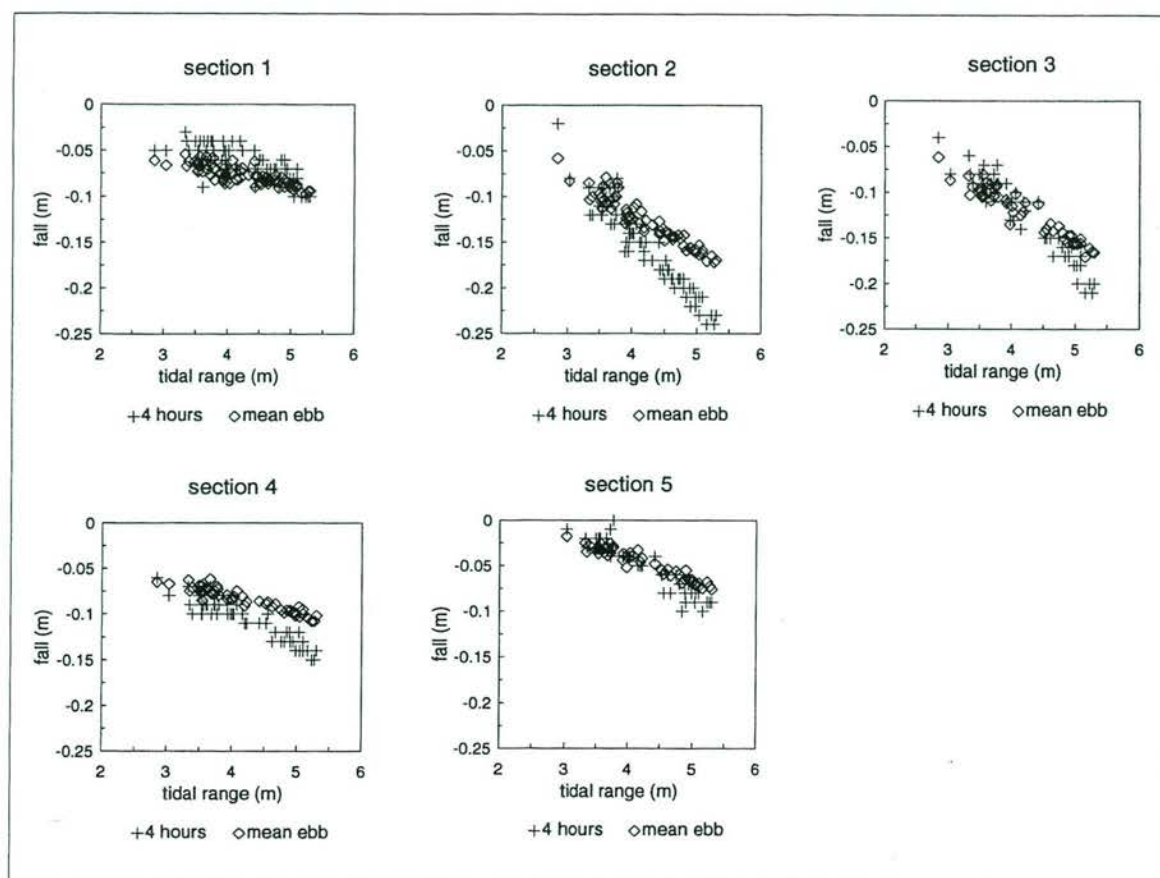


Fig. 4.15 Spatial and temporal variation in mean and maximum falls and surface slopes along the five channel sections during ebb. Maximum refers to the condition of maximum currents (= 4 hours after high water). Mean refers to the average values over the ebb period.

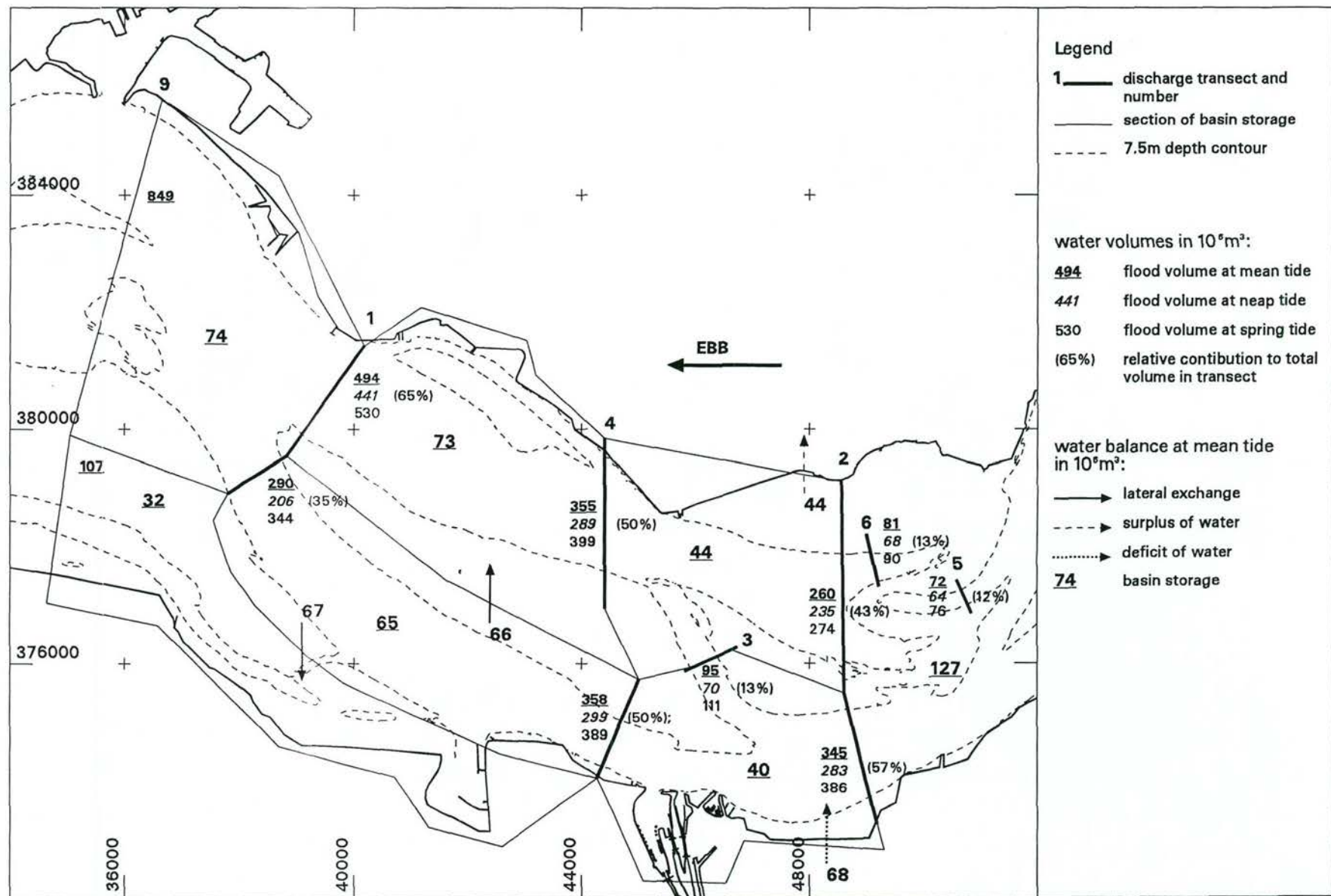


Fig. 4.16 Spatial patterns of ebb volumes for neap, mean and spring tide together with the water budgets for mean tide.

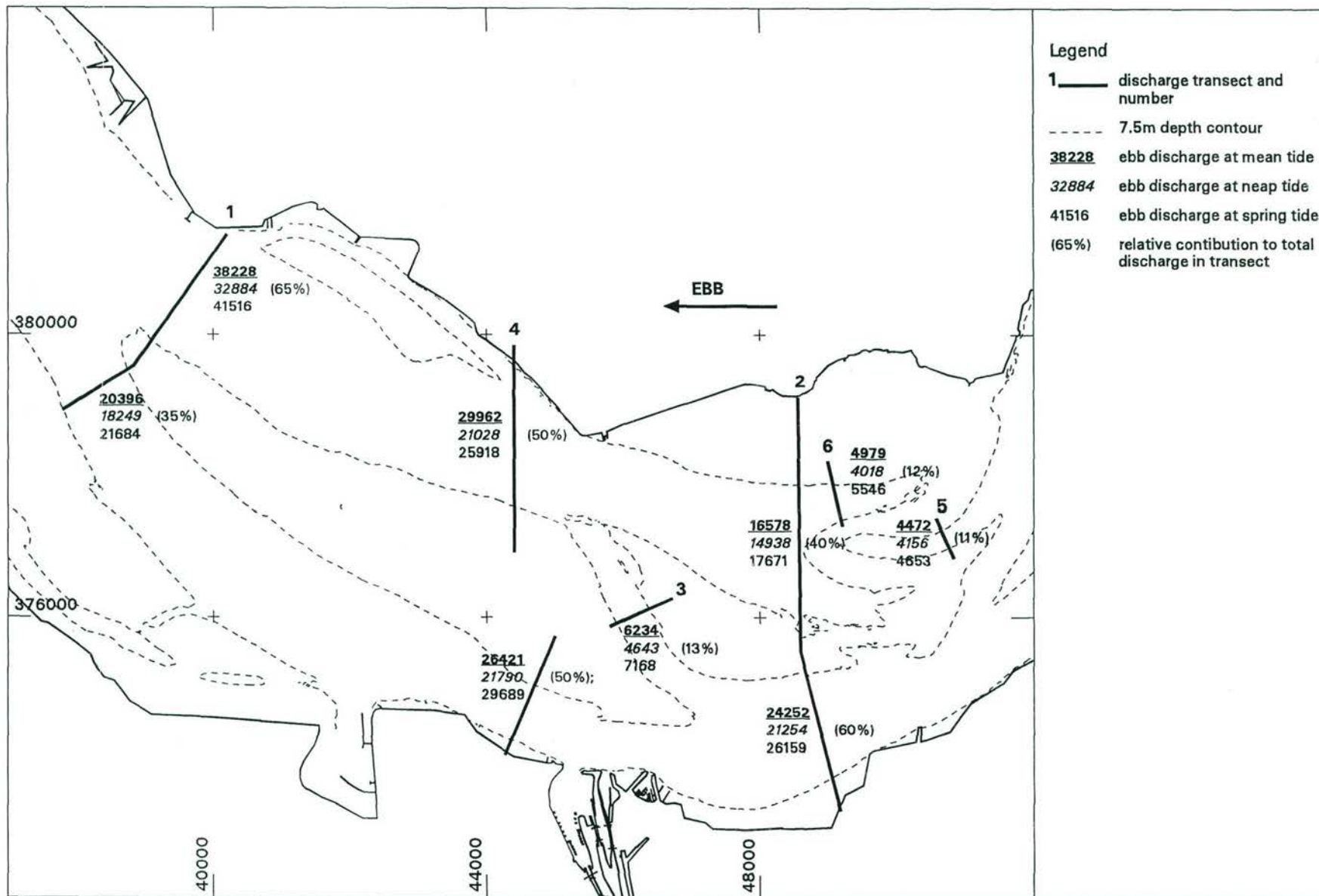


Fig. 4.17 Spatial patterns of maximum ebb discharges during mean, neap and spring tide.

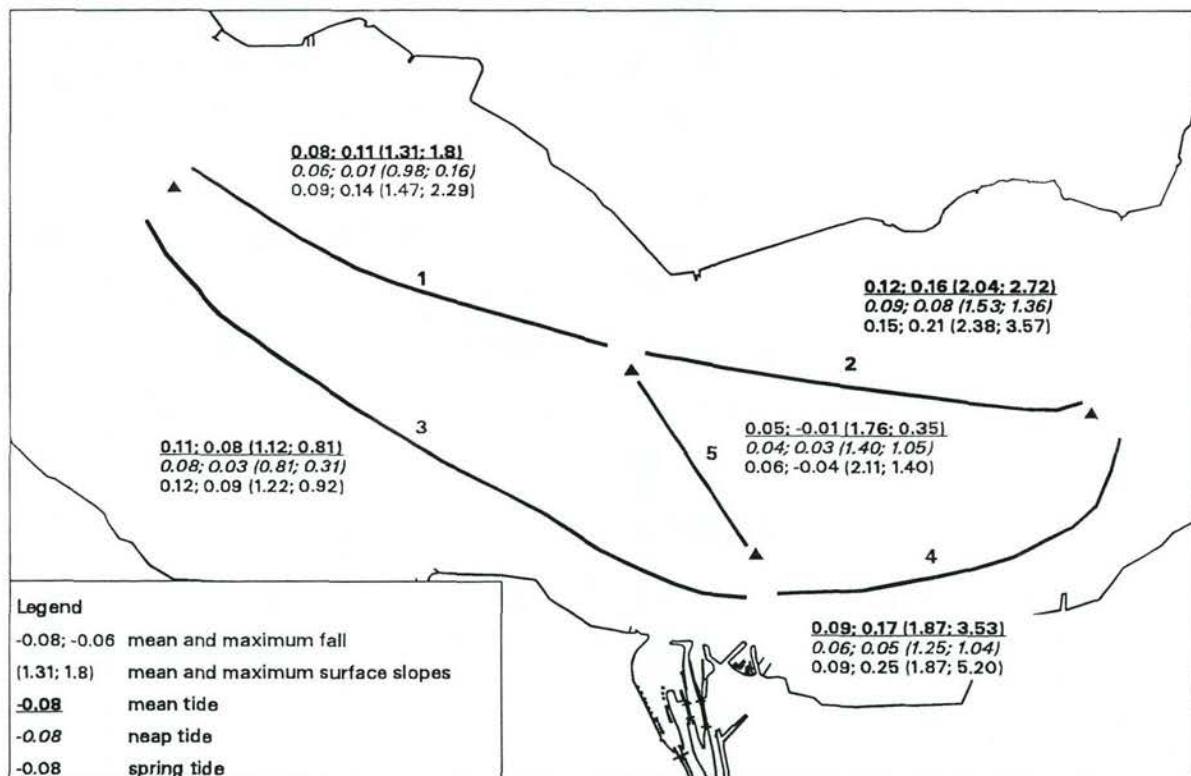
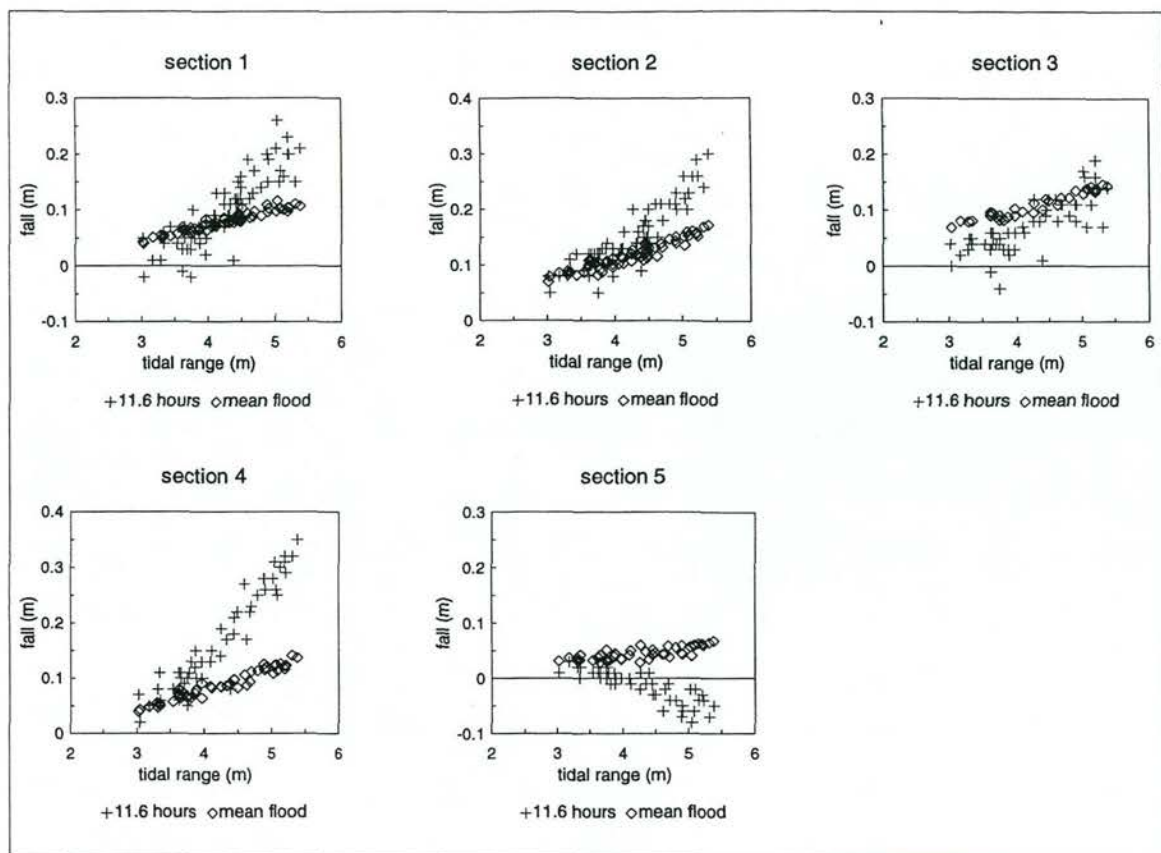


Fig. 4.18 Spatial and temporal variation in mean and maximum falls and surface slopes along the five channel sections during flood. Maximum refers to the condition of maximum flood currents (= 11.6 hours after high water). Mean refers to the average values over the ebb period.

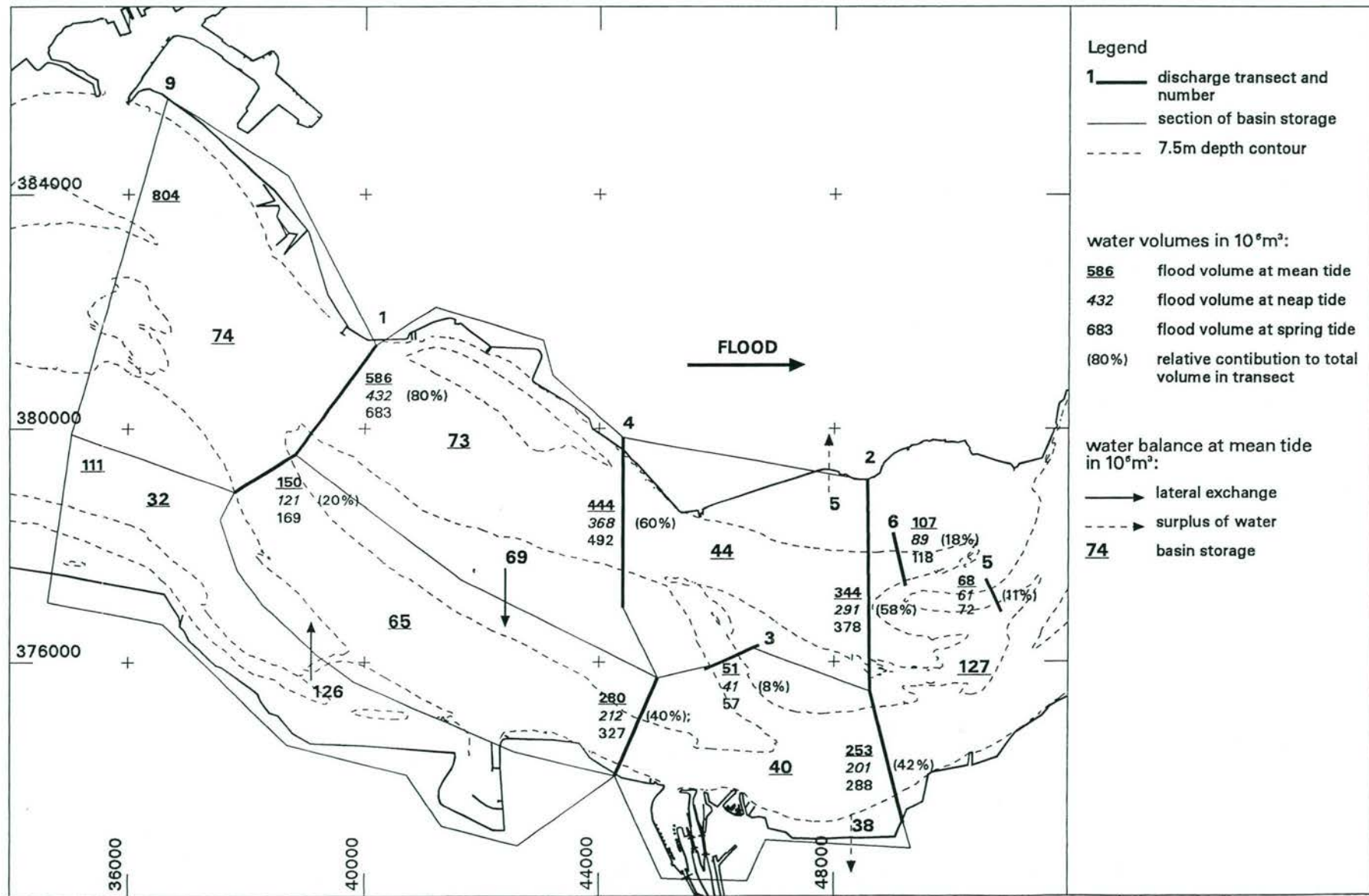


Fig. 4.19 Spatial patterns of flood volumes for neap, mean and spring tide together with the water budgets for mean tide.

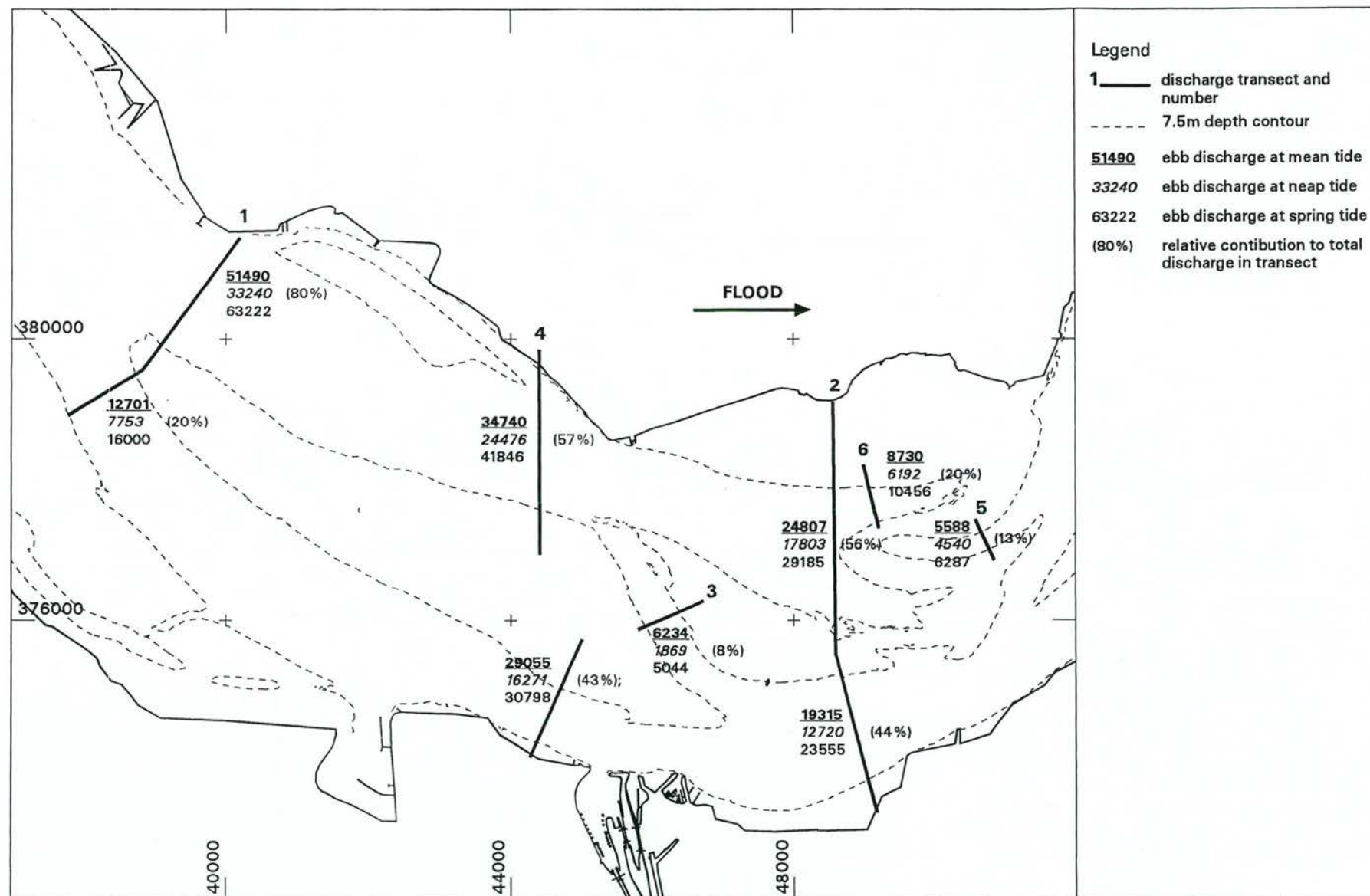
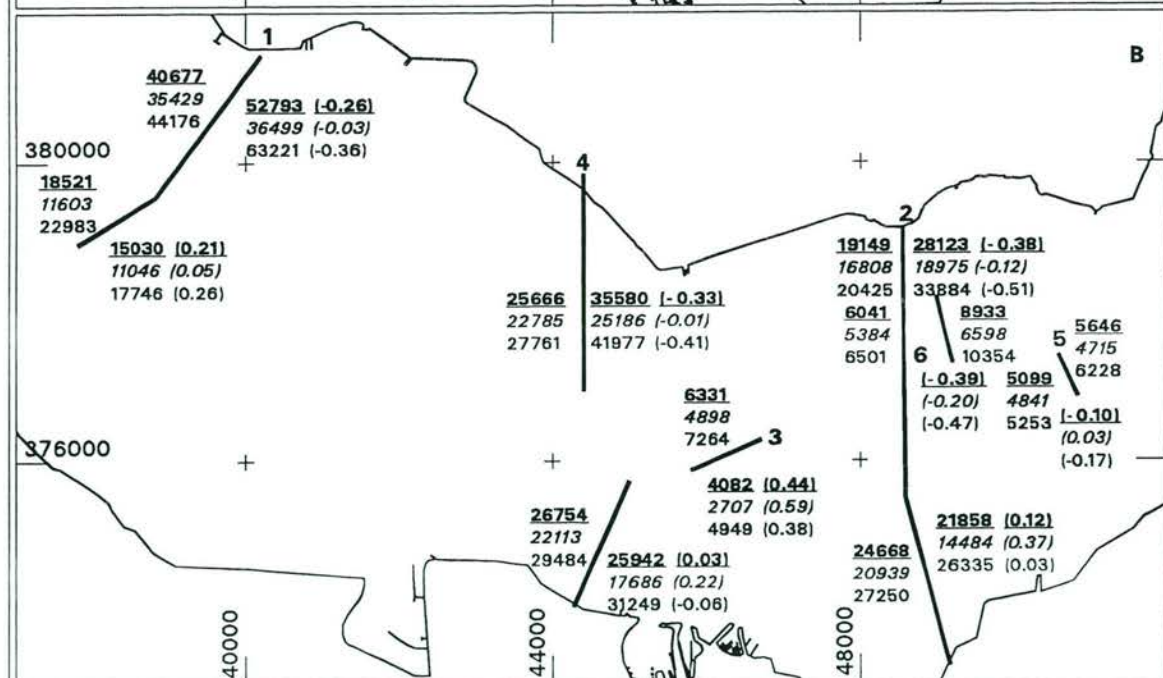
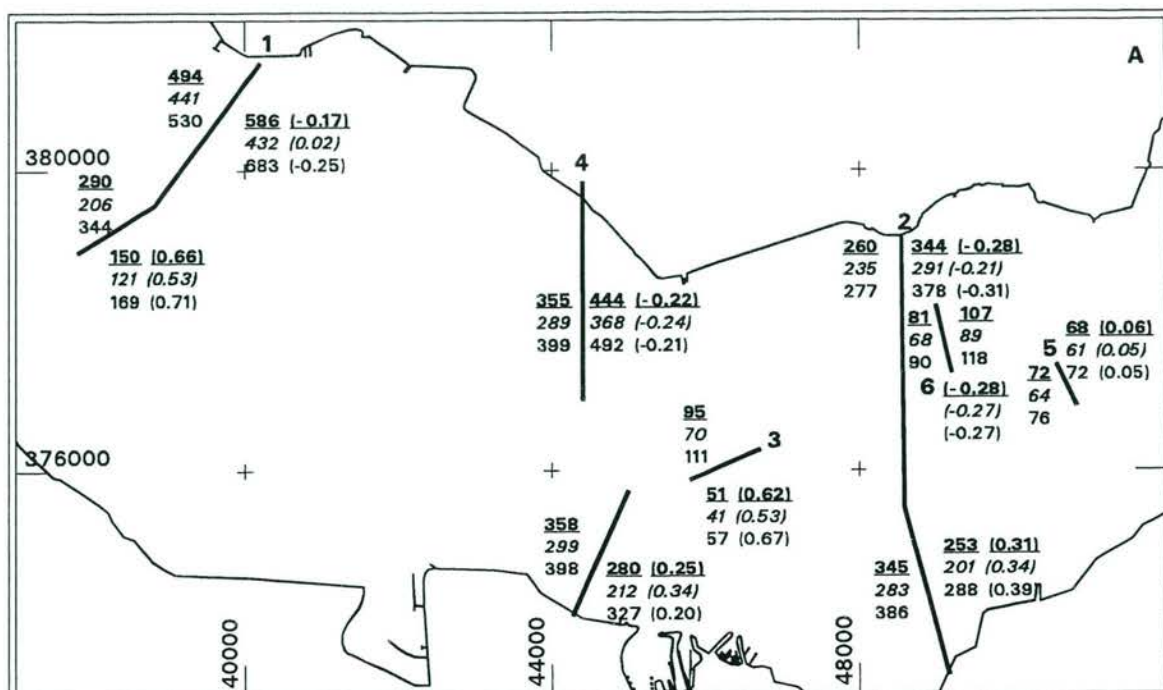


Fig. 4.20 Spatial patterns of maximum flood discharges during mean, neap and pring tide.



Legend

1 — discharge transect and number

Ebb	Flood	Asymmetry
494	586	(-0.17) mean tide
441	432	(0.02) neap tide
530	683	(-0.25) spring tide

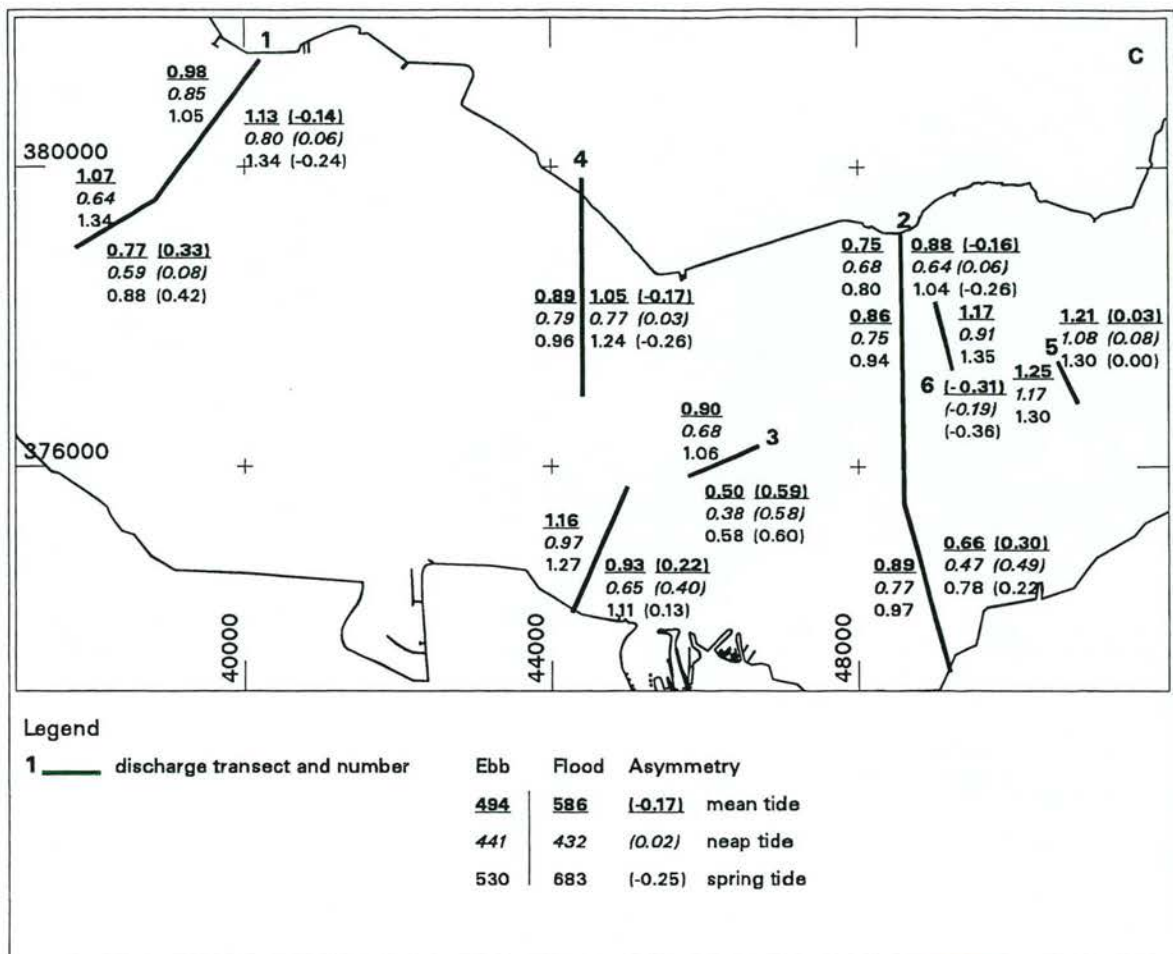


Fig. 4.21 Spatial patterns of current asymmetry and the maximum values of tidal flow during ebb and flood for mean, neap and spring tide. a) tidal volumes, b) maximum discharges, c) cross-sectional velocities.

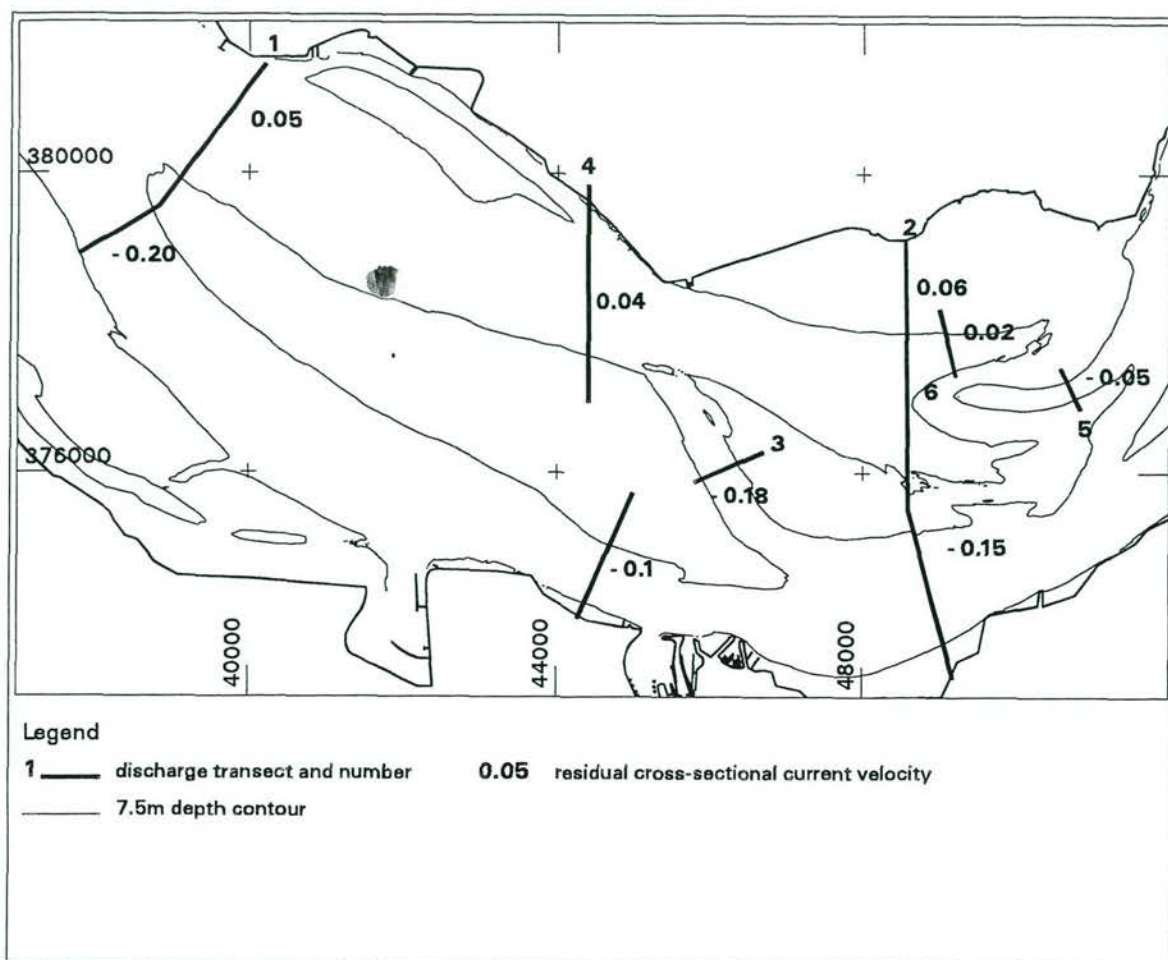


Fig. 4.22 Residual cross-sectional velocities as occurred during the measurements.

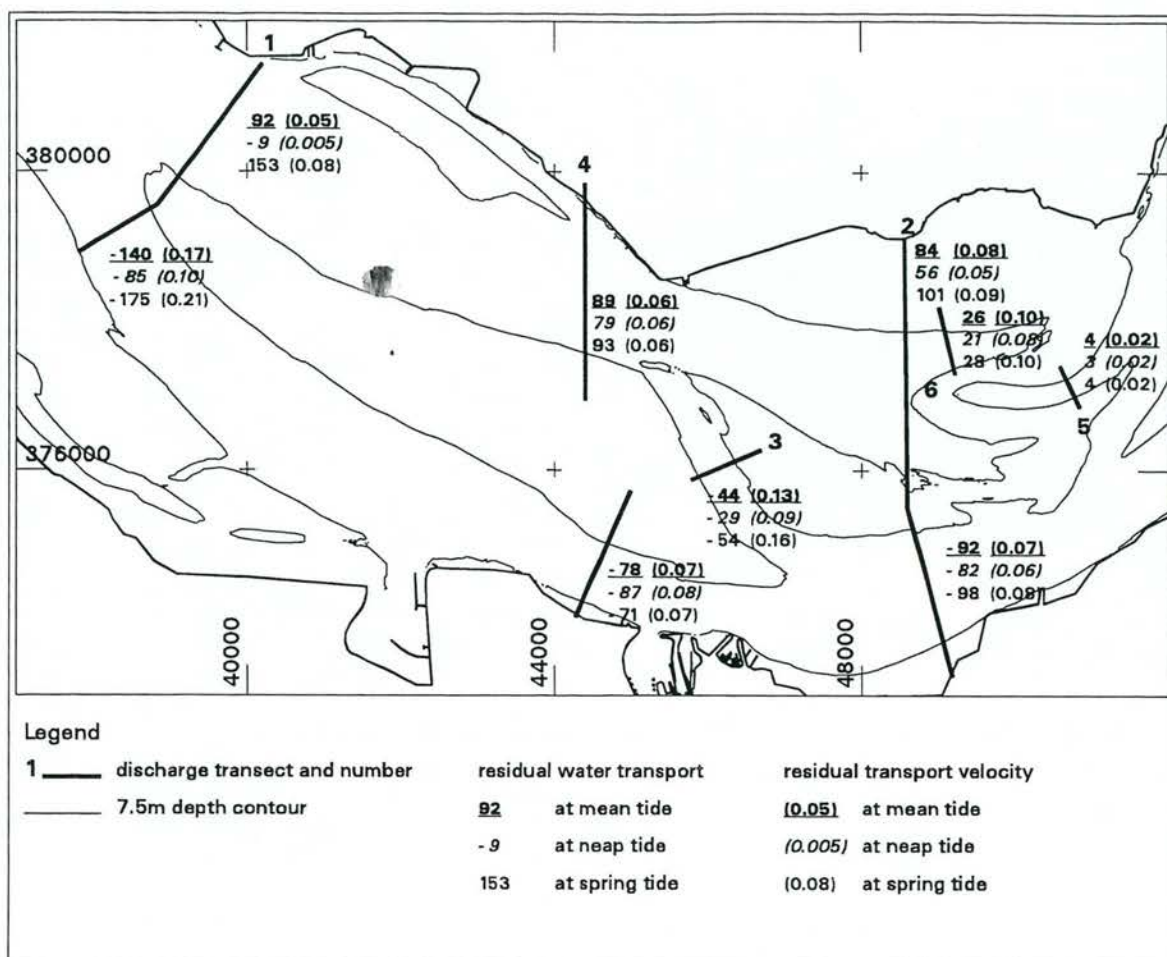


Fig. 4.23 Spatial pattern of residual water transports and transport velocities for mean, neap and spring tide.

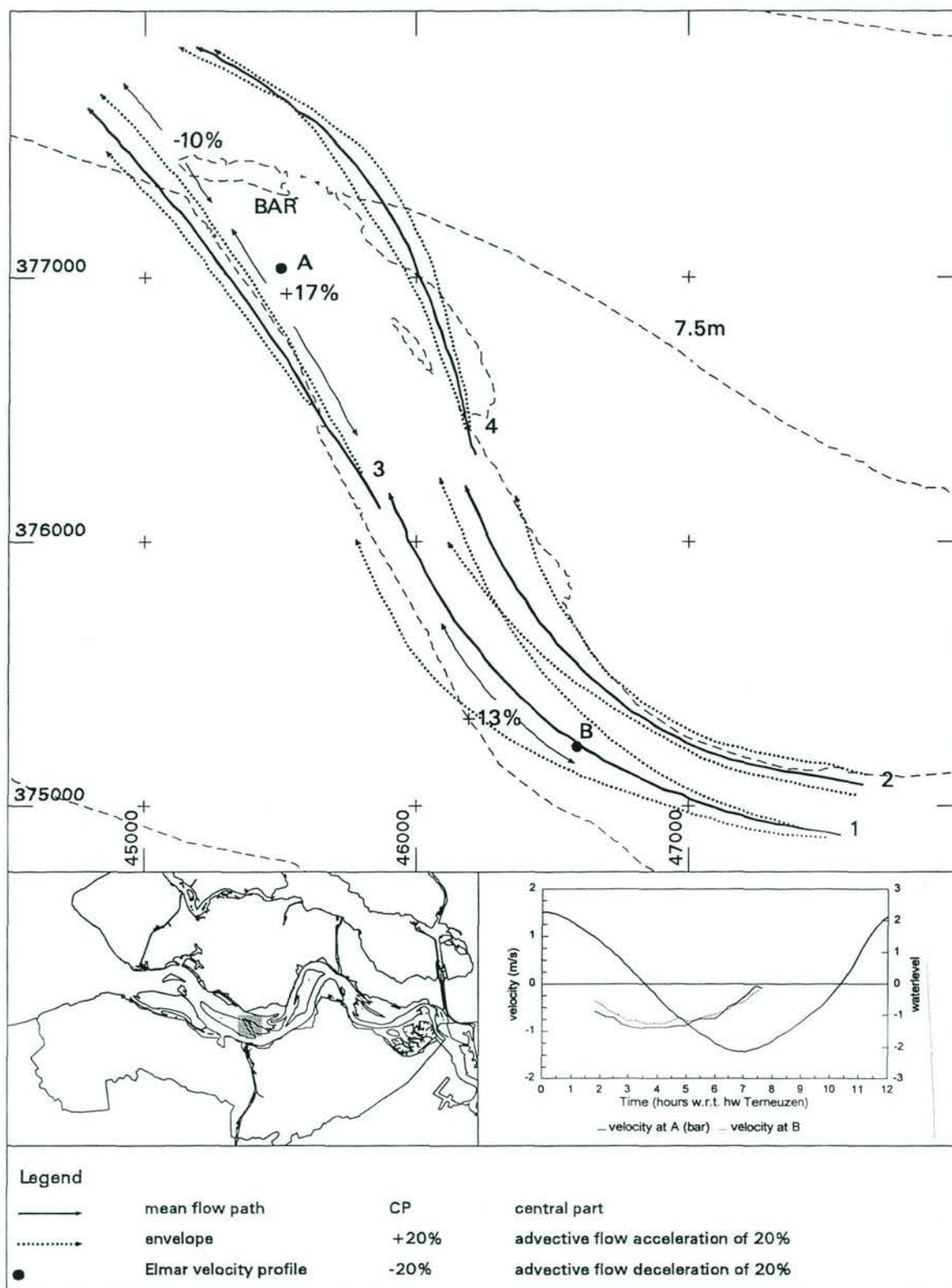
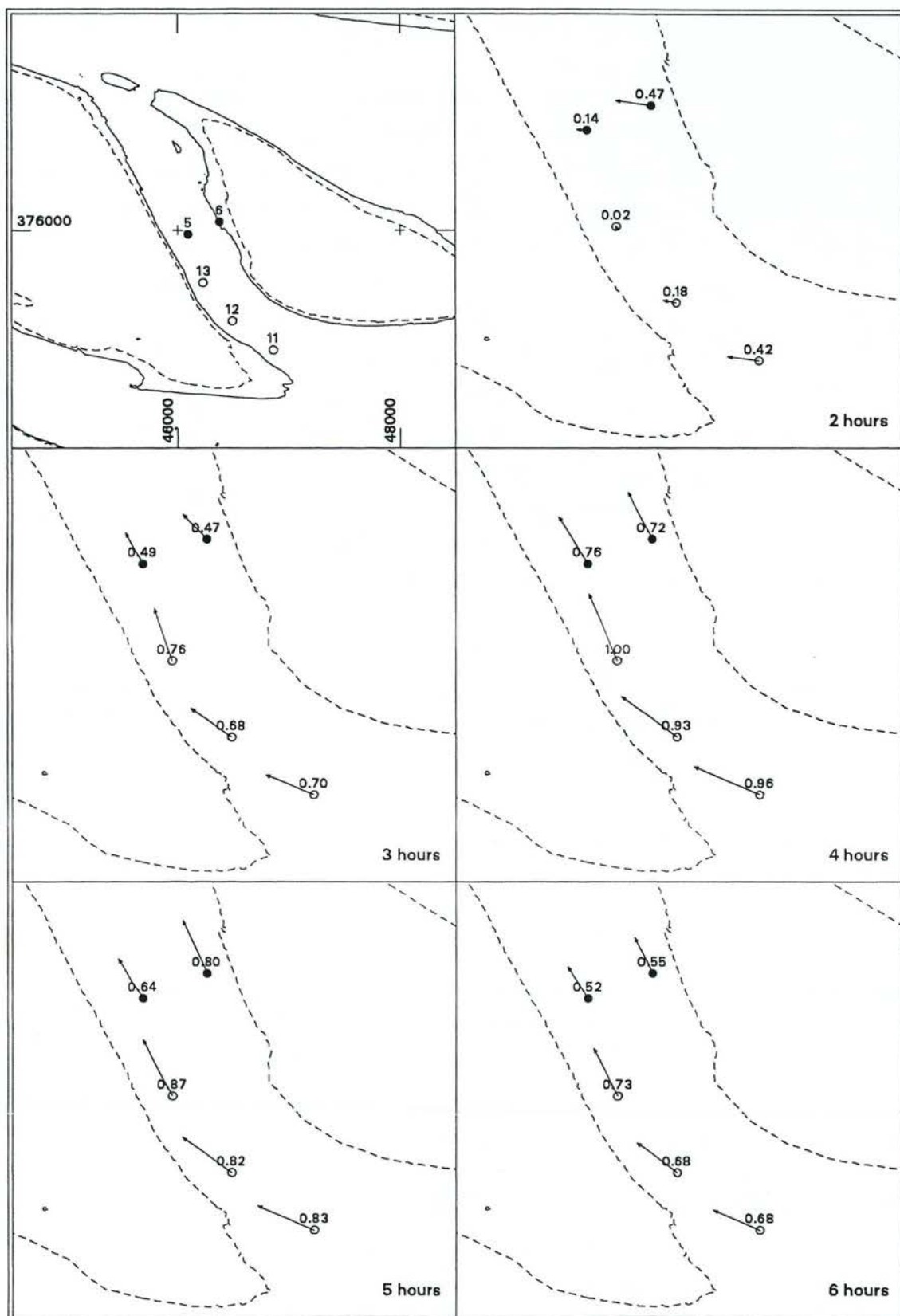
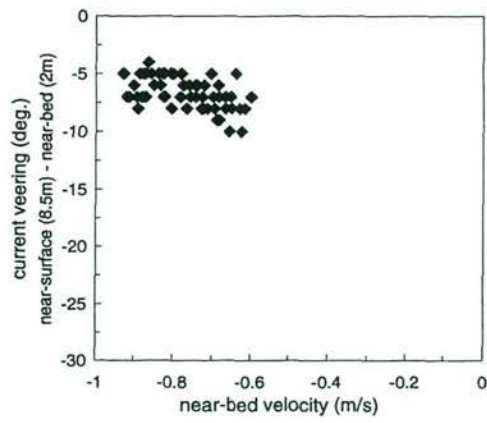


Fig. 4.24 Mean lagrangian current patterns in the cross channel during ebb.

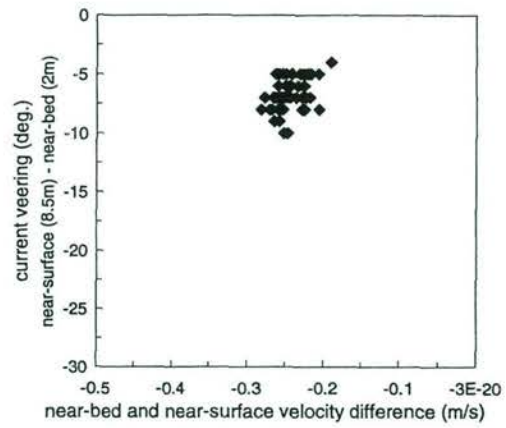
Fig. 4.25 Depth-averaged tidal current patterns in the cross channel during ebb and mean tidal conditions in April 1994 (locations 5 and 6) and November 1994 (11 to 13).



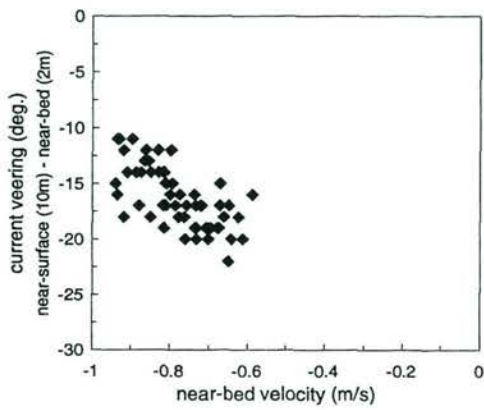
a) location 11



b) location 11



c) location 13



d) location 13

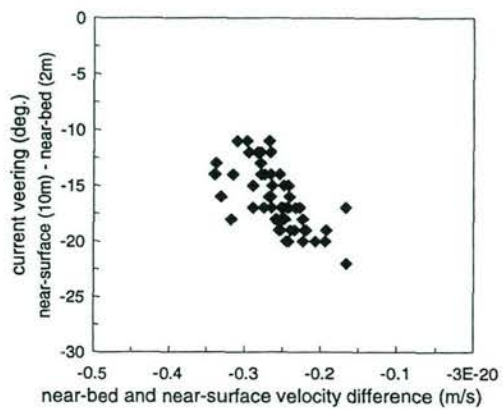


Fig. 4.26 Differences in current direction between near-surface and near-bed significant current vectors versus near-bed current velocity and velocity difference in the cross channel during ebb (locations 11 and 13, Figure 4.3).

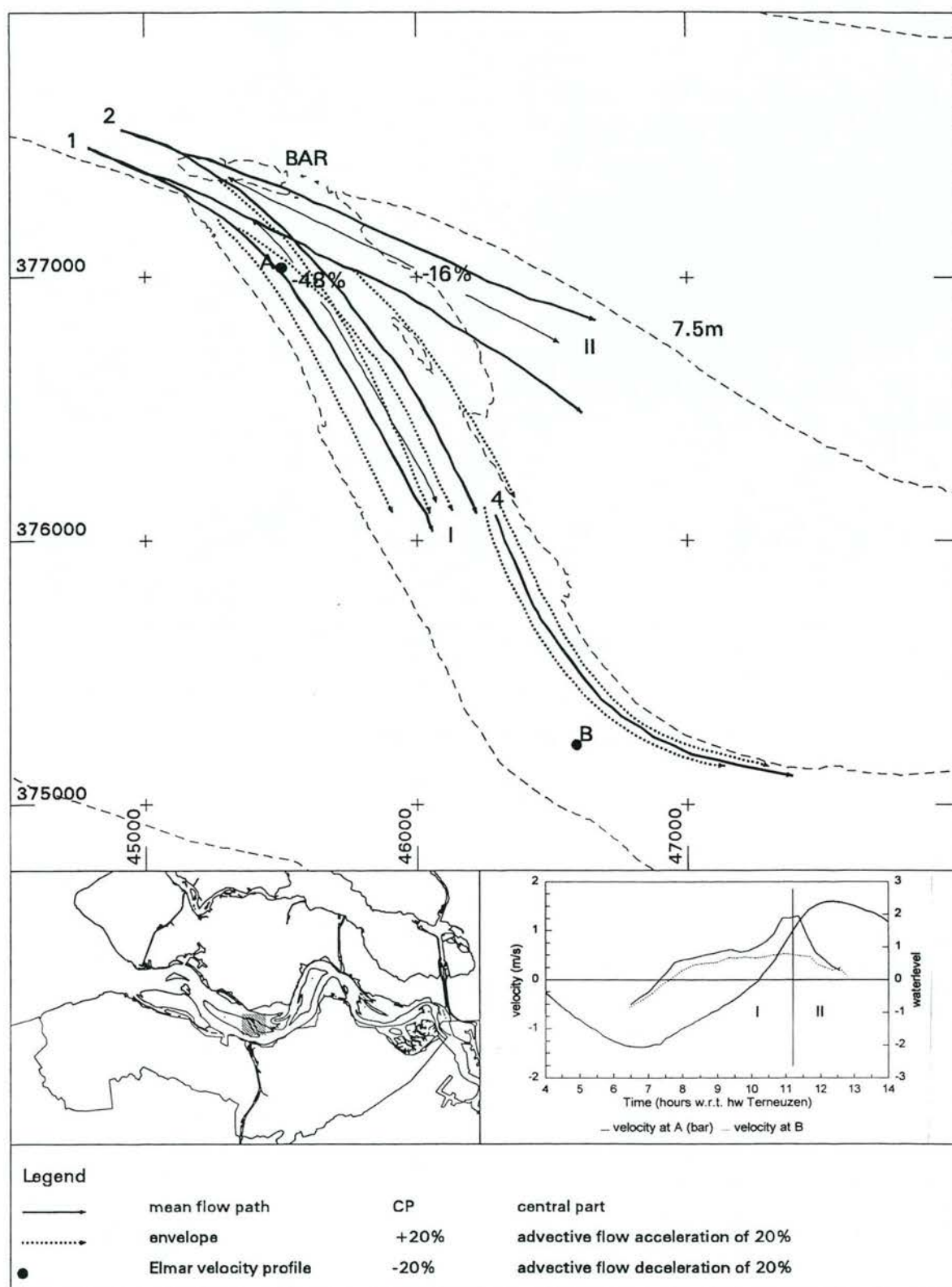
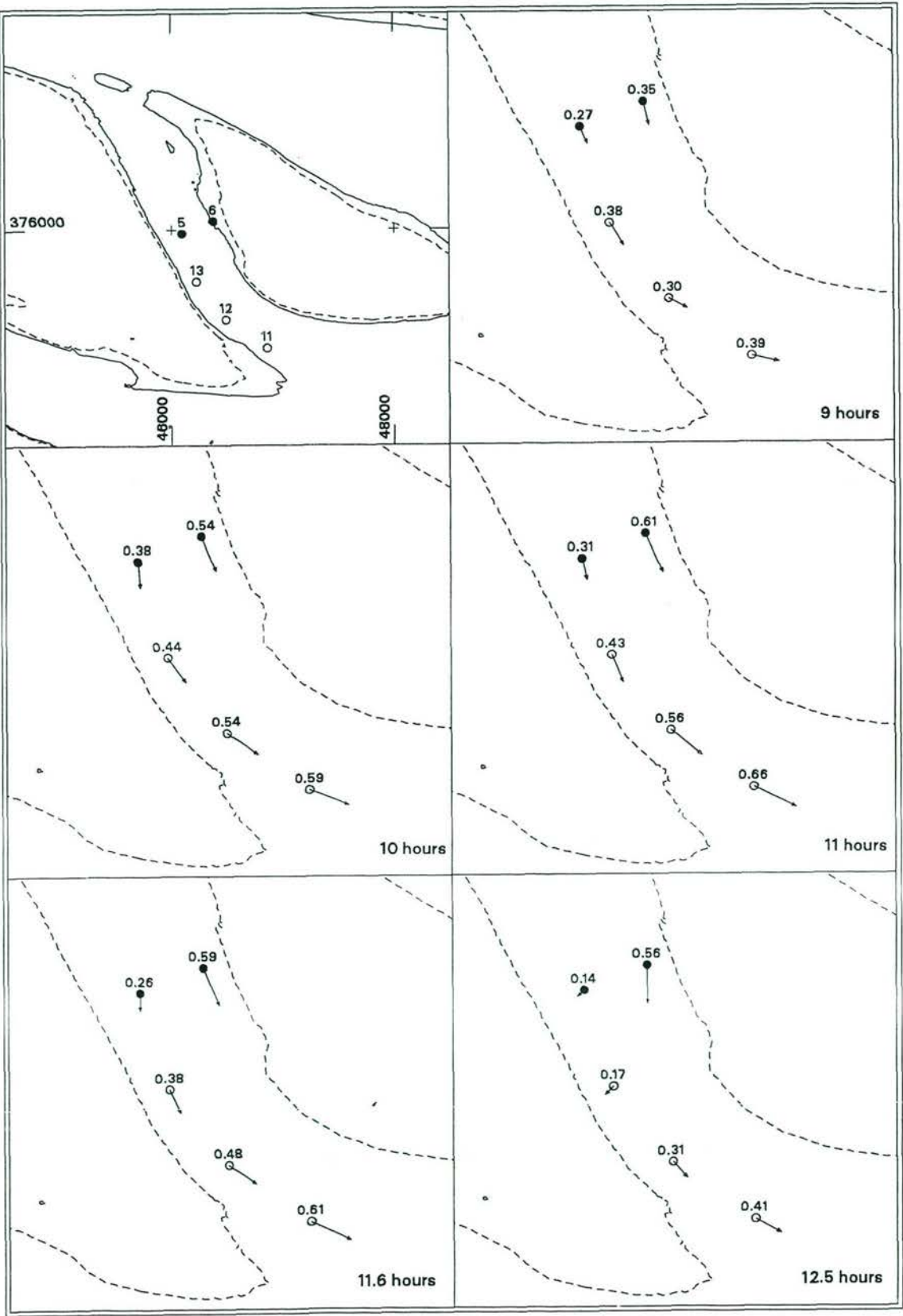


Fig. 4.27 Mean lagrangian current patterns in the cross channel during flood and mean tidal conditions on 22 November 1994.

Fig. 4.28 Depth-averaged tidal current patterns in the cross channel during flood and mean tidal conditions in April 1994 (locations 5 and 6) and November 1994 (11 to 13).



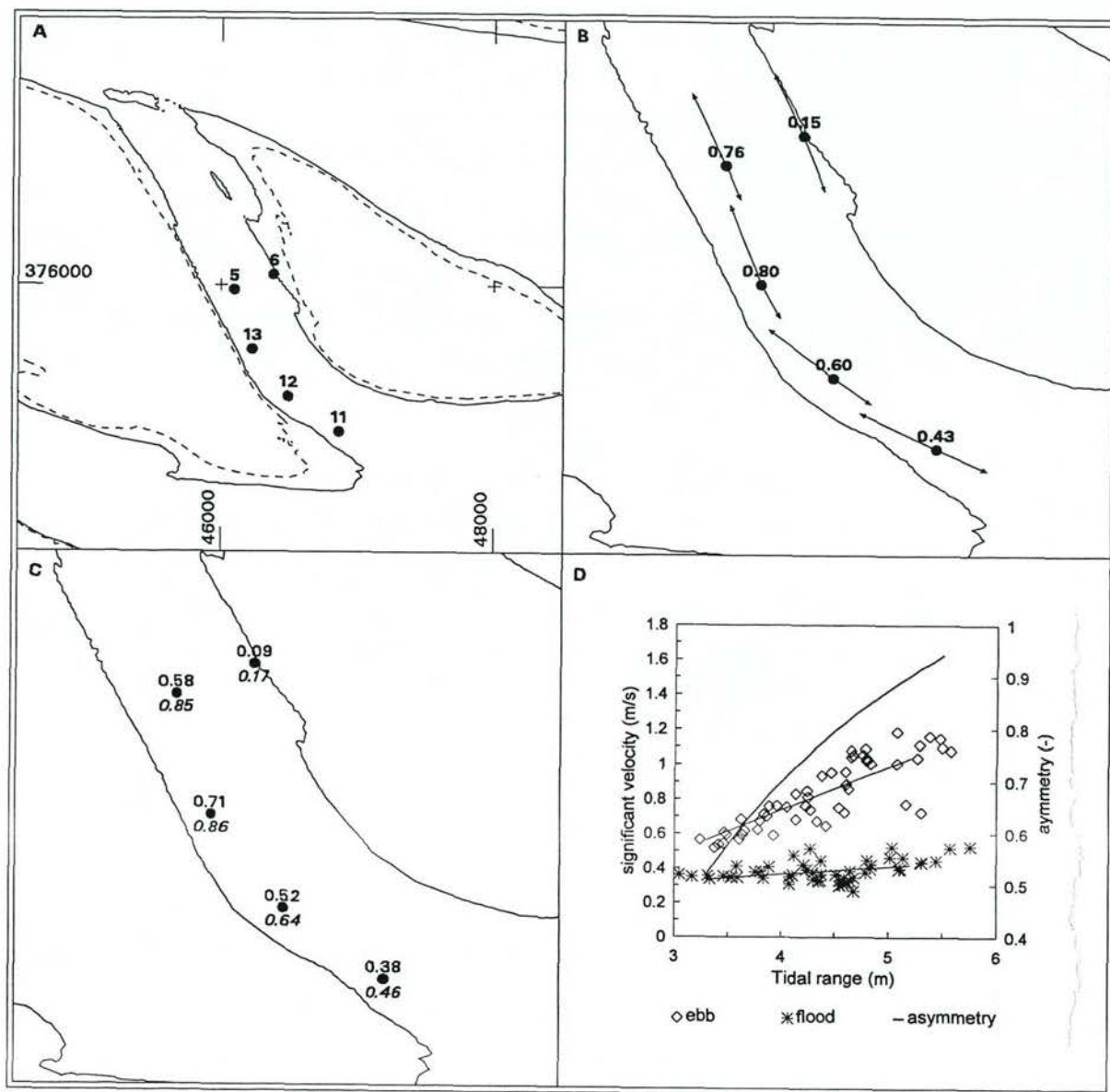


Fig. 4.29 Current asymmetry in the cross channel. a) measurement locations, b) significant current vector and asymmetry ratio's during mean tide, c) asymmetry ratio's for neap and spring tide, d) significant velocity and asymmetry versus tidal range.

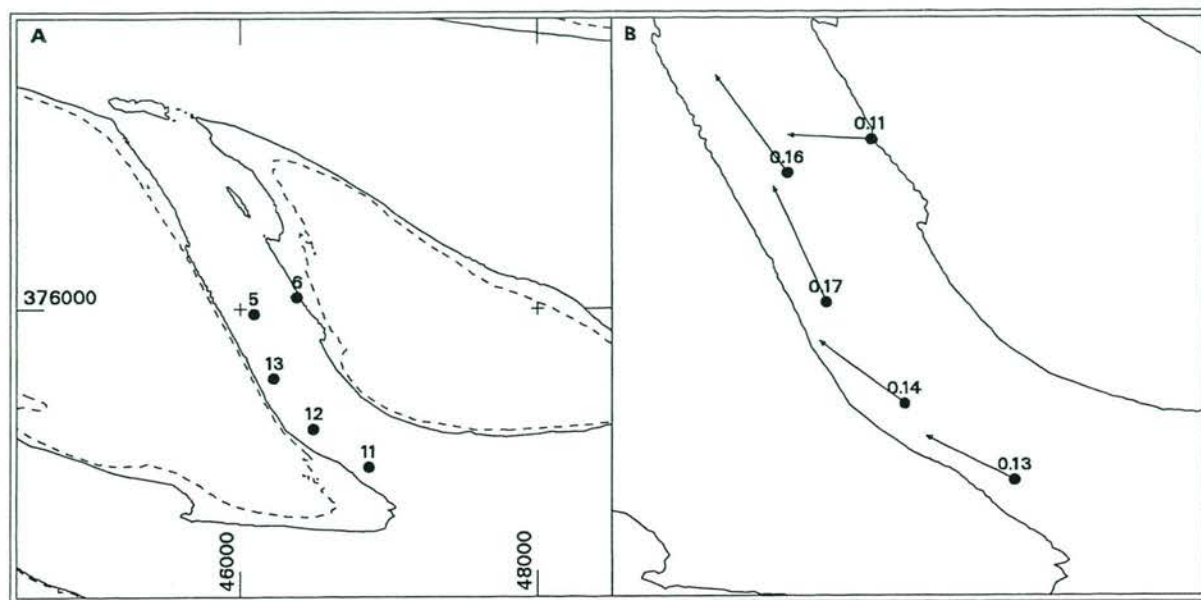


Fig. 4.30 Long-term mean depth-averaged residual current vectors in the cross channel. a) measurement locations, b) residual currents.

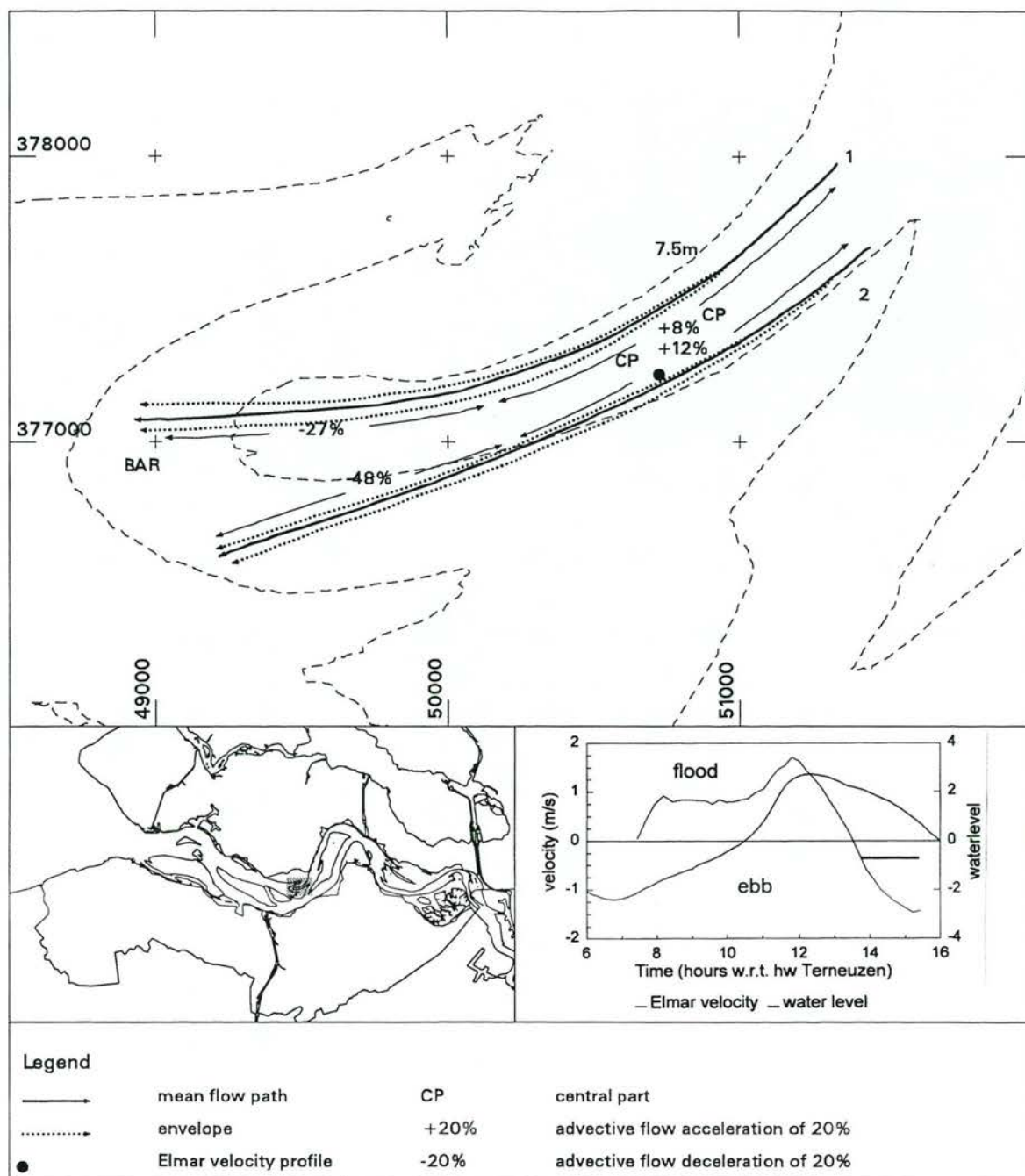


Fig. 4.31 Mean lagrangian current patterns in the ebb bar channel during accelerating ebb on 4 November 1994

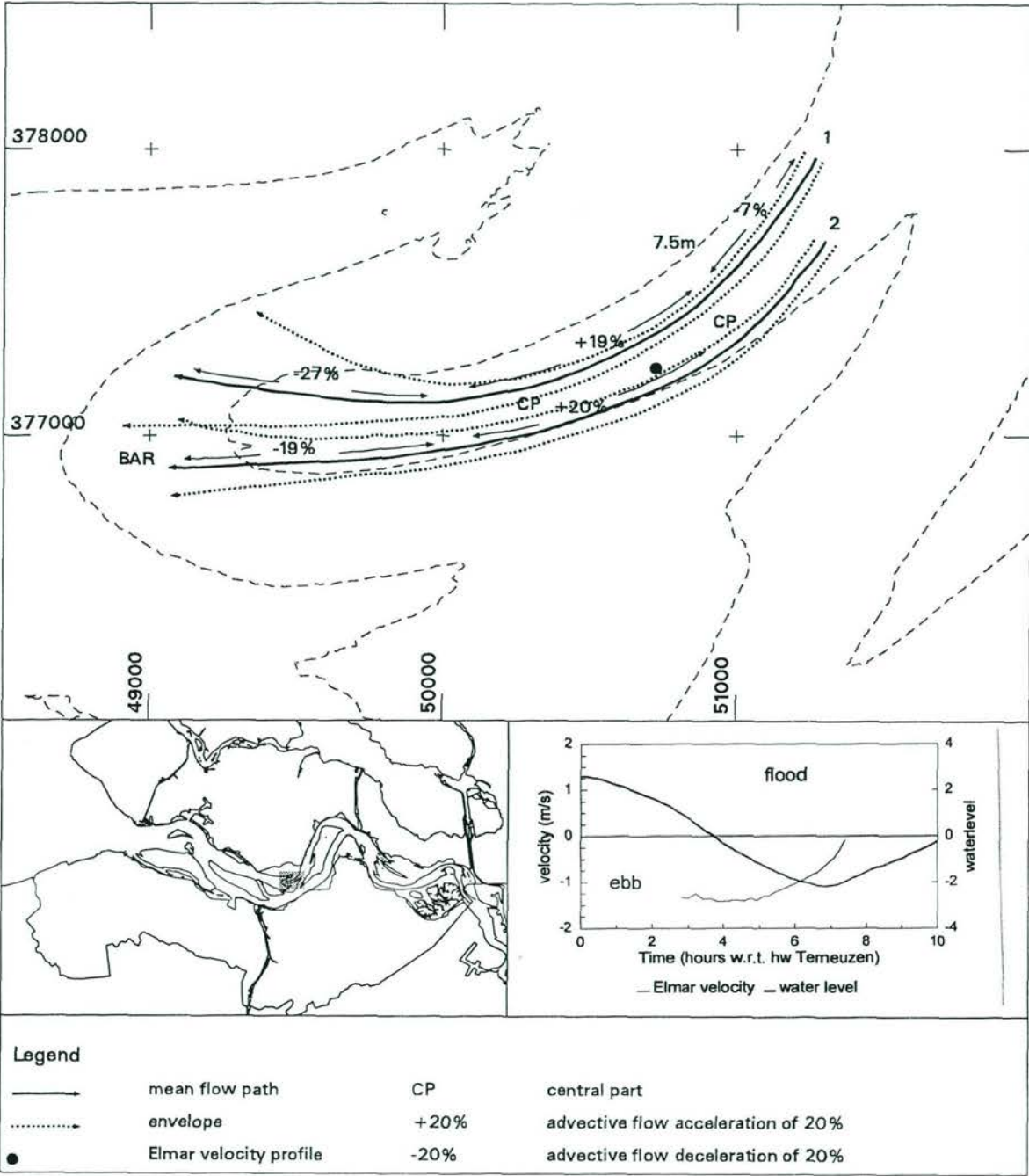


Fig. 4.32 Mean lagrangian current patterns in the ebb bar channel during maximum and decelerating ebb on 8 November 1994

Fig. 4.33 Depth-averaged current current patterns in the ebb bar channel during ebb and mean tidal conditions in November 1994

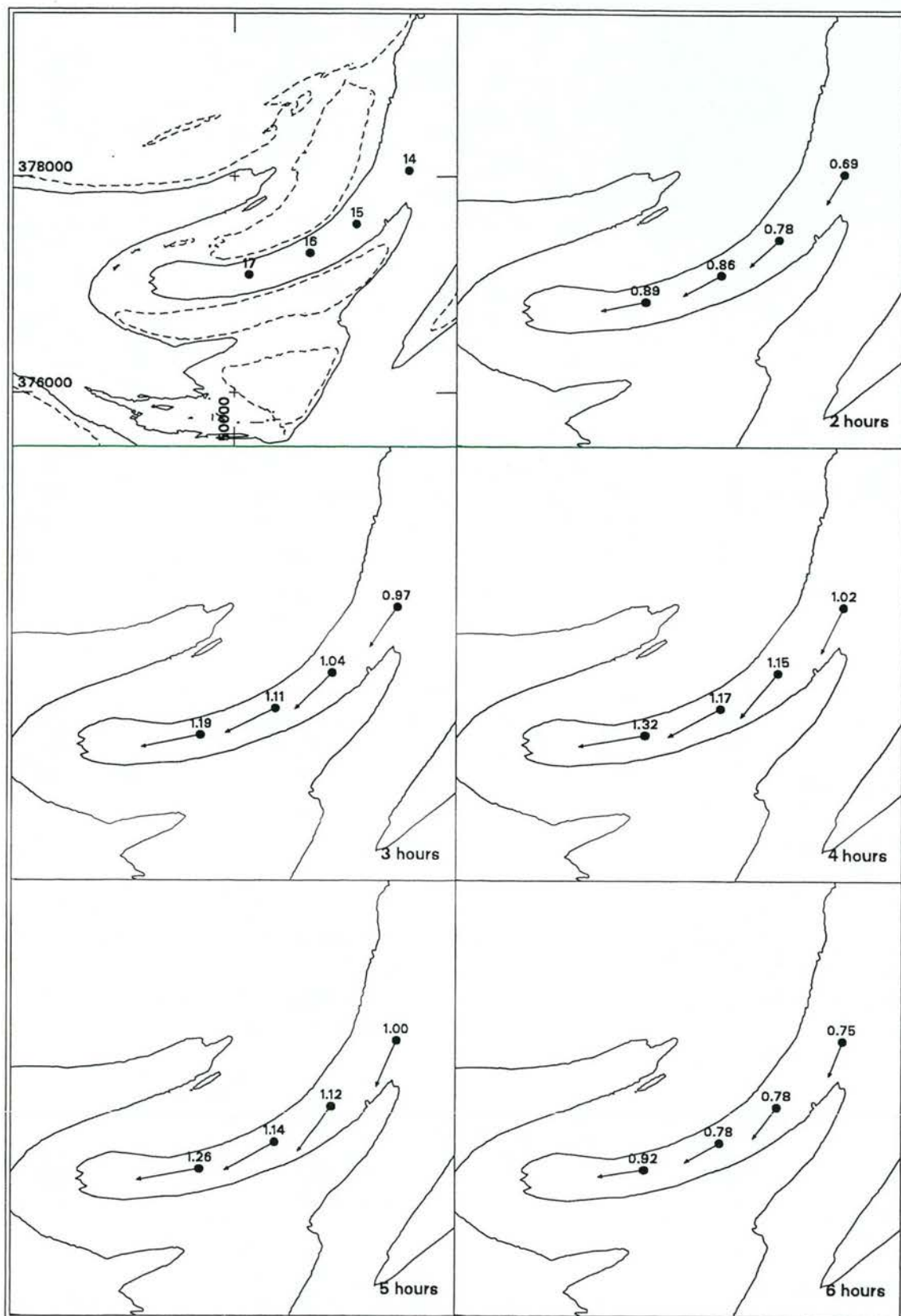
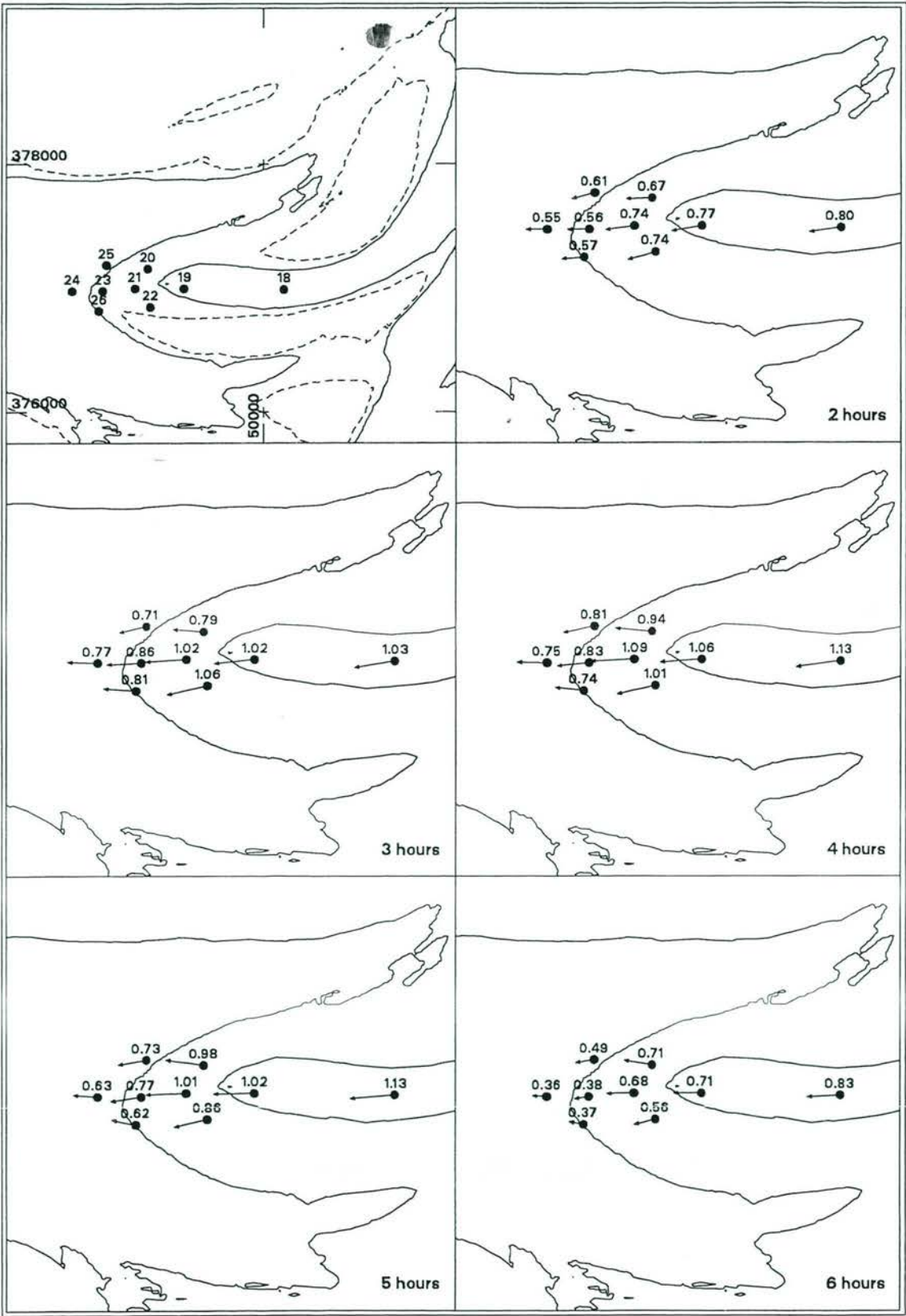


Fig. 4.34 Depth-averaged current current patterns in the ebb bar channel during ebb and mean tidal conditions in June 1995.



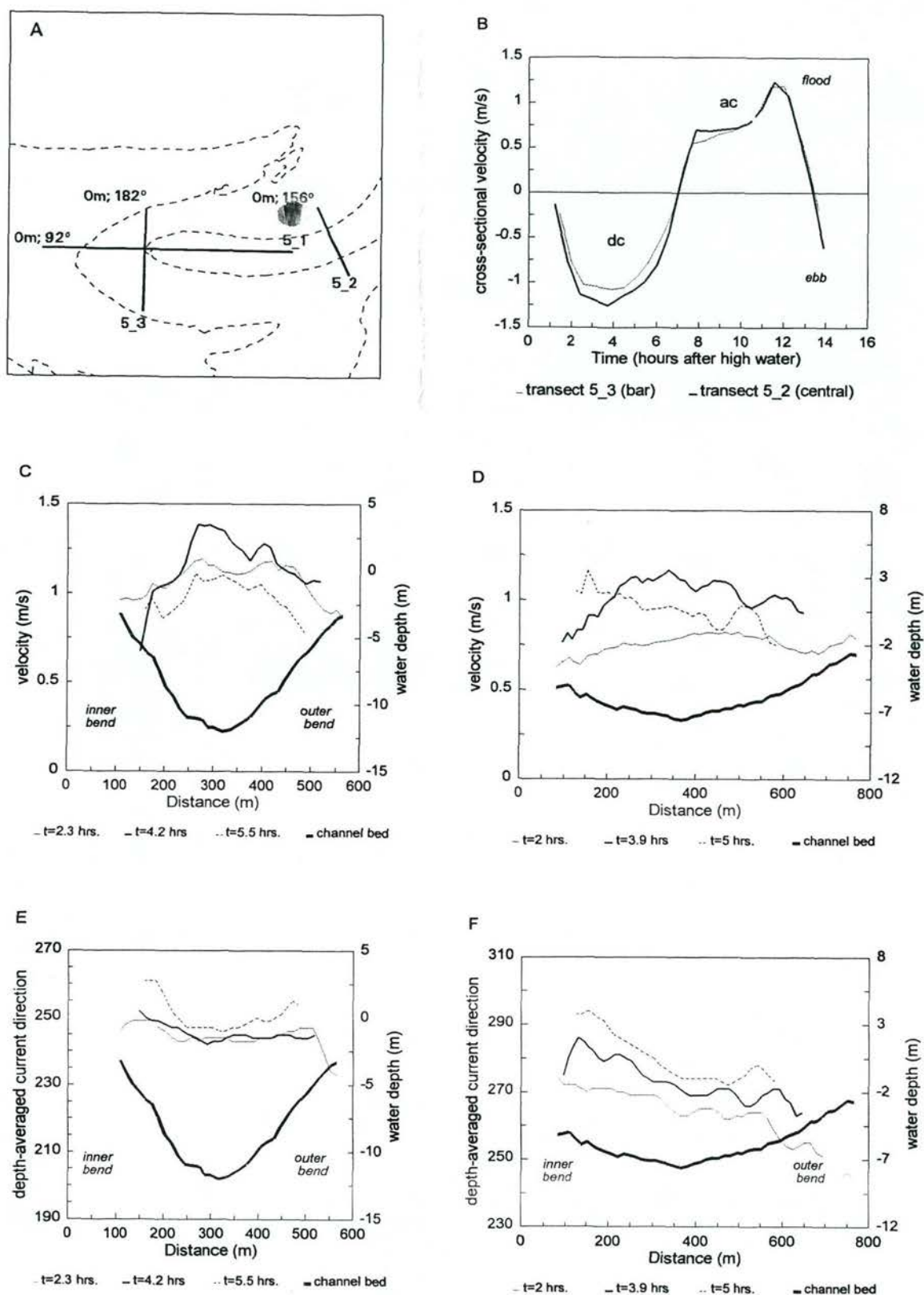


Fig. 4.35 Cross-sectionally averaged and depth-averaged currents in the ebb bar channel along transect 5_2 and 5_3 during ebb. a) locations and orientations of ADCP-transects, b) time-series of the cross-sectionally averaged currents, c) magnitude of depth-averaged current vectors along transect 5_2. d) direction of depth-averaged current vectors along transect 5_2. e) magnitude of depth-averaged current vectors along transect 5_3. f) direction of depth-averaged current vectors along transect 5_3.

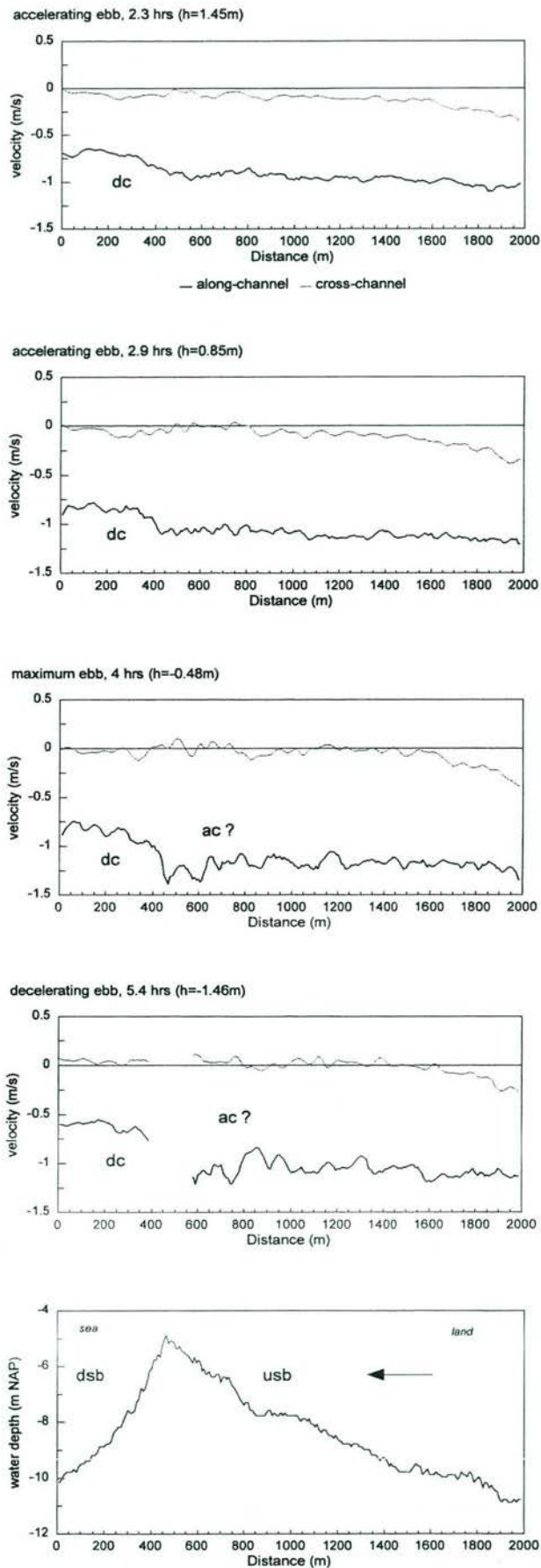


Fig. 4.36 Depth-averaged along-channel and cross-channel velocity patterns over the bar of the ebb bar channel during ebb (transect 5_1), ac= acceleration of the flow, dc=deceleration of the flow, dsb=downstream side of the bar, usb=ustream side of the bar. Negative along-channel component is ebb, positive component is flood.

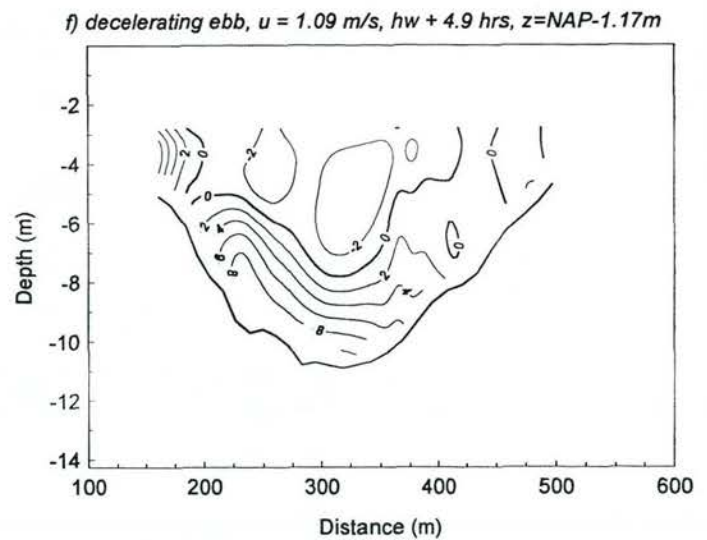
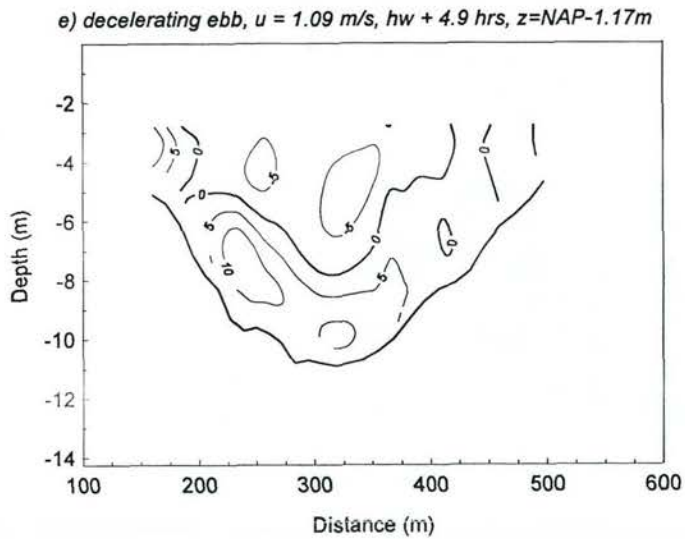
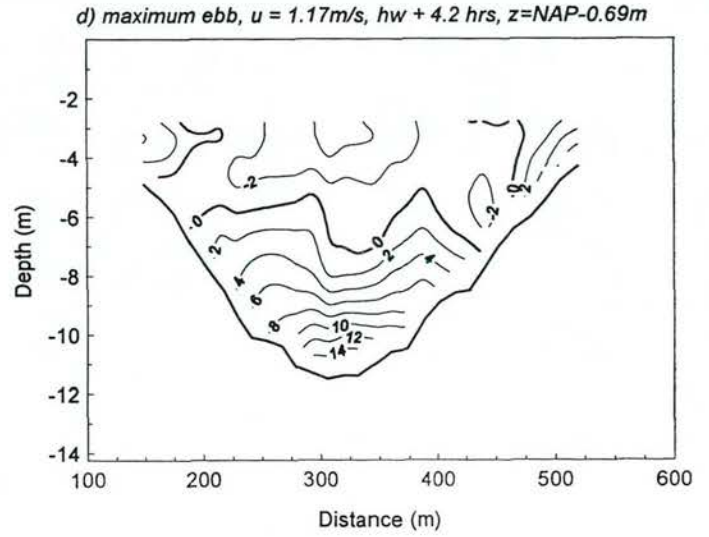
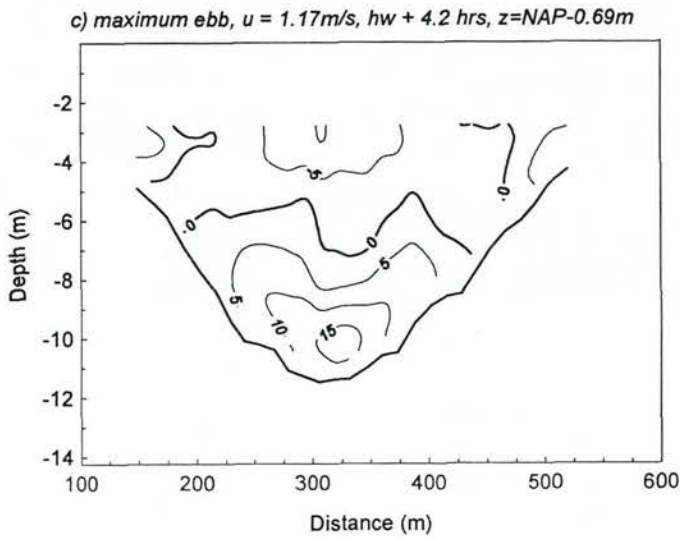
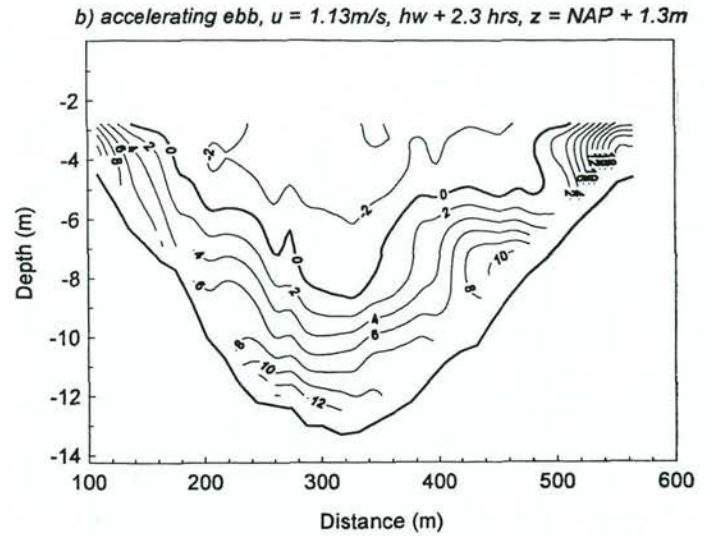
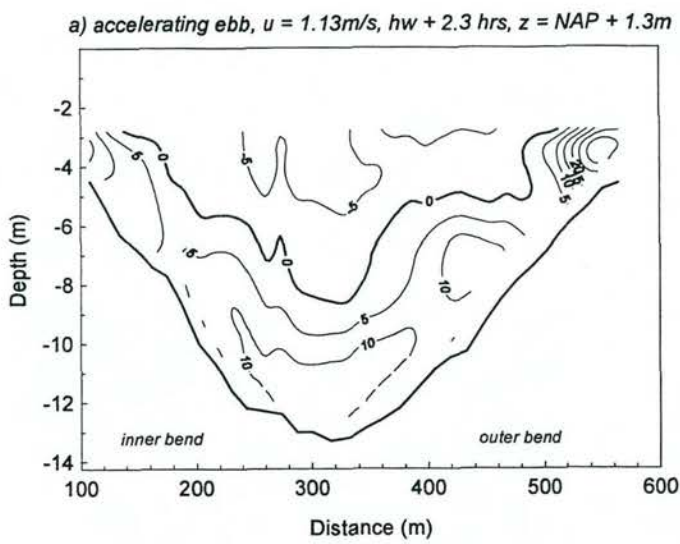


Fig. 4.37 Countour plots of the relative magnitude of the secondary flow (in % of the magnitude of the depth-averaged current velocity) and current veering with respect to the depth-averaged current direction in the central part of the ebb bar channel (transect 5_2, Fig. 5.4). a & b) accelerating ebb, c & d) maximum ebb, e & f) decelerating ebb.

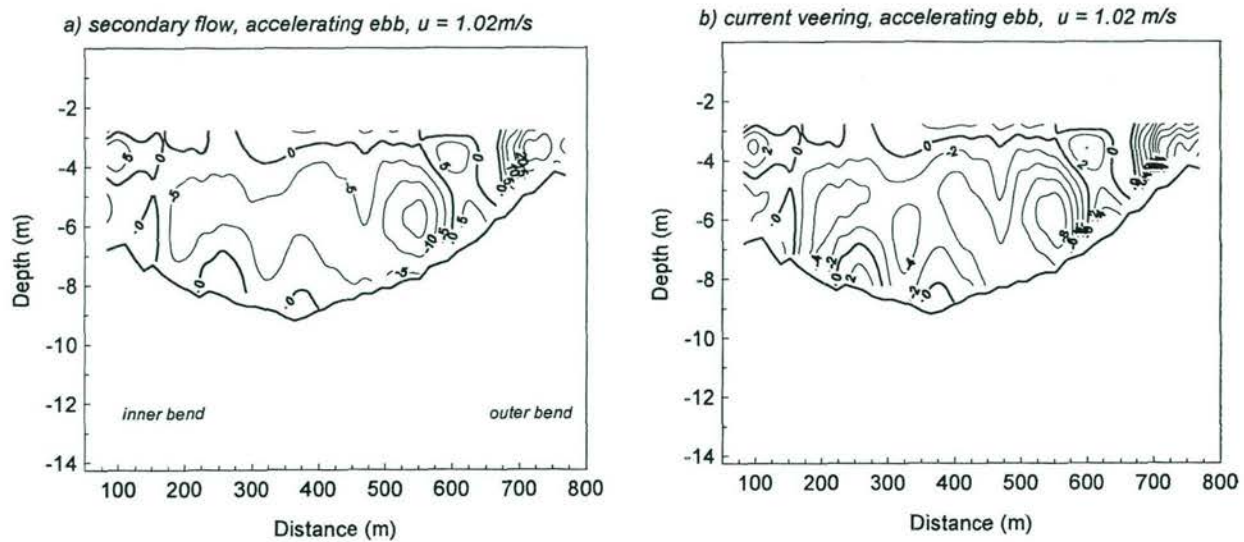


Fig. 4.38 Contourplots of the relative magnitude of secondary flow and current veering near the bar in the ebb bar channel during ebb (transect 5_3, for location see Fig. 4.5).

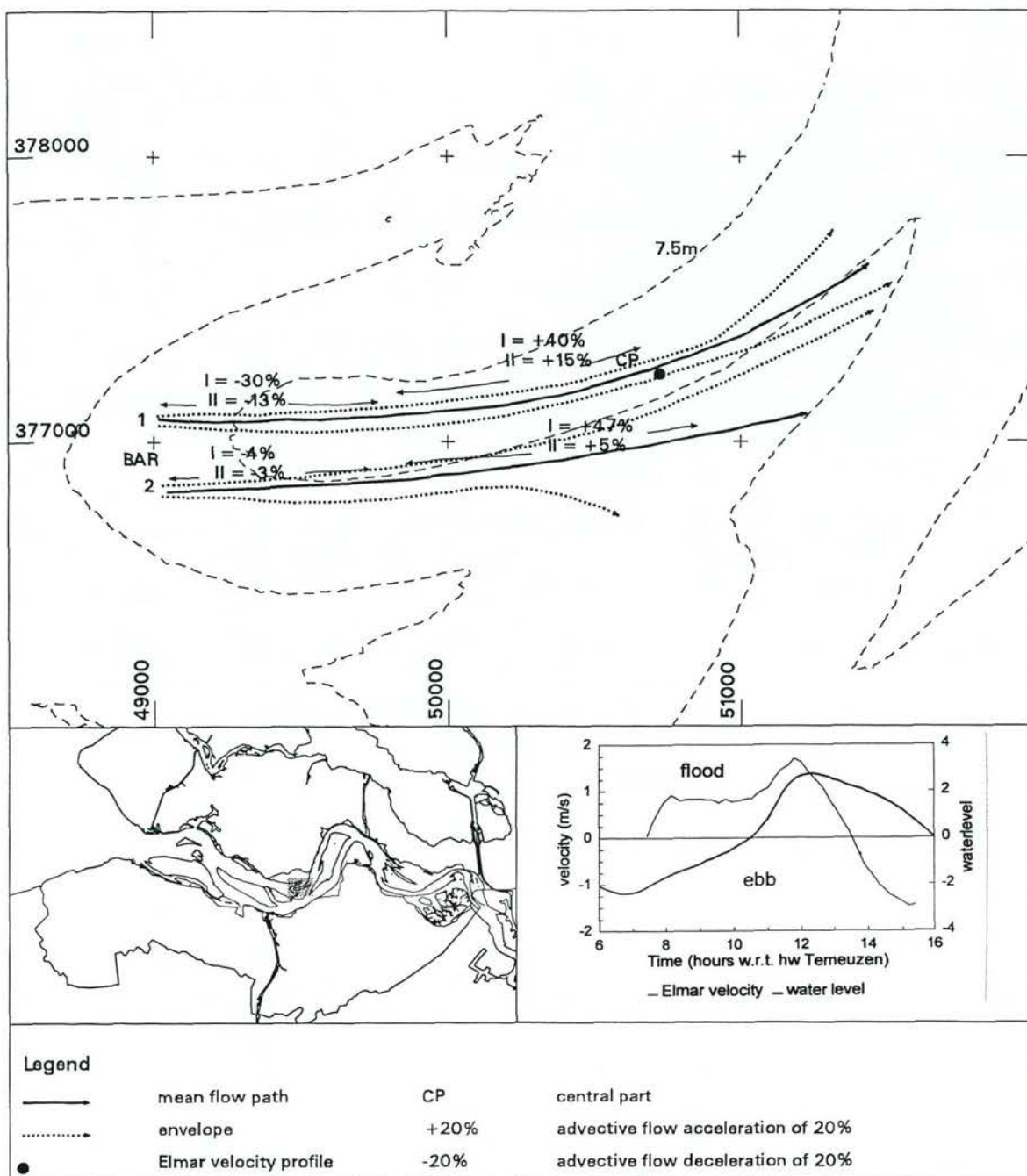


Fig. 4.39 Mean lagrangian current patterns in the ebb bar channel during flood on 4 November 1994

Fig. 4.40 Depth-averaged current current patterns in the ebb bar channel during flood and mean tidal conditions in November 1994

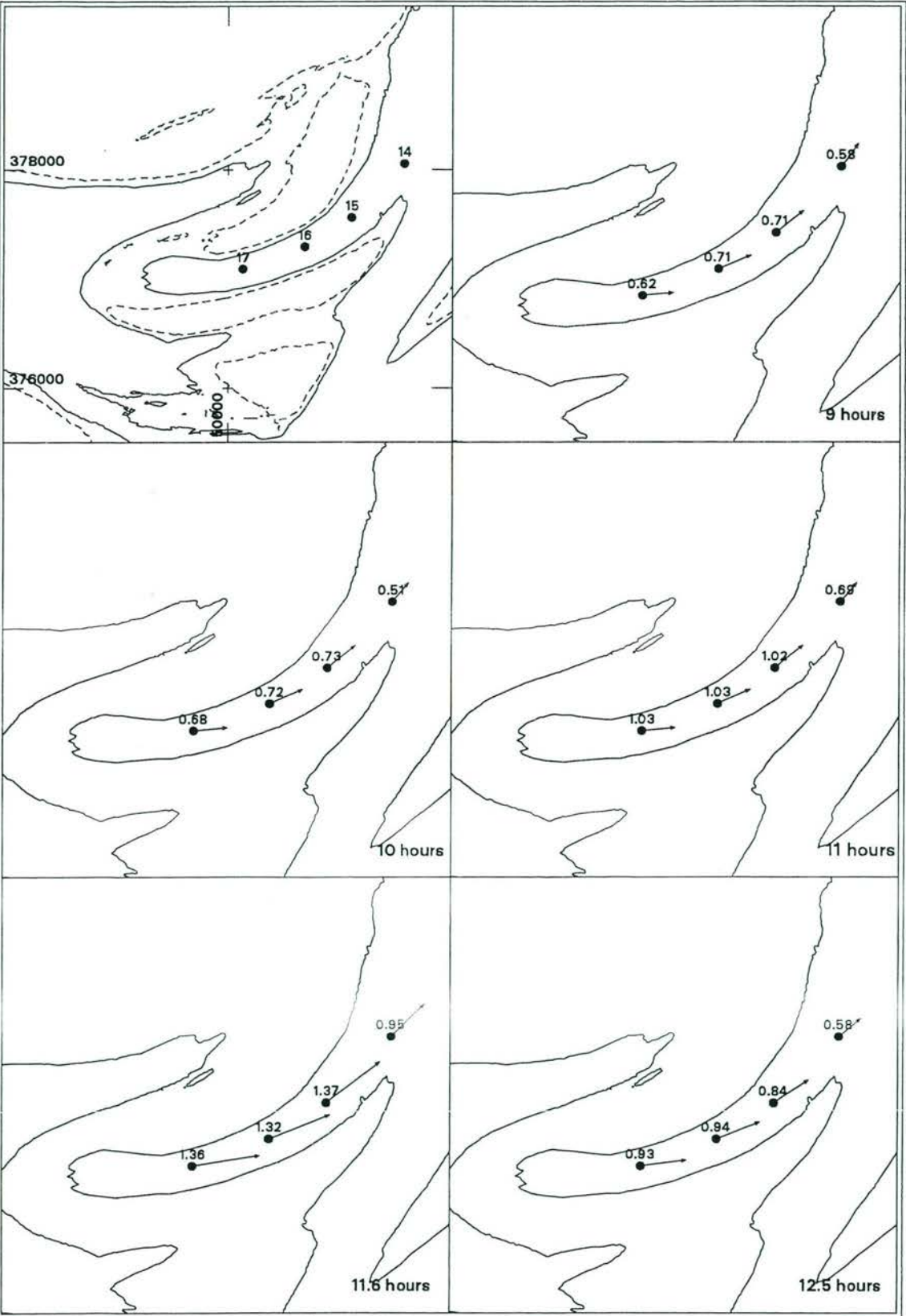
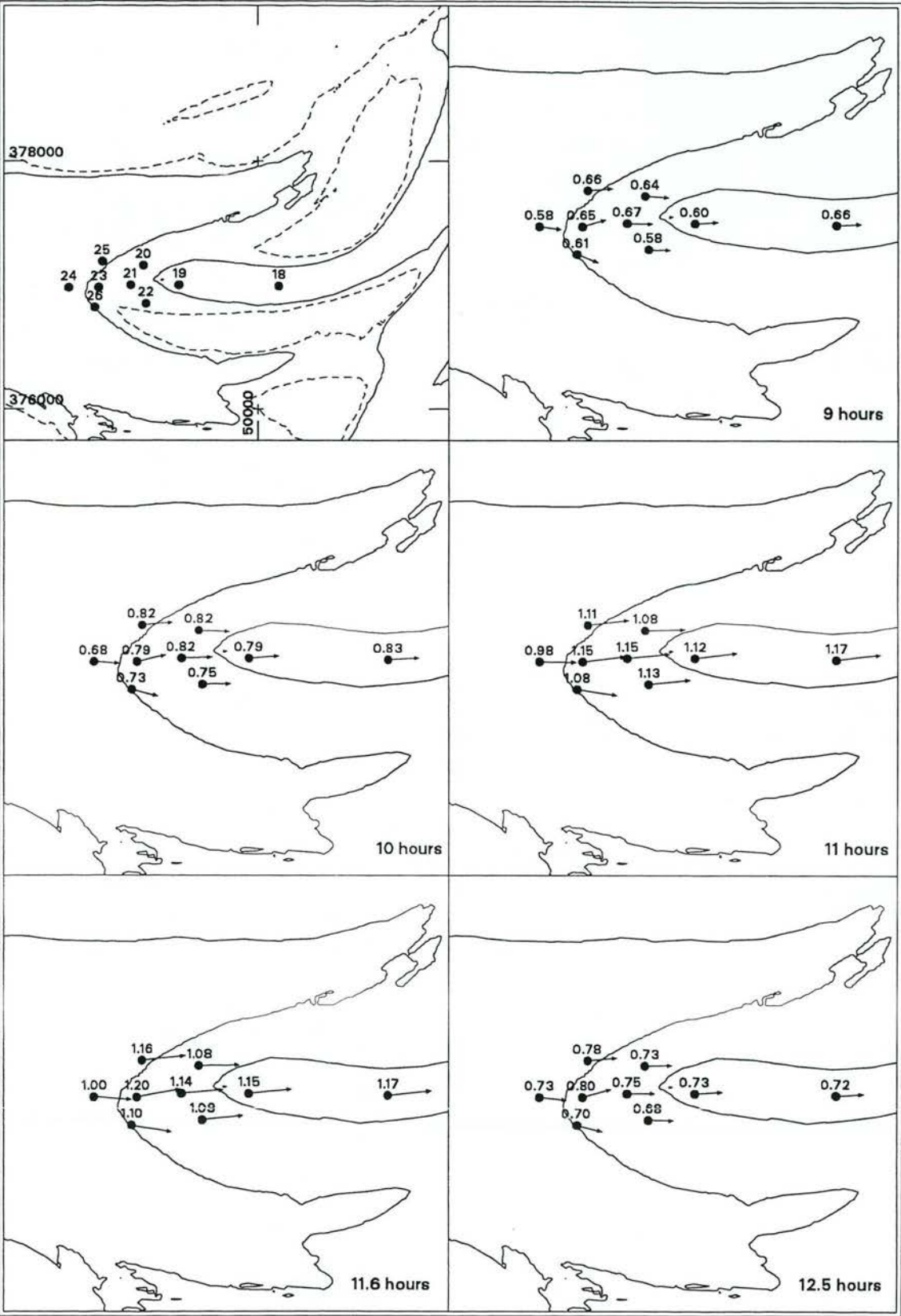


Fig. 4.41 Depth-averaged current current patterns in the ebb bar channel during flood and mean tidal conditions in June 1995.



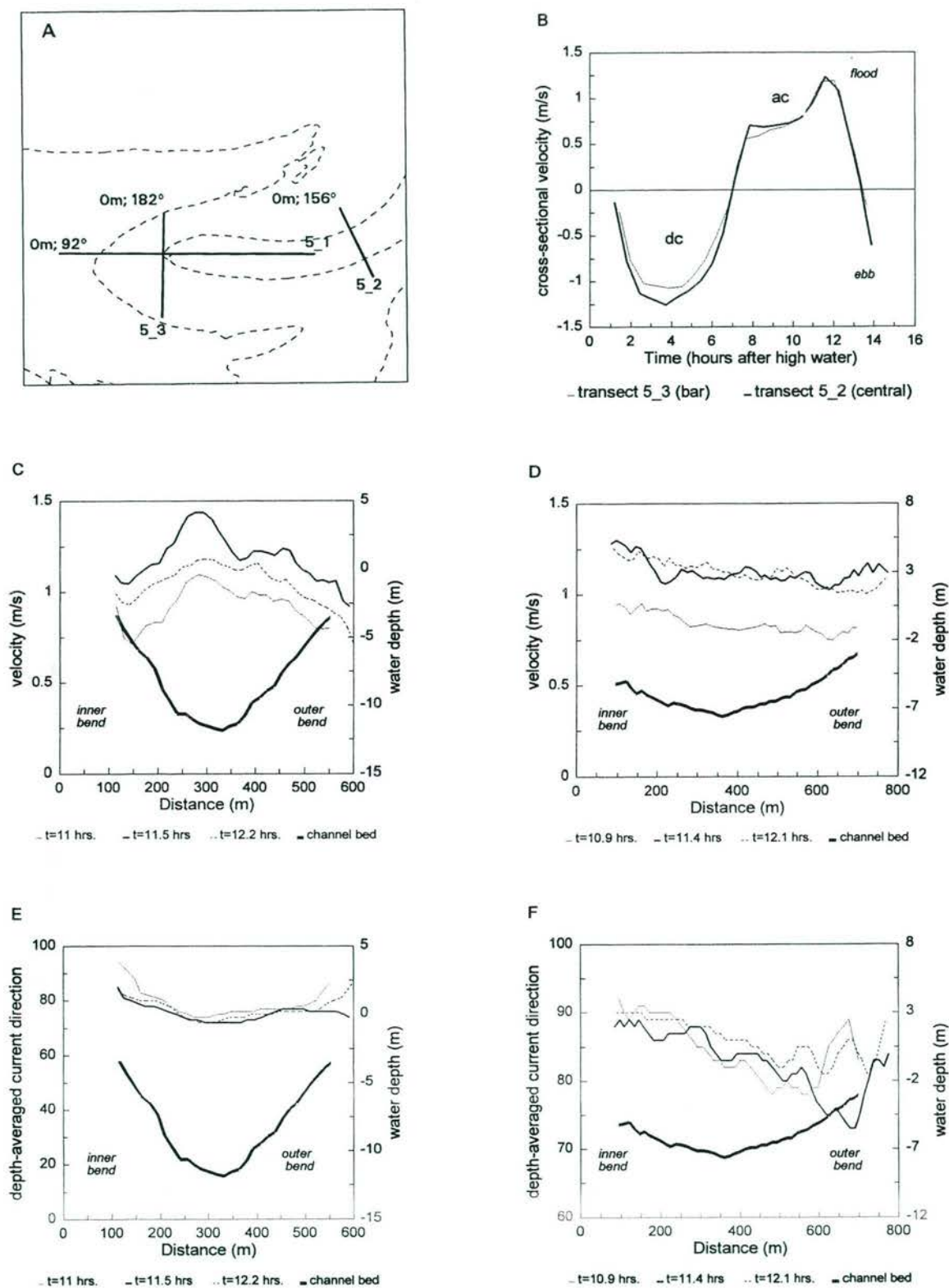


Fig. 4.42 Cross-sectionally averaged and depth-averaged currents in the ebb bar channel along transect 5_2 and 5_3 during flood. a) locations and orientations of ADCP-transects, b) time-series of the cross-sectionally averaged currents, c) magnitude of depth-averaged current vectors along transect 5_2. d) direction of depth-averaged current vectors along transect 5_2. e) magnitude of depth-averaged current vectors along transect 5_3. f) direction of depth-averaged current vectors along transect 5_3.

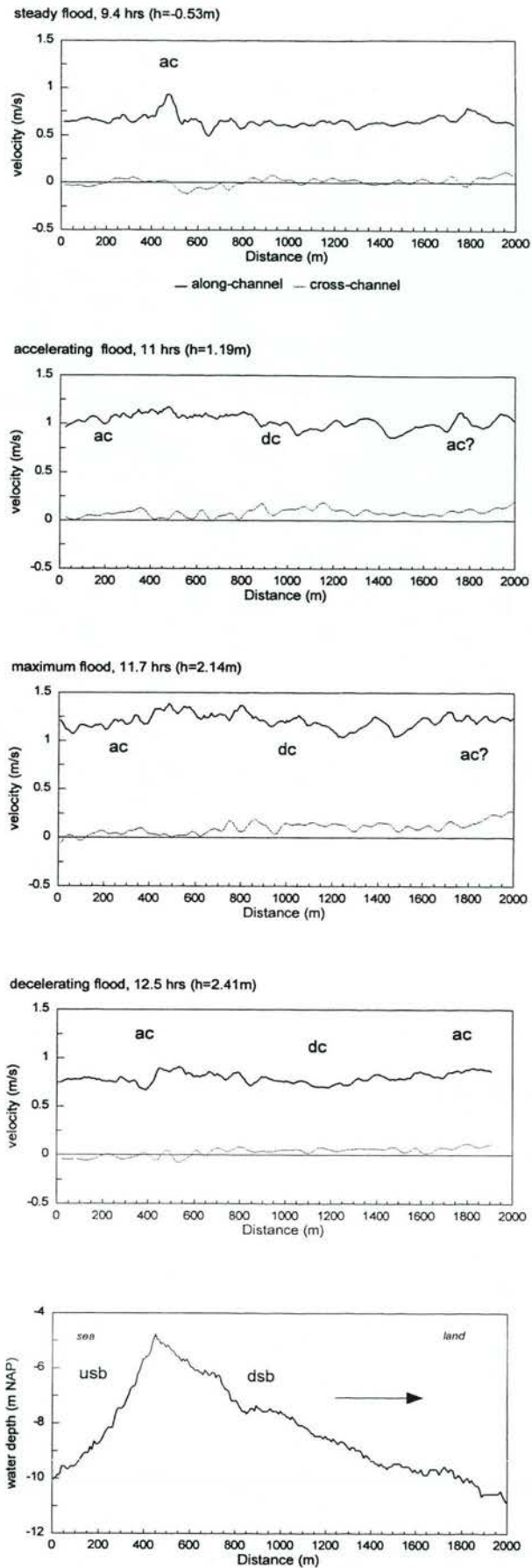


Fig. 4.43 Depth-averaged along-channel and cross-channel velocity patterns over the bar of the ebb bar channel during flood (transect 5_1), ac= acceleration of the flow, dc=deceleration of the flow, dsb=downstream side of the bar, usb=upstream side of the bar. Negative along-channel component is ebb, positive component is flood.

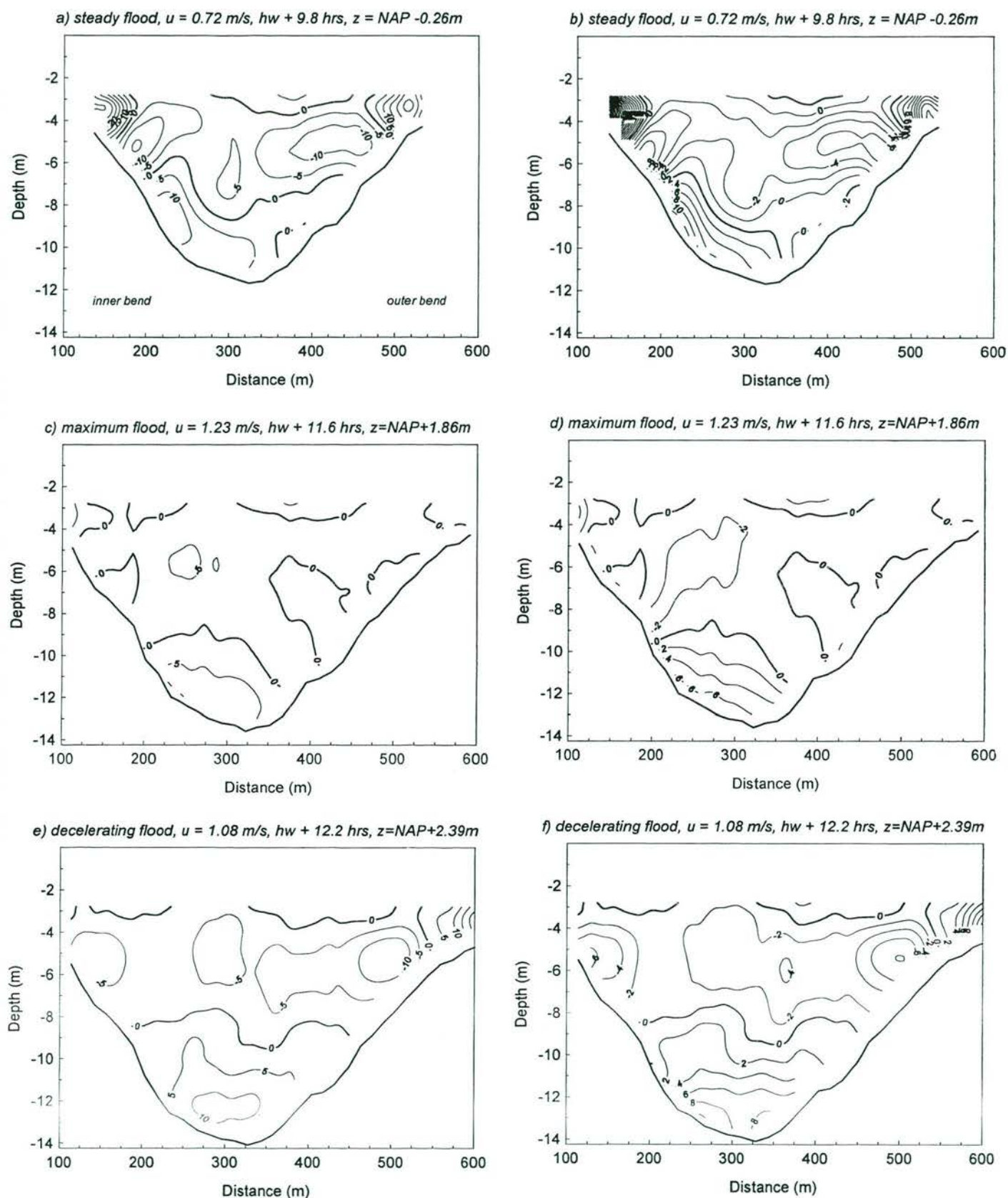


Fig. 4.44 Countour plots of the relative magnitude of the secondary flow (in % of the magnitude of the depth-averaged current velocity) and current veering with respect to the depth-averaged current direction in the central part of the ebb bar channel during flood (transect 5_2, Fig. 5.4). a & b) accelerating flood, c & d) maximum flood, e & f) decelerating flood.

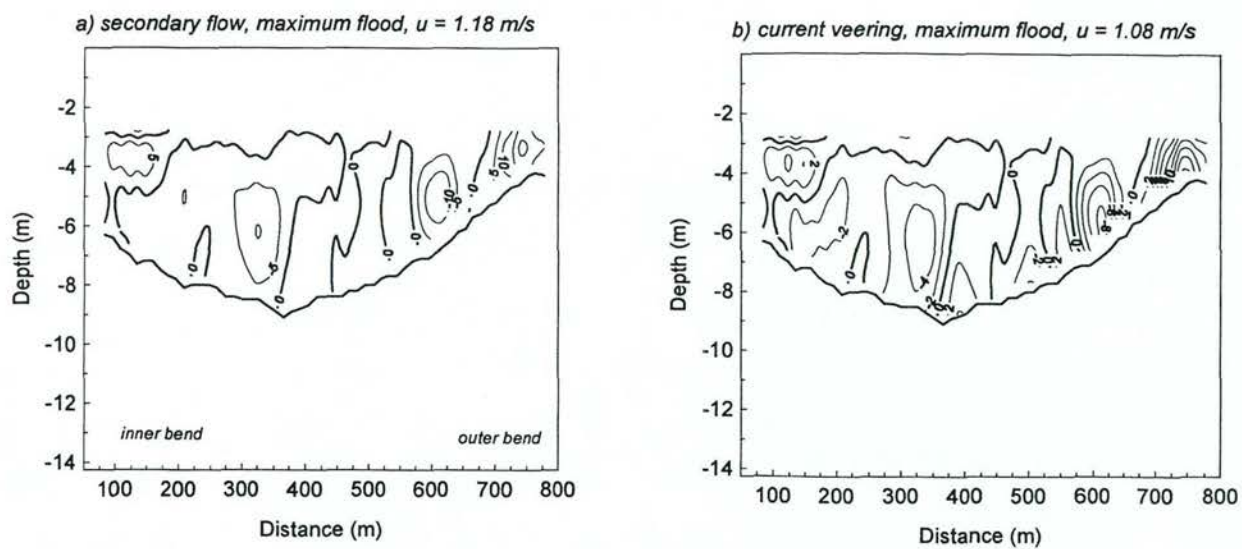
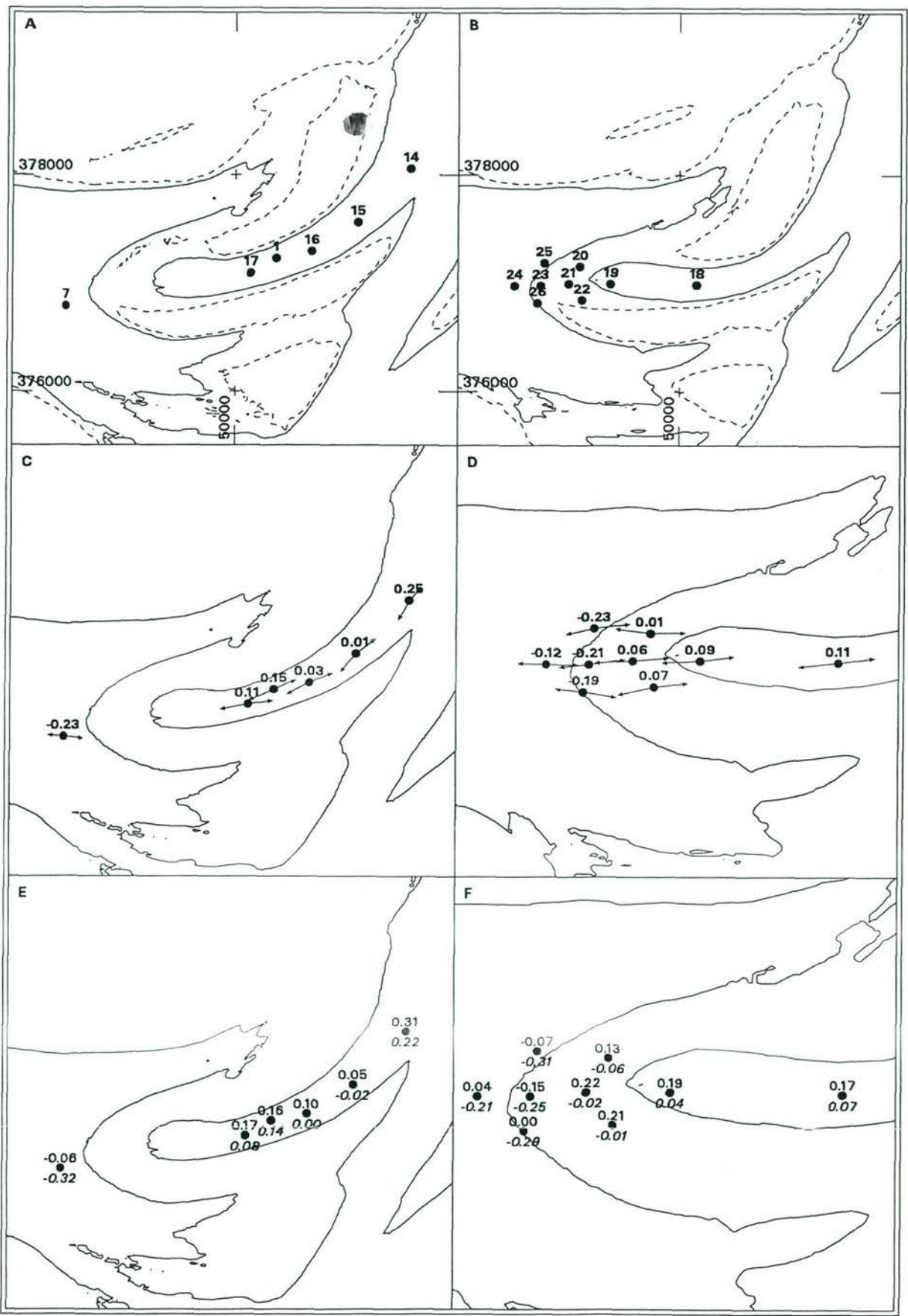


Fig. 4.45 Contourplots of the relative magnitude of secondary flow and current veering near the bar in the ebb bar channel during flood (transect 5_3, for location see Fig. 4.5).

Fig. 4.46 Current asymmetry in the ebb bar channel channel in November 1994 and June 1995. a & b) measurement locations, c & d) significant current vector and asymmetry ratio's during mean tide, e & f) asymmetry ratio's for neap and spring tide



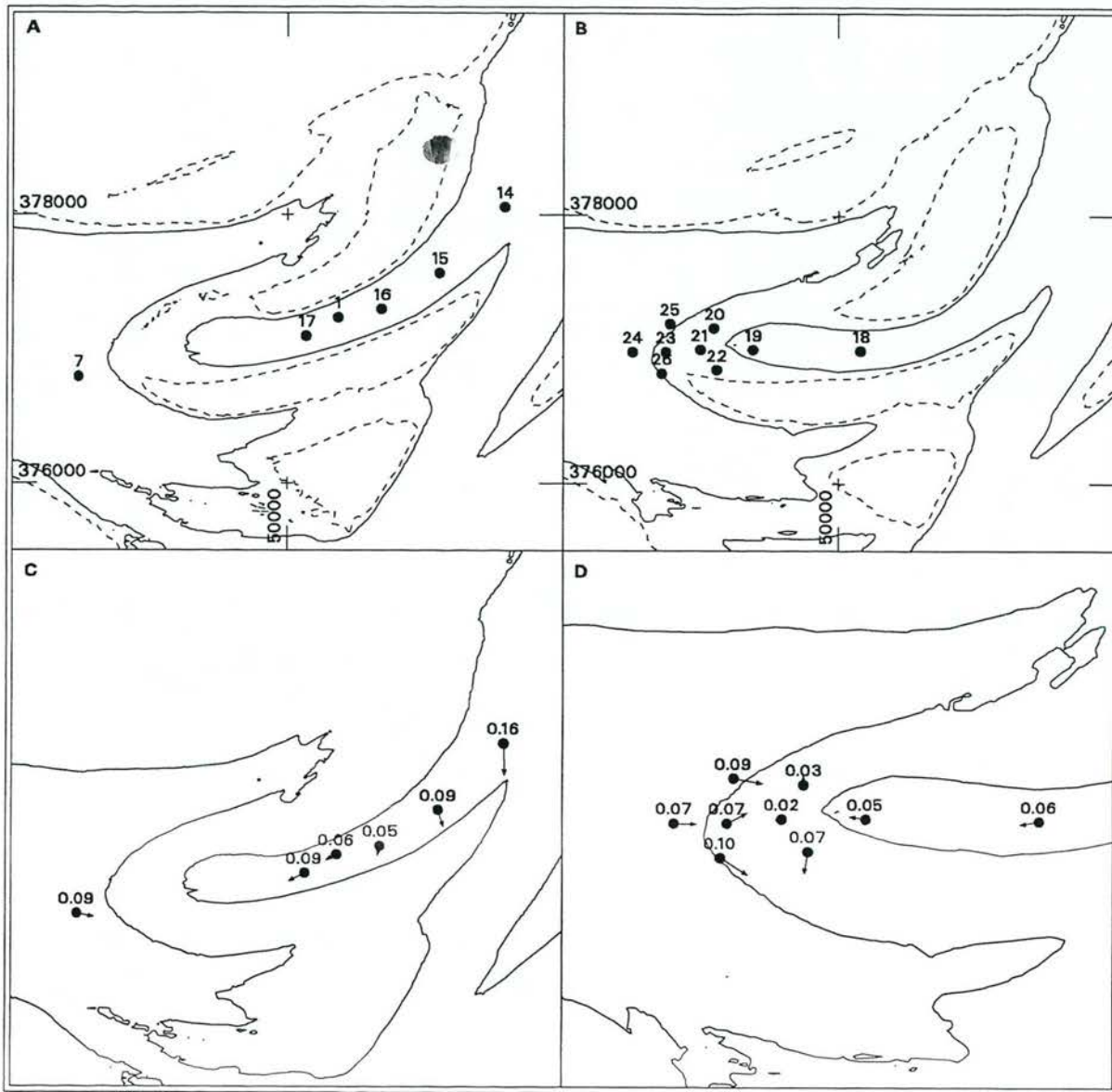


Fig. 4.47 Residual current vectors in the ebb bar channel in November 1994 and June 1995. a & b) measurement locations, c & d) long-term mean residual current vectors.

Fig. 4.48 Depth-averaged current current patterns in the flood bar channel during ebb and mean tidal conditions

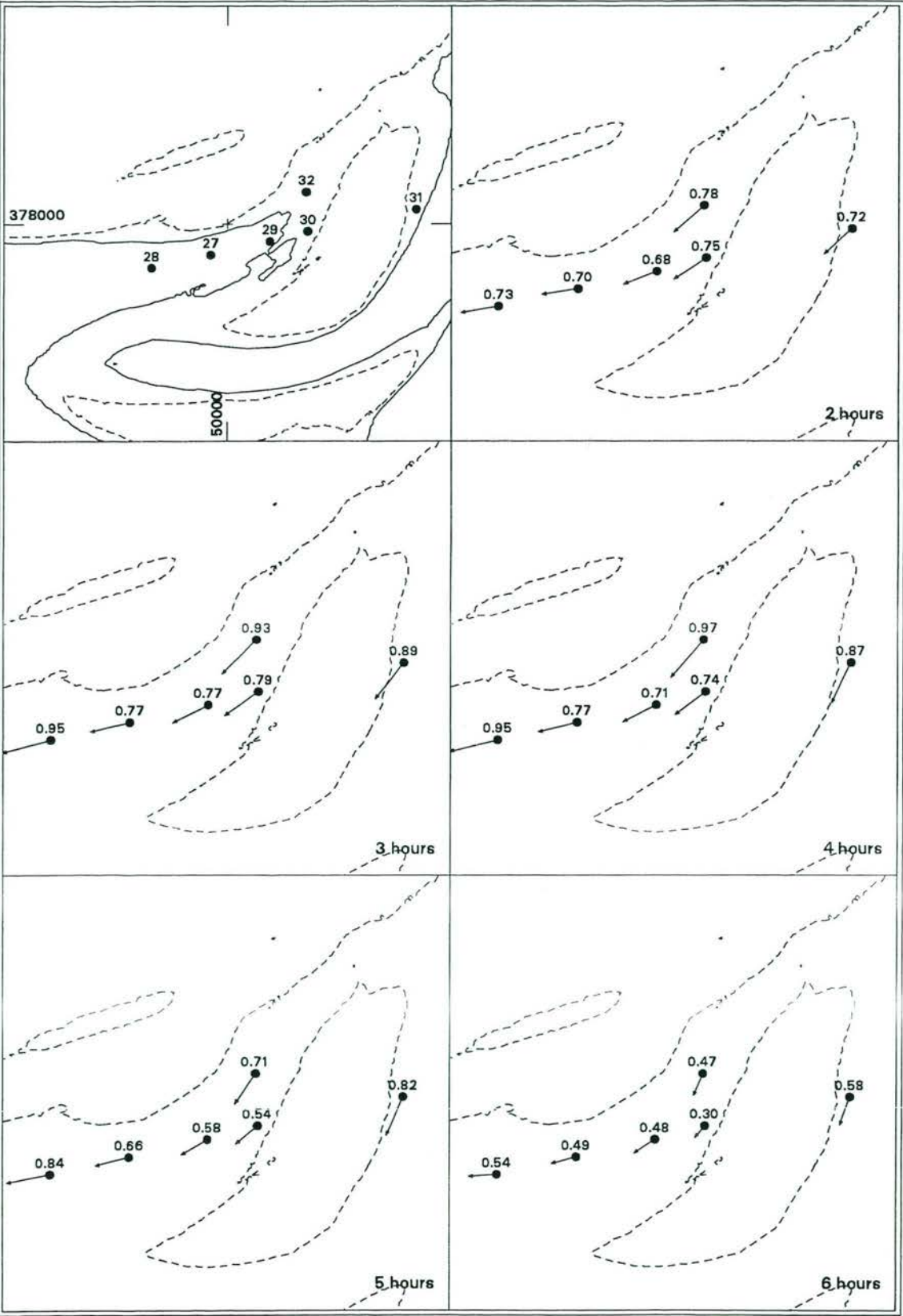
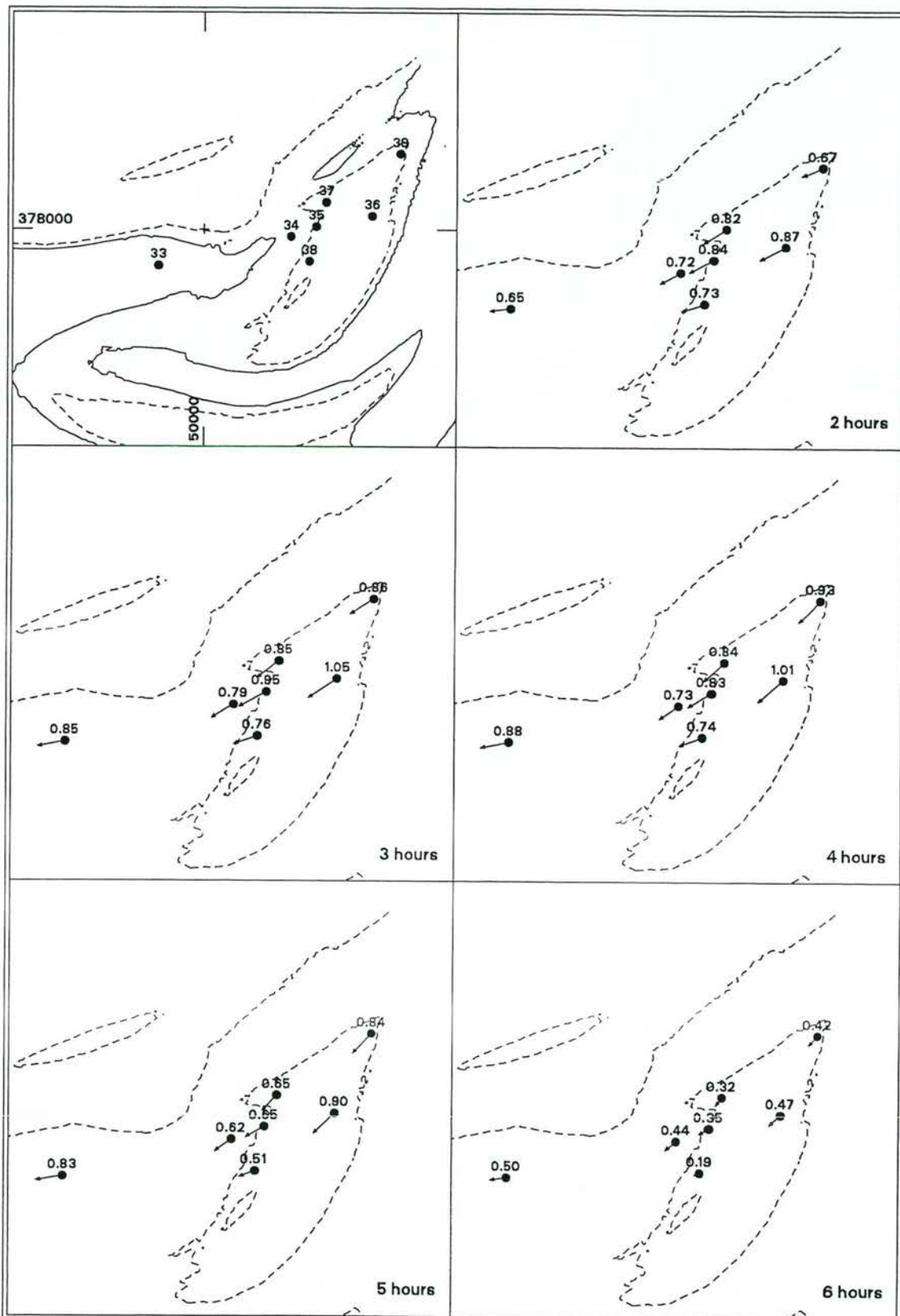


Fig. 4.49 Depth-averaged current current patterns in the flood bar channel during ebb and mean tidal conditions in February 1996.



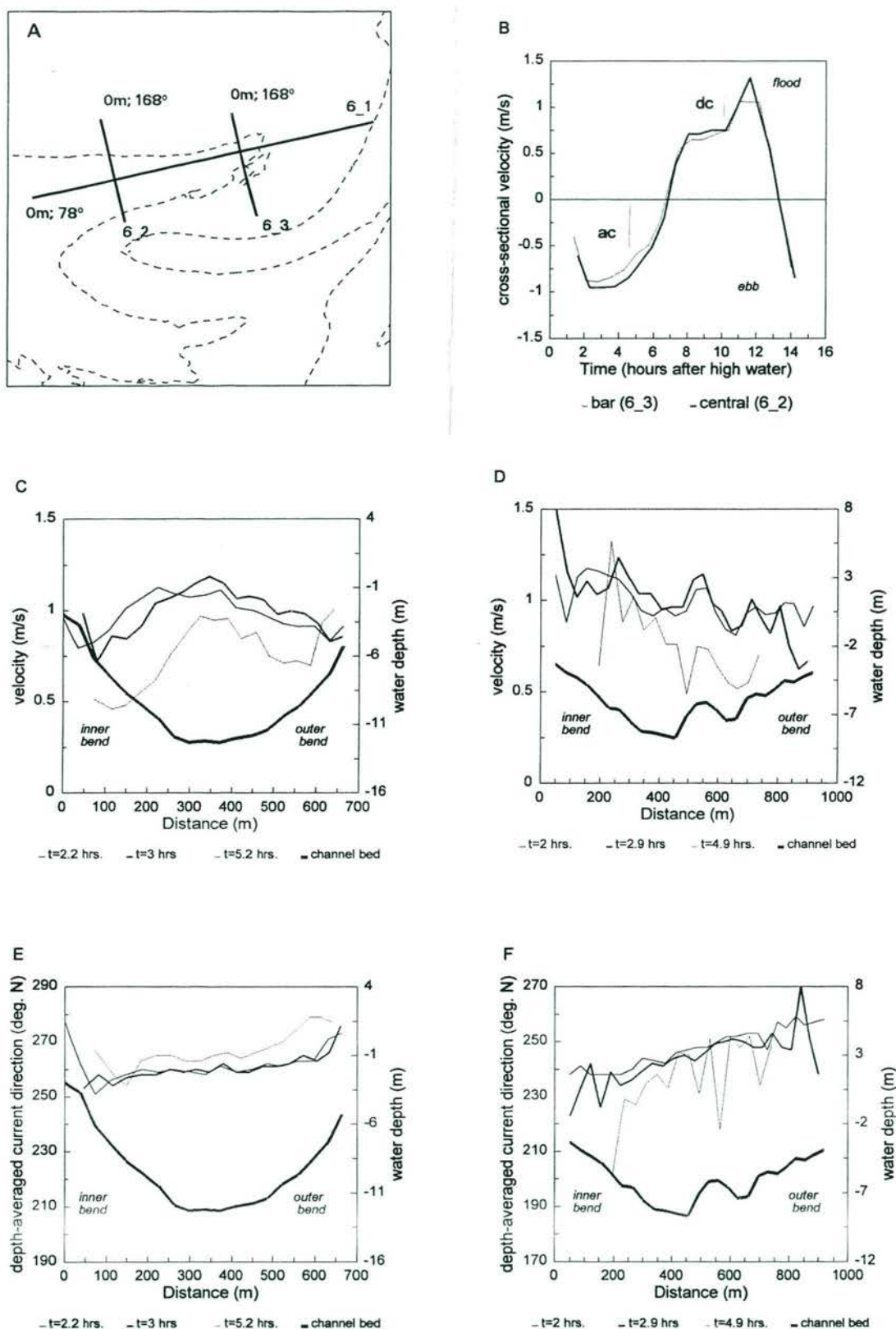


Fig. 4.50 Cross-sectionally averaged and depth-averaged currents in the flood bar channel along transect 6_2 and 6_3 during ebb. a) locations and orientations of ADCP-transects, b) time-series of the cross-sectionally averaged currents, c) magnitude of depth-averaged current vectors along transect 6_2. d) direction of depth-averaged current vectors along transect 6_2. e) magnitude of depth-averaged current vectors along transect 6_3. f) direction of depth-averaged current vectors along transect 6_3.

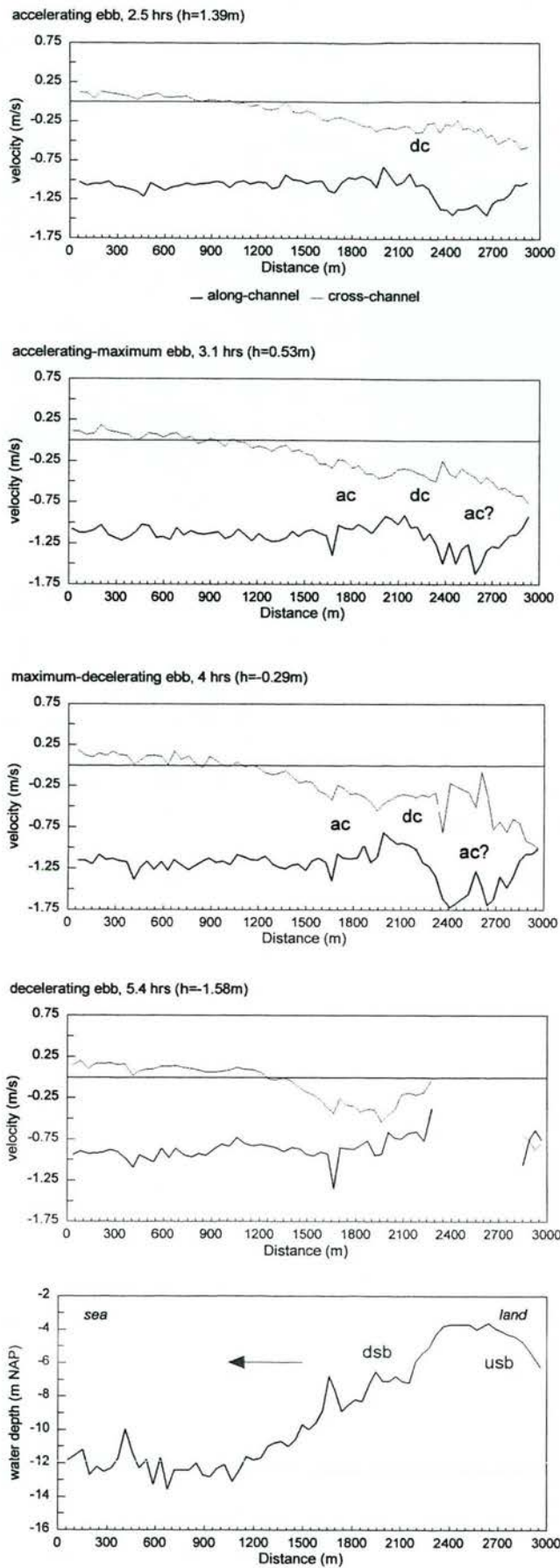


Fig. 4.51 Depth-averaged along-channel and cross-channel velocity patterns over the bar of the bar channel during ebb (transect 6_1), ac= acceleration of the flow, dc=deceleration of the flow, dsb=downstream side of the bar, usb=ustream side of the bar. Negative along-channel component is ebb, positive component is flood.

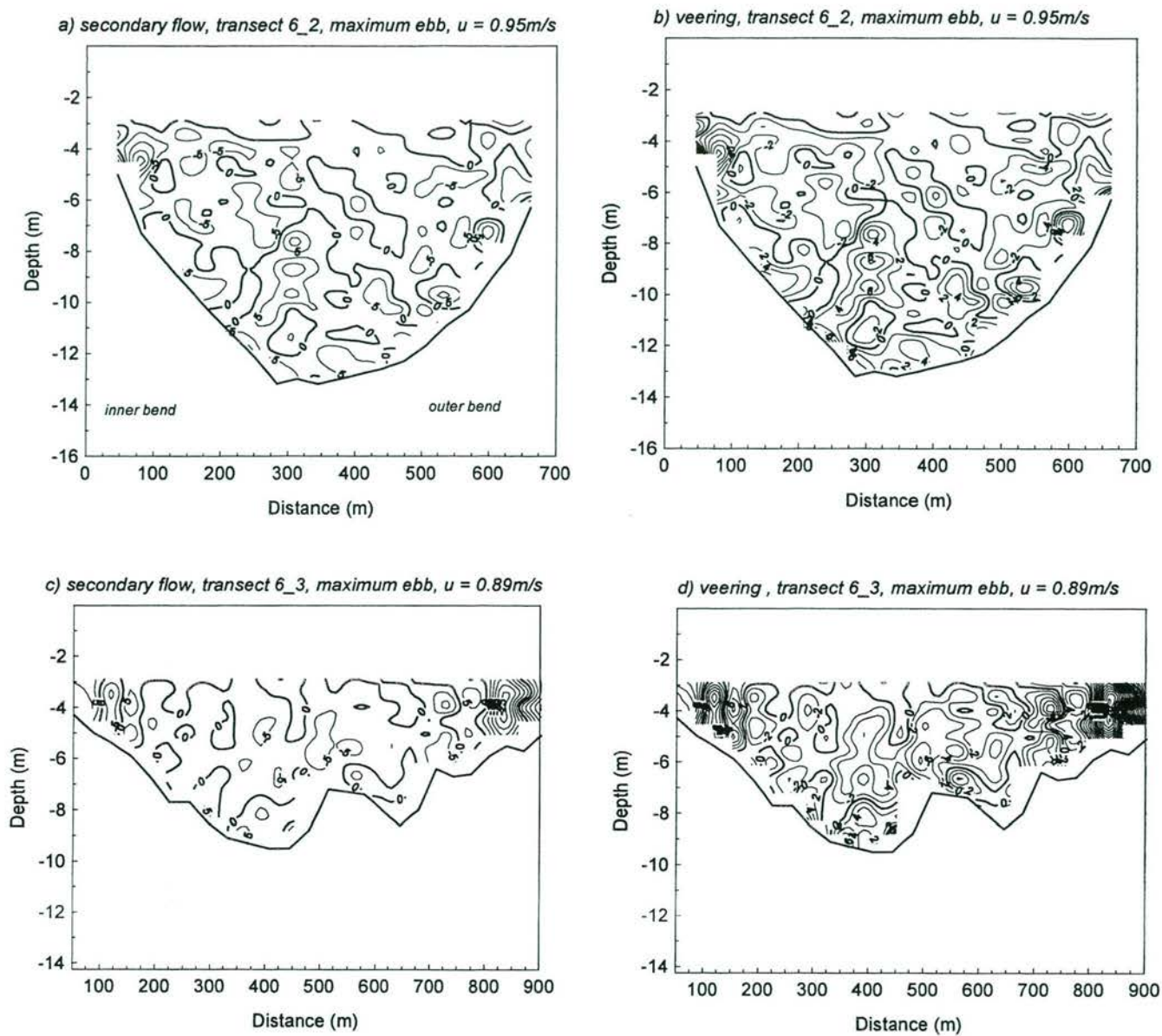


Fig. 4.52 Countour plots of the relative magnitude of the secondary flow (in %) and current veering in the central part of the flood bar channel (transect 6_2, Fig. 5.4) during maximum ebb flow. a & b) transect 6_2, c & d) transect 6_3.

Fig. 4.53 Depth-averaged current current patterns in the flood bar channel during flood and mean tidal conditions

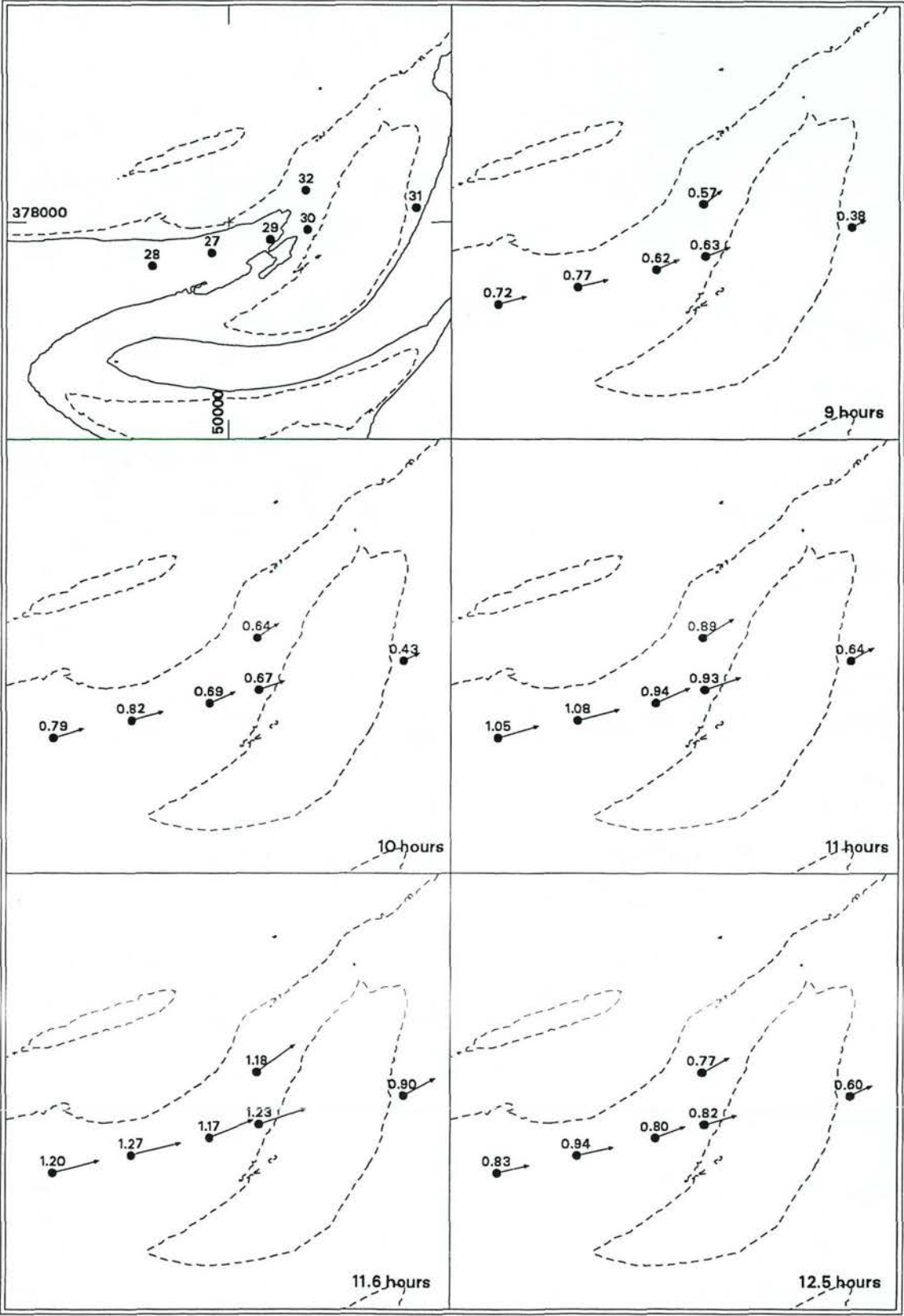


Fig. 4.54 Depth-averaged current current patterns in the flood bar channel during flood and mean tidal conditions in February 1996.



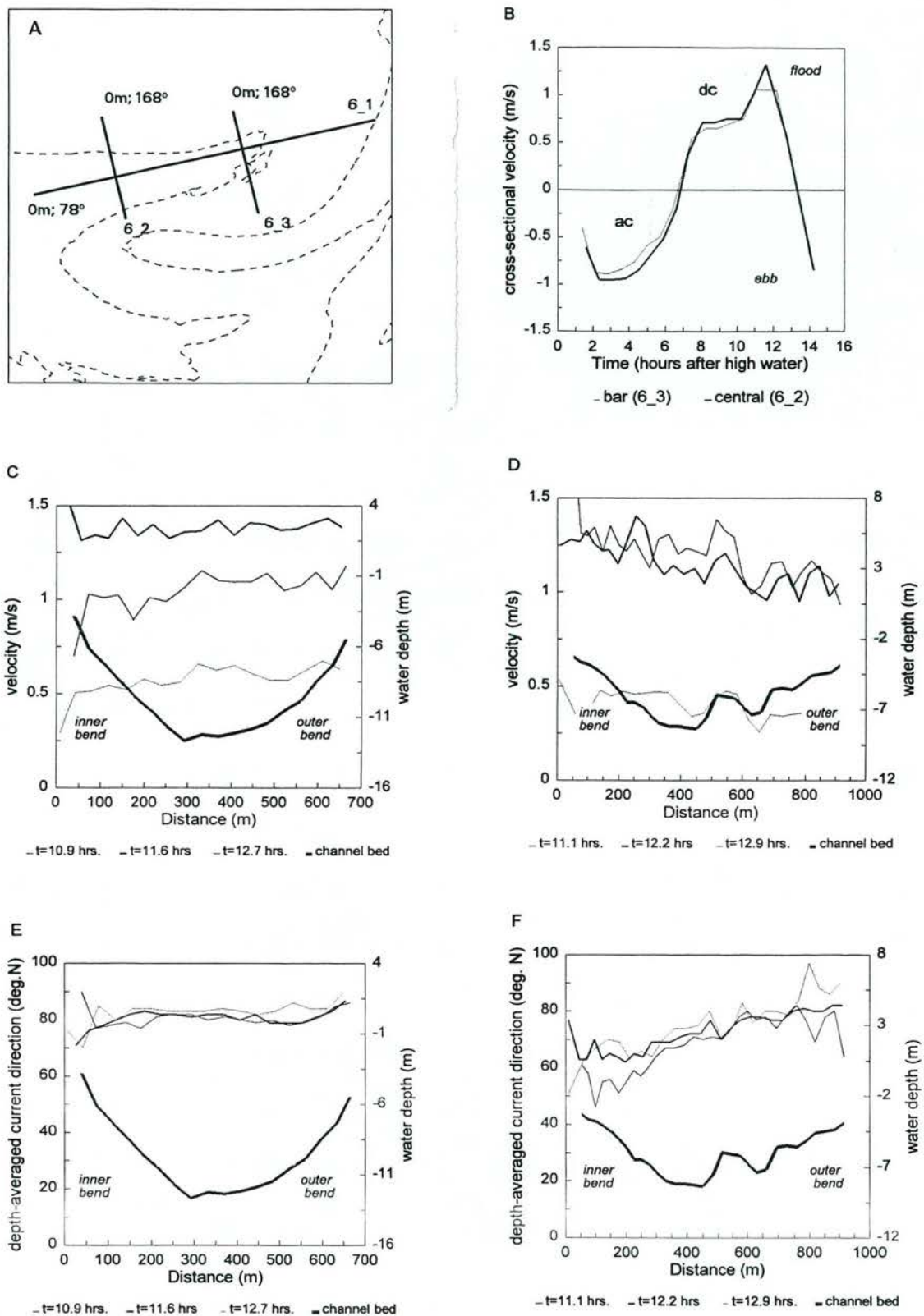


Fig. 4.55 Cross-sectionally averaged and depth-averaged currents in the flood bar channel along transect 6_2 and 6_3 during flood. a) locations and orientations of ADCP-transects, b) time-series of the cross-sectionally averaged currents, c) magnitude of depth-averaged current vectors along transect 6_2. d) direction of depth-averaged current vectors along transect 6_2. e) magnitude of depth-averaged current vectors along transect 6_3. f) direction of depth-averaged current vectors along transect 6_3.

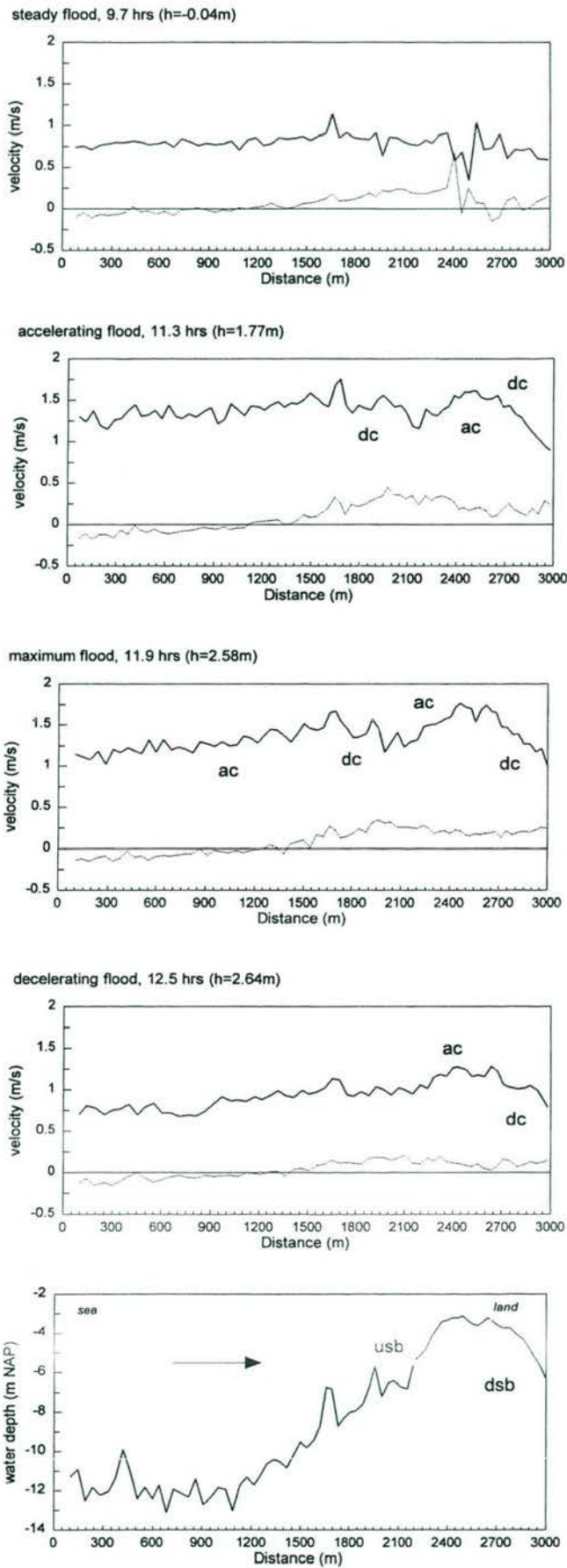


Fig. 4.56 Depth-averaged along-channel and cross-channel velocity patterns over the bar of the bar channel during flood (transect 6_1), ac= acceleration of the flow, dc=deceleration of the flow, dsb=downstream side of the bar, usb=ustream side of the bar. Negative along-channel component is ebb, positive component is flood.

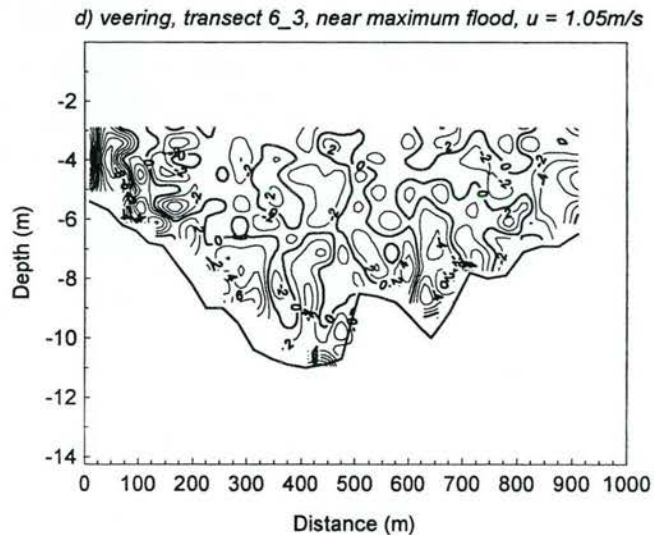
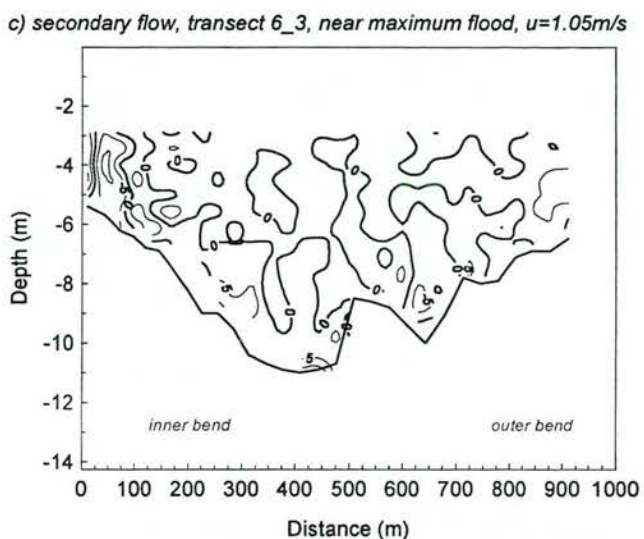
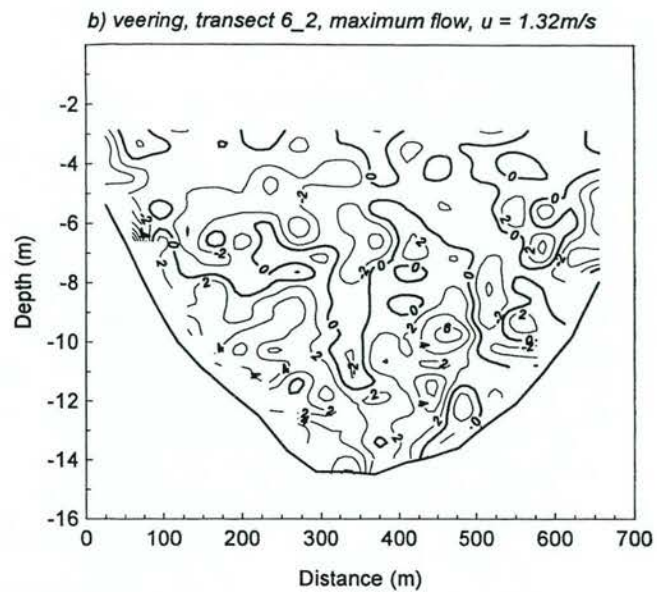
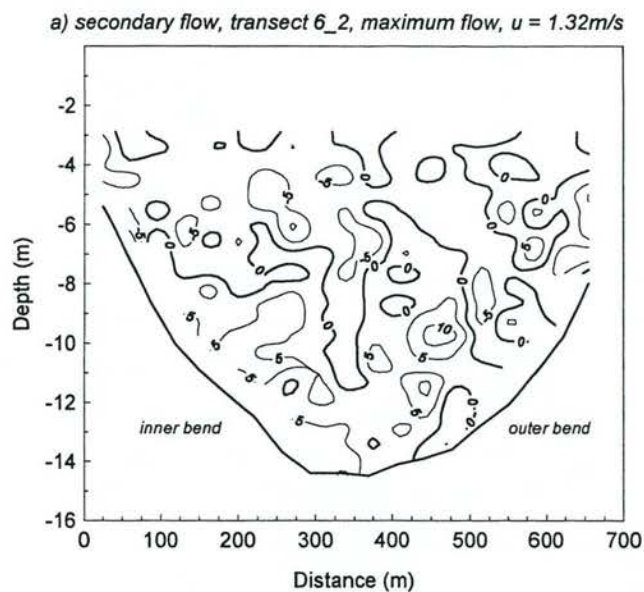
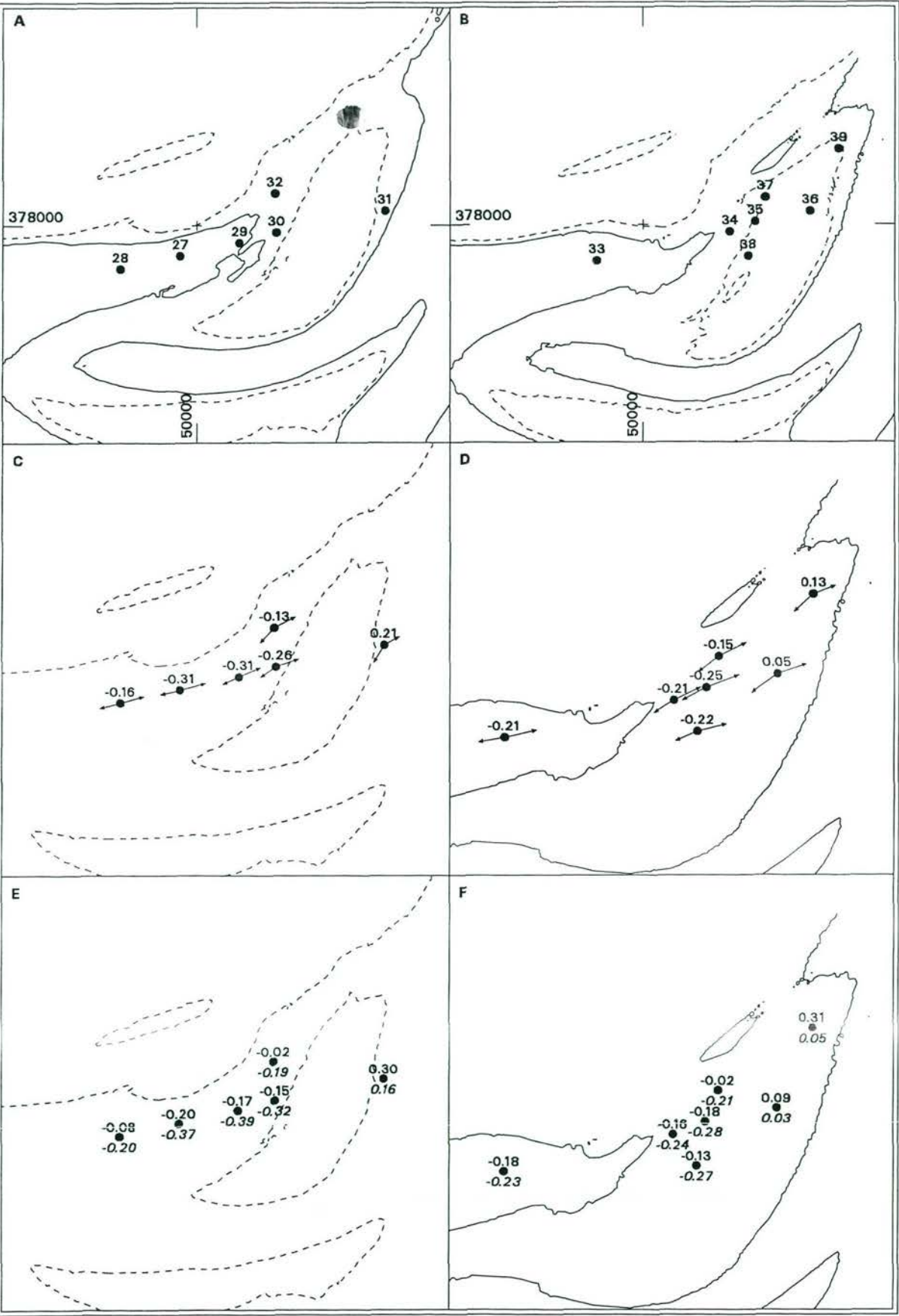


Fig. 4.57 Countour plots of the relative magnitude of the secondary flow (in %) and current veering in the central part of the flood bar channel (transect 6_2, Fig. 5.4) near maximum flood flow. a & b) transect 6_2, c & d) transect 6_3.

Fig. 4.58 Current asymmetry in the bar channel channel . a & b) measurement locations, c & d) significant current vector and asymmetry ratio's during mean tide, e & f) asymmetry ratio's for neap and spring tide



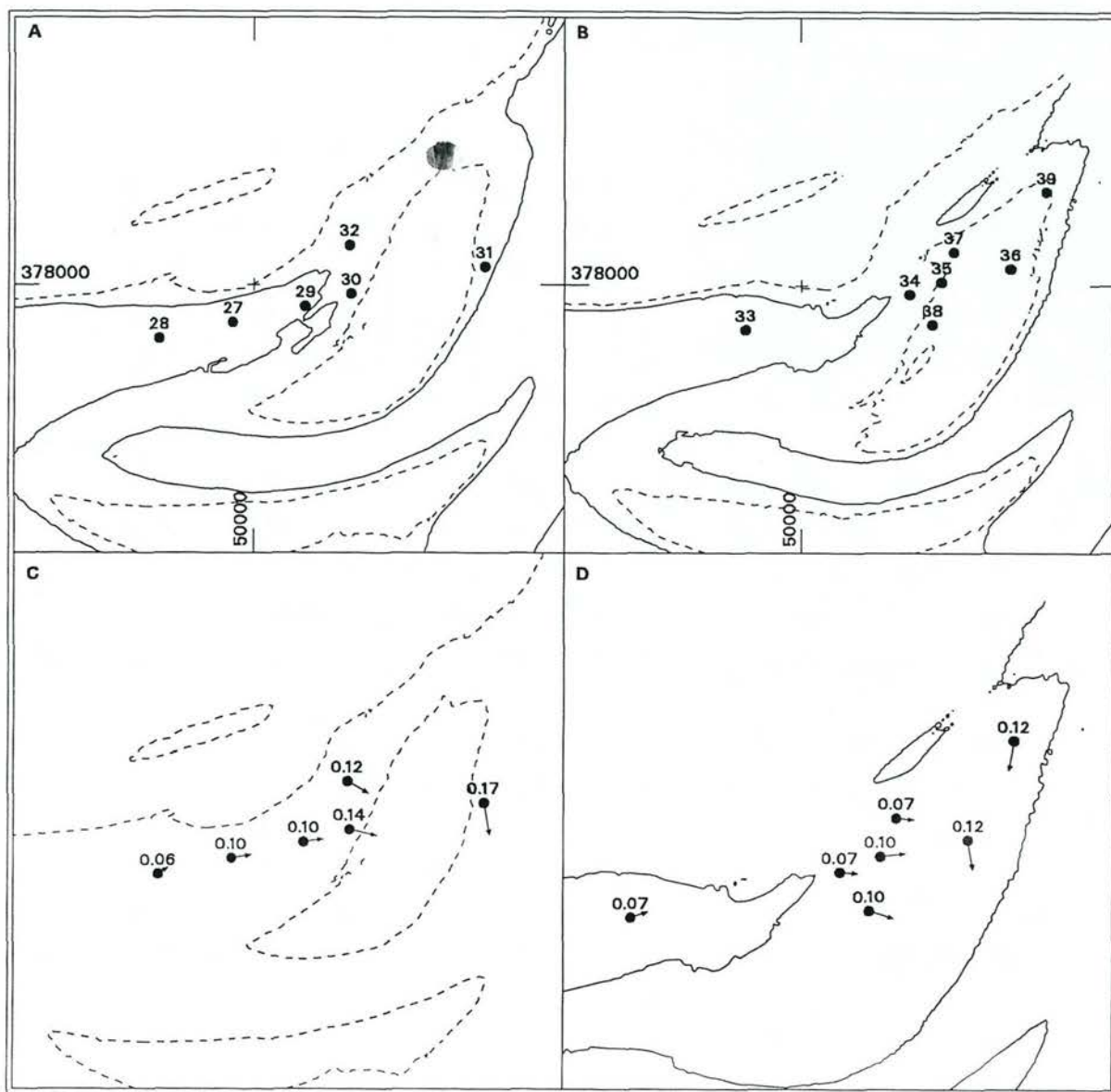


Fig. 4.59 Residual current vectors in the flood bar channel in August 1995 and February 1996. a & b) measurement locations, c & d) long-term mean residual current vectors.

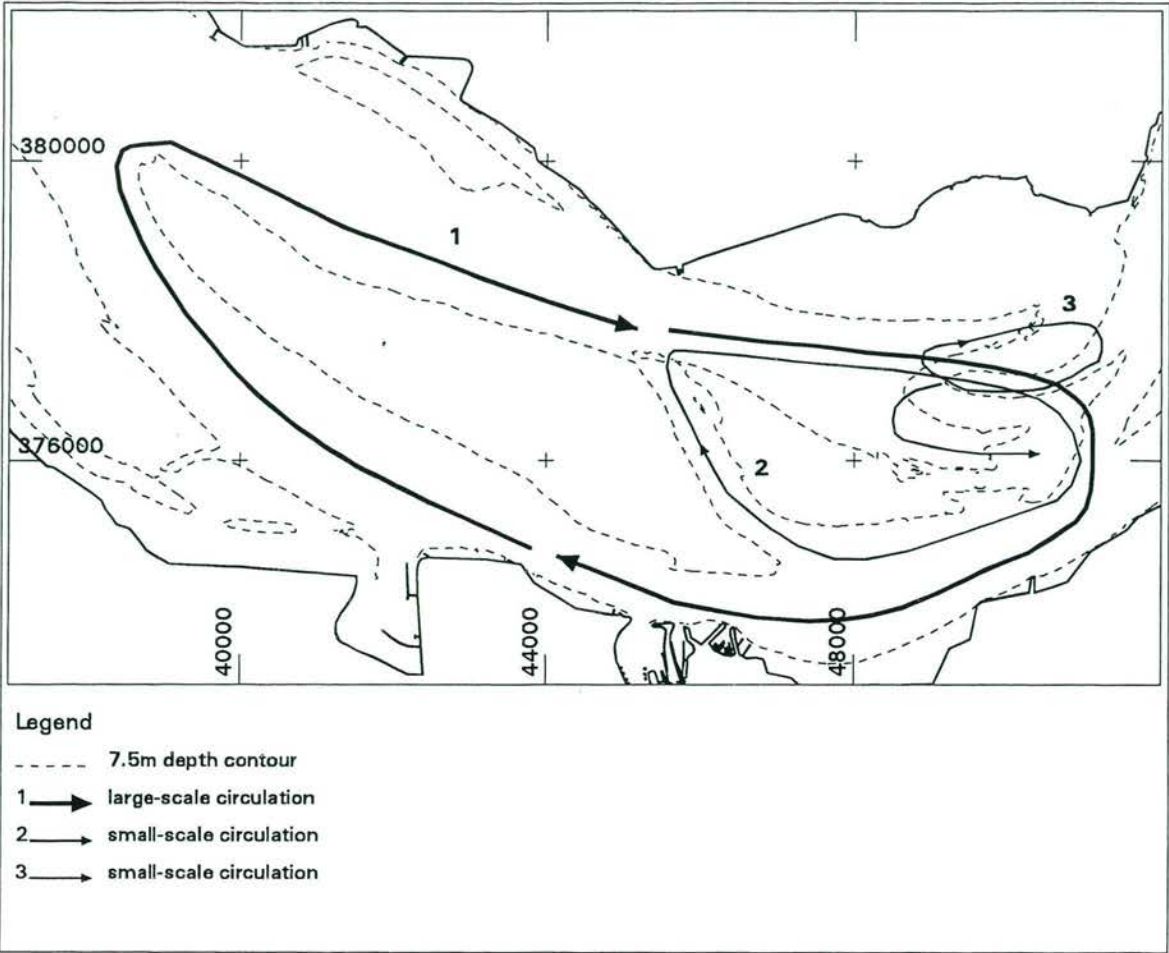


Fig. 4.60 Large and small-scale circulations of flow in the study area.

Table 3.1 Budget changes (in Mm³) in the Terneuzen and Hansweert section between 1955 and 1996

Section	Channel erosion	deposition	Shoal erosion	deposition	Total net erosion/deposition erosion	deposition	Dredging/dumping dredging	dumping	Total 'natural' erosion/deposition erosion	deposition
FC1	22		2		24			20	44	
EC1	7			3	4		18			14
CC	5		1		6		6		-	
Terneuzen section	34		-	-	34		4		30	
FC2	33			4	29			31	60	
EC2		66		2		68	8			6
Hansweert section		33		6		39		23		16

Table 3.2 Budget changes (in Mm³) in the Terneuzen section between 1955 and 1996

Section	Channel erosion	deposition	Shoal erosion	deposition	Total net erosion/deposition erosion	deposition	Dredging/dumping dredging	dumping	Total 'natural' erosion/deposition erosion	deposition
1		1.7		0.2		1.9		12.6	10.7	
2	5.7			0.8	4.9			0.4	5.3	
3	15.7		0.5		15.2			0.2	15.4	
4	4.2		2.6		6.8			6.6	13.4	
5	9.1		-	-	9.1		9.5			0.4
6	1.5			0.8	0.7		1.4			0.7
7		1.4		2.0		3.4	1.2			4.6
8		2.1	-	-		2.1	2.0			4.1
9	1.4		-	-	1.4		3.4			2
A		3.1		2.8		5.9	-	-		5.9

Table 3.3 Budget changes (in Mm³) in the Hansweert section between 1955 and 1996

Section	Channel erosion	deposition	Shoal erosion	deposition	Total net erosion/deposition erosion	deposition	Dredging/dumping dredging	dumping	Total 'natural' erosion/deposition erosion	deposition
11		17.4	1.3			16.1	2.3			18.4
12		12.3		2.7		15	0.4			15.4
13		14.5		0.3		14.8	3.2			18
14		22	-	-		22	1.7			23.7
15	3.5		-	-	3.5			23.4	26.9	
16	6.7			3.3	3.4			17.3	20.7	
17	23			1.3	21.7		9.6		13.4	

Table 4.1 Hydrodynamic and meteorological conditions during the discharge measurements

transect	date	Hydrodynamic conditions						Meteorological conditions	
		Tide						wind	
		high water (m NAP)	low water (m NAP)	tidal fall (m)	low water (m NAP)	high water (m NAP)	tidal rise (m)	velocity (m/s)	direction
1	940411	2.41	-2.16	4.57	-2.43	2.41	4.84	5-10	NW
2	940920	2.62	-2.44	5.06	-2.12	2.62	4.74	4-8	NE
3	940408	2.3	-2.12	4.42	-2	2.3	4.3	4-10	WSW-S
4	930903	2.8	-1.77	4.57	-1.91	2.8	4.71	6-10	NW
5	950629	2.38	-1.98	4.36	-1.98	2.39	4.37	4	NE
6	950830	2.82	-2.01	4.83	-2.01	2.65	4.66	3-6	N

Table 4.2 Accuracy of water level measurements

Location	instrumental accuracy (m) (0.35%/ (120) ^{0.5})	accuracy NAP level (m)	variation density (m) (1019+- 2kg/m ³)	minimum accuracy water level (m)
1	0.002	0.007	0.015	0.02
2	0.002	0.028	0.015	0.03
3	0.002	0.013	0.015	0.02
4	0.002	0.014	0.015	0.02

Accuracy of falls
section stations total accuracy (m)

1	1,3	0.04
2	3,2	0.05
3	1,4	0.04
4	4,2	0.05
5	3,4	0.04
6	1,2	0.04

Table 4.3 System configuration of the ADCP during the two surveys

location	ebb bar channel	flood bar channel
Acoustic frequency	600kHz	600kHz
Pings per ensemble	5	20
Ship speed	4m/s	4m/s
Horizontal sampling interval	15m	33m
Vertical bin size	0.5m	0.5m
Pulse length	0.5m	0.5m
Depth range	1.74-20m	1.85-20m
Velocity precision	0.06m/s	0.03m/s
Compass precision	1 degree	1 degree
Navigation	GPS	GPS

The first two bins were unreliable for an unknown reason. As a result the depth range amounted 2.74-20m and 2.85-20m in practice.

Table 4.4 Configuration and summary of the sampling procedures of the EMF-frame

Sensor	Parameter	Height above bed (m)	Sampling interval (min)	Sampling duration (min)	Sampling frequency
EMF1	current velocity (u,v)	0.28	15	5	2 Hz
EMF2	current velocity (u,v)	0.5	15	5	2 Hz
EMF3	current velocity (u,v)	1	15	5	2 Hz
EMF4	current velocity (u,v)	1.5	15	5	2 Hz
EMF5	current velocity (u,v)	2	15	5	2 Hz
EMF6	current velocity (u,v)	2.5	15	5	2 Hz
Pressure s.	water level	3.04	15	5	2 Hz
Compass	angle (hor)	?	15	5	2 Hz
Tilt	angle (ver)	?	15	5	2 Hz

Table 4.5 Current veering in the cross channel based on significant current vectors at 'Flachsee' locations 11 and 13 during ebb

Conditions	current vector at location 11		current vector at location 13	
	magnitude	direction	magnitude	direction
long-term mean values				
near-bed	0.78	295	0.78	339
depth-averaged	0.9	295		
near-surface	1.02	289	1.04	323
velocity difference & veering	0.24	-6	0.26	-16
neap tide				
near-bed	0.7	296	0.71	340
depth-averaged	0.82	295		
near-surface	0.94	288	0.94	322
velocity difference & veering	0.24	-8	0.23	-18
spring tide				
near-bed	0.87	295	0.89	337
depth-averaged	1.01	295		
near-surface	1.13	289	1.19	323
velocity difference & veering	0.26	-6	0.3	-14
local orientation of channel axis		300		325

Table 4.6 Overview of the conditions and observations during the near-bed current measurements in the channel bend of the cross channel

LOCATION	1	2	3	4	5				
HYDRODYNAMIC & MORPHOLOGIC CONDITIONS									
date (Julian days)	941108 (312)	941102 (306)	941103 (307)	941104 (308)	941107 (311)				
tidal decline (m)	4.61	5.03	5.09	5.3	4.94				
wind									
velocity (m/s)	3	3	5	4.7	1.4				
direction (deg.)	148 (SE)	200-100 (S-E)	123 (SE)	128 (SE)	134 (SE)				
water depth (NAP-m)	9.5	8.5	8.6	9.4	9.6				
channel slope (deg.)	2.5	3.6	3.9	3.6	1.6				
channel axis orientation	334	329	311	304	304				
bedforms									
length (m)	50	?	?	?	-				
height (m)	1	?	?	?	-				
location frame	top	?	top	?	-				
CURRENT OBSERVATIONS									
	velocity	direction	velocity	direction	velocity	direction	velocity	direction	velocity
accelerating ebb									
(2-3 hours after hw)									
2 m.a.b.	0.49	328	0.39	232	0.39	247	0.46	317	0.46
1.5 m.a.b	0.54	332	0.45	294	0.48	278	0.58	280	0.57
1 m.a.b.	0.57	328	0.42	312	0.41	241	0.51	312	0.51
0.28 m.a.b.	0.45	328	0.39	308	0.38	242	0.45	316	0.42
maximum ebb									
(3.5-4.5 hours after hw)									
2 m.a.b.	0.88	328	0.66	309	0.71	310	0.86	302	0.77
1.5 m.a.b	0.95	330	0.74	301	0.82	295	0.99	290	0.85
1 m.a.b.	0.98	329	0.74	305	0.77	310	0.92	303	0.85
0.28 m.a.b.	0.76	328	0.71	306	0.7	311	0.79	305	0.73
decelerating ebb									
(5-6 hours after hw)									
2 m.a.b.	0.49	331	0.42	313	0.55	302	0.7	297	0.59
1.5 m.a.b	0.56	328	0.48	298	0.64	300	0.76	294	0.67
1 m.a.b.	0.55	332	0.44	308	0.66	305	0.76	300	0.68
0.28 m.a.b.	0.34	331	0.41	308	0.58	307	0.64	301	0.57
depth-averaged velocity (elmar)									
accelerating ebb	0.6	321	0.64	311	0.61	283	0.75	285	0.65
maximum ebb	1.04	328	0.89	325	0.86	303	1.05	295	0.94
decelerating ebb	0.62	325	0.49	325	0.58	318	0.83	302	0.76
long-term current observations									
significant velocity vectors									
11 (near-surface)	0.8	296	0.93	295	0.88	296	0.91	296	0.87
11 (near-bed)	1.06	288	1.15	290	1.11	291	1.16	289	1.12
13 (near-surface)	0.88	339	0.91	338	0.89	338	0.94	339	0.86
13 (near-bed)	1.11	322	1.25	324	1.22	324	1.27	323	1.14
vertical current veering									
11		8		5		5		7	
13		17		14		14		16	

Table 4.7 Current veering in the cross channel based on significant current vectors at 'Flachsee' locations 11 and 13 during flood

Conditions	current vector at location 11		current vector at location 13	
	magnitude	direction	magnitude	direction
long-term mean values				
near-bed	0.5	114	0.36	151
depth-averaged	0.57	117		
near-surface	0.58	113	0.4	152
velocity difference & veering	0.08	-1	0.04	1
neap tide				
near-bed				
depth-averaged	0.46	115	0.34	152
near-surface	0.53	117		
velocity difference & veering	0.53	113	0.37	152
	0.07	-2	0.03	0
spring tide				
near-bed				
depth-averaged	0.54	113	0.38	150
near-surface	0.62	117		
velocity difference & veering	0.66	112	0.45	153
	0.12	-1	0.07	3
local orientation of channel axis	120		145	

Table 4.8 measured and computed maximum secondary flow

tidal phase	time (hours after high water)	water depth		curvature (m)	depth-averaged velocity (m/s)		intensity of secondary circulation (m/s)			
		maximum	mean		maximum	mean	maximum value		mean value	
							measured	computed	measured	computed
accelerating ebb	1.8	11.5	12.4	1450	0.78	0.8	0.09	0.09	0.06	0.09
accelerating ebb	2.3	12.5	12.1	1450	1.18	1.13	0.15	0.14	0.13	0.13
accelerating ebb	3.7	11.9	11	1450	1.35	1.28	0.17	0.15	0.11	0.13
maximum ebb	4.2	11.4	10.2	1450	1.35	1.25	0.23	0.14	0.13	0.12
decelerating ebb	4.9	10.8	10.1	1450	1.28	1.2	0.14	0.13	0.11	0.11
decelerating ebb	5.5	10	9.6	1450	1.07	1.04	0.1	0.1	0.04	0.09
steady flood	9	11	10.4	2000	0.8	0.75	0.07	0.06	0.05	0.06
steady flood	9.8	10.5	10.7	2000	0.7	0.78	0.09	0.05	0.06	0.06
steady flood	10.4	12.1	11.2	2000	0.86	0.84	0.07	0.07	0.04	0.07
accelerating flood	11	10.5	11.7	2000	0.9	1	0.09	0.07	0.06	0.08
maximum flood	11.5	13.3	12.6	2000	1.4	1.3	0.11	0.13	0.08	0.11
decelerating flood	12.2	13.8	13.1	2000	1.18	1.13	0.14	0.11	0.09	0.1

maximum values refer to the velocity profile with maximum secondary flow

mean values refer to the average of the velocity profiles between 200 and 400m along the transect

Appendix 3.0 Computation of the average cross-sectional area and hydraulic radius

The computation of the hydraulic radius and cross-sectional area of a channel section (not a transect) uses a hypsometric curve and the length of the channel section as input. The computation method assumes a symmetric channel shape. This is not always a realistic assumption.

The following conventions are applied:

- i = height index i from the channel bed (0=deepest point of the channel);
- i_b = height index where a vertical section starts (the base of a section);
- n = index of vertical section ($n=1 \dots N$);
- N = number of vertical sections in a cross sectional profile;
- d = depth with respect to NAP [m];
- W = mean width of the channel [m];
- L = channel (section) length [m];
- WS = wetted surface area in the horizontal plane [m²];
- P = wetted perimeter at height z [m];
- A = wetted cross sectional surface area [m²]
- R = hydraulic radius [m];

First, the vertical distribution of surface area and water volume (i.e. the hypsometric curve) is used to compute the changes in the average channel width as a function of channel depth (with respect to NAP):

$$W(d) = \frac{WS(d)}{L} \quad 3.1$$

A result of such a computation is depicted in Figure 3.1. Based on a fixed depth interval and the changes in mean channel width, the surface area described by $W(d)$ in Figure 3.1 is divided in vertical sections. The width of each vertical section n depends on the chosen depth interval and the mean bottom gradient between subsequent height indices.

For each vertical section n the wetted perimeter at height index i is approximated as (Fig. 3.1).

$$P_n(i) = 2\sqrt{\frac{((W_n(i_b+1) - W_n(i_b))^2}{4} + (d_n(i_b+1) - d_n(i))^2} \quad 3.2$$

The total mean wetted perimeter below height index i is

$$P(i) = \sum_{n=1}^N \Delta P_n(i) \quad 3.3$$

The cross-sectional area of a vertical section below height index i is defined as:

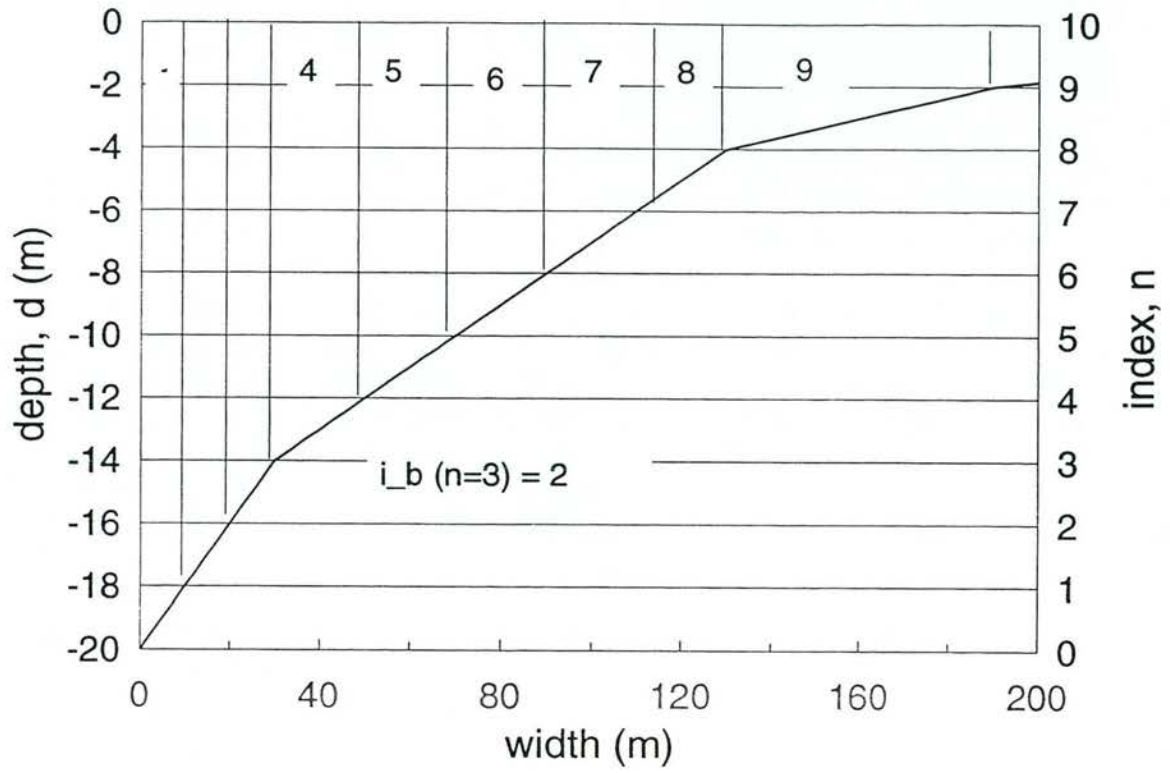
$$A_n(i) = [(B_n(i_b+1) - B(i_b)) * ((d_n(i_b+1) - d_n(i_b))/2)] * [i - i_b + (i+n)] \quad 3.4$$

The total mean wetted cross-section below height index i is

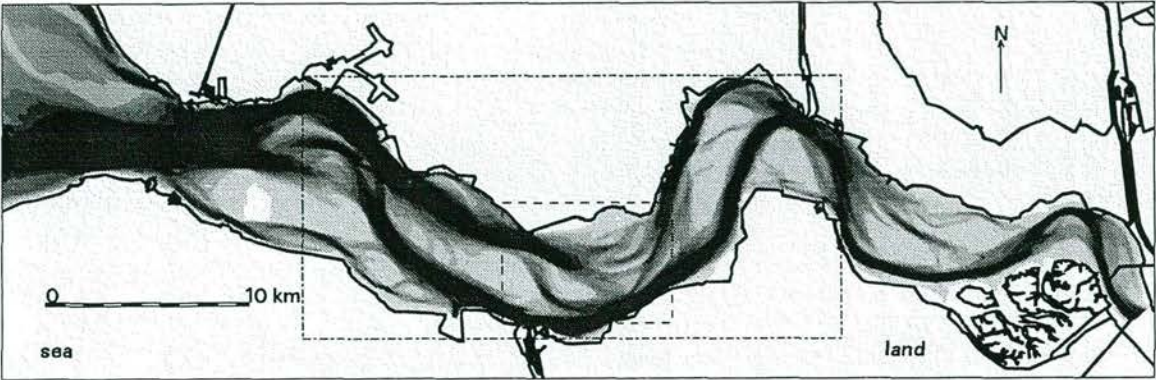
$$A(i) = \sum_{n=1}^N \Delta A_n(i) \quad 3.5$$

Finally, the average hydraulic radius of the channel section below height index i is defined as:

$$R(i) = \frac{A(i)}{P(i)} \quad 3.6$$












ENCLOSURE 1

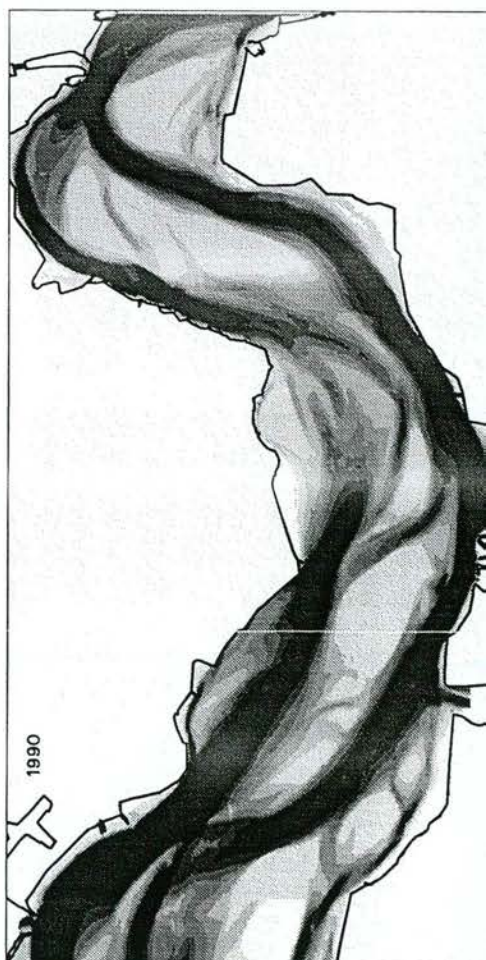
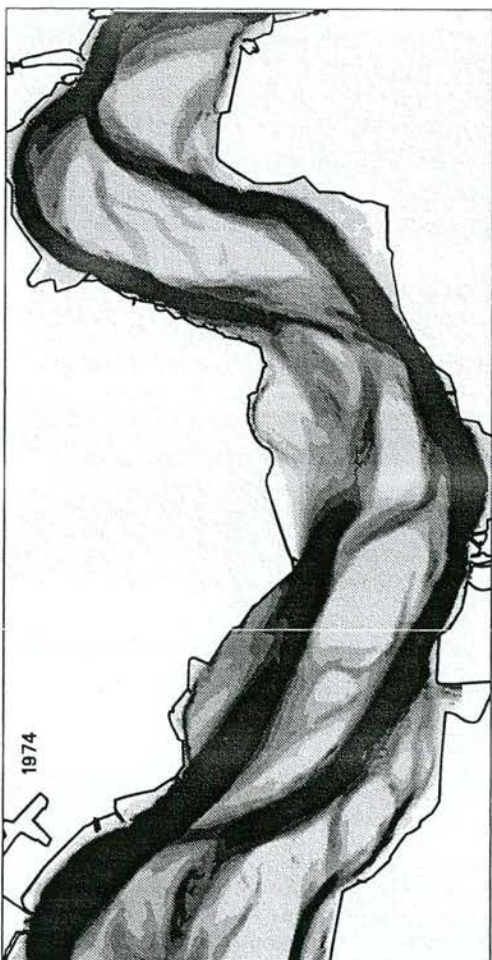
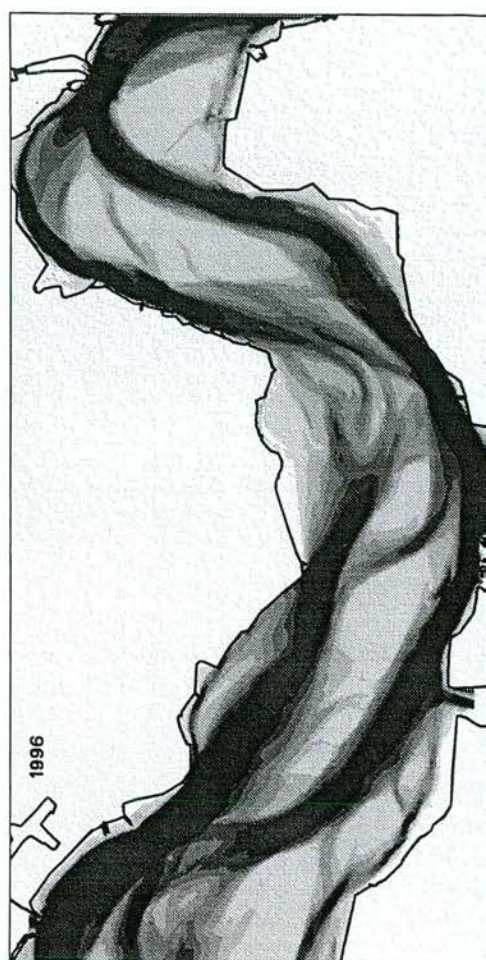
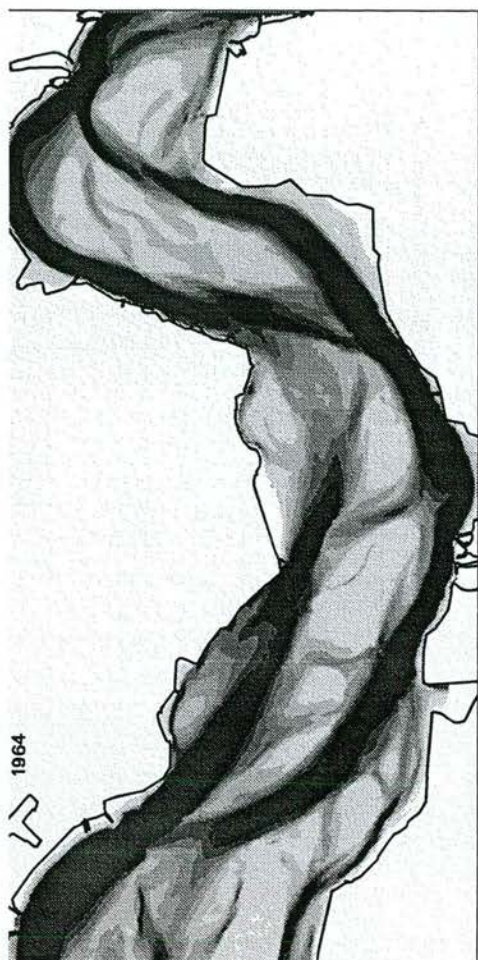


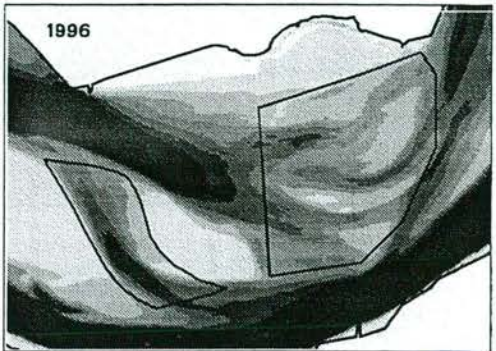
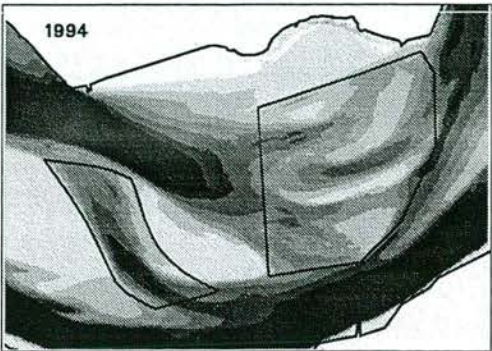
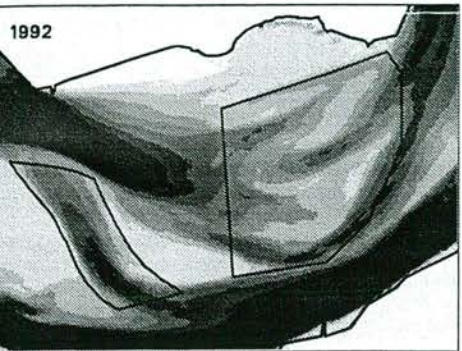
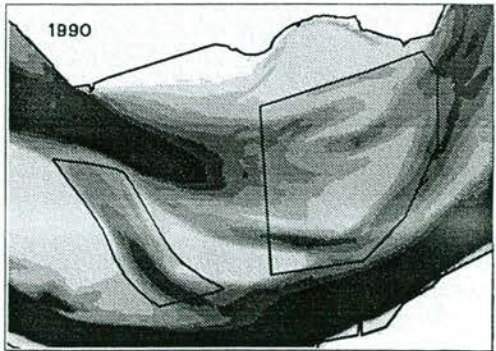
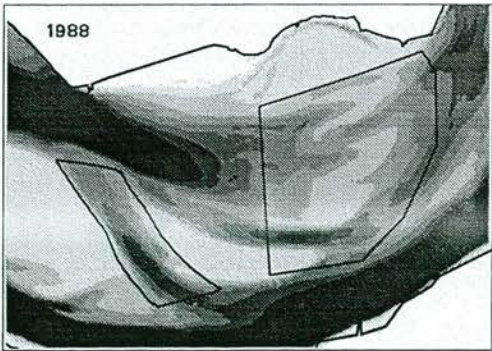
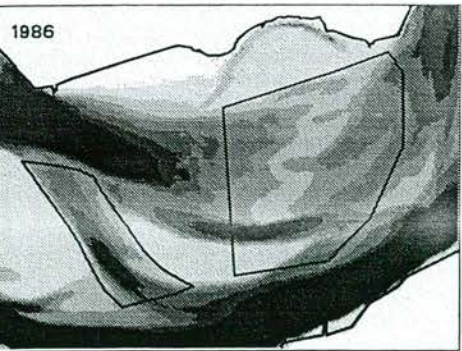
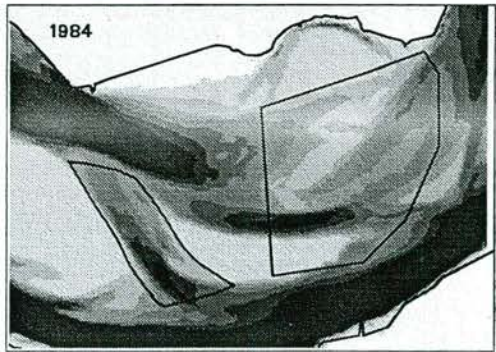
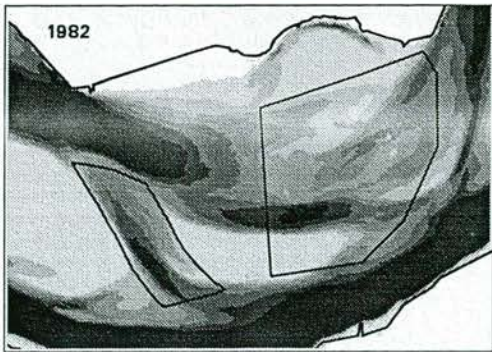
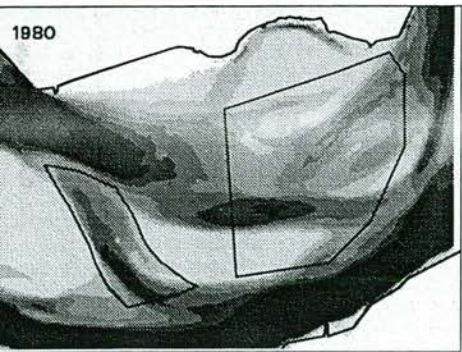
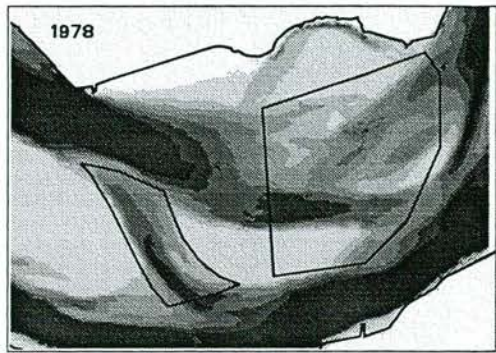
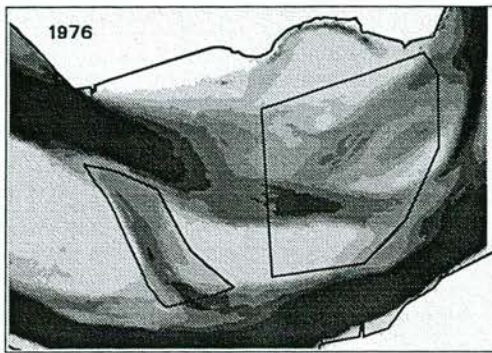
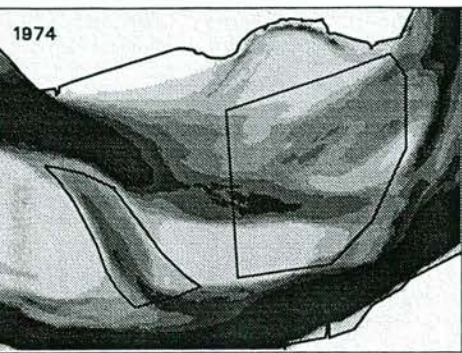
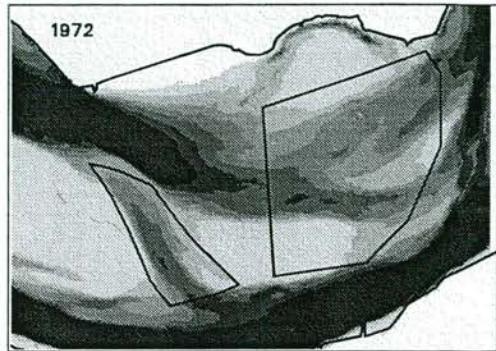
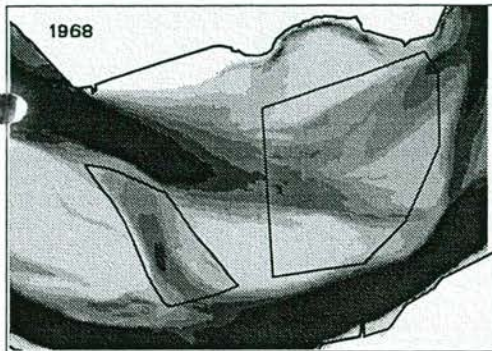
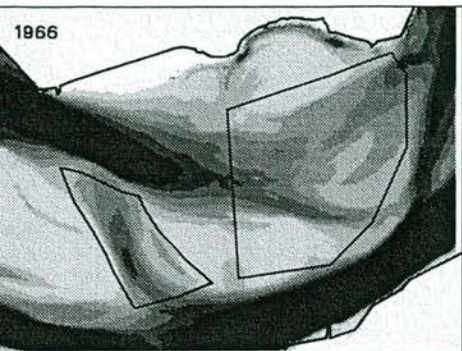
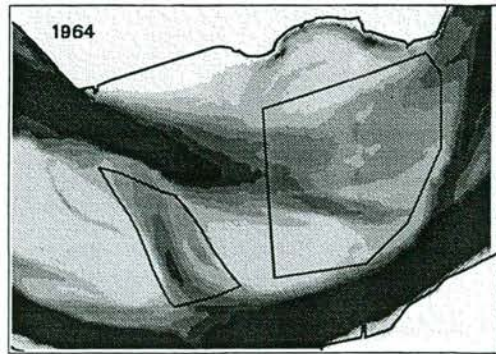
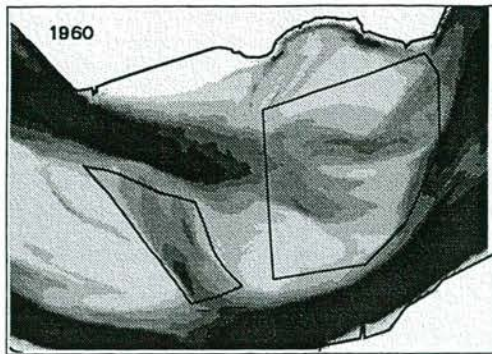
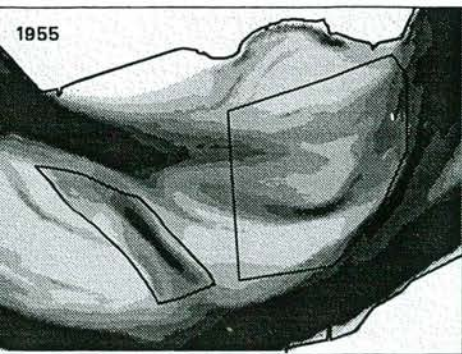
LEGEND

Depth (in meters below NAP)

-  > 15
-  12.5 - 15
-  10 - 12.5
-  7.5 - 10
-  5.0 - 7.5
-  2.0 - 5.0
-  < 2.0

-  Area enclosure 2
-  Area enclosure 3





Hydrodynamics of a bar in a flood channel - the
Westerschelde estuary

Claire Jeuken

Paper presented at the 25th International
Conference on Coastal Engineering, Orlando 1996

Hydrodynamics of a bar in a flood channel - the Westerschelde estuary

Claire Jeuken¹

Abstract

Several long-term current meter observations (30 days) over a complex flood shield, i.e. an estuarine bar, display major temporal and spatial variations in current asymmetry. The variations in current asymmetry indicate the presence of small-scale circulations of sediment that are induced by smaller channels that penetrate the bar. The current meter observations and depth-averaged current patterns obtained with an ADCP revealed processes of advective flow acceleration and deceleration, as well as flow convergence and divergence, over the bars in the small channels.

Introduction

Estuaries are important coastal systems, providing natural navigation channels as well as habitats for marine flora and fauna, and recreational space. The Westerschelde forms the seaward, marine part (length 60 km) of the Schelde estuary (total length 160 km) and has a well-developed system of channels and intertidal shoals (Fig. 1a). The meandering ebb channels form the main navigation channel for ocean shipping to the harbours of Antwerpen and Gent. The shorter, straight flood channels are only suitable for small ships as the landward channel-margin of the flood channels is marked by a shallow extensive bar. Moreover, the bars in the flood channels display a complex topography due the presence of migrating connecting channels, the smaller channels that penetrate the bar and connect the main ebb and flood channel. To maintain the shipping lane dredging is carried out at the deeper bars in the main ebb channels. At present approximately $8 \cdot 10^6 \text{ m}^3$ of sediment is dredged annually. A further deepening of the bars, to enable the passage of larger ships, is planned for the near future. A better understanding of the morphodynamics of channels and shoals and the processes over bars in tidal channels in particular, is important for the management of the estuarine system and for determining the optimal dredging strategies. Recent developments in understanding the morphodynamics of channels and shoals have resulted in the formulation of different types of models (De Vriend (1996), De Vriend and Ribberink (1996)). Bars in tidal channels are however still understudied (Dalrymple and Rhodes, 1995 for a review).

¹ Institute for Marine and Atmospheric Research, Utrecht University, Department of Physical Geography, PO box 80.115, 3508 TC, Utrecht, The Netherlands.
c/o Ministry of Transport and Public Works, Directorate Zeeland PO box 5014, 4330 KA Middelburg, The Netherlands.

This paper discusses the hydrodynamics of a complex bar at the end of a main flood channel, based on field observations. Flow computations with a 1D-network model indicate that this bar largely determines the distribution of tidal flow between the main ebb and flood channels during the periods of maximum flow (Jeuken, submitted). Objective of this study is to identify spatial and temporal variations of the tidal flow that are important for bar morphology and sediment transport patterns over the bar. Herein two aspects of tidal flow are considered: 1) Spatial velocity gradients and 2) differences between the velocity during ebb and flood, often referred to as current asymmetry. Spatial velocity gradients largely control processes of erosion and sedimentation. In literature tidal current asymmetry is often used as a first indicator for the direction of net sediment transport (e.g. Aubrey, 1986; Dronkers, 1986; Friederichs and Aubrey, 1988; Van de Kreeke and Robaczewska, 1993; Lessa and Masselink, 1995). In most studies current asymmetry is based on the amplitude of velocity components, often derived from a harmonic analysis of the velocity record. In this study a different approach is used to quantify variations in current asymmetry.

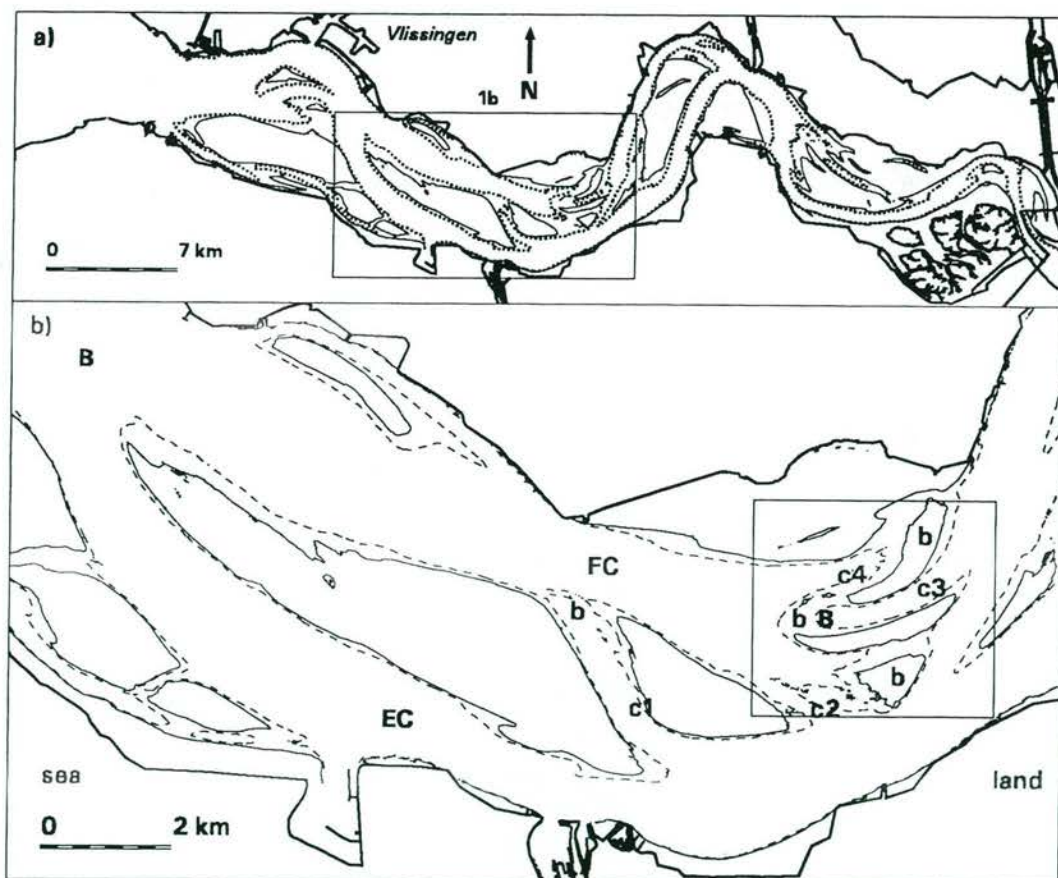


Figure 1 Location and channel configuration in the study area. a) the Westerschelde, b) the main study area. FC= main flood channel, EC=main ebb channel, c#=connecting channel (#=number), B= bar in main channel, b= bar in connecting channel.

The study area

An overview of the general hydraulic and morphologic evolution of the Schelde estuary is given by Van den Berg et.al. (in press). The main characteristics are described in this section. The Schelde is a tide-dominated meso-tidal estuary. The vertical tide displays a general asymmetry characterized by a faster rise than fall. This asymmetry increases in landward direction. In addition the vertical tide shows a pronounced neap-spring tidal variation as do the surface gradients and tidal currents. Maximum depth-averaged current velocities are in the order of 1-1.5m/s.

The larger channels in the Westerschelde display a regular returning pattern consisting of a meander-shaped ebb channel and a straight flood channel, separated by shoals (Fig. 1b). The shoals are bisected by smaller channels. These so called connecting channels form connections between the main ebb and flood channel and owe their existence to water level differences between the channels. Most connecting channels occur in the area of the bar in the main flood channel and tend to display a cyclic behaviour on the timescale of one to several decades. The shallow bar in the main flood channel is marked by various connecting channels, that originated and developed from 1986/1987. The small bars in the connecting channels are superimposed on the large bar in the main flood channel. The connecting channels C3 and C4 together reflect the morphologic characteristics of the main ebb and flood channel with respect to channel alignment and location and depth of the bars. At present (september 1996) channel C3 is rapidly degenerating. A new connecting channel has formed north of connecting channel C4.

Field observations

'Flachsee' impeller-type current meters were deployed at several locations during five measurement campaigns between April 1994 and February 1996 (Fig. 2). The current meters registered current velocity and direction for periods of thirty days with a sampling interval of ten minutes and a sampling period of one minute. At each location two current meters were deployed at the same measurement height, for validation purposes. A comparison of the double current meter deployments revealed an average difference in speed of about five percent, whereas the average difference in current direction approximated three degrees.

Detailed observations of the flow response over the small bars in two connecting channels were obtained in the summer of 1995 with a ship-borne, broad-banded two pulse Acoustic Doppler Current Profiler (ADCP). Measurements were carried out along a straight transect, oriented parallel to the general alignment of each channel, for a period of thirteen hours (Fig. 2b). The measurements along transect 1 were carried out during mean tide in June 1995. The measurements along transect 2 were obtained during spring tide in August 1995. The settings and instrumental accuracy of the ADCP during the two surveys are summarized in Table 1.

Table 1 System configuration of the ADCP during the two surveys

Transect	1	2
Acoustic frequency (kHz)	600	600
Pings per ensemble	5	20
Horizontal sampling interval (m)	10-15	40-50
Vertical bin size (m)	0.5	0.5
Depth range (m)	2.74-20	2.85-20
Velocity precision (m/s)	0.06	0.03
Compass precision (°)	1	1

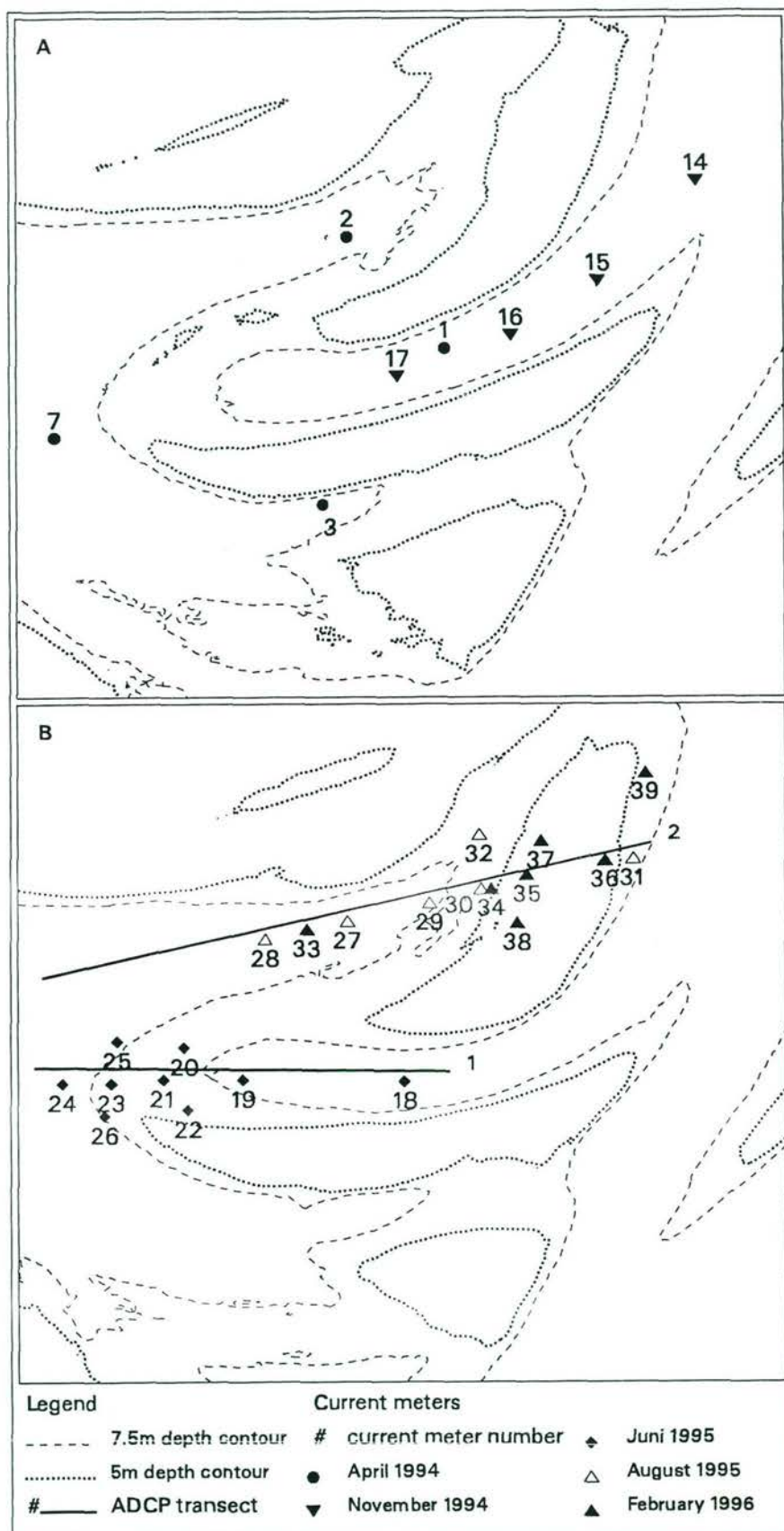


Figure 2 Locations of measurements. a) measurements in 1994 b) measurements in 1995 and 1996. For location of the bar see inset in Figure 1b.

Data-analysis

The current meter data were used to quantify temporal and spatial variations in current asymmetry and to characterize the current patterns over the small bars in the connecting channels. Prior to further analysis, the noise in the velocity data was reduced by applying a low-pass smoothing filter to the North-South and East-West velocity components.

The relative height of the current meters changed with time as a result of the large tidal range (3.3-4.75m) and the small water depths (5-13m). This variation in measurement height inhibit a comparison of measured ebb and flood velocities. Therefore measured current velocities (not direction) were converted to depth-averaged values, by assuming the logarithmic velocity profile of steady and uniform flow and an averaged roughness length based on bedform dimensions ($z_0=0.033k_s$, $k_s=0.4m$). In areas of major advective flow acceleration and deceleration this results in under-estimated (flow deceleration) and over-estimated (accelerating flow) depth-averaged velocities. These effects were not taken into account. The obtained time-series of the depth-averaged velocity vectors were then used to compute significant current vectors for each ebb and flood period. The significant velocity is defined as the mean of the 1/3 highest current velocities and represents the conditions near maximum flow over a period of about two hours. For each current meter location relationships between significant velocity (ebb and flood) and observed tidal range were determined by applying a linear regression analysis. The linear relationships were then used to compute significant ebb and flood velocities during mean, neap and spring tide. This was done by substituting the tidal range for neap, mean and spring tide in the linear relationships. Current asymmetry was then defined as the natural logarithm of the ratio of significant ebb velocity over significant flood velocity. A positive current asymmetry indicates ebb-dominated flow. A negative asymmetry indicates flood-dominated flow. The advantage of the significant velocity is, that it gives a better weighting of the tidal variation of current velocities than the often used maximum velocity.

The ADCP observations were used to determine variations in the depth-averaged flow patterns over the small bars in the connecting channels. Prior to further analysis the noise in the ADCP data was reduced by applying a low-pass, infinite impulse response filter to the North-South and East-West velocity components (Stanley et.al. 1984).

The computation of depth-averaged velocities implies extrapolation of the velocity profiles towards bottom and water surface. Extrapolation of the velocity profile was done by fitting a series of three shapefunctions through the data using a least squares method. This method has been derived from the shapefunction approach described by Zitman (1992) and has been previously applied by Van de Meene (1994). As winds were low during the ADCP measurements, the contribution of wind stress to the current velocity was neglected. Then the vertical velocity profile in North-South and East-West direction can be expressed as (Zitman, 1992):

$$u(\zeta) = \sum_{k=1}^m F_k \cdot f_k(\zeta) \quad (1)$$

where f_k is the series of shapefunctions, ζ is the dimensionless vertical coordinate and m is the number of shapefunctions ($m=3$ in the present analysis). The weights F_k are the unknowns to be determined using the measured velocity profile $u(\zeta)$. Figure 3 shows the applied shapefunctions together with an example of a curve fitted through observations. The shapefunction approach was used only as a statistical, curve-fitting tool, essentially to compute the depth-averaged current vectors in an objective way. The advantage of this approach is that it is possible to

describe velocity profiles that deviate from e.g. a parabolic profile.

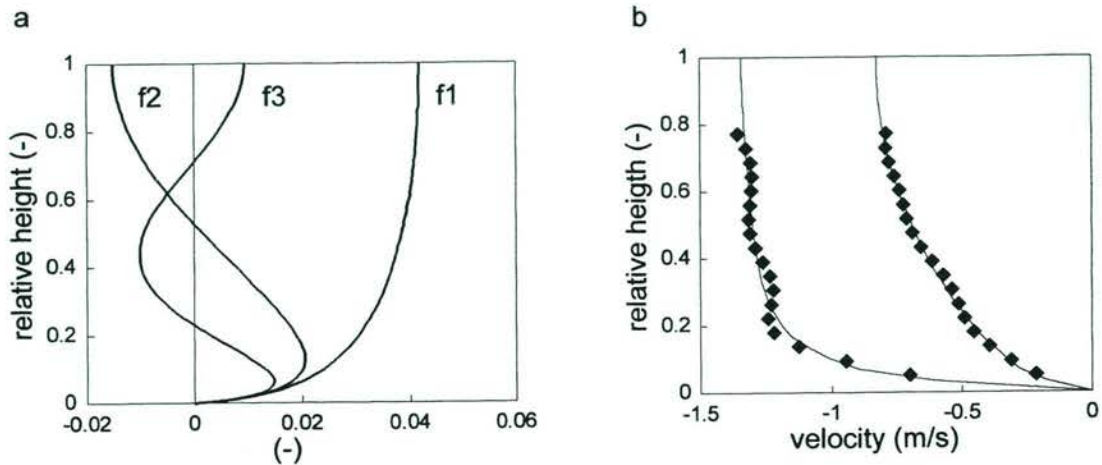


Figure 3 Shapefunction approach. a) the three shapefunctions used in the analysis, b) comparison of measured velocity components (\blacklozenge) and fit (-).

Variations of current asymmetry over the bar in the main flood channel

Figure 4 shows spatial patterns of current asymmetry over the bar in the main flood channel for mean, neap and spring tide. The spatial variation of current asymmetry in Figure 4a is related to the presence and morphology of the connecting channels. In the connecting ebb channel and at the landward side of the bar in the connecting flood channel current asymmetry ranges between 0 and 0.11, indicating that ebb velocities exceed flood velocities by about 0 to 12 percent. In the connecting flood channels and at the seaward side of the bar in the connecting ebb channel, negative current asymmetries of -0.12 to -0.31 occur, indicating flood-dominated flow. In these areas flood velocities are 12 to 40 percent stronger than the ebb velocities. The bars in the connecting channels form the transition zones between ebb-dominated and flood-dominated flow. Current asymmetry changes with tidal range (Fig.4b). In the connecting ebb channel and at the landward side of the bar in the connecting flood channel, current asymmetry decreases with 6 to 25 percent when tidal range increases from 3.3 to 4.75m. At some locations in the connecting ebb channel tidal flow becomes even slightly flood-dominated during spring tide (locations 15, 20, 21 and 22 in Fig. 2). In the connecting flood channels and at the seaward side of the bar in the connecting ebb channel current asymmetry increases with 10 to 34 percent with increasing tidal range.

The spatial variation in current asymmetry indicates small-scale circulations of net sediment transport over the bar in the main flood channel, that are induced by connecting ebb and flood channels (Fig. 5a). This means net ebb transports in the ebb channel and net flood transports in the flood channel. The circulations confirm the concept of mutually evasive ebb and flood channels of Van Veen (1950), who identified the presence of ebb-dominated and flood-dominated channels on the basis of net water transports and the location of the bars in tidal channels. The changes in current asymmetry with tidal range, has two important implications for the small-scale circulations (Fig. 5b): 1) The intensity of the circulation is not constant in time and 2) the circulation is not closed. The changes in current asymmetry over the neap-spring tidal cycle indicate that the magnitude of net sediment transport, the intensity,

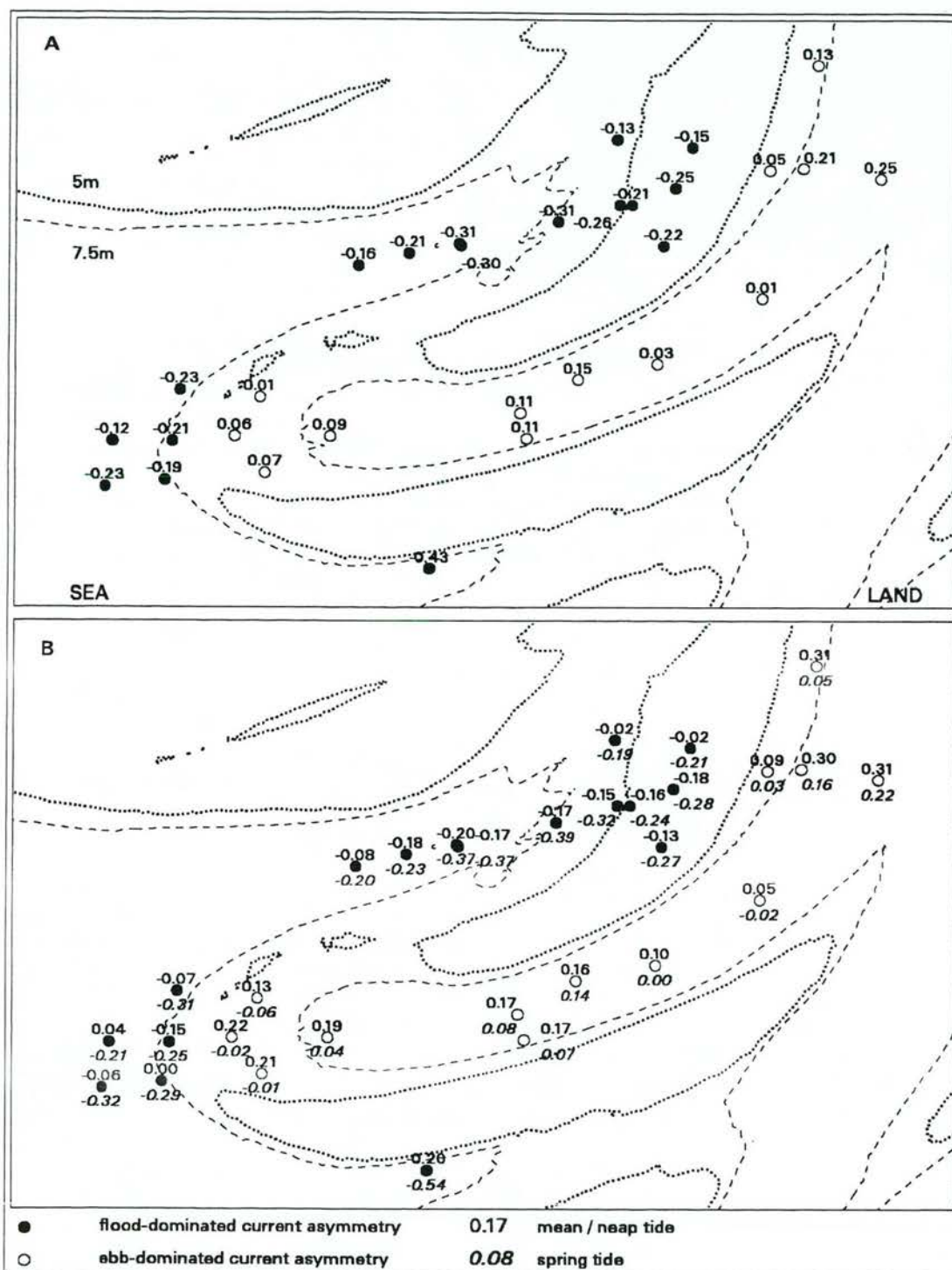


Figure 4 Patterns of current asymmetry. a) mean tide, b) neap and spring tide

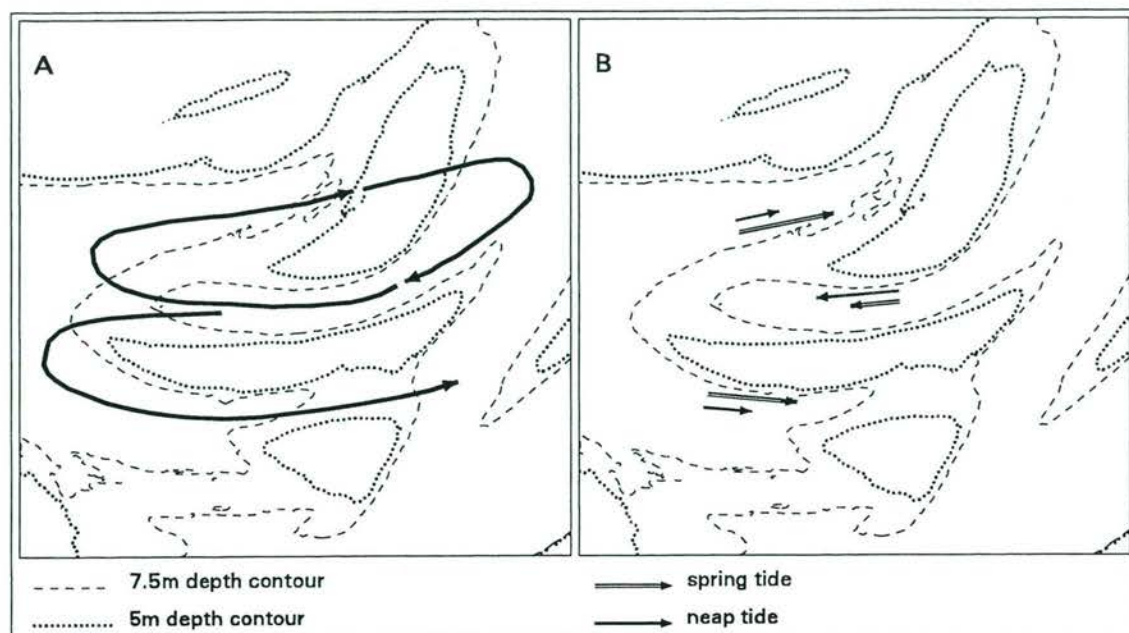


Fig. 5 Implications of the variations in current asymmetry for the patterns of net sediment transport. a) Small-scale circulations, b) the relative magnitude of net sediment transports during neap and spring tide

changes with tidal range. The decrease in current asymmetry in the ebb channel with increasing tidal range indicates larger net ebb transports in the ebb channel during neap tide than during spring tide. The increase of current asymmetry in the flood channel indicates smaller net flood transports during neap tide than during spring tide. This difference between ebb and flood channel means that the circulation is not closed. A net flood-dominated component that increases with tidal range is likely as the flood-dominated current asymmetry is larger than the ebb-dominated current asymmetry. Moreover the morphology of the bar is dominated by connecting flood channels. Computed sediment transports (not shown), based on the current observations, confirm the above inferred spatial and temporal variations in net sediment transport.

Flow response over the bars in two connecting channels

Figure 6 and 7 summarize the flow characteristics over the bar in the connecting ebb channel during mean tidal conditions. Figure 6 shows the pattern of significant current vectors in June 1995. Figure 7 displays the pattern of depth-averaged along-transect and cross-transect velocities during accelerating, maximum and decelerating tidal flow. During ebb the pattern of significant current vectors displays an ebb flow flowing around the bar (Fig. 6a). At the upstream side of the bar the ebb flow diverges and shows minor flow decelerations towards the bar of about 7 percent (0.08m/s). Significant current directions at location 20 and 22 differ by twenty degrees (see Fig. 2b for locations). At the downstream side of the bar the ebb flow converges and strongly decelerates with about 25 percent (0.25m/s). The ADCP observations confirm the patterns of flow deceleration (Fig. 7). The depth-averaged velocity pattern shows an instantaneous drop in current velocity as soon as the ebb flow passes the top of the bar. The depth-averaged velocity reduces with 28 percent (0.3m/s) on average. The flow reduction tends to increase with time and decreasing

water level. In addition the ADCP observations show a tendency towards small flow acceleration just before the top of the bar during maximum and decelerating ebb flow. The small cross-channel velocity component, both during ebb and flood, indicates tidal flow approximately parallel to the ADCP-transect (with 5°). Thus the ebb flow diverges and decelerates towards the bar, slightly accelerates near the top of the bar and converges and strongly decelerates after passing the top of the bar.

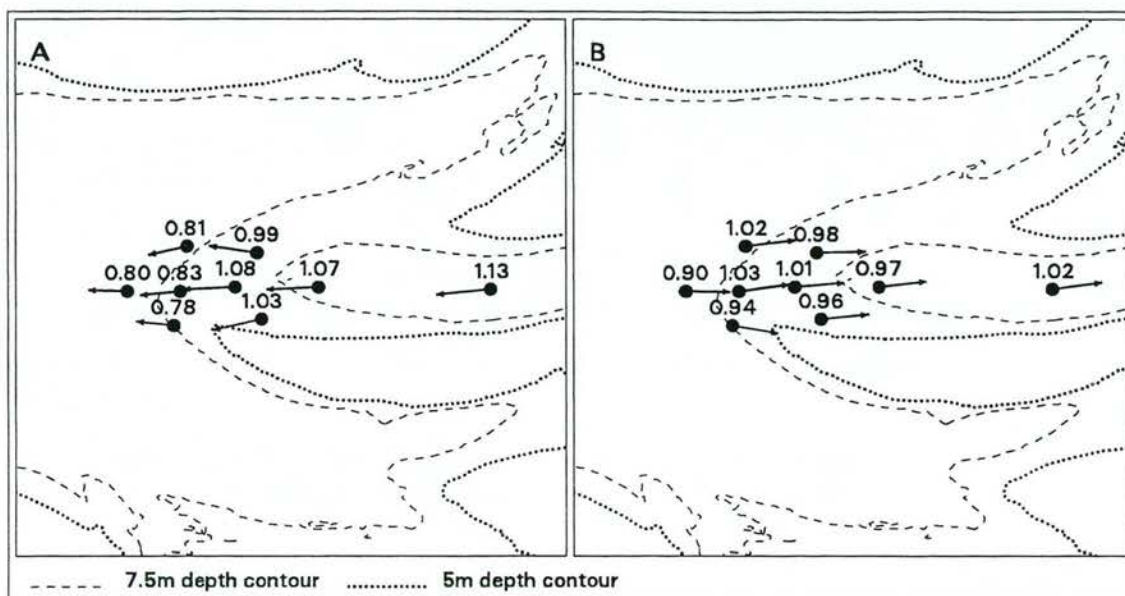


Fig. 6 Mean significant current vectors over the bar in the connecting ebb channel during mean tide in June 1995. a) ebb, b) flood.

The flood displays a small tendency towards flow around the bar (Fig. 6b). The pattern of significant current vectors shows flow divergence at the upstream (seaward) side of the bar that is accompanied by an increase in current velocities of about 14 percent (0.13m/s). At the downstream side of the bar the current vectors are aligned more or less parallel and only minor velocity gradients are observed. The ADCP observations also display flow acceleration at the upstream side of the bar (Fig. 7). Depth-averaged velocities increase with about 10 percent (0.1m/s). At the downstream side, between 500 and 1200 meters, reductions in current velocity of about 10 percent (0.1m/s) are observed. Thus the flood flow slightly diverges and accelerates and decelerates over the bar.

The characteristics of the flow pattern over the bar in the connecting flood channel during spring tide, measured in August 1995 and February 1996, are summarized in Figures 8 and 9. During ebb the significant current pattern displays flow deceleration over the bar (Fig 8a). At the downstream side of the bar current velocities are 15 to 30 percent smaller than near the top of the bar (location 36, Fig. 2b). The gradual change in current direction between locations 37 and 38 of fourteen degrees, indicates a tendency towards flow convergence. The ADCP observations (Fig. 9) reveal deflection of the ebb flow at the upstream side of the bar, where the current vectors are inclined towards the ADCP-transect by 15-25 degrees (not shown). Despite this current deflection a major velocity gradient over the bar can be identified. On average current velocities at the top of the bar exceed currents at the upstream and downstream side of the bar by 30 percent (0.4-0.5m/s). These large velocity differences indicate flow acceleration at the upstream side of the bar and

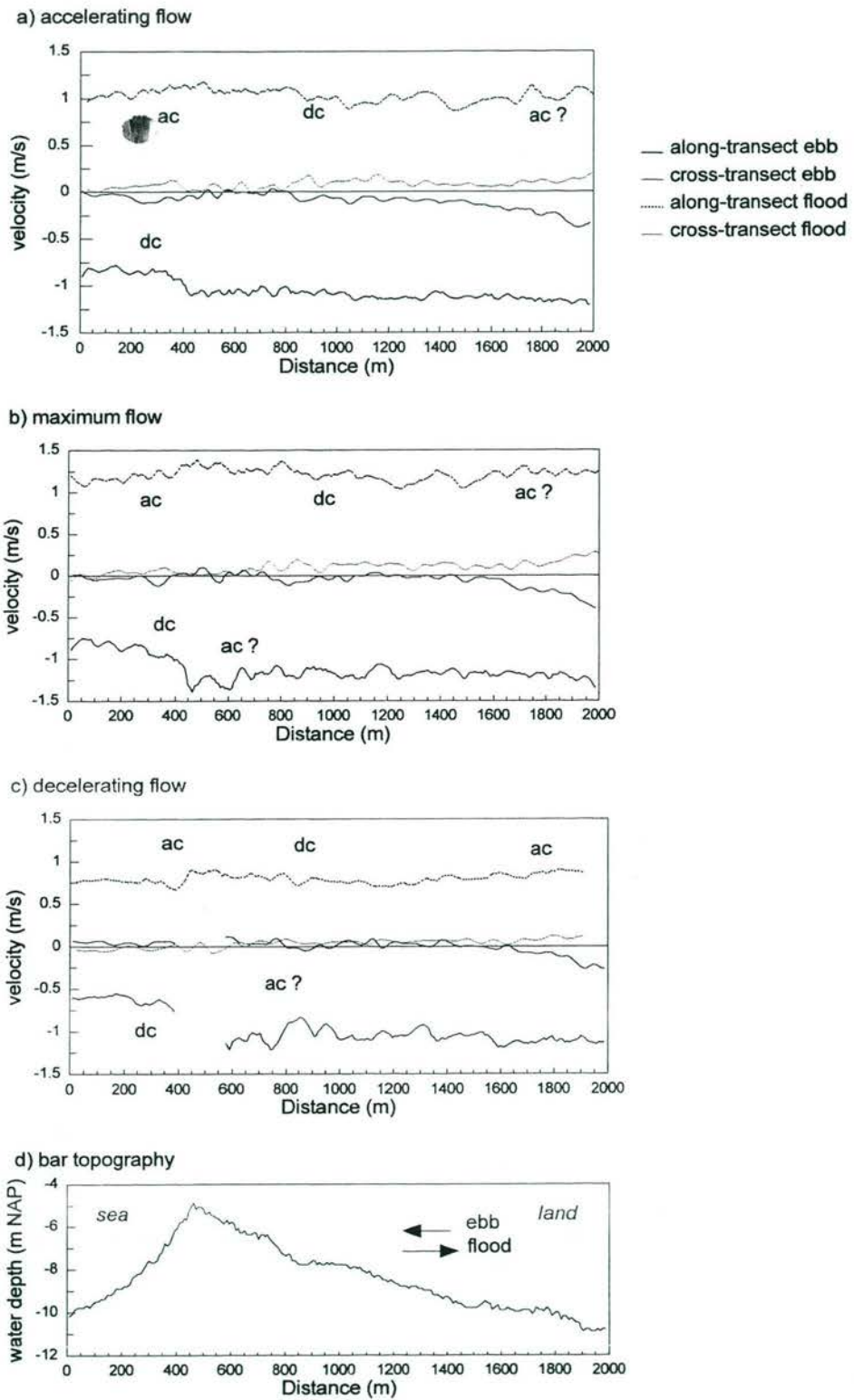


Figure 7 Depth-averaged along-transect and cross-transect velocity over the bar in the connecting ebb channel during ebb and flood on 29 June 1995. Ebb is negative, flood is positive, ac=acceleration, dc=deceleration.

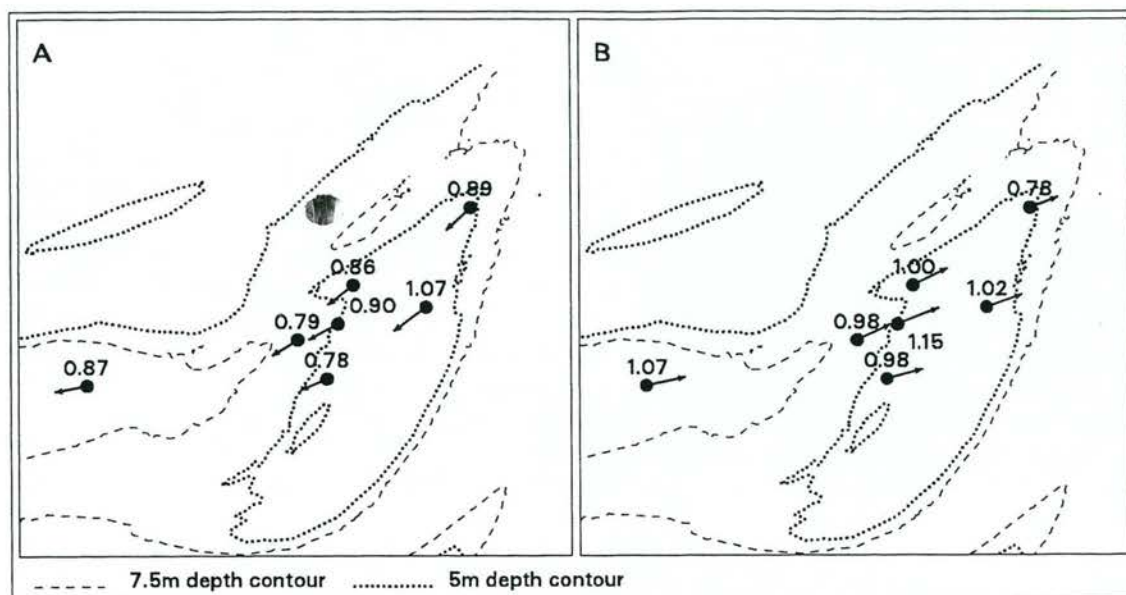


Figure 8 Mean significant current vectors over the bar in the connecting flood channel during spring tide in February 1996. a) ebb, b) flood.

flow deceleration at the downstream side of the bar. Thus the ebb flow accelerates towards the top of the bar and decelerates and converges at the downstream side of the bar. During flood the significant current vectors show a flow acceleration of about 17 percent (0.17m/s) at the upstream side of the bar (Fig. 8b). Significant current directions gradually change with twelve degrees between locations 37 and 38 (see Fig. 2b for locations), indicating minor flow divergence. The current velocity at the upstream side of the bar is 12 to 22 percent ($0.13\text{-}0.22\text{m/s}$) stronger than at the downstream side of the bar. This means that the flood flow decelerates over the bar. The ADCP observations show a flow deceleration of about 20 percent just before the bar (between 1700 and 2200m, Fig.9), where the flood flow diverges (not shown). At the upstream side of the bar the flood flow accelerates with about 30 percent ($0.3\text{-}0.4\text{m/s}$). At the downstream side flow decelerations of 40 to 50 percent ($0.5\text{-}0.7\text{m/s}$) are observed. The cross-transect velocity components indicate that the flood flow is less deflected by the topography of the bar than the ebb flow (inclination of $6\text{-}12^\circ$ with respect to the ADCP-transect, not shown). Thus the flood flow diverges and decelerates towards the bar, accelerates near the top of the bar and strongly decelerates after passing the top of the bar.

The ADCP observations are marked by second-order fluctuations. The amplitude and length scale of these fluctuations increase with time and decreasing water level. The unfiltered velocity data display similar fluctuations. The cause of the fluctuations is not clear. Both turbulence and depth variations may cause such fluctuations.

The pronounced topography of the small bars in the connecting channels is reflected in the hydrodynamics: 1) The bars in these channels demarcate the transition zones between ebb-dominated and flood-dominated flow, 2) Neap-spring tidal variations in current asymmetry change over the bar and 3) The ebb and flood flow tend to flow around the bars of the channels and display non-uniform velocity patterns. In the connecting ebb channel largest velocity gradients are observed during ebb. In the connecting flood channel largest velocities and velocity gradients tend to occur during flood. Fluid continuity across the bar may explain the observed flow

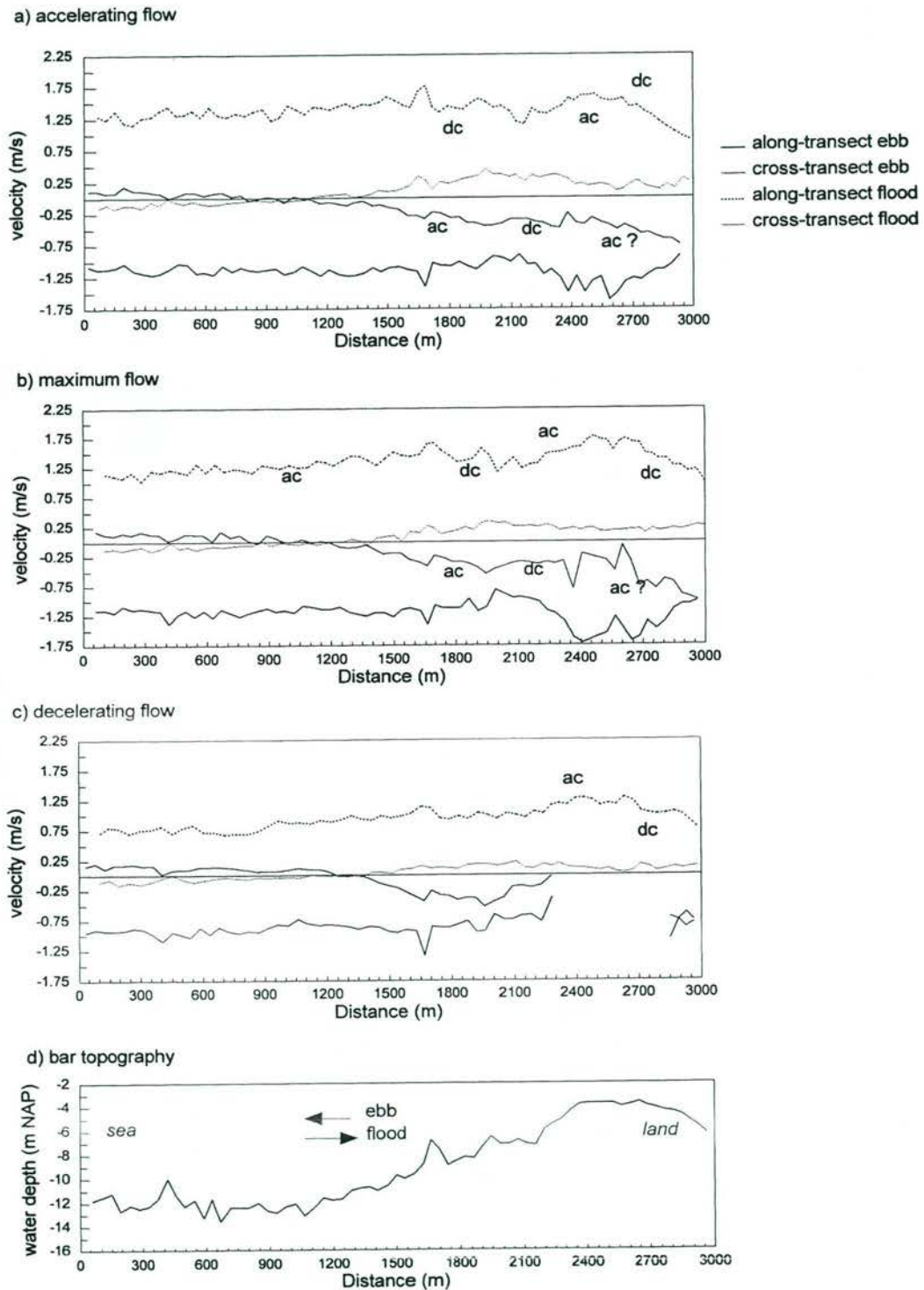


Figure 9 Depth-averaged along-transect and cross-transect velocity over the bar in the connecting flood channel during ebb and flood on 30 August 1995. Ebb is negative, flood is positive, ac=acceleration, dc=deceleration.

around the bars. Fluid continuity implies that the discharge Q (m^3/s) does not change much across the bar. The overall discharge Q is defined as $Q=b\bar{u}h$, where b is the width of the imaginary stream tube (m), \bar{u} is the depth-averaged current velocity and h is the water depth. The changes in channel depth over the bar may result in changes in the width of the stream tube and the depth-averaged velocity. At the upstream side of the bars the flow diverges. The width of the stream tube increases. At the downstream side the flow converges. The width of the stream tube decreases. In addition to these changes in width the depth-averaged velocity increases and decreases across the bars, whereas the water depth increases and decreases. The flow over the bars shows a tendency towards flow deceleration and accelerations at the upstream side of the bar and deceleration at the downstream side. The pattern reverses every tidal phase. The implications of these flow phenomena for sediment transports, the patterns of erosion and sedimentation and the net effect over e.g. one semi-diurnal period are not evident. The implications depend on the magnitude and duration of flow accelerations and decelerations, as well as the effect of variations in stream tube width and water depth, differences in current asymmetry and the dominant sediment transport mode. The small bars are stable morphological features despite the observed flow accelerations and decelerations. This indicates that relaxation of the suspended transport may be important for the maintenance of the estuarine bars.

Conclusions

Variations of the tidal flow over the bar in the main flood channel are strongly determined by connecting channels:

- 1) Spatial variations in current asymmetry indicate the presence of small-scale net circulations of tidal flow and sediment transports over the bar, that are induced by connecting ebb and flood channels.
- 2) The changes in current asymmetry with tidal range indicate that the intensity of the circulations is not constant and that the circulations are not closed.

The flow over the small bars in the connecting channels is non-uniform and displays tendencies towards divergence, decelerations and accelerations of the flow at the upstream side of the bar and convergence and deceleration of the flow at the downstream side of the bar. The implications of the flow patterns for sediment transports and the maintenance of the bars are not evident and will be further elaborated on the basis of computations with a mathematical model and morphological analysis.

Acknowledgements

This study was funded by Directorate Zeeland of the Ministry of Transport Public Works and Water Management. The measurements were carried out by the survey department of Directorate Zeeland. Ir A. Langerak, drs A. Van Kleef and dr J.R. Van de Berg are greatly acknowledged for their useful comments.

Appendix

Aubrey, D.G. (1986). Hydrodynamic Controls on Sediment Transport in Well-mixed Bays and Estuaries. In: J. Van de Kreeke (ed.). Physics of shallow estuaries and Bays, p. 245-258.

- Dalrymple, R.W. and R.N. Rhodes (1995). In: G.M.E. Perillo (ed.), Estuarine dunes and bars. *Geomorphology and Sedimentology of Estuaries. Developments in Sedimentology* 53, p. 359-422.
- De Vriend, H.J. (1996). Mathematical Modelling of meso-tidal barrier island coasts. Part I: empirical and semi-empirical models. In: P.L.F. Liu (ed.), *Advances in coastal and ocean engineering* (2), p.115-149.
- De Vriend, J. and J.S. Ribberink (1996) Mathematical Modelling of meso-tidal barrier island coasts. Part II: process-based simulation models. In: P.L.F. Liu (ed.), *Advances in coastal and ocean engineering* (2), p.151-197
- Dronkers, J. (1986). Tidal asymmetry and estuarine morphology. *Neth. Jour. of Sea Res.* 20 (2/3), p. 117-131.
- Friederichs C.T. and D. Aubrey (1988). Non-linear Tidal Distortion in Shallow Well-mixed Estuaries: a Synthesis. *Est. Coast. and Shelf Sci.*(27), p. 521-545.
- Jeuken, M.C.J.L. (submitted for review). Morphodynamics of connecting channels in the Westerschelde estuary (the Netherlands). *Proc. Conf. Physics of Estuaries and Coastal Seas*, The Hague, 1996.
- Lessa, G. and G. Masselink (1995). Morphodynamic evolution of a macro-tidal barrier island. *Marine Geology* 129: 25-46.
- Stanley, D.W., G.R. Dougherty and R. Dougherty (1984). *Digital Signal Processing*, Prentice Hall, 514 p.
- Van de Kreeke, J. and K. Robaczewska (1993). Tide-induced residual transport on coarse sediment: application to the Ems estuary. *Neth. Jour. of Sea Res.* 31 (3), p.209-220.
- Van de Meene, J.W.H. (1994). The shoreface-connected ridges along the central Dutch coast, Ph.D. thesis, IMAU, Utrecht Univ., *Neth. Geogr. Studies* 174, KNAG, Utrecht, 256 p.
- Van den Berg, J.H., M.C.J.L. Jeuken and A. F. van der Spek (in press). Hydraulic processes affecting the morphology and evolution of the Westerschelde estuary. In: K.F. Nordstrom and C.J. Roman (eds.). *Estuarine Shores: Evolution, Environments and Human Alterations*.
- Van Veen, J. (1950). Eb- en vloedscharen in de Nederlandse getijwateren. *Tijdschr. Kon. Ned. Aandr. Gen.* 67, p. 303-335 (in Dutch).
- Zitman, T.J. (1992). Quasi three dimensional current modelling based on a modified version of Davies' shapefunction approach. *Cont. Shelf Res.*, 12(1), p. 143-158.

Bijlage B: verdere uitwerking van de verkennende modelsommen uit hoofdstuk 2.

MORPHODYNAMICS OF CONNECTING CHANNELS IN THE WESTERSCHELDE ESTUARY (THE NETHERLANDS)

M. Claire J.L. Jeuken

Institute of Marine and Atmospheric research Utrecht, Utrecht, The Netherlands

ABSTRACT: This paper discusses the influence of a connecting channel (type I) between an ebb and flood channel on the general flow pattern and hydrodynamic stability of the ebb flood channel system, based on computations with a 1D network model and field observations. During the bed-forming conditions tidal flow in the channel system is friction-dominated and largely determined by the presence of the shallow bar in the main flood channel. The tidal flow and morphology of the main ebb and flood channel are adjusted to the presence of connecting channels.

1 INTRODUCTION

Estuaries, like the Schelde, are important coastal systems, providing natural navigation channels and sheltered mooring places, as well as habitats for marine flora and fauna, and recreational space. The Westerschelde forms the seaward, marine part (length 60 km) of the tide-dominated Schelde estuary (total length 160 km). To maintain the shipping lane to the harbours of Antwerp and Gent approximately $8 \cdot 10^6 \text{ m}^3$ of sediment is dredged annually. A further deepening of the shipping lane, to enable the passage of larger ships, is planned for the near future. A better understanding of the morphodynamic behaviour of the channels and shoals is important for the management of the estuarine system and for determining the optimal dredging strategies.

Tidal inlets and estuaries often display patterns of alternating ebb and flood channels (Van Veen, 1950). Recent developments in understanding the morphodynamics of such systems have resulted in the formulation of different types of models. A review of modelling approaches is given by De Vriend (1996) and De Vriend and Ribberink (1996). The evolution of the channel and shoal system in the Westerschelde has been modelled by two different models: a dynamic/empirical model and a morphodynamic model (e.g. Fokkink et.al., this volume).

In the present study field observations and a one-dimensional flow model are used to study tidal flow in a section of the Westerschelde. Objective is to

identify the influence of connecting channels and channel geometry on the general flow pattern and hydrodynamic stability of an ebb and flood channel system.

2 THE STUDY AREA

2.1 Morphology

The Westerschelde has a funnel-shaped geometry and a well developed system of channels and shoals (Figure 1a). The larger channels in the Westerschelde display a regular returning pattern, referred as estuarine section. Each pattern consists of a meandering ebb channel and a straight flood channel, usually separated by intertidal shoals (Figure 1b). The ebb channel has a relatively deep bar at the seaward end of the channel, whereas the flood channel has a shallow extensive bar at the landward end. The connecting channels form connection between the main ebb and flood channel. The channels owe their existence to water level differences between the ebb and flood channel, which are due to differences in channel geometry and tidal propagation between the two main channels. Most connecting channels occur in the area of the shallow bar in the main flood channel. In the estuarine section two different types of connecting channels may exist. Connecting channels which occur in the bar of the main flood channel (type I), and connecting channels which bisect the intertidal

between the ebb and flood channel (type II). On the timescale of one to several decades, the connecting channels tend to display a cyclic behaviour marked by three successive stages: 1) formation, 2) expansion and migration, followed by 3) degeneration.

The study site covers one estuarine section in the seaward part of the Westerschelde (Figure 1b). The straight flood channel has a length of about 12 kilometre. The cross-sectional area of the flood channel decreases in *landward* direction, towards the bar, from about 42320 m² in transect 1 to 23650 m² in transect 2. The mean channel depth decreases from 18m to 6.6m. The spatial variation in cross-sectional geometry along the 15 kilometre long meandering ebb channel is smaller. In *seaward* direction the cross-section decreases from 28210 m² (transect 2) to 18000 m² (transect 1), whereas the channel depth increases from 12 to 14 meters. In the study area an abundance of different connecting channels occurs. The large connecting channel C2 (type II) originated near the bar in the main flood channel around 1940. Since then the channel migrated in seaward direction with average migration rates of about 30m per year. It's predecessor C1 (type II) originated at a similar location around 1890 and disappeared in 1992. The various connecting channels in the bar area of the main flood channel (type I) originated and expanded from 1986/1987. At present the connecting ebb channel C4 is degenerating.

2.2 Hydrodynamics

The Schelde estuary is a meso-tidal estuary. Water level observations along the Schelde estuary show an increase in mean tidal range between Vlissingen and Antwerpen (78km upstream of Vlissingen) from 4m to 5.2m. This amplification of the tidal range is due to landward convergence, shoaling and partial reflections. Landward of Antwerpen the tidal range decreases as a result of frictional damping. The tide shows an asymmetry. The duration of falling tide exceeds that of rising tide and increases in landward direction. During mean tidal conditions the duration difference amounts 30 minutes at Vlissingen and 100 minutes at Antwerpen (Claessens and Meyvis, 1994). The marine part of the estuary is well-mixed. The mean river outflow is about 120m³/s, or 2.5*10⁶m³ per ebb or flood period. This is less than one percent of the tidal volume of 1*10⁹m³/s at the seaward boundary.

In the study area the tidal range at mean tidal

conditions amounts 4.2m. The average time lag between the water level at the seaward and the landward margin of the study area approximates 15 minutes. Given the length of the estuarine section of 12 kilometres, this time lag indicates a propagation velocity of the tidal wave of approximately 10 m/s and an average depth of 10m in the estuarine section. Maximum water level differences along the estuarine section range between 0.2m and 0.5m over the neap spring tidal cycle. The total ebb and flood volumes amount 800*10⁶m³/s on average. Maximum depth-averaged current velocities are typically in the order of 1-1.5m/s.

3 METHODS

To study the general characteristics of tidal flow in the study area, the one-dimensional network model DufLOW was used. The curved alignment of both the estuarine geometry and the tidal channels suggest the presence of 2 and 3 dimensional processes, like flow curvature, which may accompanied by cross-channel variations in water level gradients. These secondary processes are however not expected to influence the general pattern of along-channel velocities, discharges and water level gradients in a significant way.

The model has been generally validated, based on water level and discharge measurements along the entire Westerschelde (Bollebakker, 1985). In the present study the model is used to analyse tidal flow in the channel sections. To verify the results and validity of the 1-dimensional approach, flow computations are compared in more detail with observations of the flow pattern.

3.1 Flow computations

The DufLOW model solves the 1-dimensional equations of motion and fluid continuity by discretization in time and space using the four-point implicit Preissmann scheme (Spaans et.al. 1989). Neglecting the influence of wind and density differences, the equations of fluid continuity and motion read as,

$$B \frac{\delta h}{\delta t} + \frac{\delta Q}{\delta x} = 0 \quad (3.1)$$

$$\frac{1}{gA} \left[\frac{\delta Q}{\delta t} + \frac{\delta}{\delta x} \left(\frac{Q^2}{A} \right) \right] + \frac{\delta h}{\delta x} + \frac{Q|Q|}{C^2 A^2 R} = 0 \quad (3.2)$$

where Q is the discharge (m^3/s), h the water level (m), A cross-sectional area (m^2), R the hydraulic radius (m), B the channel width (m), t is time and x is distance along the channel axis. The Chezy coefficient C ($\text{m}^{0.5}/\text{s}$) is computed via the depth-dependent Manning formulation and ranges from about 50 to $75 \text{ m}^{0.5}/\text{s}$.

The boundary conditions used in the computation consist of a river discharge (about $50 \text{ m}^3/\text{s}$) at the landward boundary (Gent, in Belgium) and mean spring tidal water levels at the seaward boundary (Vlissingen, Figure 1a). For the verification of the model, additional computations were carried out with the seaward boundary conditions as occurred during the measurements. The bottom schematization dates from 1982 and divides the estuary in about 200 section. The study area itself is divided in 23 channel sections (Figure 2). For the interpretation and presentation of the results the channel geometry and computed flow pattern were simplified to five channel sections (Figure 2) by averaging and summing over the section lengths.

To analyze the character of tidal flow and the influence of channel geometry on tidal flow, the terms in the momentum equation were quantified based on the results of the computation. For this purpose the terms in the momentum equation were expressed as a difference in head over the section length. This approach involves integration of the various terms in 1D equations over the section length (Δx). As all terms in the rewritten momentum equation have the same dimensions (L), the relative magnitude of friction (F) can be defined as

$$F = \frac{\text{friction}}{\text{inertia}} = \frac{g \Delta x Q_{av} |Q_{av}|}{\left[\frac{dQ_{av}}{dt} \Delta x + \frac{Q_2^2}{A_2} - \frac{Q_1^2}{A_1} \right] (C^2 AR)_{av}} \quad (3.3)$$

Tidal flow is considered friction-dominated for $F > 2$, inertia-dominated for $F < 0.5$, and of the mixed type for $0.5 < F < 2$.

To estimate the sediment transport capacity of the flow in the five schematized channel sections, the cross-sectional velocity was raised to the fifth power. Various sediment transport measurements in the Westerschelde indicate that this velocity parameter fairly represents the general characteristics of the tidal variation in sediment transport.

The impact of the connecting channel on the general hydrodynamics was estimated by simulating the situation with and without the connecting channel. To evaluate the influence of the connecting channel, the relative differences in current velocity in

the four main channel sections were computed as,

$$V = \left(\frac{u_{without}}{u_{with}} \right) \cdot 100 - 100 \quad (3.4)$$

Under the assumption that an increase in current velocity will induce a similar increase in channel geometry, the results may be checked. This was done by step-wise adjusting the geometry of the four main channel sections, until the differences in flow pattern between the situation with and without the connecting channel approximated zero. As the freedom of movement and an increase in width of the main channels are limited, changes in cross-sectional area were assumed to be the result of a change in channel depth.

3.2 Field observations

At four locations water level and discharge measurements were carried out (Figure 1b). Water level observations were obtained with pressure sensors installed in 8 meter long gauging tubes. The gauging tubes were mounted at measuring poles at a distance of one meter, perpendicular to the main flow direction. The measured pressure was compensated for air pressure by using double ventilating wires. Pressure measurements were obtained every 10 minutes with a sampling period of 1 minute and a sampling frequency of 2 Hz, during a period of about one month. At four occasions discharge measurements were carried out over a period of 12.5 hours. Simultaneous measurements of the vertical velocity profile, with Elmar impeller-type current meters from about 10 anchored ships, formed the basis for the computation of discharges. The conditions during the discharge measurements ranged from mean tide to spring tide.

The water level measurements were used to compute water level differences along the five channel sections depicted in Figure 2. Under the assumption of a hydrostatic pressure distribution and a constant water density of 1019 kg/m^3 , measured time-series of pressure were converted to water levels and water level differences. Prior to further analysis noise in the time-series of falls was reduced by applying a smoothing filter in the time domain. For this purpose a quadratic equation, written as a moving average, was fitted by least squares to nine points of the time series (1.5 hours). The accuracy of the water level measurements is largely determined by the determination of the height of the pressure

sensors with respect to the Dutch Ordnance Level. The accuracy of the determination of the height of the pressure sensors is $\pm 0.025\text{m}$. This implies a maximum systematic error in falls of $\pm 0.05\text{m}$.

The measured velocity profiles were used to compute discharges. Except for the interpolation of velocities between measurement locations, the computation resembles the method described by De Jonge (1992). Because of the limited spatial resolution, the depth-averaged currents were interpolated between two successive measurement locations as function of water depth. The accuracy of the instantaneous discharges is estimated to be $\pm 15\%$.

4 RESULTS AND DISCUSSION

4.1 *Verification of the 1D-approach*

Figure 3 compares the measured and computed water levels at the four water level stations during mean spring tidal conditions. This figure shows that the agreement between the two is fairly good. The zero water level crossing during tidal rise and high water coincide. The computed high water level at locations 2, 3 and 4 is about 0.1m larger than the measured level. Computed and measured tidal falls show a phase difference with a maximum of about 20 minutes at location 4.

Figure 4 shows a validation of the water level differences along the five channel sections (differences in channel length are accounted for). For this purpose falls at maximum flow, at 4 and 11.7 hours after high water respectively, are plotted versus tidal range. At maximum ebb computed and measured falls show good agreement along the four main channel sections (1 to 4). Along the connecting channel (section 5) computed falls are about 0.03m larger than the measured fall. Although this difference falls within the measurement uncertainty, it may be partially explained by the phase shift of 20 minutes (see Figure 3) which also marks the time-series of falls along the connecting channel. Cross-channel water surface slopes in the main ebb channel due to streamline curvature may add to the observed difference. At flood the differences between observation and computation are larger with a maximum of approximately 0.05m in section 1 and 5.

Figure 5 compares computed and measured discharges through the channels, based on the discharge measurements in transects 2, 3 and 4 (see Figure 1b). It is noted that a water balance of measured tidal volumes and basin storages indicates

that the measured discharge in the ebb channel in transect 4 is about 10% too small. At ebb computed and measured discharges in the main channels show differences in maximum discharges of about 15-20%. The validation shows differences in the distribution of the ebb discharge over the main channels. In the flood channel the computed discharge exceeds the observed discharge, whereas in the ebb channel the opposite is true. The general validation of the model did not reveal this phenomenon (Bollebakker, 1985). A reduction of the bottom friction coefficient in the flood channel equal to the value in the ebb channel, improves the relative distribution of discharges with 5 to 10%, but results in a worse picture of the water levels and falls. Except for the consistent time lag of 20 minutes, computed and observed ebb discharges in section 5 show good agreement. The cause of the time lag is not yet clear. The seaward migration of the channel, 300 meters since 1982, and bottom friction in the main channels do not explain this time lag. In a simulation of the flow pattern with a 2DH flow model this time lag is not observed. This suggests that the channel length in the model is not properly defined. Figure 5 shows good agreement between computed and measured flood discharges in channel sections 1, 2 and 3, whereas differences of about 15-25% are observed in sections 4 and 5. Computed discharges in the connecting channel show a flood peak, which is hardly present in the observations. The smaller flood peak in reality is related to the process of flow separation. Due to inertia of flow and the cross-wise orientation of the connecting channel with respect to the main channels, maximum flood flow tends to shoot along the entrance of the connecting channel. This 2D-phenomenon is not incorporated in the 1D-model. The larger computed discharge in the connecting channel partly explains the differences in section 4. The remaining part of the differences between the two discharges in section 4 is explained by too small measured discharges.

The overall comparison of observed and computed tidal flow is satisfying. The overestimated maximum flood discharge in the connecting channel is the most important shortcoming of the model. As a result the impact of the connecting channel on the general flow pattern during flood will be smaller than suggested by the computations. The conclusions based on the computations remain however qualitatively valid.

4.2 *The character of tidal flow*

Figure 6 shows time series of the transport capacity and the relative magnitude of friction in two of the

five channel sections (the extremes with respect of the moment of maximum flow). The moments of maximum flow in the 5 channel sections approximately coincide. Due to the propagation of the tidal wave maximum flow in channel sections 1 and 3 precedes maximum flow in sections 2 and 3 by 10 to 15 minutes. In the connecting channel maximum ebb lags behind the ebb flow in the main channels by 30 minutes. Friction and inertia are equally important during a considerable period of time ($0.5 < F < 2$, Figure 6b). However during the periods of maximum velocity and transport capacity tidal flow is friction-dominated ($F > 2$). Figure 7 shows the fraction of the total transport capacity during the periods in which tidal flow is friction-dominated ($F > 2$) in all five channel sections. In the considered flood period (20 minutes) about 35% of the total transport capacity takes place (Figure 7). During ebb about 55% of the total transport takes place within 80 minutes of the ebb period.

Assumed that enough sediment is available for transport, the magnitude of the transport capacity and spatial gradients in transport capacity largely determine channel morphology. The results show that most of the sediment transport occurs during the periods of maximum flow, when the energy for sediment transport is largest and tidal flow is friction-dominated. As flow is friction-dominated largest spatial velocity gradients will also exist during the periods of maximum flow, indicating maximum transport gradients and erosion and sedimentation. Thus the conditions of friction-dominated, maximum flow can be considered bed-forming, as largest sediment transports and transport gradients occur during these conditions.

4.3 *The influence of channel geometry*

During the bed-forming conditions of maximum flow, tidal flow is friction-dominated in all five channel sections. The average magnitude of friction during these conditions offers a means to identify the channel sections which influences the flow pattern and hydrodynamic stability in the study area most. To neutralize spatial differences related to the propagation of the tidal wave, and to obtain a better weighting, mean values of the relative friction were determined for ebb and flood (average over 20 minutes during flood and 80 minutes during ebb). Figure 8 shows the results. Striking is the relative large friction in section 2, the shallow bar in the main flood channel, both during ebb and flood. Friction in section 2 is 2.5 to 4.5 times larger than in the other channel section. The large friction means

that this channel section largely determines the flow pattern and hydrodynamic stability in the study area during the bed-forming conditions. Squeezing the discharge over the bar, by for example extensive disposal of dredged sediment, affects the currents in the other 4 channel sections and the small connecting channel (section 5) in particular. Based on flow computations for the western Dutch Wadden Sea with a 2DH model Ridderinkhof (1989) also showed the dominance of friction during maximum flow and an increase of friction with decreasing water depth.

In the connecting channel (section 5) friction is larger during ebb than during flood, indicating that the influence of the connecting channel on the flow pattern is most important during ebb. The simulation of the situation with and without connecting channel confirm this. Figure 9 schematically shows the relative changes in velocity (eq. 4) during the bed-forming conditions of maximum flow. Changes in velocity pattern are larger during ebb than during flood. Removal of the connecting channel results in an increase of current velocities of about 8-14 % in the relatively shallow channel sections 2 and 3. Current velocities decrease with 8 to 13% in the deeper entrances of the channels, section 1 and 4. Under the assumption that changes in velocity primarily affect the channel depth (see 3.1), it is possible to quantify the hydraulic geometry of the main channels which are accompanied by a zero velocity in the connecting channel. This was done by increasing the depth and cross section in channel sections 1 and 3, and decreasing these values in sections 1 and 4. Figure 10 shows the relative changes in velocity in the main channels and absolute changes in fall along the connecting channel as a result of the changes in hydraulic geometry. A deepening of sections 2 and 3 and a shoaling of sections 1 and 4 results in a decrease of the velocity differences depicted in Figure 9 and a strong decrease of the fall between the main channels along section 5. The results in Figure 9 and 10 indicate that the morphology of the main channels is adjusted to the presence of the connecting channel. In the situation with connecting channel the 'bar' sections 2 and 3 have a smaller cross-sectional area and channel depth than in a situation without connecting channel. The reverse is true for the entrances of the main channels, section 1 and 4. Thus differences in channel depth between the main ebb and flood channel are larger in the situation with connecting channel than in the situation without connecting channel. In other words the connecting channel reinforces the initial differences in channel depth between the ebb and flood channel.

The foregoing discussion showed the importance of the shallow bar in the flood channel and the connecting channel for the general flow pattern in the study area. In addition tidal flow over the bar and the connecting channel are interdependent. The connecting channel reduces falls and redistributes the discharge between the main channels in such a way, that the channel tends to reinforce the cause of its own existence (i.e. differences in channel geometry). This implies however an unstable channel system (positive feedback), which is not observed in nature. The morphological evolution is known to be dynamically stable, indicating that negative feed-back mechanisms are operating. At the time scale of several years the seaward migration of the connecting channel may act as a negative feed-back. As the channel migrates in seaward direction, the importance of the bar in the flood channel for the generation of water level differences diminishes. As result falls and current velocities decrease and the connecting channel will start to degenerate. A second feed-back mechanism at the scale may be the formation of new connecting channels in area of the bar, i.e. a cyclic forcing. At a smaller scale changes in bed-roughness may cause a feedback. As current velocities increase the dimensions of the bed forms increase resulting in a larger flow resistance and a reduction of current velocities. The relative importance of these mechanisms or the existence of other feedback mechanisms is not yet known and is subject of further research.

5 CONCLUSIONS

- 1 The short periods of maximum flow (20-80 minutes) are dominated by friction and can be considered as the bed-forming conditions.
- 2 The shallow bar in the main flood channel largely determines the flow pattern in study area during the bed-forming conditions.
- 3 The differences in cross-sectional geometry between the main channels are partly due to connecting channel, which reduces falls and redistributes the discharge between the main channels.

ACKNOWLEDGEMENTS

This study was funded by Directorate Zeeland of the Ministry of Transport, Public Works and Water Management. The measurements were carried out by the 'Meetdienst' of Directorate Zeeland. Ir. A. Langerak is greatly acknowledged for the time he

spent on the useful discussions on the interpretation of the results.

REFERENCES

- Bollebakker, G.P.(1985). Ijking en verificatie van het één-dimensionaal mathematisch model Implic voor het Schelde bekken met bodemligging 1991. Report WWKZ-85.v006 (in Dutch).
- Claessens, J. & L. Meyvis (1994). Overzicht van de tijwaarnemingen in het Zeeschelddebekken gedurende het decennium 1981-1990. Ministerie van de Vlaamse gemeenschap, Antwerpse Zeehavendienst (report).
- De Jonge, V.N. (1992). Tidal Flow and Residual Flow in the Ems Estuary. *Estuarine, Coastal and Shelf Science* (1992) 34: 1-22
- De Vriend, H. J. (1996). Mathematical modelling of meso-tidal barrier island coasts. Part I: empirical and semi-empirical models. In: *Advances in Coastal and Ocean Engineering*. Liu, P.L.F. (ed.):....
- De Vriend H.J. & J. Ribberink (1996). Mathematical modelling of meso-tidal barrier island coasts. Part II: process-based simulation models. In: *Advances in Coastal and Ocean Engineering*. Liu, P.L.F. (ed.):....
- Fokink, R.J., B. Karssen, Z.B. Wang, J. Van Kerckhoven & A. Langerak. Morphological modelling of the Western Scheldt Estuary. *This volume*.
- Ridderinkhof, H. (1988). Tidal and residual flow in the western Dutch Wadden Sea I: numerical model results. *Netherlands Journal of Sea Research* 22 (1): 1-21.
- Spaans, W., N. Booij, N. Praagman, N. Noorman & J. Lander (1989). DufLOW, a Micro-Computer Package for the simulation of One-Dimensional Unsteady Flow in Open Channel Systems. SAMWAT, The Hague, 92 pp.
- Van Veen, J. (1950). Eb- en vloed-schaar systemen in de Nederlandse getijdewateren. *Tijdschr. Kon. Ned. Aardr. Gen.*, 67: 303-325

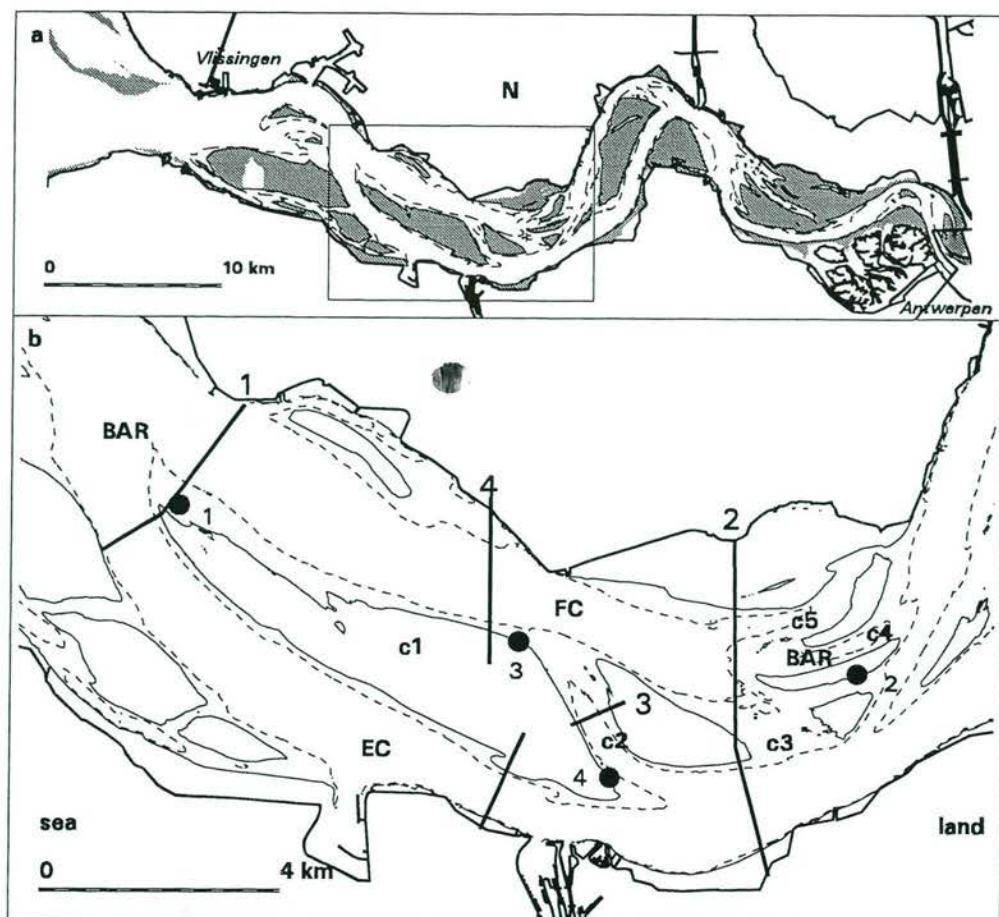


Figure 1 Overview of the morphology of the study area and measurement locations. •=water level station, thick solid line = discharge transect, — = 5m depth contour, ---- = 10m depth contour. FC=flood channel, EC= ebb channel, C#= connecting channel.

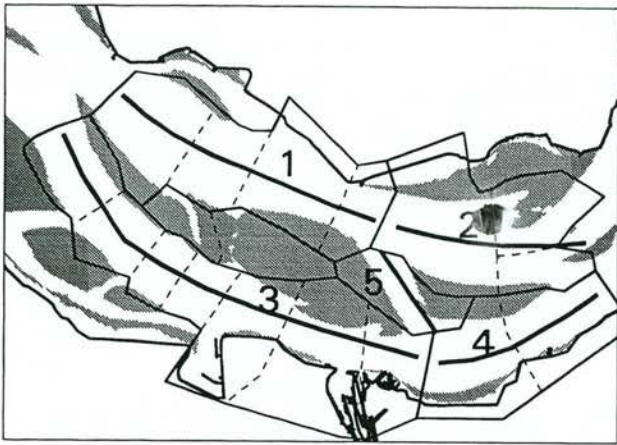


Figure 2 Network schematization in the Duflow model and the simplified channel geometry.

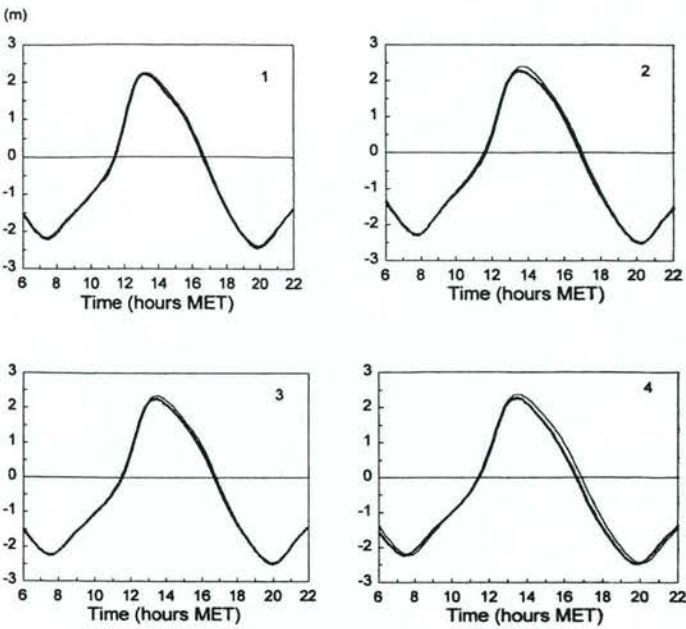


Figure 3 Computed (thin line) and observed (thick line) water levels (for locations see Figure 1b).

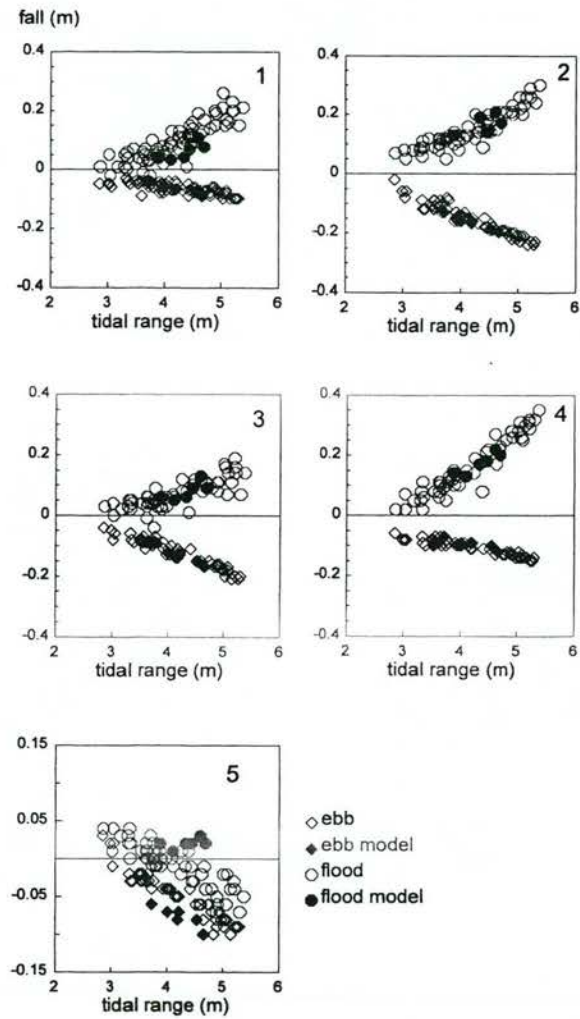


Figure 4 Computed and observed falls during maximum flow versus tidal range

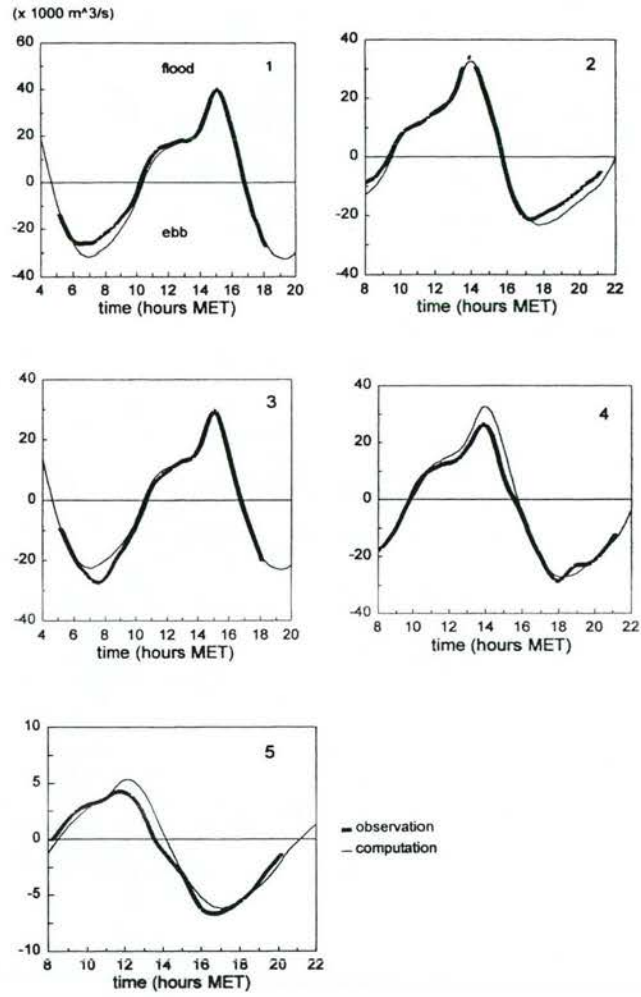


Figure 5 Computed (thin line) and observed (thick line) discharges in the five channel sections based on discharge transect 2,3 and 4 (for see Fig. 1 and 2)

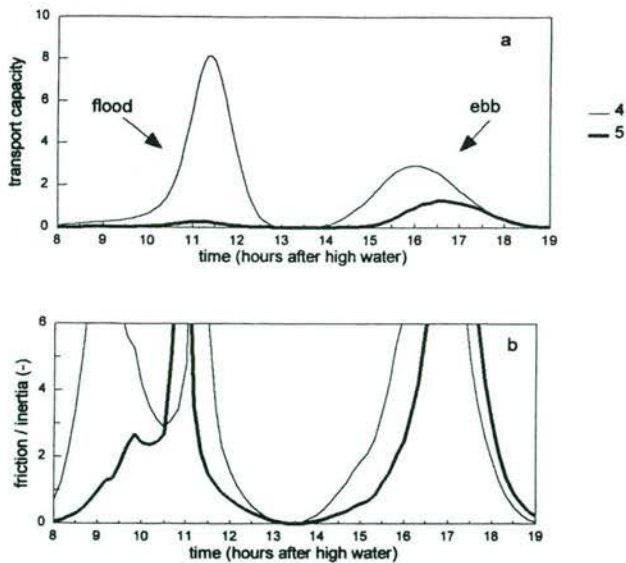


Figure 6 The character of tidal flow. a. transport capacity. b. relative magnitude of friction

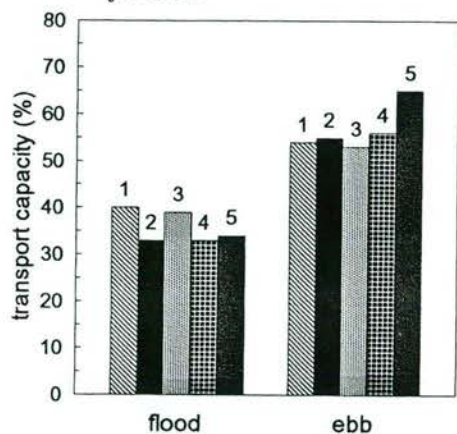


Figure 7 Fraction of sediment transport during the bed-forming conditions

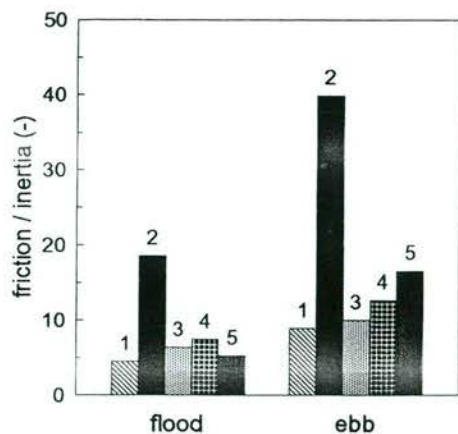


Figure 8 Relative magnitude of friction during the bed-forming conditions.

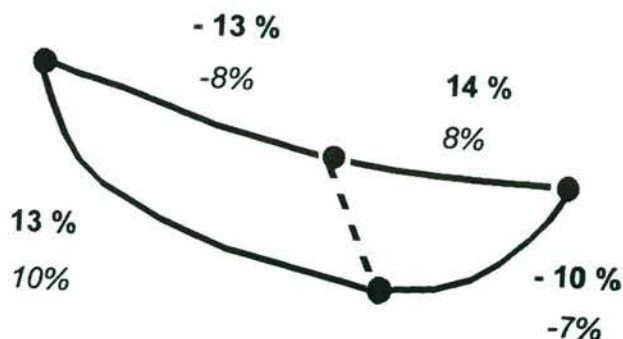


Figure 9 The influence of the connecting channel on the flow pattern in the main channels. Velocity changes due to the removal of the connecting channel (eq. 3.4). 10% = ebb, 10% = flood.

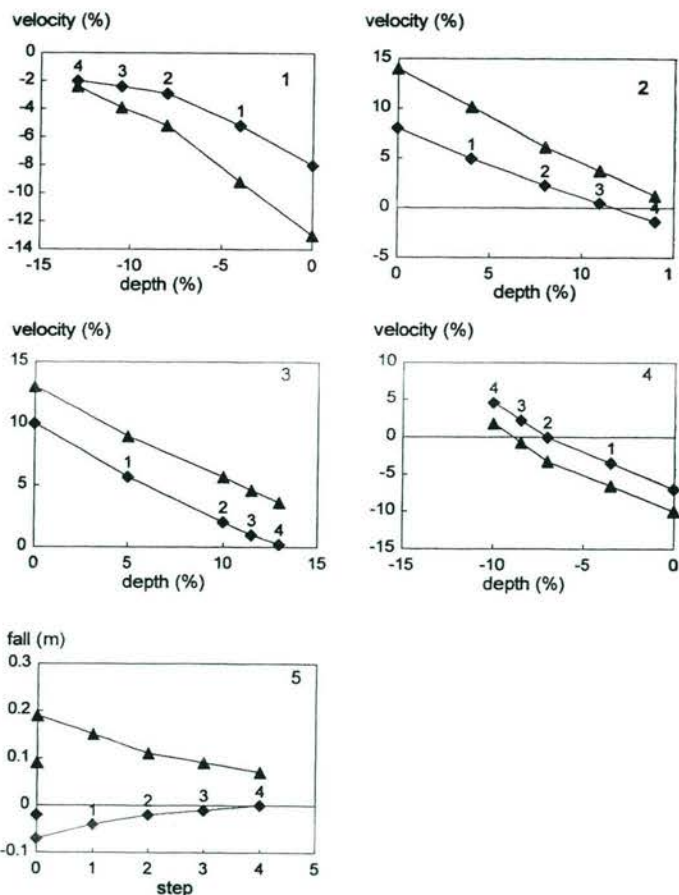


Figure 10 Changes in velocity pattern and falls (\triangle = ebb, \blacklozenge = flood) due to the adjustment of the hydraulic geometry of the main channels.

